Marshall Space Flight Center Faculty Fellowship Program

N.F. Six, Program Director
Marshall Space Flight Center, Huntsville, Alabama

G. Karr, Compiler
The University of Alabama in Huntsville, Huntsville, Alabama

The NASA STI Program…in Profile

Since its founding, NASA has been dedicated to the advancement of aeronautics and space science. The NASA Scientific and Technical Information (STI) Program Office plays a key part in helping NASA maintain this important role.

The NASA STI Program Office is operated by Langley Research Center, the lead center for NASA's scientific and technical information. The NASA STI Program Office provides access to the NASA STI Database, the largest collection of aeronautical and space science STI in the world. The Program Office is also NASA's institutional mechanism for disseminating the results of its research and development activities. These results are published by NASA in the NASA STI Report Series, which includes the following report types:

- TECHNICAL PUBLICATION. Reports of completed research or a major significant phase of research that present the results of NASA programs and include extensive data or theoretical analysis. Includes compilations of significant scientific and technical data and information deemed to be of continuing reference value. NASA's counterpart of peer-reviewed formal professional papers but has less stringent limitations on manuscript length and extent of graphic presentations.

- TECHNICAL MEMORANDUM. Scientific and technical findings that are preliminary or of specialized interest, e.g., quick release reports, working papers, and bibliographies that contain minimal annotation. Does not contain extensive analysis.

- CONTRACTOR REPORT. Scientific and technical findings by NASA-sponsored contractors and grantees.

- CONFERENCE PUBLICATION. Collected papers from scientific and technical conferences, symposia, seminars, or other meetings sponsored or cosponsored by NASA.

- SPECIAL PUBLICATION. Scientific, technical, or historical information from NASA programs, projects, and mission, often concerned with subjects having substantial public interest.

- TECHNICAL TRANSLATION. English-language translations of foreign scientific and technical material pertinent to NASA's mission.

Specialized services that complement the STI Program Office's diverse offerings include creating custom thesauri, building customized databases, organizing and publishing research results…even providing videos.

For more information about the NASA STI Program Office, see the following:

- Access the NASA STI program home page at <http://www.sti.nasa.gov>

- E-mail your question via the Internet to <help@sti.nasa.gov>

- Phone the NASA STI Help Desk at 757–864–9658

- Write to:
  NASA STI Information Desk
  Mail Stop 148
  NASA Langley Research Center
  Hampton, VA 23681–2199, USA

Marshall Space Flight Center Faculty Fellowship Program

N.F. Six, Program Director
Marshall Space Flight Center, Huntsville, Alabama

G. Karr, Compiler
The University of Alabama in Huntsville, Huntsville, Alabama

Acknowledgments

TRADEMARKS

Available from:

NASA STI Information Desk
Mail Stop 148
NASA Langley Research Center
Hampton, VA 23681–2199, USA
757–864–9658

This report is also available in electronic form at
<http://www.sti.nasa.gov>

EXECUTIVE SUMMARY

The Marshall Faculty Fellowship program was revived at NASA Marshall Space Flight Center (MSFC) in the summer of 2015, following a period of demise starting in 2006 when budget cuts in the Headquarters' Education Office required realignment. Several senior MSFC Managers recognized the need to involve the nation's academic research talent in NASA's missions and projects to the benefit of both entities. These managers invested their funds to establish the Marshall Faculty Fellowship program in 2015. The 2016 program involved 19 faculty in the laboratories and offices at MSFC. These faculty engineers and scientists worked with NASA collaborators on NASA projects, bringing new perspectives and solutions to bear.

This Technical Memorandum is a compilation of the research reports of the 2016 Marshall Faculty Fellowship program, along with the Program Announcement (Appendix A) and the Program Description (Appendix B). The research touched the following six areas: (1) propulsion, (2) materials, (3) spacecraft systems, (4) vehicle systems, (5) science and technology, and (6) test.

The propulsion studies included the water hammer effect, equations of state, bubble transport, and green propellants. The materials investigations involved iodine plasma effects, friction stir welds, and plug welding. Spacecraft Systems research was conducted on wireless technologies, close-proximity sensors, and aerosol jet 3D printing of avionics. Vehicle Systems studies were performed on small satellite formation control, Near Earth Asteroid Scout Mission instruments—sun sensors and inertial measuring units—and Iodine Satellite. The Science and Technology group investigated additive construction applied to Mars and lunar resources, medical uses of 3D printing, detection of solar neutrinos, a new gamma-ray burst polarimeter, and lightning observations using interferometers and mappers, while the test laboratory measured pressure vessel leakage and crack growth rates. Our goal is to continue the Marshall Faculty Fellowship program with Center funds in succeeding summers.

TABLE OF CONTENTS

2016 Marshall Faculty Fellows

From Left to Right:
    Row 1—F. Six, K. Zuo, J. Schneider, H. Alkhateb, A. Mazzeo, R. Branam
    Row 2—D. Bullock, E. Colllins, R. Sonnenfeld, C. Coates, A. Carrano, A. Bandyopadhyay
    Row 3—R. Damiani, R. McTaggart, R. Preece, A. Abedi, Z. Deng, S. Whitmore, C. Wu, F. Fahimi,
        G. Karr
Not shown: D. Edberg

Wireless Technology Use Case Requirement Analysis for Future Space Applications

Ali Abedi[1]
University of Maine, Orono, ME, 04469

DeLisa Wilkerson[2]
NASA MSFC, Huntsville, AL, 35812

Abstract

This report presents various use case scenarios for wireless technology -including radio frequency (RF), optical, and acoustic- and studies requirements and boundary conditions in each scenario. The results of this study can be used to prioritize technology evaluation and development and in the long run help in development of a roadmap for future use of wireless technology. The presented scenarios cover the following application areas: (i) Space Vehicles (manned/unmanned), (ii) Satellites and Payloads, (iii) Surface Explorations, (iv) Ground Systems, and (v) Habitats. The requirement analysis covers two parallel set of conditions. The first set includes the environmental conditions such as temperature, radiation, noise/interference, wireless channel characteristics and accessibility. The second set of requirements are dictated by the application and may include parameters such as latency, throughput (effective data rate), error tolerance, and reliability. This report provides a comprehensive overview of all requirements from both perspectives and details their effects on wireless system reliability and network design. Application area examples are based on 2015 NASA Technology roadmap with specific focus on technology areas: TA 2.4, 3.3, 5.2, 5.5, 6.4, 7.4, and 10.4 sections that might benefit from wireless technology.

Nomenclature

b/s	=	bit per second
dB	=	decibel
E_b	=	energy per bit
G	=	giga
Hz	=	Hertz
k	=	kilo
K	=	temperature unit in Kelvin
M	=	mega
N_0	=	noise power spectrum density
S	=	Sample
s	=	second

I. Introduction

This report integrates input from 2015 NASA Technology Roadmap[1], NASA Technical reports, and recent developments in wireless communications research area as relates to space applications. An introduction to wireless communications and networking area including both sensing and communications applications is presented in this section. Basic definitions of parameters characterizing a wireless system is also defined in this section. One of the widely used family of wireless standards is IEEE 802, which includes 802.11[2] (used in WiFi), 802.15.1[3] (Bluetooth), and 802.15.4[4] (ZigBee). Due to high consumer demand for WiFi and Bluetooth devices and industry

---

[1] Professor, Electrical and Computer Engineering Department, University of Maine.
[2] Branch Chief, Electronic Design Branch (ES36), NASA Marshall Space Flight Center.

need for ZigBee networks, necessary components to build a working system can be obtained at low cost with high reliability. This includes transceiver chips, break out boards, interfaces, and antennas. The down side of using popular technologies such as IEEE 802.11 (WiFi) is interference caused by increasing number of users, devices, and demand for bandwidth. Although, WiFi has 14 channels to scan and choose the least crowded one, but in reality only 3 of those channels are non-overlapping and truly interference free at any given time[5] (fig. 1).
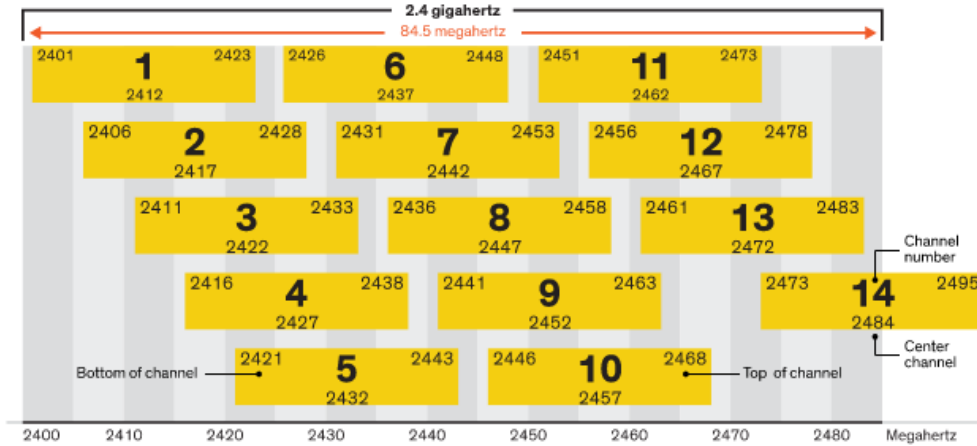
Figure 1. Illustration of 14 available and 3 non-overlapping (at any specific time) WiFi channels.

Some other members of this family of standards are 802.15.3[6] (high data rate WPAN: wireless personal area network) and 802.16[7] (WiMAX). The former is faster version of ZigBee for applications that require higher throughput such as video transport network, while the latter is used for mobile and fixed high speed access at long ranges. WiMAX is not well adopted in the US, where LTE (Long term evolution) and LTE-A (advanced) are currently used with LTE-U (unlicensed) scheduled to hit the market in near future. WiMAX is heavily used in India and a slightly modified version called WiBro was rolled out in South Korea. The main differences between WLAN (Wireless Local Area Network) standards such as WiFi and WPAN standards such as ZigBee are: Power consumption; Coverage; Device type; and Network lifetime. WLAN has much larger lifetime, coverage area, and consumes more power as compared to WPAN, which is often deployed for a short period of time using simple and low power devices. More details on Bluetooth and ZigBee protocols based on IEEE 802.15 family of standards are presented next.
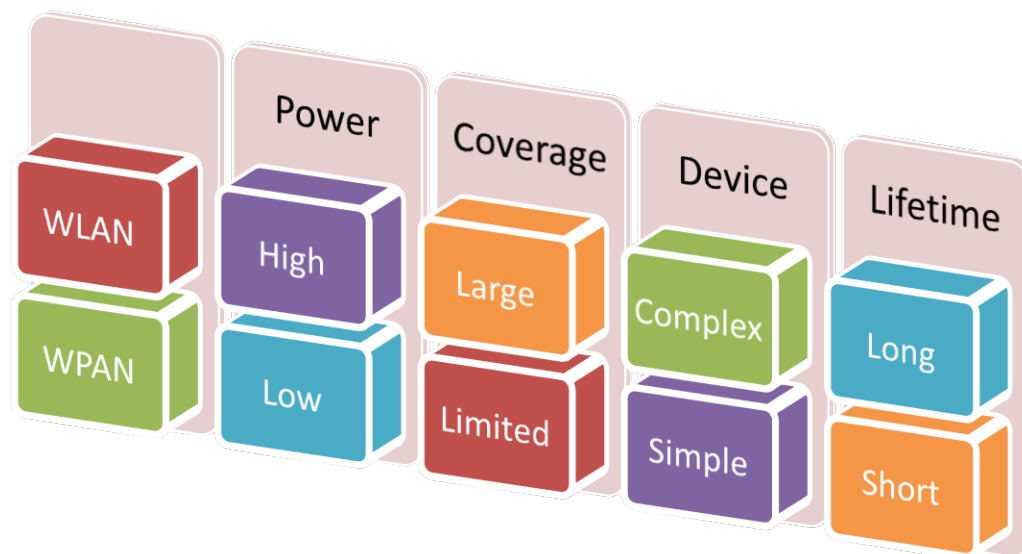
Figure 2. Comparison between WLAN and WPAN.

A. Bluetooth Physical Layer and Interference Challenges

Bluetooth physical layer is based on IEEE 802.15.1, operating at 2.4 GHz using Frequency Hopping (FH) scheme and can achieve 1 MS/s with Gaussian Binary frequency shift keying modulation (GFSK). Resource sharing is managed using time domain duplexing (TDD) and its effective one-way data rate is 732.2 kb/s. This is achieved with 0 dBm transmit power over a 10 m range. Increasing the power to 20 dBm extends the range to 100m for long range applications. Data delivery is protected against error and packet loss using forward error correction codes of rate 1/3 and 2/3 and automatic retransmission request (ARQ) in a fast unnumbered manner. Two way 128 bit authentication and 128 bit payload cipher is complimented with a PIN based user initiated process for added security.
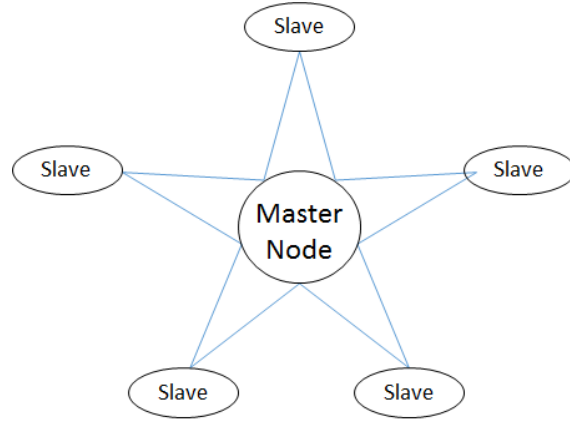
Figure 3. Bluetooth Master-slave structure.

Networking of up to 7 active or 200+ inactive devices connected to a single Master node is provisioned in the standard. The main concern when using WPAN 802.15.1 in presence of infrastructure based WLAN 802.11 (WiFi) is interference. WPAN hops into 22 out of 79 sub-channels used by WLAN. This causes the WLAN to experience interference too, hence increasing temporal duration of its packets, which in turn causes more and more interference to WPAN leading to less and less data rate for both networks. This interference problem between WPAN and WLAN may be addressed in multiple ways. The first order approach is for WLAN to avoid 24 sub-channels (including two adjacent to the 22 used by WPAN), but that leads to fixed decrease in throughput and increase in latency. Several collaborative and non-collaborative coexistence mechanism such as Alternating wireless medium access (AWMA), packet traffic arbitration (PTA), and deterministic interference suppression (DIS) have been proposed in the literature to address this issue. For more details on these methods refer to IEEE standard 802.15.2[8].

B. ZigBee Physical Layer and Its Applications

ZigBee physical layer is based on IEEE 802.15.4, operating at 868 MHz, 915 MHz, and 2.4 GHz at 20, 40, and 250 kb/s rates with 1, 10, and 16 available channels, respectively. The lower frequency bands utilize binary phase shift keying (BPSK) and direct sequence spread spectrum (DSSS) with differential encoding and raised cosine pulse shaping, while the higher frequency band communicates 32 chips PN sequences using offset quadrature phase shift keying (OQPSK) modulation and half-sine pulse shaping. Transmit power of -3 dBm provides a low power short range (few 100 ft) networking that can support mesh and ad hoc networking. Both secure (7 security suites are available) and unsecured operation modes

Figure 4. ZigBee mesh network structure.

are available. Secure mode include authentication and key establishment, access control list, data encryption, and frame integrity. Resources are shared the medium access control layer (MAC) using carrier sense multiple access with collision avoidance (CSMA/CA) and random back off timer.

ZigBee supports mesh networking and is scalable to a large network with the following provisions. The data sampling rate should be kept to a minimum in networks with large number of sensors to minimize the effect of interference/collisions, which may prevent nodes from finding open slots in the network for transmitting their packets. The number of hops between information source and network sink or data processing center should also be

kept to a minimum to preserve data quality and avoid unbalanced power consumption in the network. It should be noted that nodes at the edge of the network needs to be designed with different capabilities and resources as compared to the ones in the center. High data rate WPAN and WiFi have similar characteristics and mainly used when power consumption is not limited and high data rates are required. Portable devices (that can be moved but needs to be normally plugged in) mostly use these standards as compared to mobile devices that often use low power solutions such as ZigBee and Bluetooth. Therefore, this section does not elaborate more on 802.15.3 and 802.11 and refers the reader to IEEE standards.

C. Basic Parameters of a Wireless System

Power consumption and bandwidth requirements are the first parameters that come to mind when reviewing requirements of a wireless application. However, in order to evaluate performance and reliability of wireless systems in a network setting more detailed parameters need to be considered. In a point to point analog communication link, the main measure of channel quality or link reliability is signal to noise ratio (SNR). This parameter can be augmented to include interference in a networked environment (SINR). Modern digital communication systems have replaced conventional analog systems in recent years due to their high spectrum and power efficiency. Therefore, the focus of this section will be on performance indicators of digital communication systems. Each data source needs to be sampled and digitized before entering a digital wireless system. The information content of the source or bandwidth of the analog signal dictates sampling rate, and accuracy requirements guide the digitization resolution. For instance, phone quality voice with 4 kHz bandwidth sampled at 8 kHz and quantized with 8 bits/sample renders a 64 kb/s digital stream at the input of a wireless communication system. This digital data can be compressed (source coding) to remove redundancy and then encoded (channel coding) to be protected against noise and interference and modulated using a high frequency (RF) signal for longer range transport in the network. The first parameter for performance evaluation of such a system is called BER or bit error rate. For example, 3 bits error in a million bit stream results in BER = 3E-6. In multiuser networked systems, collision may occur, which can cause packet loss (PL). This is another parameter used for performance evaluation of a networked system. Environmental conditions and settings that a wireless system is designed for can yield to modeling the stochastic wireless channel using some of the widely used channel models. This allows for BER and PL estimation using simulation tools such as MATLAB (Mathworks Inc.) before a system is implemented and tested. Additive White Gaussian Noise (AWGN) channel is the most widely used model in fixed networks. In mobile networks with multipath fading and several scattered signal beams, Rayleigh channel model is a good fit. Adding a strong line of sight to the scattered signals, Rician model becomes a better fit. Depending on the application scenario, environmental conditions, and users' location and behavior one of these models may be preferable over the others. An example is provided in the figures below, where the standard ZigBee system is enhanced by adding an optimized error correction code. BER performances are evaluated over AWGN (left) and Rayleigh fading (right) channels[9]. This shows how significant reliability can be achieved at very low cost.
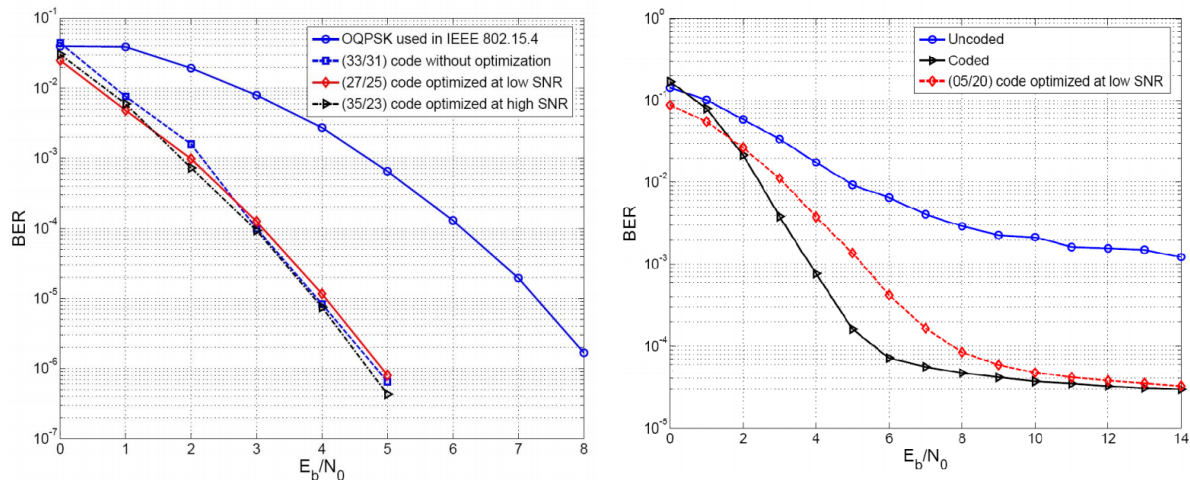

Figure 5. BER Performance of un-coded IEEE 802.15.4 and coded version with optimized error correction code over AWGN (left) and Rayleigh Fading (right) channels.
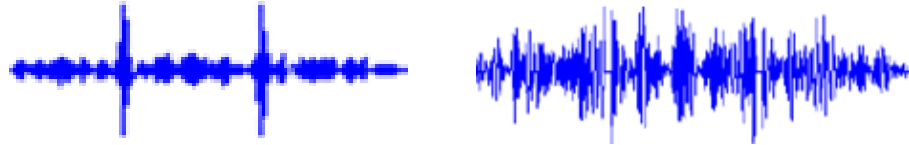
Figure 6. Responses of a single passive sensor (left) vs aggregate response of multiple passive sensors (right).

Measuring reliability of a wireless network not only depends on reliability of each individual link, but also on the network ability to manage interference. Another example is provided to demonstrate how to measure reliability of a passive wireless sensor network by looking at the aggregate interference. Figure 6 shows a single sensor response (left) with main information in the two peaks locations and aggregate response of multiple sensors (right) where peaks are not easy to detect any more being buried in side lobes.

To measure the reliability of a single link, a new parameter such as peak to side-lobe ratio (PSLR) may be defined much like signal to noise ratio in analog communication links. The higher the PSLR, the lower the chance of losing peak locations in multi-sensor response in a network. Extending this concept to network reliability measurement, ratio of PSLR to absolute power of side-lobes (on average or to be conservative on maximum sense) determines how many sensors can operate in such a network with acceptable reliability without any interference cancellation. Methods such as the one presented in[10] may be used for managing the interference, hence increasing the number of sensors in such a network.

II. Use Case Scenarios and Environmental Requirements

This section introduces space related use case scenarios that may benefit from wireless technology. These include (i) Space Vehicles (manned/unmanned), (ii) Satellites and Payloads, (iii) Surface Explorations, (iv) Ground Systems, and (v) Habitats. Some common environmental conditions to space applications according to a recent study at NASA MSFC include[11]: High Radiation (10krad – 1Mrad); Cryogenic Temperatures (H_2: 20K; O_2: 90K; CH_4: 112K); High Temperatures (400K-3000K); and Harsh chemical environments. Each use case scenario and its specific boundary conditions relevant to wireless system design are presented next.

A. Space Vehicles

Space vehicles operate in extreme conditions with notable vibrations on their various sub-systems, which might exclude or limit usage of specific types of sensors and electronics such as micro-electro-mechanical systems (MEMS). Monitoring critical systems such as thermal and pressure systems, cryogenic fluid management, Heating Ventilation and Air Conditioning (HVAC), Environmental Control and Life Support System (ECLSS), Lighting Monitoring, Docking, and Rendezvous systems require specific considerations as follows. Most of these systems are in hard to reach areas that are not easily accessible. The wireless system design need to accommodate operations in confined spaces and often closed metallic chambers or sometimes even inside fluid environments at cryogenic temperatures (wireless acoustic or low frequency magnetic coupling might be considered in these situations). A recent work at NASA MSFC demonstrated proof of concept for wireless sensing inside a fuel tank[12]. Monitoring the engine and heat shield requires sensors that can operate in high temperature environments with harsh chemical vapors present. Constant monitoring of pressure and temperature at various locations of the engine can assist in real-time performance measurement and dynamic performance control using sensors and actuator networks. Usage of RF signals and electronics in close proximity of fuel lines and tanks in launch vehicles should be reviewed from safety point of view to avoid any potential case of RF waves heating up fuel or causing sparks or premature ignitions. This is not a critical concern and can be avoided by careful design, placement and insulations.

Challenges:
- Wide range of temperature variations and Vibration tolerance
- Accessibility in confined environments
- Signal propagation in metallic enclosures

Benefits:
- Acquiring more data from supporting structures and engine itself
- Reducing weight due to cable elimination
- Dynamic performance control with wireless sensing and actuation

B. Satellites and Payloads

Satellites and payloads operate in harsh environment and often require monitoring and protection against extreme temperature changes and radiation. Whether using radiation hardened hardware or adding internal heaters or coolers to keep the equipment in desirable environmental condition, it is necessary to monitor the internal temperatures and radiation doses at all times. Although, it may not make sense to replace a short few cm wire inside a small satellite with wireless, for some applications where drilling a hole in the payload or satellite's exterior body may lead to loss of heat and energy, short range magnetic coupling wireless solutions will become important. Other applications include monitoring external solar arrays for MMOD impact or damage evaluation as well as transferring power between two disjoint sections.

Challenges:
- Wide range of temperature and radiation variations
- Size and weight limitations
- Signal propagation in metallic enclosures
- Power constraints

Benefits:
- Wireless connection between two disjoint sections
- Reducing heat loss by avoiding drilling holes
- More efficient use of harvested power

C. Surface Explorations

Autonomous exploration of planetary surfaces may require machine vision and robotics arms to recognize various object types and manipulate them, drill ground to collect soil samples, and navigate to return samples to the base. All these applications can benefit from wireless sensors. For instance, Infrared sensors can be used alongside visible light cameras for object detection and classification and assisting the robotics arms to maneuver accurately. Humidity and temperature sensors can be used during ground drilling, while vibration sensors can monitor the drill operation. Navigation without Global Positioning System (GPS) on planetary surfaces requires dedicated active wireless links with precise time of arrival measurements (e.g. one example is the ultra-wide-band (UWB) radios developed at NASA JSC[13]). Other techniques such as passive radio frequency identification (RFID) tags and readers may also be used to find assets in known areas pre-marked with tags.

Challenges:
- Capability to operate and survive dust or radiation storm
- Mobile chemical and biological sensor units
- Long range reliable link back to base with navigation capabilities

Benefits:
- In situ testing of samples
- Navigation without need for GPS
- Dynamic control of robotic arms using wireless sensors and actuators

D. Ground Systems

Ground testing often requires structural sensors such as strain gauges, accelerometers, and deflection sensors. Testing fuel tanks may require leak detection sensors, hydrogen (or other gas) sensors, humidity, and temperature sensors. Performance tests are conducted in controlled environment with thermal cycles that mimic space conditions. Therefore, all these instrumentation, although used on earth, need to be capable of operating in harsh environments. Wiring and cabling may be cumbersome, costly, or may be infeasible in some cases. Therefore, wireless sensing in ground system can open up lots of new opportunities to gather critical data.

Challenges:
- High precision in sampling and data transfer
- Interference management among large number of sensors sending data
- Working within limitations of test setup at specific distances

6

Benefits:
- Acquiring more data for structural analysis that is not possible using wires
- Reducing cost of tests due to cabling elimination
- Flexibility of test for adding more sensors later without redesigning the whole wiring plan
- Versatility in programming test beds for future tests

E. Habitats

Autonomous monitoring of habitats, living conditions, and inventory tracking are the main use case scenarios that can benefit from wireless technology. RFID based inventory tracking methods for autonomous logistical management (ALM) is being developed at JSC and can tie into the habitat monitoring itself. Integrating sensors as load on RFID devices and reading the changes in the response in addition to ID numbers is a promising approach in this direction. Monitoring living conditions including physical (temperature, humidity, and radiation), chemical (air and water quality) and biological (mold and mildew or other airborne bacteria) are some critical applications that benefits from wireless sensors. Another important aspect of monitoring habitat systems is evaluating cognitive changes of its inhabitants, i.e. crew health monitoring. Real time vital signs tracking and wireless sensors for sleep behavior monitoring are essential for ensuring mission success. For more info on habitat systems refer to section 3.6 in this report.

Challenges:
- Wide range of temperature and radiation variations
- Aggregation challenges in multi modal sensor data with different sampling rates and precisions
- Signal propagation in metallic enclosures

Benefits:
- Acquiring more data from habitat structure
- Reducing weight due to cable elimination
- Flexibility of change in design and sensor location after the deployment

III. Application Specific Requirements

In this section application specific requirements from data transport and reliability points of view are studied. Application area examples are based on 2015 NASA Technology roadmap with specific focus on the following technology areas: TA 2.4, 3.3, 5.2, 5.5, 6.4, 7.4, and 10.4 sections that might benefit from wireless technology[1]. Each section starts with the definition of the technical area followed by discussion of current and future technologies that might benefit this area.

A. TA2.4: Engine Health Monitoring

"TA2.4.1: Use of simulation and data processing to determine and mitigate operational, safety, and reliability risks and issues in the propulsion system. In general, the key metrics for health monitoring for in-space propulsion are reliability, weight, and cost."

This technology area is closely connected to section 2.1 on this report titled: Space Vehicle. A combination of wireless solutions such as RF, optical, and Acoustic may be needed to cover all subsystems of a space vehicle in a reliable manner. Most sensors used in these applications such as temperature, pressure, fuel level, and gas sensors are low data rate with the exception of engine health monitoring, which requires high speed sampling of accelerometers or load sensors. Operation in extremely low or high temperature may require specially coated material to withstand those temperatures. Some technologies such as SAW devices may be a good potential for these applications at extreme temperatures[14,15,16,17].

Video monitoring of environment for short duration events or monitoring vehicles for performance verification is also of interest in space applications. For example, a short video of landers thrusters sent to control station for verification purposes can help in improving design and real time performance adjustments. High data rate WPAN standards such as IEEE 802.15.3 are good standards suitable for these kind of applications.

B. TA3.3: Wireless Power Transmission

"TA3.3.4: This area describes needed enhancements in short-range, low power wireless power transmission for battery charging and instrumentation and in longer range, high power surface element applications."

Wireless power transfer for remote operation of battery-less sensors has received recent attention. Either for short range applications (near field magnetic coupling) or longer range operations (RF energy harvesting), some commercial systems offer practical solutions. The transmitted power in both cases will be used to power a remote unit and get data for a short period of time. NASA MSFC in collaboration with JACOBS have demonstrated short and medium range systems based on commercial and custom made near-field coupling systems. Efficient antenna design with phased-array steering beam capabilities can be used to extend the range of such systems, while focusing the power more efficiently. Transmission scheduling is also another technique presented in this report that is capable of achieving longer lifetime for remotely communicating nodes for a fixed transferred power. The idea is based on the fact that wireless channel is not always reliable and occasionally packets are lost or received with errors beyond correction capabilities of the receivers. If the remote transmitter considers its current energy level and wireless channel condition to determine whether it is best to transmit or wait until next time slot, the harvested power will not be wasted on transmitting a packet with low chance of delivery. Simulation results demonstrate lower outage probabilities may be achieved if an acceptable channel threshold is used to guide decisions at the transmitter.

C. TA5.2: Radio Frequency Communications

"Radio Frequency (RF) Communications strives to dramatically accelerate techniques in use today for NASA's missions. RF technology development concentrates on getting more productivity out of the constrained spectrum bands that are allocated to space users. Although it is quite a bit more mature than optical communications, there is still a great deal of promise for technology breakthroughs in the RF domain. The focus of RF technology development will be on the RF spectrum allocated and needed for space use by the International Telecommunication Union (ITU), where adequate bandwidth would provide a useful service, or where the application is beyond the near-Earth environment."

Although spectrum-efficient and power-efficient technologies are separated into two categories in this technical area, they are not precluded from being used together in an integrated manner. If the propagation model is properly selected, spectrum efficient modulation and RF front end can be designed to take the most advantage of the channel. Power efficiency can be achieved in one layer below, i.e. the baseband of physical layer, where error correction codes can be used to achieve a desirable bit error rate with much less transmit power. All these sub-systems of an RF communication unit have to work seamlessly and efficiently with antenna system. Antenna needs to be efficient in terms of power transfer (matching circuitry), while it can play an integrated role in advanced coding schemes such as Space-time codes implemented over multiple-input multiple-output (MIMO) systems.

One recent hot research topic in RF communication is full duplex. Motivated by ever increasing demand for data rate and throughput, number of users/nodes, and limited spectrum and acceptable latency values, researchers are looking at new ways to increase the RF communication system capacity and achievable throughput. Current RF transceivers operate in half-duplex mode, meaning that they can not simultaneously transmit and receive on the same frequency band. The transmitter and receiver either transmit at different times or on different frequencies. The potential to use both time slots and frequencies to simultaneously transmit and receive is tempting researcher for an easy way to achieve double data rate. The challenge is the several orders of magnitude difference between transmitted and received signals, making it almost impossible for the receiver to detect low power received RF signal in presence of high power interfering transmitter signal. Highly accurate echo cancellation methods at antenna level, analog RF front end, and digital baseband levels need to work hand in hand to make full duplex a reality.
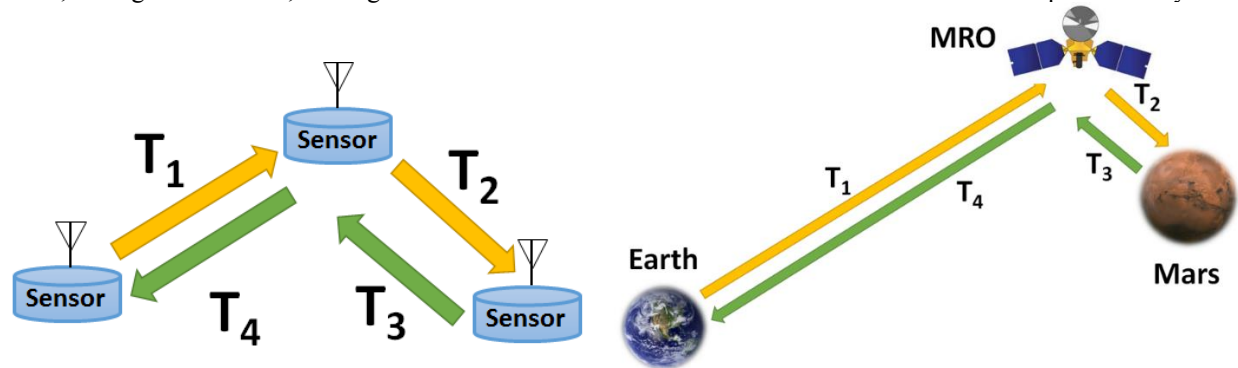

Figure 7. Four step packet exchange in traditional two way relay channel between wireless sensors (left) and Earth and Mars via MRO (right).

For deep space application, due to large distances between two communicating entities, latency is of critical importance. The full duplex method can potentially cut latency in half, enabling new applications and faster data exchange rates. Another method to double the throughput or cut the latency in half is called network coding. Due to large distances in space applications, exchanging data between two RF nodes often requires a relay and at least 4 time slots (fig. 5). As an example, Earth to Mars communication through Mars Reconnaissance Orbiter (MRO) is considered in this section.

The first time slot is used by the ground station to send its packet to the MRO (serving as relay) that will forward that data to Mars surface station in the second time slot. The same process is followed by Mars surface station to send its packet to earth via MRO. Network coding can be used to enhance throughput by a factor of two, when both Earth and Mars nodes send their data at the same time to the MRO to later broadcast the superimposed signals back to them. In this case, each node can extract the other packet using a simple mathematical operation. Network coding can be performed at network layer or physical layer. A simple XOR operation at the network layer can provide notable efficiency as compared to traditional two-way relay channels without network coding. However, significant throughput enhancement can be achieved if physical layer network coding is used[18]. This method is applicable to both deep space communication networks and short to medium range wireless sensor networks.

D. TA5.5: Cognitive Networks

"TA5.5.3: Cognitive Networks: Communications system in which each communications node on the network is dynamically aware of the state and configuration of the other nodes to autonomously optimize their operational parameters in response to changes in user needs or environmental conditions."
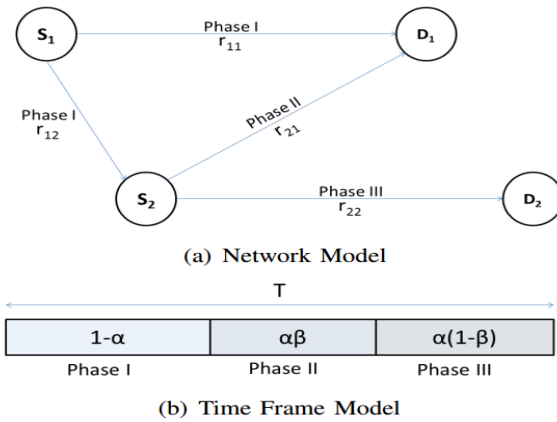

(a) Network Model

(b) Time Frame Model

Figure 8. Network (top) and Time frame (bottom) model for cognitive cooperation scheme.

Scarce spectrum calls for an efficient method for sharing among multiple users. A large scale network with multiple nodes and various traffic priorities may render a complicated optimization problem to solve the resource allocation challenge. In space applications often two types of critical and non-critical sensors are utilized. Allocating dedicated spectrum to critical sensors ensures their operations is carried out with desired high reliability. On the other hand, non-critical sensors can use the same spectrum provided when it is not in use by critical sensors. Game theoretical approaches offer a tractable solution to analyze such systems[19]. Assuming different users with different priorities, as depicted in Figure 1, lower priority users (S_2) may act as relay for higher priority users (S_1) during a portion of each time slot ($\alpha\beta$) to increase their throughput and open up more opportunities in future time slots for low priority users to send their data. Ensuring that a dedicated portion of time slot ($1-\alpha$) is allocated to high priority users, guarantees their cooperation in this game theoretical resource allocation scheme. This combined cooperative and cognitive radio approach may be the key for future implementation of cognitive networks. Noting that complete interference alleviation is unavoidable, if high priority traffic from critical users are always prioritized over less sensitive traffic, low priority users can never get any data across. Cooperative relaying is the price that low priority users pay to gain access to the spectrum during a predetermined ($\alpha(1-\beta)$), but dynamic portion of each time slots.

E. TA6.4: Environmental Monitoring and Sensors

"TA6.4.1: Sensors: Air, Water, Microbial, and Acoustic: The objective of this area is to provide future spacecraft with advanced, networks of integrated sensors to monitor environmental health and accurately determine and control the physical, chemical, and biological environments of crew living areas and their environmental control systems."

This section is closely connected to section 3.1 of this report. Sensors and wireless systems required for environmental monitoring inside the vehicle or habitats (see sections 2.1 and 2.5 of this report) can be designed with less stringent requirements as opposed to engine health monitoring system. The interior environment is mainly shielded from extreme thermal fluctuations and radiations, but pose other challenges such as multi-path reflections and scattering of wireless signals no matter if they are RF, acoustic, or even optical (which requires line of sight).

F. TA7.4: Habitat Systems

"TA7.4.1: Integrated Habitat Systems: Addresses acoustical treatments and noise reduction; solar optic lighting and heating; low-toxicity, fire-retardant textiles; antimicrobial and surface coatings; and embedded sensors that monitor system performance. Additional dependency technologies that support Integrated Habitat Systems capabilities are being developed under other technology areas, such as TA 4 Robotics and Autonomous Systems, TA 6 Human Health, Life Support, and Habitation Systems, TA 8 Science Instruments, Observatories, and Sensor Systems, TA 11 Modeling, Simulation, Information Technology and Processing, and TA 12 Materials, Structures, Mechanical Systems and Manufacturing."

Figure 9. Exterior view (left) and inside view (right) of Inflatable lunar habitat (42 ft diameter 10 ft high concentric torus) designed and built by NASA JSC and instrumented with wireless sensors by University of Maine's WiSe-Net Lab team.

This section is closely connected to section 2.5 of this report, where design requirements and environmental conditions of habitats are discussed. Figure 9 shows the outside and inside views of NASA's inflatable lunar habitat, a 42 ft diameter concentric torus that is built by NASA JSC and instrumented by the University of Maine's WiSe-Net laboratory researchers with 124 passive and 48 active sensors. These sensors monitor the structural integrity of the habitat. They localize impact, find leaks, and track temperature and humidity. The results are visualized on a tablet app with easy to view data using a multi-color heat map.

This example demonstrates what can be done with current technology when it comes to monitoring habitat systems. Other types of habitats such as the ones at NASA MSFC made of metal or wood (vs fabric) may require other modes of communications, being RF or acoustic or even optical depending on the use case. The interior size and shape of a metal cavity will determine the best frequency to use and what frequencies to avoid. The inflatable example is a great test-bed for technology demonstration as well as outfitting exercise including human factors perspective.

It is important that both wireless technology developers and human factor researchers work together when creating monitoring systems for habitats. Other monitoring needs in habitats that might benefit from wireless sensing are biological sensing of air and habitat interior to prevent bacteria growth on the interior walls due to condensation and chemical monitoring of air and water systems using wireless sensor for added spatial and temporal resolution without adding too many extra wires.

G. TA10.4: Sensors and actuators

"TA10.4.1: Sensors and Actuators: Nanotechnology-based sensors include systems for the detection of chemical and biological species to support planetary exploration and astronaut health, in addition to state (temperature, pressure, strain, damage) sensors for use in vehicle health management. Nanotechnology can lead to low-volume, less invasive sensors and actuators with better performance and lower power demand for new designs of morphing vehicle control surfaces, rovers, and robotic systems."

Eliminating wires from sensors and actuators network will certainly presents significant savings in weight and cost. However, new challenges need to be overcome before this approach becomes a reality. Several applications of sensors and actuators requires a feedback control system to act on sensed data in a timely fashion and still remain

stable. Wireless feedback control systems with noise and delay in feedback link are studied recently[20]. The effect of noise in the wireless channel is modelled using AWGN noise, while delay is assumed to be constant (a function of end to end wireless system delay). Preliminary results indicate that new controllers can be designed to operate satisfactorily in these environments as long as the noise and delay are below specific thresholds. This is an ongoing research area with more results to emerge soon. Although the focus of this technical area TA 10.4 is on nano-sensors, but it is noteworthy to mention that micro-sensors capable of detecting bio-chemical species are also a viable candidate to consider for sensor actuator networks. Technologies such as surface acoustic wave with thin film deposited on their exterior surface can be designed to be sensitive to a variety of physical, chemical, or biological substances.

IV. Implementation Roadmap

Depending on various applications and their operational environment, a specific wireless technology may be more desirable from power, spectrum efficiency, reliability, and cost points of view. This report also considers network architectures and their scalability (for future expansion) and flexibility (programmable and fault tolerance). Heterogeneous wireless networks with fall back provisions enhance the overall link reliability.

The future of space exploration is being built on space launch system (SLS) which is not designed for a specific mission, but rather for developing capabilities to be able to adopt to various deep space missions. It makes sense to develop a wireless sensing system with the same vision, not for a specific application, but rather with a modular design that can be tailored to various applications needs. Different radio technologies that were presented in this report, along with multiple sensor types, and various ways of powering them including some interfaces in between create a flexible architecture for data communication with no wire. Figure 10 shows an analogy with SLS. MSFC's approach to modular design that covers usability, applicability, and operability of transmission methods for different power methods and environments is depicted in Figure 11.

Table 1 summarizes potential technology areas that can impact the general five use case scenarios. Dark shaded squares indicate closely related technical areas and application use cases, while lightly shaded cells indicate potential benefit from wireless technology broadly defined.

Table 1. Potential technology areas that can impact different use case scenarios.

Use case \ Technology area	TA2.4 Engine Health	TA3.3 Wireless Power	TA5.2 RF Comm	TA5.5 Cognitive Networks	TA6.4 Environmental Monitoring	TA7.4 Habitat Systems	TA10.4 Sensors& Actuators
2.1. Space vehicles	■	■	■	▨	■		■
2.2. Satellites and payloads			■	■			
2.3. Surface explorations		■	■		▨		▨
2.4. Ground systems		■	■				■
2.5. Habitats		▨	■	▨	■	■	■

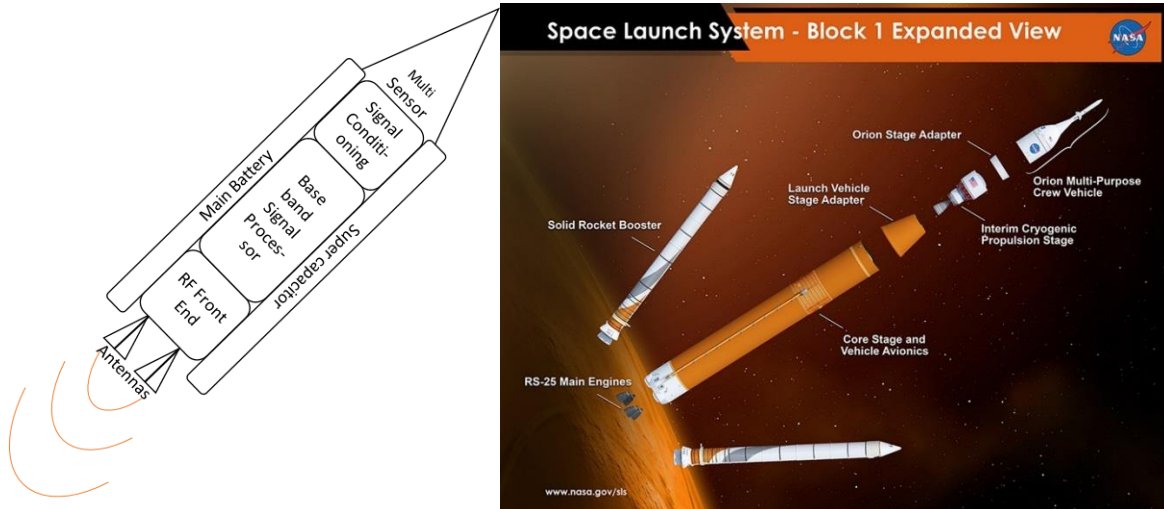**Figure 10. A modular flexible wireless system architecture that can be adapted to different missions by swapping antenna options, exchanging sensors, and reprogramming the baseband stage, while keeping the broadband RF front end and power system fixed. Very much similar to the concept of SLS that can be adapted to different missions.**
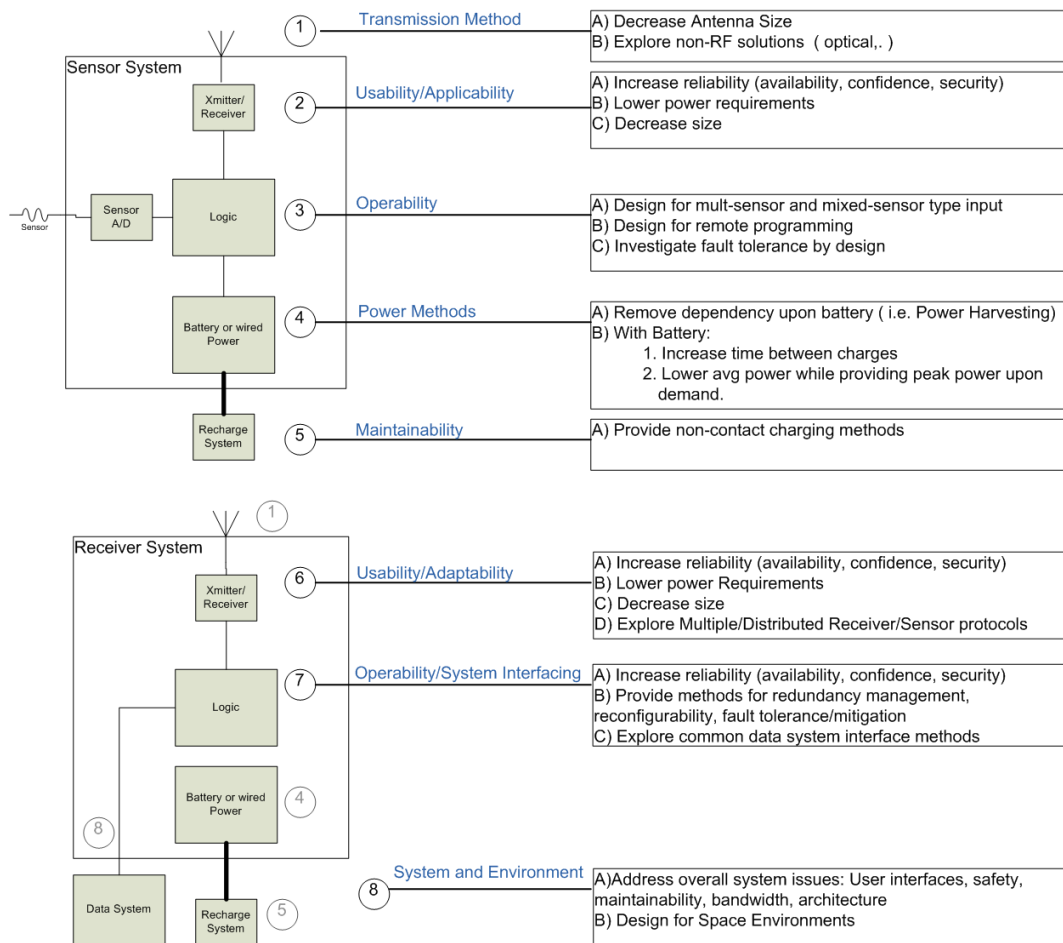

Figure 11. Current wireless interest areas at NASA MSFC.

Guided by Table 1, the current state of wireless communications networks in space applications and desired state in short and long term are summarized in the following roadmap (Table-2). Technology needs requiring less than 5 years to develop are labeled as short term. These include more mature technology areas such as scalability of networks with large number of sensors, and eliminating battery dependency through wireless power transfer or passive sensing as described in this report. Other technology areas which require more basic and applied research and development are categorized as long term with estimated 5-10 years development plan.

Table 2. Roadmap for Wireless Technology Development.

Where we are	Short term <5 Yr	Long term, 5-10 Yr	Where we want to go
1. Not space certified, rad tolerant or rad hard		X	1. Space certified
2. Low reliability		X	2. High reliability
3. Limited# of networked nodes	X		3. Large network sizes
4. Not scalable	X		4. Scalable
5. Not reconfigurable		X	5. Reconfigurable
6. Lack of coexistence in transmit protocols		X	6. Coexisting protocols with cognition
7. Battery dependent	X		7. Battery free

V. Conclusions and Future Directions

Wireless Technology has the potential to be used in space applications and provide unique capabilities that are not obtainable in wired systems. The space environment application areas are varied and each have a unique set of requirements that will require further development and maturation of wireless technology. Fortunately wireless technology in the commercial world is developing rapidly and the networking, management, reliability, and security techniques developed within this environment can be used as stepping stone for adopting this technology for space. Looking at the history of wireless can help in predicting the future direction and potential growth opportunities. The 1st generation of analog communication (AMPS) quickly turned into 2G (GSM/CDMA) or digital. The data rates were further improved when 3G (e.g. UMTS, HSPA and 1X-EV-DO) was introduced. The improvements continued with current 4G (LTE, LTE-A) standard very quickly. Some future directions in wireless communications industry motivated by exponential increase in demands include a wide array of new technologies under research and development under the 5G (5th generation) umbrella. According to a report[21] published by IEEE 5G Initiative group, the following technologies are the key to 5G implementations and will affect both cellular and sensor networks as one unified internet of thing (IoT):

- Massive MIMO
- RAN Transmission cm and mm Waves
- New Waveforms
- Shared Spectrum Access
- Advanced Inter-Node Coordination
- Simultaneous Transmission Reception
- Multi-RAT Integration & Management
- D2D Communications

- Efficient Small Data Transmission
- Wireless Backhaul/Access
- Integration
- Flexible Networks
- Flexible Mobility
- Context Aware Networking
- Information Centric Networking
- Moving Networks

Acknowledgments

References

[1] NASA Technology Roadmap, 2015, URL: http://www.nasa.gov/offices/oct/home/roadmaps/

[2] IEEE Standard for Information technology--Telecommunications and information exchange between systems Local and metropolitan area networks--Specific requirements Part 11: Wireless LAN Medium Access Control (MAC) and Physical Layer (PHY) Specifications," in IEEE Std 802.11-2012 (Revision of IEEE Std 802.11-2007) , vol., no., pp.1-2793, March 29 2012.

[3] IEEE Standard for Information technology-- Local and metropolitan area networks-- Specific requirements-- Part 15.1a: Wireless Medium Access Control (MAC) and Physical Layer (PHY) specifications for Wireless Personal Area Networks (WPAN)," in IEEE Std 802.15.1-2005 (Revision of IEEE Std 802.15.1-2002) , vol., no., pp.1-700, June 14 2005.

[4] IEEE Standard for Local and metropolitan area networks--Part 15.4: Low-Rate Wireless Personal Area Networks (LR-WPANs) Amendment 3: Physical Layer (PHY) Specifications for Low-Data-Rate, Wireless, Smart Metering Utility Networks," in IEEE Std 802.15.4g-2012 (Amendment to IEEE Std 802.15.4-2011) , vol., no., pp.1-252, April 27 2012.

[5] T. Ngo, Why WiFi stinks and How to fix it, IEEE Spectrum Magazine, June 2016.

[6] IEEE Standard for Information technology-- Local and metropolitan area networks-- Specific requirements-- Part 15.3: Amendment 2: Millimeter-wave-based Alternative Physical Layer Extension," in IEEE Std 802.15.3c-2009 (Amendment to IEEE Std 802.15.3-2003) , vol., no., pp.1-200, Oct. 12 2009.

[7] IEEE Standard for Air Interface for Broadband Wireless Access Systems," in IEEE Std 802.16-2012 (Revision of IEEE Std 802.16-2009) , vol., no., pp.1-2542, Aug. 17 2012.

[8] IEEE Recommended Practice for Information technology-- Local and metropolitan area networks-- Specific requirements-- Part 15.2: Coexistence of Wireless Personal Area Networks with Other Wireless Devices Operating in Unlicensed Frequency Bands," in IEEE Std 802.15.2-2003 , vol., no., pp.1-150, Aug. 28 2003.

[9] Bingxin Shen and A. Abedi, "Error correction in heterogeneous wireless sensor networks," Communications, 2008 24th Biennial Symposium on, Kingston, ON, 2008, pp. 111-114.

[10] A. Abedi and K. Zyck, "Iterative interference management in coded passive wireless sensors," SENSORS, 2013 IEEE, Baltimore, MD, 2013, pp. 1-4.

[11] L. Fabisinski, D. Wilkerson, "Wireless Sensors Applications at Marshall Space Flight Center," IEEE International Conference on Wireless for Space and Extreme Environments (WiSEE), Dec 2015, Orlando, FL.

[12] G. Merrill, D. Wilkerson, "NASA Fuel Tank Wireless Power and Signal Study," IEEE International Conference on Wireless for Space and Extreme Environments (WiSEE), Dec 2015, Orlando, FL.

[13] J. Ni, et. al., "UWB Tracking System Design for Lunar/Mars Exploration," IEEE International Conference on Wireless; 13-16 Mar. 2006; Sydney; Australia.

[14] B. H. Fisher and D. C. Malocha, "Cryogenic Liquid Sensing Using SAW Devices," 2007 IEEE International Frequency Control Symposium Joint with the 21st European Frequency and Time Forum, Geneva, 2007, pp. 505-510.

[15] W. C. Wilson et al., "Orthogonal Frequency Coded SAW Sensors for Aerospace SHM Applications," in IEEE Sensors Journal, vol. 9, no. 11, pp. 1546-1556, Nov. 2009.

[16] D. C. Malocha et al., "Orthogonal frequency coded SAW sensors and RFID design principles," 2008 IEEE International Frequency Control Symposium, Honolulu, HI, 2008, pp. 278-283.

[17] D. C. Malocha, B. Fisher, R. Youngquist, A. Weeks and M. Gallagher, "Surface Acoustic Wave Pulsed-Correlator Transceiver for Aerospace Applications," in IEEE Sensors Journal, vol. 14, no. 11, pp. 3775-3781, Nov. 2014.

[18] K. Yasami, A. Razi, A. Abedi, "Analysis of Channel Estimation Error in Physical Layer Network Coding," IEEE Communications Letters, vol. 15, no. 10, pp. 1029-1031, October 2011.

[19] F. Afghah, M. Costa, A. Razi, A. Abedi and A. Ephremides, "A reputation-based Stackelberg game approach for spectrum sharing with cognitive cooperation," 52nd IEEE Conference on Decision and Control, Firenze, 2013, pp. 3287-3292.

[20] L. Labonte, J. Castro, M. Razfar, A. Abedi, R. Rezaei, F. Ghabrial, P. Shankar, E. Besnard, "Wireless Sensor and Actuator Networks with Delayed Noisy Feedback (WiSAN)," IEEE International Conference on Wireless for Space and Extreme Environments, Nov 2013, Baltimore, MD.

[21] A. Dutta, H. Freeman, President's page: 5G Perspective, IEEE Communications magazine, May 2016, pp. 4-5.

14

Optimization of Magnesia-Based Cements for Additive Construction from Mars and Lunar In-Situ Resources

Hunain Alkhateb[1]
The University of Mississippi, University, MS, 38655

Jennifer Edmunson[2] and Michael Fiske[3]
Jacobs Technology NASA-MSFC, Huntsville, Al, 35806

and

John Fikes[4]
NASA-MSFC, Huntsville, Al, 35812

NASA's anticipated date to send humans to an asteroid is 2025 and to Mars is 2030's which requires constructing habitats on Mars prior to human arrival. Developing new materials for planetary surface construction necessitates extensive research to reduce the amount of materials launched from earth. It also requires developing in-situ binders that are suitable for additive construction and are capable of resisting the exterritorial environmental surroundings. In this study we will focus on magnesia-based cements to assess their viability and availability on Mars for additive construction applications. The two types of magnesia based cements studied were magnesium oxychlorides (MOC) and magnesium phosphate cements (MPC). The research conducted will enhance understanding the transformation of planetary in-situ materials into construction materials. The mechanical properties of magnesium based cement (MPC and MOC) mortars with different molar ratio and water/solid ratios have been investigated. The results reported indicate the high influence of these ratios on setting time and the compressive strength.

Nomenclature

ACME	=	Additive Construction with Mobile Emplacement
AM	=	Additive Manufacturing
NIRG	=	Nano Infrastructure Research Group
MC	=	Magnesia-Based Cement
MOC	=	Magnesium Oxychloride Cement
MOS	=	Magnesium Oxysulfates Cement
MPC	=	Magnesium Phosphate Cement
SEM	=	Scanning Electron Microscope
XRF	=	X-ray Fluorescence

I. Introduction

Magnesia-based cement (MC) are mineral binders that are known for being light, high strength, with a very rapid setting time. Magnesium oxychlorides cement (MOC), and magnesium phosphates cement (MPC) will be the main focus of this research. MOC is formed by mixing a reactive magnesium oxide, in a powder form, with a brine solution of magnesium chloride ($MgCl_2$). MPC is formulated by mixing soluble phosphates and a solution of magnesium hydroxide, when both components are mixed together, insoluble magnesium phosphate precipitates. The focus of this report will be MPC, and MOC will be the focus of another research study by the same

---

[1] Assistant Professor, Civil Engineering, NIRG, The University of Mississippi, 210 Carrier Hall, University, MS 38655.
[2] Geologist, In-Space Manufacturing Engineer, Jacobs Technology NASA-MSFC.
[3] Principal Investigator, Jacobs Technologies Inc., Building 4201, Room 230, NASA/Marshall Space Flight Center, AL 35812
[4] ACME Project Manager, Building 4201, Room 224A, NASA/Marshall Space Flight Center, AL 35812

group. Magnesium phosphate cement (MPC), formed by the reaction between magnesium oxide and a soluble phosphate, such as potassium, phosphate monobasic (KH_2PO_4) to form struvite- $K(MgKPO_2.6H_2O)$ which is naturally cementitious. Since both Moon and Mars surfaces are rich with magnesium smectites,[3] utilizing in-situ materials indicates that MCs could be a good cementitious binder candidate. Although MCs exhibit many superior properties to Portland cement, the extremely prompt setting time (few seconds) excludes this great in-situ candidate from technology transformation. In other words, the rapid initial setting time may not allow it to be utilized via additive construction. For the initial stage of this research, the investigators have identified several additives (such as boric acid, fly ash, sodium bicarbonate, and dolomite) to reduce the Sorel cements initial setting time without compensating its mechanical and physical properties.[4-10] These additives and composite mixes need to be optimized to fit the Additive Construction with Mobile Emplacement (ACME) technology requirements.

The main Objectives for the research conducted are the following: 1. to conduct a thorough literature review for the available resources and mineralogy for Mars; 2. to identify potential binders, that could be extracted from Mars regolith and/or atmosphere; and 3. to design a matrix of potential and possible magnesia based mixes for ultimate compressive strength testing, initial setting, and curing rates.

In this study, MPC binders were evaluated mainly via compressive strength at 7 and 28 days. Several preliminary SEM image were captured, but further analysis and verification will be required coupled with some X-ray Fluorescence (XRF) analysis, for more precise conclusions. The main objective of the research conducted was to develop binder mixes that will deliver the compressive strength and initial setting time, which will allow utilizing these potential binders for concrete contour crafting.

II. Innovation

Concrete additive manufacturing, is still in its infancy stages worldwide and in the USA. The largest 3D printer by far is created by Winson in China to build furniture, houses and even five story buildings. The second largest is created by Amesterdam Canal House. In the USA, the concrete 3D printers are only manufactured by USC contour crafting. The stated facts above, stress the necessity of advancing this technology. Terrestrial concrete additive construction is still in its infancy, and there are numerous vital challenges associated with this technology that are related to materials characteristics. Construction material behavior during the additive construction process, as well as how these materials behave in planetary surface environments, needs to be immensely explored prior to utilizing this technology on other planets. Compatibility of in-situ resources, additive construction processes, structure requirements, and the effects of the space environment are significant issues that need to be addressed. Five of the most critical concrete additive construction materials properties include flowability, extrudability, buildability, set time, and interlayer adhesiveness See Figure 1. These challenges also require multiscale multifunctionality optimization to meet the design requirements within a reasonable cost.

Figure 1. Some of the Main Challenges for the Concrete Contour Crafting.

Utilizing in-situ resources for the construction of habitat structures on the moon and mars will increase the competence of the long duration space missions and will reduce the number of freights necessary, thus reducing cost. Hence, there is a critical need to understand the transformation of in-situ materials from extraterrestrial destinations such as Martian regolith and any respective atmospheric constituents into revolutionary superior

construction materials[1]. Also, a need exists to a better comprehend the relationship between potential research/settlement sites and the available in-situ resources as construction materials at those locations, which will result in optimal composites. Along with the formulation several magnesia-based composite mixes, developing these materials will require intensive multiscale/multifunctional characterization and fundamental modeling and validation of autonomous contour crafting.[2]

III. Materials Used

Several binders were identified as extraterrestrial construction materials, depending on their in-situ availability and the possibility of utilizing these potential materials via autonomous systems. Some of the materials identified with high potential were: magnesia-based cements, polymers, silicates, sodium silicates, glass, sulfur, Martian regolith, ordinary Portland cement, and igloos. Two types of Magnesia-based cements will be the main focus of this research. The first is magnesium phosphate cement (MPC), formed by the reaction between magnesium oxide and a soluble phosphate, such as potassium phosphate monobasic (KH2PO4),[4-10] and the second is magnesium oxychloride (MOC), which is formed by the combination of magnesium oxide and magnesium chloride solution. Later, the researchers will be optimizing and evaluating other cementitious binders such as magnisum oxysulfates (MOS), and geopolymers. Table 1, displays all the materials used in this research and their source.

Table 1. Materials used and their sources.

Material	Source
MgO	Premier Magnesia, LLC
KH_2PO_4	Premier Magnesia, LLC
$MgCl_2$ Flakes	Premier Magnesia, LLC
Boric Acid	Premier Magnesia, LLC
MKP	Premier Magnesia, LLC
Borax	
OptiBor$^®$	20 Mule team Borax
Fly Ash Class F	
Stucco	

IV. ACME System

V. Mix Design

Several MPC mixes were tested for their early compressive strength (at 7 days), see Table 2 for more details about mixes compositions. The first composition tested was prepared by mixing MgO with mono potassium phosphate of a 9.5 molar ratio, with 5% boric acid and a high water/cement (w/c) ratio of 0.9. Although the Sorel cement setting time increased from less than a minute to several hours; the high content of water resulted in very poor ultimate strength properties. Hence, in the second composition the researchers have reduced the w/c ratio to 0.5. The decrease in the water content has improved the ultimate strength of the tested cubes tremendously (~10 times) compared to the first composition, yet the setting time was still very short, barely enough to mix and pour the cubes. The fast setting has resulted in defects in the cubes geometry, which impacted the caused ultimate strength. In the third group composition, a different type of boric acid was used (OptiBor$^®$), to evaluate the effect of the boric acid source on the setting time and ultimate compressive strength. The testing demonstrated that minor effect in the ultimate strength has been noticed, though the setting time of this set was slightly better. Finally for the fourth batch, stucco of 1.8% by dry mass has been added to a mix that is similar to what has been tested in the third composition. The small addition of stucco has resulted in an improved setting time, better cube geometry quality, with no reduction in the ultimate compressive strength. In the fifth, sixth, seventh, and eighth compositions we will be utilizing ready monopotassium MKPC powder instead of mixing the magnesia with the mono potassium phosphate separately with a predetermined M/P molar ratio. The MKP powder was sourced from Premier Magnesia LLC. We also have introduced fly ash class F to enhance the setting time and improve the strength.

For the MOC pastes the formulations designed for this research were based on the variation of the molar ratios for $MgO/MgCl_2$ and $H_2O/MgCl_2$. Unfortunately, for all the mix composition listed in Table 3, there was no compressive strength results to be reported. They all have led to an expansion of the cubes followed by an explosion. This could be an indication of the high reactivity in the MgO provided.

Table 2. Formulation of MPC Pastes and Mortars.

Batch Number	Composition
1st	500gm MgO, 177.66 gm KH_2PO_4, 33.883gm Borax, and 640.0 gm water.
2nd	500gm MgO, 177.66 gm KH_2PO_4, 33.883gm Borax, and 355.8 gm water.
3rd	500gm MgO, 177.66 gm KH_2PO_4, 33.883gm OptiBor, and 355.8 gm water
4th	500gm MgO, 177.66 gm KH_2PO_4, 33.883gm Borax, and 355.8 gm water, 12.8gm stucco
5th	700 gm MKP, 35 gm Borax, and 367.5 gm water, 300 gm fly ash
6th	500gm MKP, and 200 gm water, 214 gm fly ash class F
7th	750 gm MKP, 225 gm water
8th	750 gm MKP, 225 gm water, 15 gm stucco

Table 3. Formulation of MOC pastes.

Mix #	$MgO/MgCl_2$	$H_2O/MgCl_2$
1	5	8,12,16,20
2	8	8,12,16,20
3	11	12,16,20
4	14	12,16,20
5	18	16,20

VI.   Results and Discussions

A. Compressive Strength
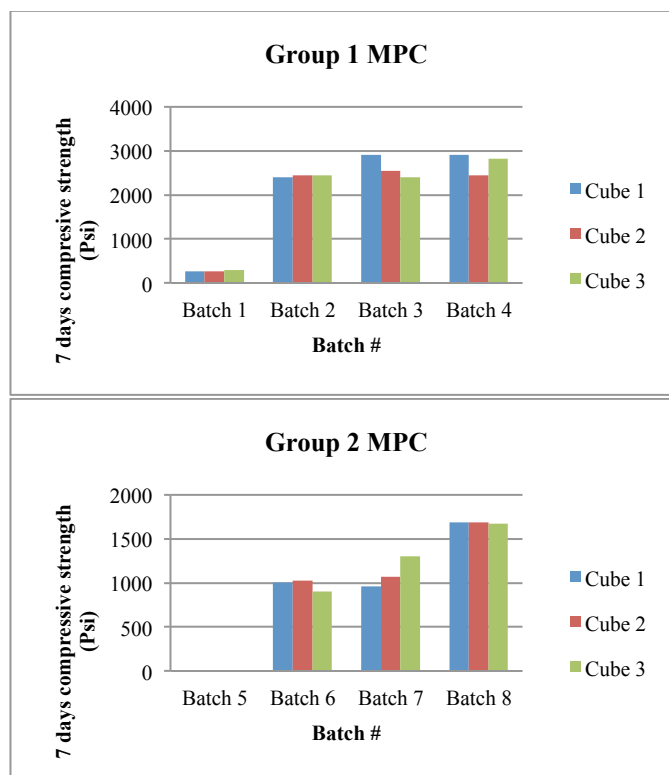
Figure 2. Compressive Strength Results.

From Figure 2, it can be demonstrated that the compressive strength increases with decreasing the water/ solids (w/s) ratios and introducing stucco in the mixes. It also can be noted that the presence of boric acid has increased the initial setting time (See Appendix for more details), however, The effect of boric acid source had slightly affected the mechanical responses. To verify the changes and to verify whether it is a chemical or a physical effect, further

18

investigation will be required. There was no results to report for the MOC matrix provided, all the mixes proposed has caused the cubes to explode, after casting them in the molds. This could be due the high reactivity of the MgO, the authors have ordered dead burnt magnesia oxide for further investigation.

B. Scanning Electron Microscopy (SEM)

Scanning electron microscopy (SEM) images for MPC batches 2, 6, 7, and 8 are shown in Figure 3. The SEM

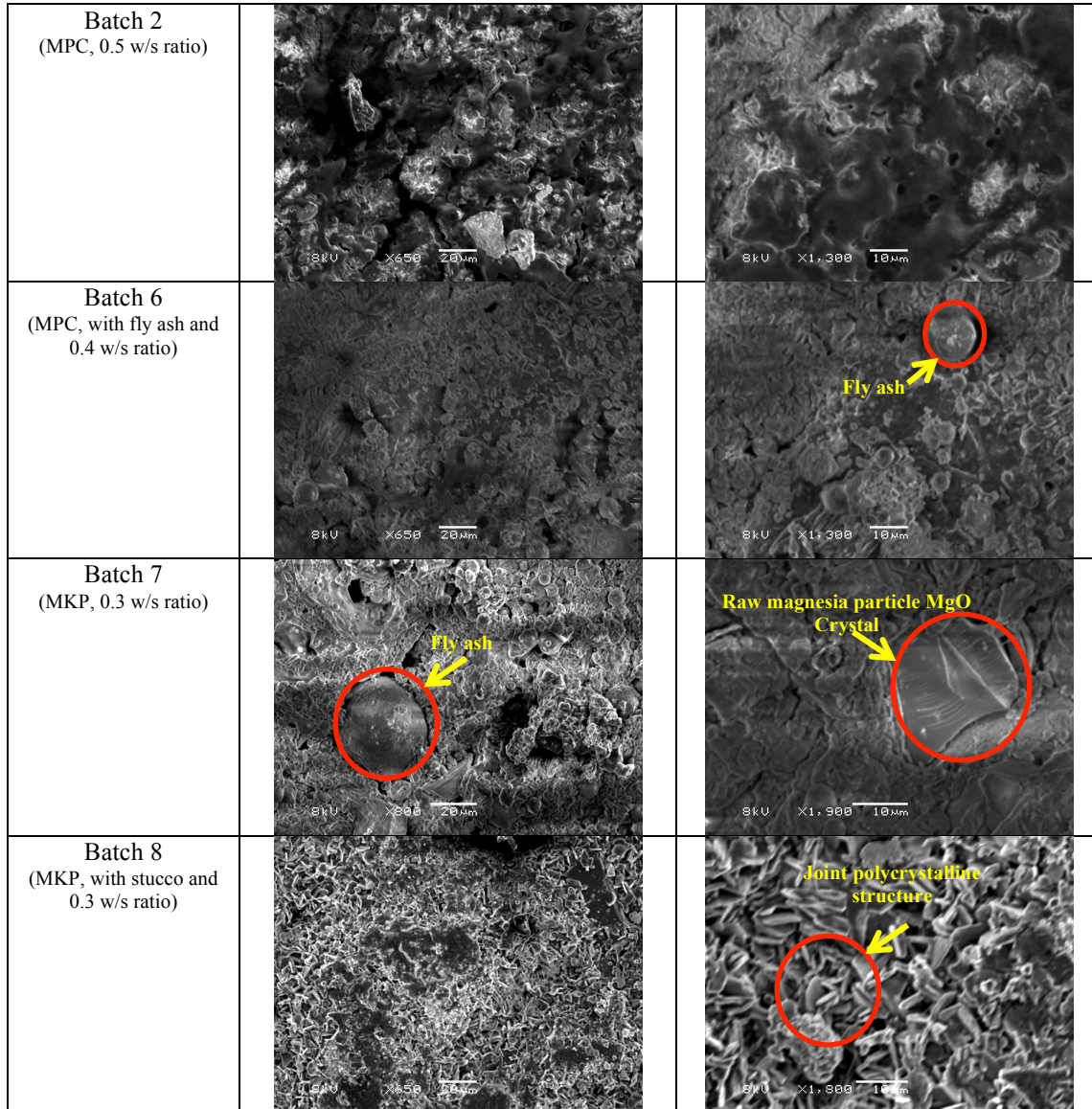| Batch 2 (MPC, 0.5 w/s ratio)		
Batch 6 (MPC, with fly ash and 0.4 w/s ratio)		
Batch 7 (MKP, 0.3 w/s ratio)		
Batch 8 (MKP, with stucco and 0.3 w/s ratio)		

Figure 3. SEM images for batches 2, 6, 7, and 8.

From the SEM images of batches 2 and 6, with a variation of w/s ratios, a denser micro structure has formed for the lower W/Solids ratio which is reflected in the compressive strength of the tested mixes. Comparing the SEM images from batch 7 and 8, it seems that the presence of stucco has formed a better polycrystalline structure. Howeverm, this will need further investigation and verification via X-ray diffraction.

VII. Conclusion

The research conducted in this report, is still at its early stages. However, the results generated are very interesting and had developed several material optimization techniques, along with identifying numerous potential

additives to improve the magnesia-based cements. In addition, several other binders have been identified with a high potential for additive construction transformation such as Sorel cements, geopolymers, and polymer concretes utilizing the lunar and martian regolith.

Appendix

Lab Notes:
1ˢᵗ batch

Present: Mike Fiske, and Hunain Alkhateb
Lab: 4739
Time: June-28-2016, 8:00-9:30 am
Goal: Hunain and Mike attempted to pour some MOP Sorel cements for test control.
- Two batches were mixed
- 1ˢᵗ batch: 500gm MgO, 177.66 gm KH2PO4, 33.883gm Borax, and 640.0 gm water.
- The M/P ratio was 9.5, and the W/C(solids) ratio was 0.89 for workability purposes
- We weighed the ingredients, started with MgO and added water. Later we added the dry mixture of boric acid and KH2PO4. The mix was very dry (apple pie crumbly dough) and we had to add water at two more stages, which resulted in a water cement ratio of 89.9%. After adding all this water, the mix was very runny, but had clumps (very similar to cake batter).
- The second mix, we weighed the same amount of dry contents, but we reduced the W/C ratio to 0.5 judging from what had happened in the first mix. Also, we wanted to explore another mixing technique
- In a big bowl, mix water with boric acid.
- Add MgO powder gradually to the boric acid water mixture, continue mixing until all lumps disappear. Add the KH2PO4 and mix quickly, you have only a couple seconds to 1 minute. To pour it before it sets.

Sample	Compressive Strength 7 days	Compressive Strength 28 days
B1-1	260 psi (1.8 MPa)	NA
B1-2	269 psi (1.9 MPa)	NA
B1-3	291 psi (2.0 MPa)	NA
Avg	273 psi	

Notes: This mix set very fast! We had to pour it within a couple of seconds. We also tried to add water to magnesia, the mix turned out to be very dry, which resulted in adding more water. It is very critical to add the magnesia to the water slowly and mix very well. Not the other way

2ⁿᵈ batch

Present: Mike Fiske, and Hunain Alkhateb
Lab: 4739
Time: June-29-2016, 9:30-11:15 am
Goal: Hunain and Mike attempted to mix some MOP Sorel with a lower w/c ratio.
- 2ⁿᵈ batch: 500gm MgO, 177.66 gm KH_2PO_4, 33.883gm Borax, and 355.8 gm water.
- The M/P ratio was 9.5, and the W/C(solids) ratio was 0.5 for workability purposes
- For this mix, we weighed the same amount of dry contents, but we reduced the W/C ratio to 0.5 judging from what had happened in the first mix. In a big bowl, mix water with boric acid.
- Add MgO powder gradually to the boric acid water mixture, continue mixing until all lumps disappear. Add the KH_2PO_4 and mix quickly, you have only a couple seconds to 1 minute. To pour it before it sets.

Sample	Compressive Strength 7 days	Compressive Strength 28 days
B2-1	2406 psi (16.6 MPa)	NA
B2-2	2445 psi (16.9 MPa)	NA
B2-3	2449 psi (16.9 MPa)	NA
Avg	2433	

Notes: The mix still set very fast, but we were able to mix the dry contents with a lower w/c ratio. This has highly impacted the mechanical response of the Sorel cement.

3rd batch

Present: Jennifer Edmunson, and Hunain Alkhateb

Lab: 4739

Time: July-01-2016, 2:00-3:30 pm

Goal: Hunain and Jennifer attempted to mix some MOP Sorel with a different (Boric acid source- OptiBor)

- 3rd batch: 500gm MgO, 177.66 gm KH_2PO_4, 33.883gm OptiBor, and 355.8 gm water.
- The M/P ratio was 9.5, and the W/C(solids) ratio was 0.5 for workability purposes
- For this mix, we weighed the same amount of dry contents, W/C ratio was kept to 0.50. In a big bowl, mix water with boric acid.
- Add MgO powder gradually to the boric acid water mixture, continue mixing until all lumps disappear. Add the KH_2PO_4 and mix quickly, you have only a couple seconds to 1 minute. To pour it before it sets.

Sample	Compressive Strength 7 days	Compressive Strength 28 days
B3-1	2913 psi (20.08 MPa)	NA
B3-2	2544 psi (17.5MPa)	NA
B3-3	2405 psi (16.5 MPa)	NA
Avg	2602	

Notes: OptiBor performed better in terms of increasing the set time, compared to the second batch as well as ultimate compressive strength results. Optibor is recommended over boric acid.

4th batch

Present: Jennifer Edmunson, and Hunain Alkhateb

Lab: 4739

Time: July-01-2016, 2:00-3:30 pm

Goal: Hunain and Jennifer attempted to mix some MOP Sorel with OptiBor, as well as adding 1.8% by dry mass stucco

- 4th batch: 500gm MgO, 177.66 gm KH_2PO_4, 33.883gm Borax, and 355.8 gm water, 12.8gm stucco
- The M/P ratio was 9.5, and the W/C(solids) ratio was 0.5 for workability purposes
- For this mix, we weighed the same amount of dry contents, but we reduced the W/C ratio to 0.5 judging from what had happened in the first mix. In a big bowl, mix water with boric acid.
- Add MgO powder gradually to the boric acid water mixture, continue mixing until all lumps disappear. Add the KH_2PO_4 and mix quickly, you have only a couple seconds to 1 minute. To pour it before it sets.

Sample	Compressive Strength 7 days	Compressive Strength 28 days
B4-1	2911 psi (20.1 MPa)	NA
B4-2	2445 psi (16.9 MPa)	NA
B4-3	2818 psi (19.43 MPa)	NA
Avg	2724.7	

Notes: Setting time improved slightly with the addition of a small percentage of stucco. However, more time is needed. One or two minute's improvement will not allow to 3D print this Sorel cement composition. Other alternatives need to be explored.

5th batch

Present: Jennifer Edmunson, and Hunain Alkhateb

Lab: 4739

Time: July-08-2016, 9:30-10:45 am

Goal: Hunain and Jennifer attempted to mix some MOP (ready dry mix) Sorel 70% with OptiBor 5%, and 30% by dry mass fly ash class F

- 5th batch: 700 gm MPC, 35 gm Borax, and 367.5 gm water, 300 gm fly ash
- The M/P ratio was 9.5 (check supplier, and the W/C(solids) ratio was kept 0.5 for workability purposes
- In a big bowl, mix water with boric acid.

- Add MPC powder gradually to the boric acid water mixture, continue mixing until all lumps disappear. Add the fly ash and mix quickly. To pour it before it sets.

Sample	Compressive Strength 7 days	Compressive Strength 28 days
B5-1	8 psi ((.055 MPa)	NA
B5-2	psi (MPa)	NA
B5-3	psi (MPa)	NA

Notes: This mix didn't set fast, adding the OptiBor and the fly ash has increased the setting time tremendously. However, for some reason after pouring these samples the water started leaking out of the molds, and cubes were shrinking! It could be the excessive boric acid content, since the MPC already contains boric acid. One hour after pouring it, it was still runny. The samples were very soft and crumbly, they very much resemble a wet mix of sand clay and water. It seemed that the MPC did not set, or even react as a true binder. Although the testing failed, we definitely need to run an XRD and SEM for the cured powder.

6th batch
Present: Jennifer Edmunson, and Hunain Alkhateb
Lab: 4739
Time: July-08-2016, 9:30-10:45 am
Goal: Hunain and Jennifer attempted to mix some MOP (ready dry mix) 70% Sorel and adding 30% by dry mass fly ash class F, No boric acid was added. Also W/C ratio was reduced to 0.40.
- 6th batch: 500gm MPC, and 200 gm water, 214 gm fly ash class F
- The M/P ratio was 9.5, and the W/C(solids) ratio was reduced to 0.4
- For this mix, we weighed the dry contents, but we reduced the W/C ratio to 0.4 judging from what had happened in the first mix. In a big bowl, mix water with MPC
- Add MPC powder gradually to the water; continue mixing quickly until all lumps disappear. Add the fly ash and mix. Pour it before it sets.

Sample	Compressive Strength 7 days	Compressive Strength 28 days
B6-1	1001 psi (6.9 MPa)	NA
B6-2	1025 psi (7.06 MPa)	NA
B6-3	905 psi (6.24 MPa)	NA

Notes: This mix didn't set fast, the fly ash has increased the setting time tremendously. Reducing the water content slightly, and not adding OptiBor has cut the water leaching. On the same day we tried to mix the same batch with 70% stucco, to improve the strength and the setting time, there was heat generated from the reaction, the mix was very dry, resulted in adding more water, the delay has caused this composition to set faster. It is recommended to reduce stucco content.

7th batch
Present: Jennifer Edmunson, and Hunain Alkhateb
Lab: 4739
Time:
Goal: Hunain and Jennifer attempted to mix some MPC (ready dry mix) Sorel, no fly ash, only a reduced W/C ratio to .3
- 7th batch: 750 gm MPC, 225 gm water
- W/C ratio was 0.3
- Add MPC powder gradually to the water, continue mixing until all lumps disappear. To pour it before it sets.

Sample	Compressive Strength 7 days	Compressive Strength 28 days
B7-1	961 psi (MPa)	NA
B7-2	1072 psi (MPa)	NA
B7-3	1302 psi (MPa)	NA

Notes: from testing the 5th and 6th batches we noticed that MPC seemed not reacting with the fly ash as anticipated. Further investigation regarding the composition of the MPC was carried which indicated that it already contains 30-50% fly ash. Hence, we decided not to add any extra fly ash for the future mixes.

8th batch

Present: Jennifer Edmunson, and Hunain Alkhateb

Lab: 4739

Time:

Goal: Hunain and Jennifer attempted to mix some MPC (ready dry mix) Sorel, reduced W/C ratio to .3 and 2% by cement weight stucco

- 8th batch: 750 gm MPC, 225 gm water, 15 gm stucco
- W/C ratio was 0.3
- Add MPC powder gradually to the water, continue mixing until all lumps disappear. To pour it before it sets.

Sample	Compressive Strength 7 days	Compressive Strength 28 days
B8-1	1685 psi (MPa)	NA
B8-2	1687psi (MPa)	NA
B8-3	1672 psi (MPa)	NA

References

[1]NASA Technology Roadmaps TA 6: Human Health, Life support, and Habitation Systems, 2015.

[2]Cesaretti, G., Dini, E., Kestelier, X. D., Colla, V., and Pambaguian, L. "Building components for an outpost on the lunar soil by means of a novel 3D printing technology" *Acta Astrunautica* Vol. 93, 2014, pp. 430-450.

[3]Werkheiser, N. J., Edmunson, J. E., Fiske, M.R., and Khoshnevis, B. "On the development of additive construction technologies for application to development of lunar/martian surface structures using in-situ materials," *AIAA Space 2015 Conference*, Pasadena CA, 2015, pp 4451.

[4]Gardner, L. J., Bernal, S. A., Walling, S. A., Corkhill, C. L., Provis, J. L., and Hyatt, N. C. "Characterisation of magnesium potassium phosphate cements blended with fly ash and ground granulated blast furnace slag," *Cement and Concrete Research*, Vol. 74, 2015, pp.78-87.

[5]Ring T. A., Ping E. "Sorel Cement Reactions and their Kinetics"

[6]Gartner, E. M., and Macphee, D. E. "A physico-chemical basis for novel cementitious binders," *Cement and Concrete Research* Vol. 41, 2011, pp. 736-749.

[7]Zhou, H., Agarwal, A. K., Goel, V.K., and Bhaduri, S. B. "Microwave assisted preparation of magnesium phosphate cement (MPC) for orthopedic applications: a novel solution to the exothermicity problem," *Material Science Engineering C Mater Biol Appl.* Vol. 33(7), 2013, pp. 4288-7294.

[8]Biwan, X., Hongyan, M., Chuanlin, H., Shuqing, Y., and Zongjin, L. "Influence of curing regimes on mechanical properties of magnesium oxychloride cement-based composites," *Construction and Building Materials* Vol. 102(1), 2016, pp. 613–619.

[9]Zongjin. L, and Chau, C. "Influence of molar ratios on properties of magnesium oxychloride cement," *Cement and Concrete Research* Vol. 37(6), 2007, pp. 866-870.

[10]Ying, L., Zongjin, L., Huafu, P., Hongfa, Y. "The influence of $FeSO_4$ and KH_2PO_4 on the performance of magnesium oxychloride cement," *Construction and Building Materials* Vol. 102(1), 2016, pp. 233-238.

Water Hammer Analysis during Priming of Evacuated Line

Alak Bandyopadhyay[1]
Computer Science, Alabama A & M University, Normal, AL 35762

Alok K. Majumdar.[2]
Thermal and Combustion Analysis Branch, NASA Marshall Space Center, Huntsville, AL 35812

ABSTRACT

Water hammer analysis in pipe lines, in particularly during priming into evacuated lines is important for the design of spacecraft and other in-space application. In the current study, a finite volume network flow analysis code is used for modeling three different geometrical configurations: the first two being straight pipe, one with atmospheric air and other with evacuated line, and the third case is a representation of a complex flow network system. The numerical results show very good agreement qualitatively and quantitatively with measured data available in the literature. The peak pressure and impact time in case of straight pipe priming in evacuated line shows excellent agreement.

Nomenclature

A	=	Area
K_f	=	Friction Factor
L_g	=	Gas (air) column length
L_l	=	Liquid (water) column length
L_t	=	Total length of the pipe
$\dot{m}$	=	Mass Flow Rate
p	=	Fluid Pressure, psia
p_{air}	=	Air pressure downstream of valve
p_{atm}	=	Atmospheric pressure, psia
p_R	=	Reservoir or supply pressure, psia
Δp	=	Pressure Drop, psf (pounds per square feet)
T	=	Temperature, F

I. Introduction

Water hammer and Pressure surges are critical in the design of spacecraft propellant feed lines. The water hammer pressure transients that occur during priming of feed lines are very important in the design and analysis of liquid propulsion systems. During the start-up of the propulsion system of a spacecraft, the process of filling of an evacuated pipeline, is called priming. Priming can generate severe pressure peaks due to the slam (water hammer) of the propellant against a closed thruster valve. The downstream conditions strongly affect the pressure surge. In space systems, satellites, or interplanetary probes, the propellant lines are vacuum-pumped or filled with low pressure helium or nitrogen before the launch. Before operations, these lines are primed with a vaporizing liquid, sometimes in the presence of a non-condensable gas (NCG), which produces water hammer phenomena. These phenomena occur regularly in aerospace applications. There are many other applications as well, such as fuel injectors in engines, fire sprinklers, and water hoses etc. When a valve is opened, quick filling of lines produces a shock wave, known as water hammer which travels through the feed lines, induces pressure peaks and frequencies which can cause serious damage not only to the lines but with the associated equipment too.

The water hammer in pipe line have been studied by many authors in the past, experimentally, analytically and numerically. There have been a review of water hammer theory and practice done by Ghidaoui et al in 2005 [1]. However, there have been numerous works in this area since then, in particularly for aerospace applications [2, 3, 4, 5]. However, except for a few, not much study have been done in the area of priming, in particularly for priming in a flow network containing numerous flow components. Prickett et al [6] have done some testing of priming problem in straight pipe as well as in a flow network using water as a reference fluid. They have also compared their test data with simplified analytical model. Lecourt and Steelant [7] have used ethanol, acetaldehyde and a real propellant

---

[1] Associate Professor, Computer Science, Alabama A & M University
[2] Insert Job Title, Thermal and Combustion Analysis Branch, NASA Marshal Space Flight Center

mono-methyl-hydrazine as a test fluid for priming in simplified feed lines. Bandyopadhyay and Majumdar [8] have studied the water hammer analysis in a closed pipe with entrapped air.

The objective of the current study is to use a finite volume based network flow solver by solving relevant governing equations to simulate the problem of priming to completely evacuated line as well as presence of low pressure air downstream of the valve. The numerical results are tested with data available from the measurement data of Prickett et al [6].

II. Problem Description and Computational Model

The water hammer problem in a pipe filled with water and entrapped air and in pipe (pipes) in evacuated lines are considered for this study. All the cases can be solved using similar algorithm. The three specific cases considered for the current study are: a) Water hammer pressure prediction in a straight pipe with entrapped air, b) priming in a straight evacuated pipe and c) priming in a flow network.

In the first case, water hammer in a closed pipe with entrapped air is considered; the physical geometry is shown in figure 1. In a long pipe with water reservoir to the left, the water region is initially on the left side of the ball valve (location CD) whereas the entrapped air is on the right side of the valve till the end of the pipe as shown in the figure. The pipe is 20 ft. long from the reservoir to the start of ball valve (designated by L_l in figure 1), and the gas or air column length (L_g) varies depending on the ratio of air column length to total length. The ball valve starts opening gradually from 0.2 s to 0.5 sec and it is fully open at 0.5 sec. The geometrical setup and operating conditions are identical to experimental setup of Lee [9]. This problem have been solved by Bandyopadhyay and Majumdar [8] using network flow solver. However, in that numerical model, the entrapped air region was lumped into a single node and the water to air interaction was accounted thermodynamically. The model was able to predict the peak pressure at the dead end with reasonable accuracy, however, that model was not able to predict the pressure distribution along the entire pipe length consisting both the water and air region. This drawback is overcome in the current model by using two fluids (water and air) and also by placing the ball valve in the correct geometrical location (section CD). The ball valve opening angle (0: closed, 90 degree: full open) is shown in figure 2 as a function of time. In the numerical model, all the related equations (continuity, momentum, energy and species-concentration) are solved in the entire pipe length, not only in the water region unlike [8].

Figure 1. Schematic of the water pipe with entrapped air [Lee, 9].
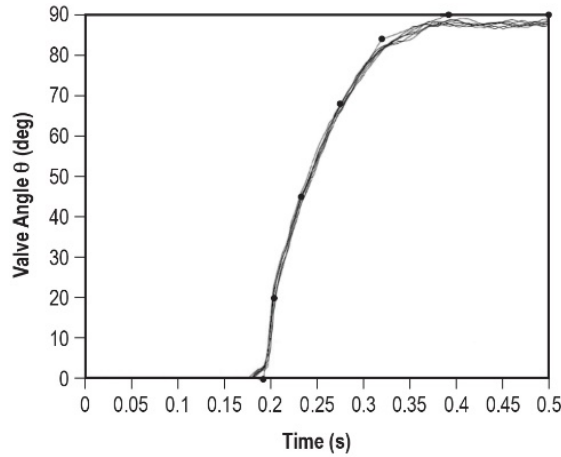
Figure 2. Ball valve angle change with time [9].

The computational model in which the entire pipe is divided into a set of nodes and branches as shown in figure 3 below. Node 1 represents the reservoir, which is a boundary node, and the restriction in branch 1112 indicates the ball valve. The ball-valve opening is provided to the solver through an input file where the time and valve area open at an instant are supplied. Node 20 represents the dead end. Each branch as shown in red color, represent a pipe segment of length 24 inches and pipe diameter of 1.025 inches. Increasing number of branches more than what are being used does not change the result. The details of the governing equations and solution procedure will be briefly described at the end of this section.
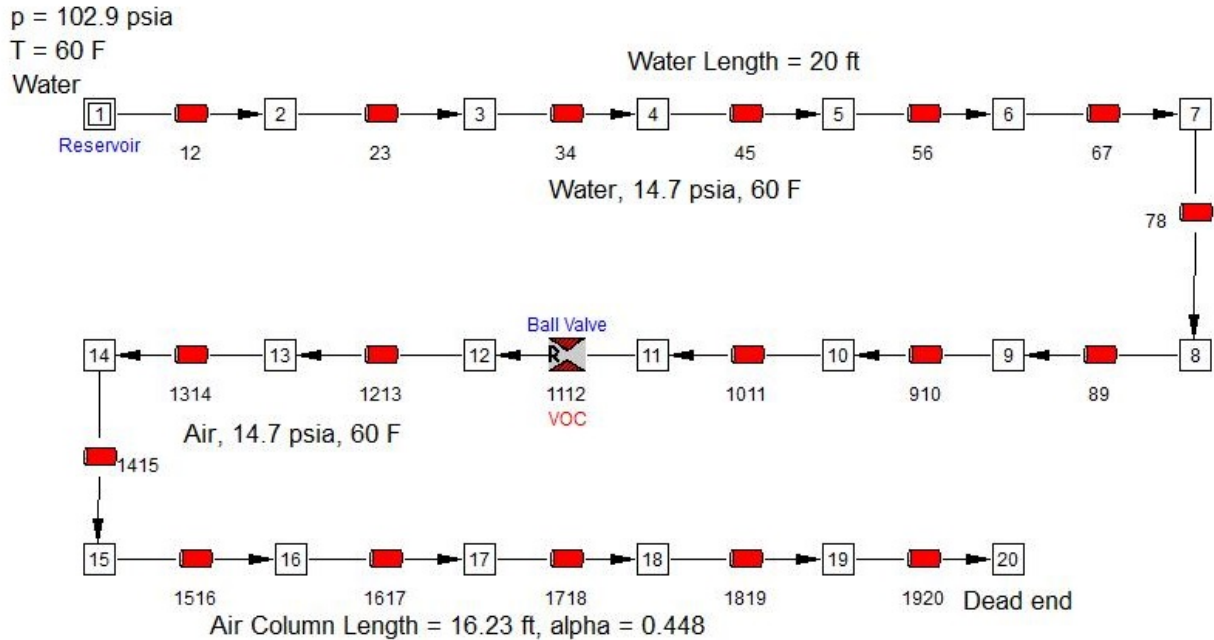
Figure 3. GFSSP Model for the Entrapped Air Pipe

The boundary node, node 1 is kept at reservoir (or supply pressure) p_R which varies from 29.4 psia to 102.9 psia (2 times to 7 times more than standard atmospheric pressure). The water concentration at nodes upstream of valve 1112, is fixed to 1 and air concentration to 0. Similarly the air concentration in the downstream of valve, that is in nods 12 through 20 are kept at 0 (for water concentration) and 1 (for air concentration) respectively.

The next two cases are dealing with priming in feed lines, First priming into a straight pipe is considered as shown in figure 4 below. The geometry considered in the current research are identical to experimental study of Pricket et al [7]. In the figure shown are the reservoir on the left, pipe lines, hand valves (HV), the main supply valve (Latch Valve

– LV), along with pressure transducers at three different points (P1, P2 and P3). The latch valve opens almost instantaneously, and water flows from the reservoir to the evacuated pipe. The pipe upstream of the latch valve is 12 inches long and 3/8 inches in diameter and the downstream of the latch valve, the pipe is 96 inches long and ¼ inches in diameter.   The supply pressure varies from 30 psia to 120 psia.
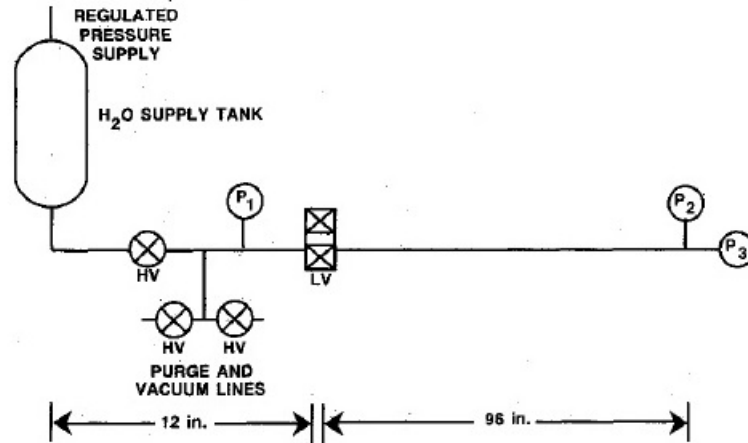

Figure 4. Schematic of Single Feed Line (courtesy: Pricket et al [7])

The physical problem is converted into the GFSSP's numerical model by dividing the entire domain into 8 pipe segments, and a restriction for the latch valve as shown in figure 4 below.
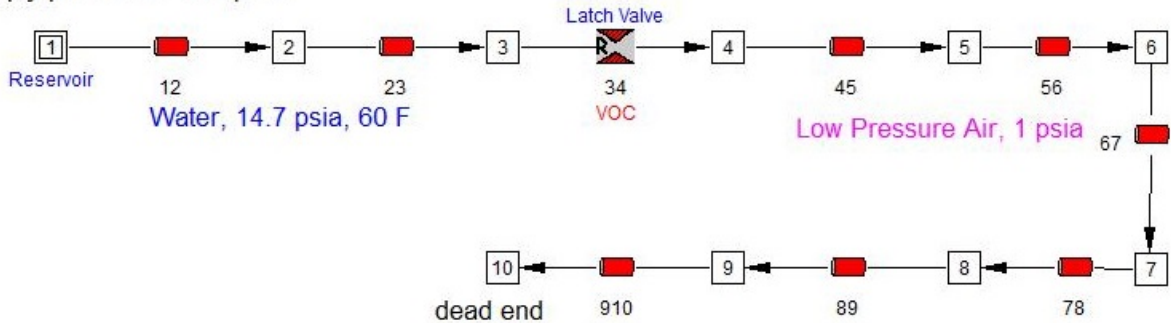
Figure 5. Computational Domain for the Single Feed Line

In order to model initially evacuated line downstream of the latch valve, air at very low pressure is assumed to be present in the pipe line, and the initial pressure of air (p_{air}) is a numerical adjusting parameter. In the current simulation this pressure is varied and gradually lowered to see when the numerical solution is virtually independent to this pressure. This is discussed in the results and discussion section later.

The last and the third case considered in the current work is priming in a flow network consisting several components as shown in figure 6 below. The network is quite complex and consists of several hand valves (HV), latch valve (supply valve), volume reservoirs (indicated by V1 through V4), and pipe lines. The fluid (water) flows from a reservoir through the hand valve (HV1) and controlled by the latch valve (indicated by R1) and it branches out into three directions: a) going straight to hand valve 2 (HV11), which is considered a dead end to compare with one of the test run of Pricket et al, b) branching out through hand valve HV3, and ending into a volume reservoir, and c) branching out through a filter and rest of the network. The volume of the reservoirs are given in the table 1. The hand valves are used for control of system purging and evacuation. In the current numerical model they are assumed to be fully open.
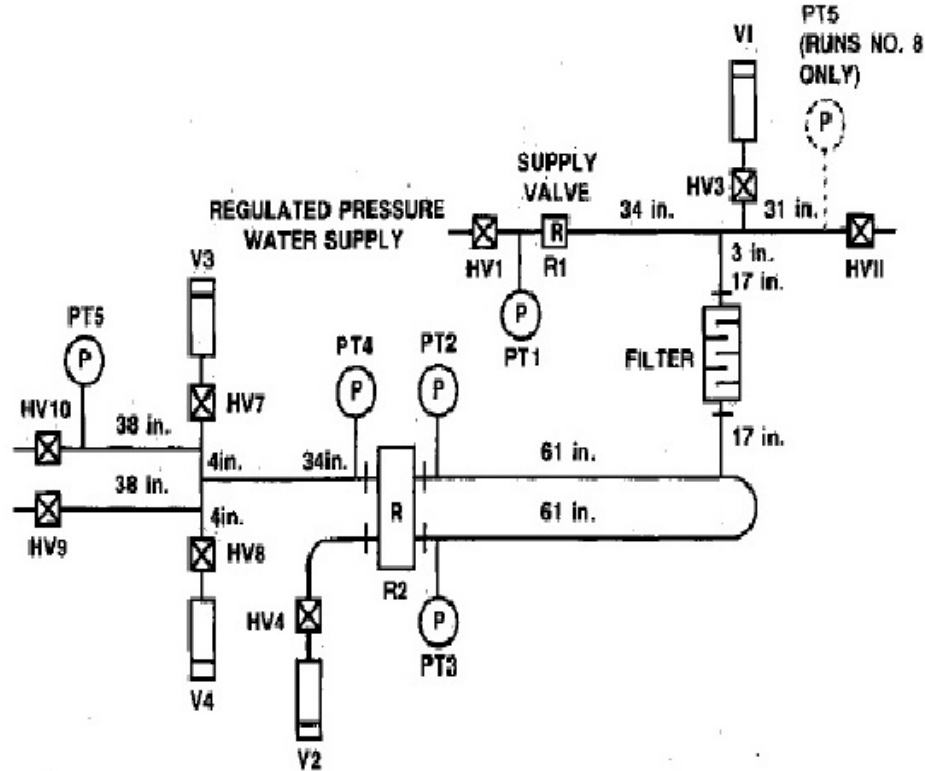
Figure 6. Schematic of a flow network (courtesy: Prickett et al)

Volume Reservoir	Volume in inch^3
V1	3.55
V2	14.55
V3	5.68
V4	4.68

Table 1. Volume Reservoir Information

The filter as shown in figure 6 above, is a liquid filter in which etched disk are stacked in a titanium casing, and the filter specification is given in table 2 below.

Filtration Rating	10 μm
Internal Volume	0.915 in^3
Pressure Drop	Δp, psia $= 15.92(GPM)^{1.18}$ GPM = discharge rate in gallons per min

Table 2. Liquid Filter Specifications

In the network, the main supply valve as indicated by R1 in figure 6, is a latch valve which opens instantaneously allowing the fluid to enter into the network from the main reservoir. There is another set of valves called the replacement component, indicated as R2 in the figure, is an attachment that can have different type of flow attachments (orifice, valves etc.) as used for testing by Prickett et al. For the current simulation, it is assumed that there are a pair of control valves that are initially open, but closes sharply at about 0.5 second, to see the effect of it on the water hammer pressure surges. The supply pressure varies, and for the current simulation 240 psia is

28

used as supply pressure as that was one of the worst case scenario regarding system failure as reported by Prickett et al in their experimental work.

Computational Model for the Flow Network is shown below in figure 7. Node 1 is the boundary node representing supply reservoir, and the volume reservoirs are labelled V1 through V4 in the figure.
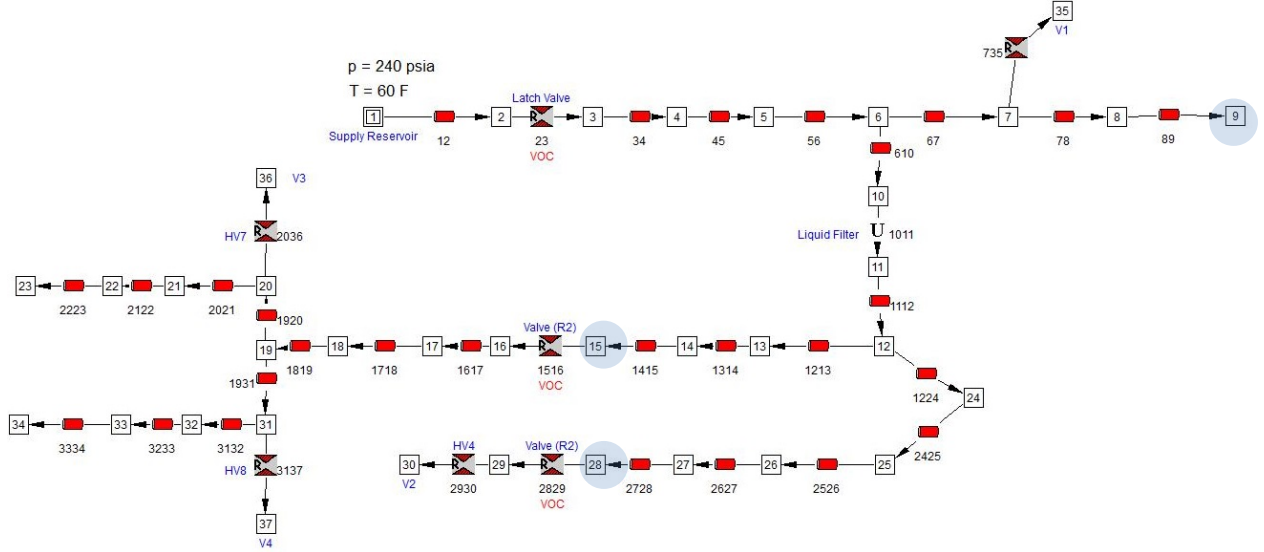

Figure 7. Computational Domain for the Flow Network

As hand valves 9, 10 and 11 were not used and the pipe line are assumed to be closed in the specific testing by Pricket el al, those are not considered in the current computational model. Nodes 9, 15 and 28 are highlighted as these are the nodes where the simulations results are monitored. The liquid filter is modeled by using the correlation for pressure drop given in table 2, and suitably converting into the form:

$$\Delta P = K_f \dot{m}^2.$$

III. Results and Discussion

The computational results are presented separately for all the three different case studies as mentioned in the earlier section In all three cases, the primary interest is finding the pressure distribution, and the results are reported at the locations consistent with the locations where test data are available in the literature for comparison.

**Case Study 1**: Water hammer in straight pipe with entrapped air

The first case study is the water hammer into a pipe with entrapped air. The two most important input parameters for this study are: $P_R = p_R/p_{atm}$ and $\alpha = L_{air}/L_{tot}$. Based on the value of α, three different geometrical configuration with initial air column length of 16.23 ft ($\alpha = 0.448$), 4.85 ft ($\alpha = 0.195$), and 1.23 ft ($\alpha = 0.058$) are considered for the study. As obtained from Lee's [9] experimental study, the experimental measurements of pressure at three different locations along the pipe are available. Two of these locations are at the ball valve and dead end. For the first geometrical case ($L_{air} = 16.23$ ft), the additional location is at midair and for the other two geometrical case the third location is at about mid water (10.9 ft from the pipe entrance location). Figures 9, 10 and 11 show the comparison of current numerical results with the measured data for Lee [9] for the three different α values. Results qualitatively match quite well in all the cases, except for the peak pressure is about 20% off from in the worst case. The frequency of pressure oscillations match quite well for most of the cases.
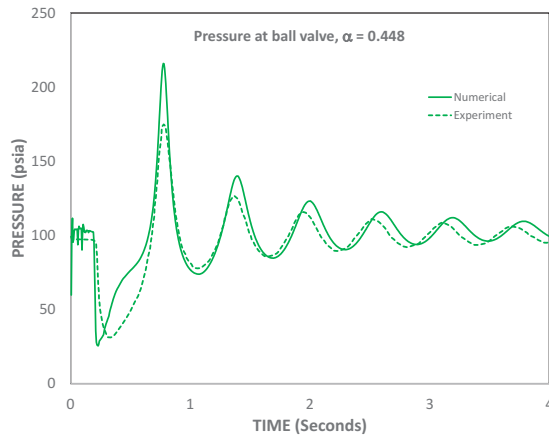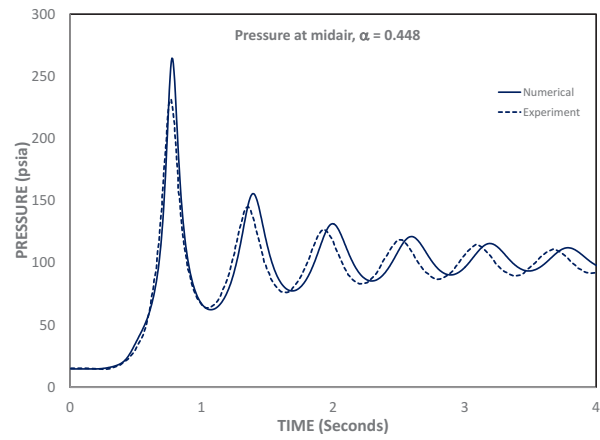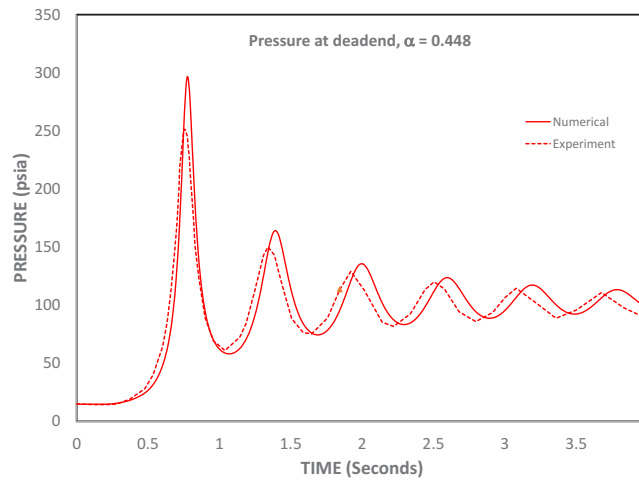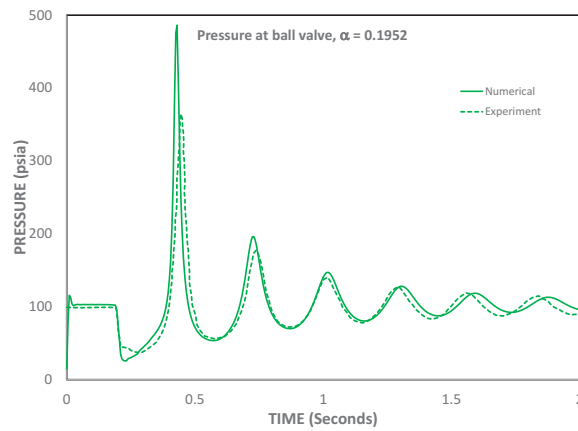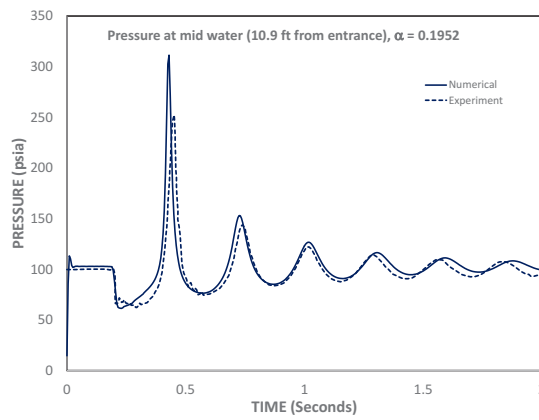
Figure 9. Pressure at (a) ball valve (b) midair and (c) dead end for $P_R = 7$ and $\alpha = 0.448$
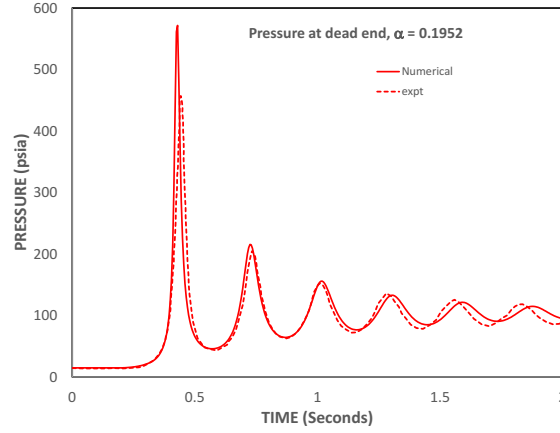
Figure 10. Pressure at (a) midwater (b) ball valve and (c) dead end for $P_R = 7$ and $\alpha = 0.1952$
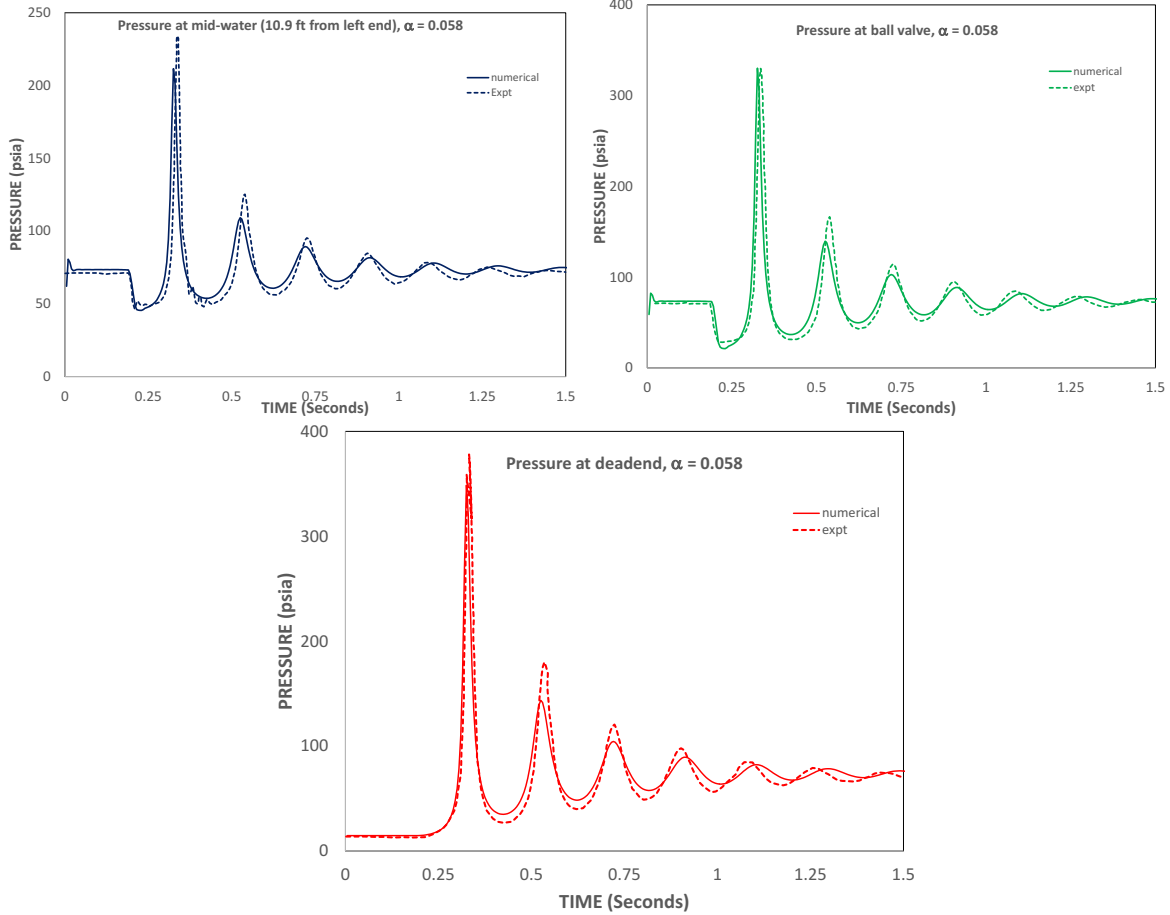

Figure 11. Pressure at (a) mid-water, (b) ball valve and (c) dead end for $P_R = 5$ and $\alpha = 0.058$

Case Study 2: Priming in evacuated straight pipeline

Two of the most important parameter in priming problem is the peak pressure and the impact time. The current numerical algorithm is validated against the test data for a supply pressure of 120 psia for which the peak pressure of 2350 psia and impact time of 0.17 seconds are measured by Prickett et al in their test facility. The current numerical model of using two fluids, the pressure in the air region is varied in order to obtain a virtually evacuated condition when the numerical value of peak pressure does not change appreciably. Another important numerical parameter in this transient study is the time step. A time step of 0.1 ms (milliseconds) and air pressure of 1 psia are used as optimized parameter so as to obtain a numerically time step independent result in idealized situation of evacuated

line. Figure 12(a) and (b) show this parametric study to obtain the optimized time step and downstream air pressure respectively.
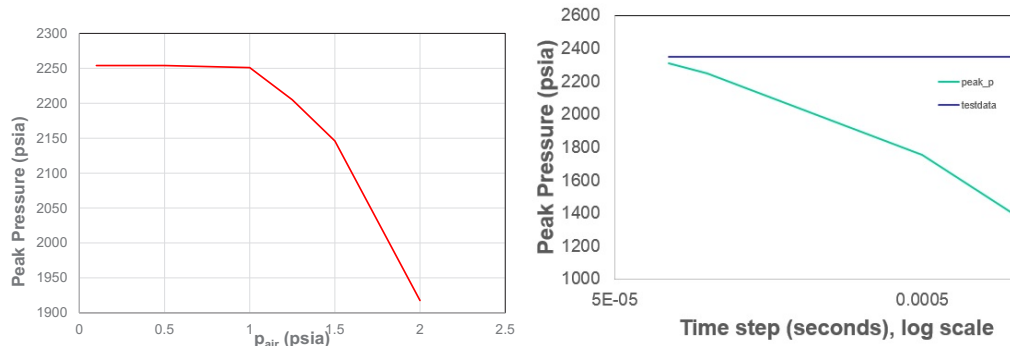

Figure 12. Optimization of the numerical parameters

For all the plots in the current simulation, time step of 0.1 millisecond and air pressure of 1 psia is being used. The maximum pressure rise occurs at the dead end and at time = 0.176 seconds as shown in figure 13 (A and B) below. Both the diagram represent same plots, A is enlarged view of B, in the neighborhood of peak pressure domain. The peak pressure is 2279 psia as compared to experimental data of 2350 psia. In fact the numerical results go even closer to the experimental data and is 2330 psia when the time step is reduced further to 0.075 second. However, lowering the time step causes numerical convergence issue. The impact time, the time taken to reach the maximum after the valve is opened is 0.173 second, which matches very well with the experimental result of 0.170 second.
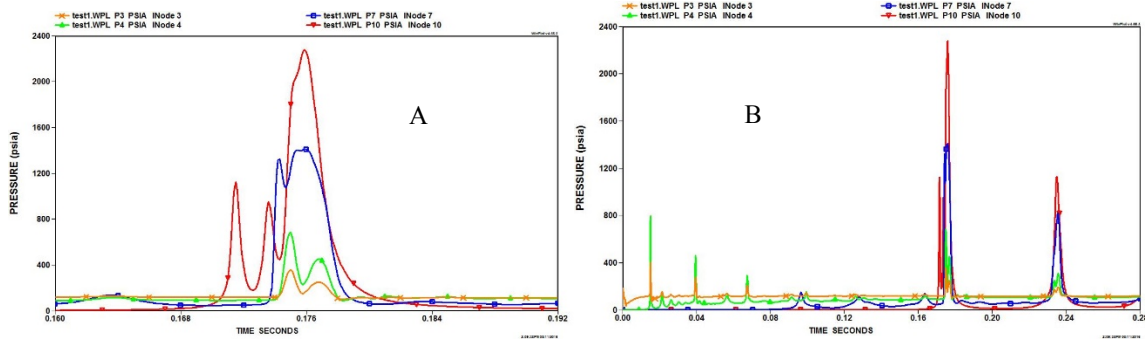

Figure 13. Pressure at various nodes

Case Study 3: Priming in a flow network
The pressure distribution in the straight region and in the branches are shown in figures 14 and 15 respectively.
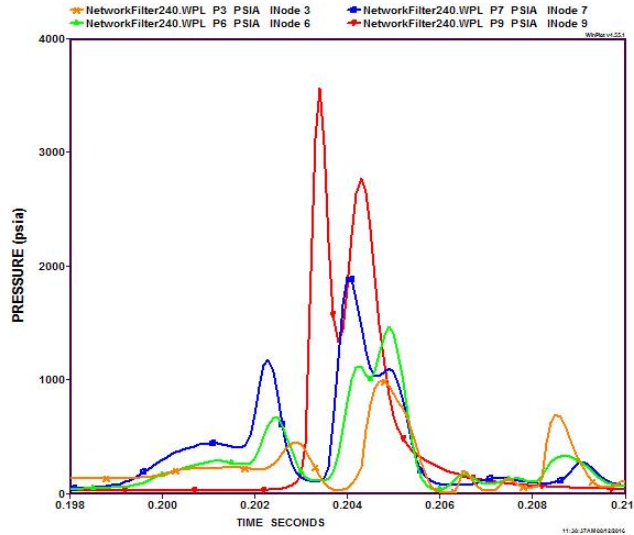
32

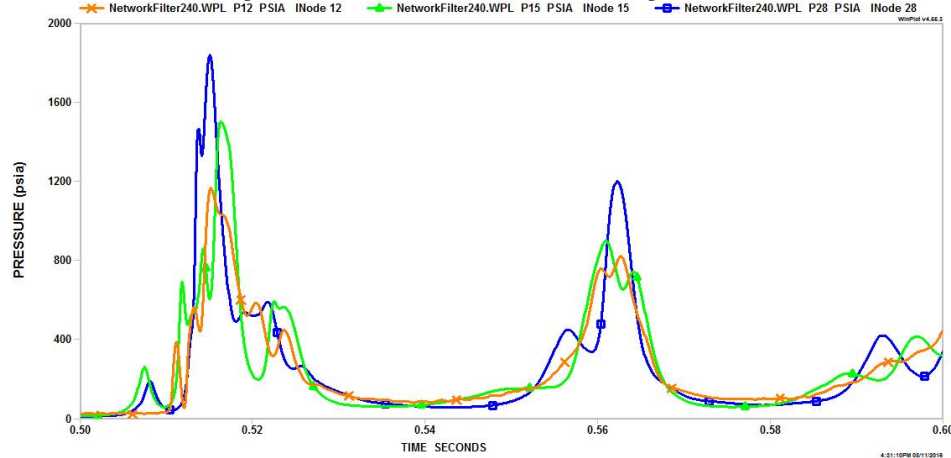Figure 14. Pressure Distribution in Straight Branch

Figure 15. Pressure Distribution in Bottom Branches, near the valve closing region.

The peak pressure occurs at the dead end of the straight branch, and numerically it is found to be little above 3500 psia. The pressure on the bottom branch, the peak occurs at node 28 and is found to be 1837 psia as compared to test data as reported by Prickett et al as 1800 psia. The peak pressure at dead end (node 9) can further be reduced using uinsteady friction factor model [11, 12] as shown in figure 16 below. Overall, the numerical prediction matches well with experimental data. However, due to lack of information from the literature the peak pressure at node 9 could not be compared. The pressure distribution in the frequency domain is obtained using a fast Fourier transformation and is shown in figure 17 below.
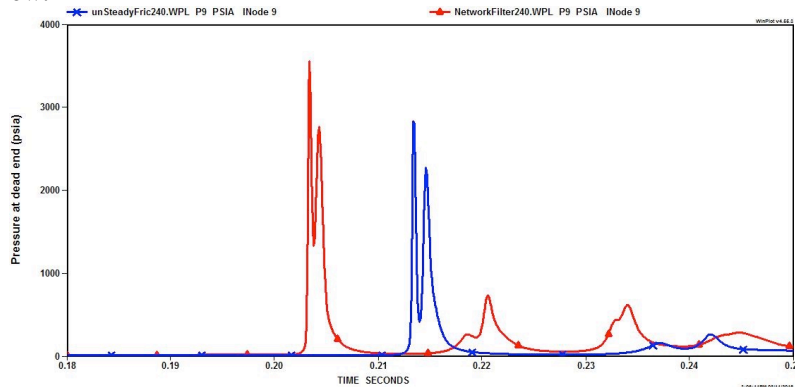

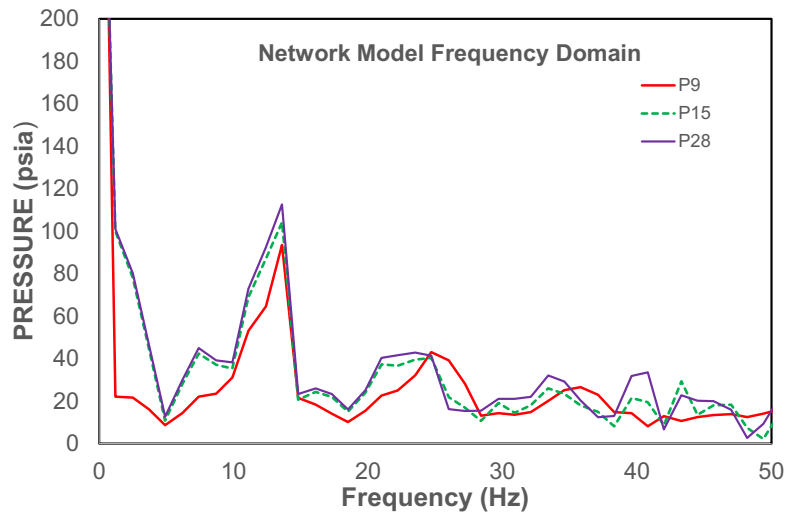Figure 16. Comparison between two different friction factor model

33

Figure 17. Pressure in frequency domain

IV. Conclusions

The two-fluid model produced very good agreement in all three case studies. The pressure at various locations, both upstream and downstream of the valve are computed and compared with measured data of Lee [9] for the entrapped air problem. The frequencies match very well except the peak pressure are slightly over predicted, a maximum of 18% error is found. The priming in straight pipe, the numerical prediction match very well with less than 1 % error. The unsteady friction factor helped reducing the peak pressure in the network model. There needs to be more testing done in this regard using the unsteady friction model. The work can be extended for water hammer analysis with real propellants which can be of more practical and real space craft use.

Acknowledgments

References

[1]Ghidaoui M.S., Zhao M., Mclnnis D.A., and Axworthy D.H, "A review of water hammer theory and practice", *Trans. ASME,* Jan. 2005, vol. 58, pp 49-76.

[2]Lin, T.Y., Baker, D., "Analysis and Testing of Propellant Feed System Priming Process," *J. Propulsion Power*, Vol. 11, No. 3, pp. 505–512, May–June 1995.

[3]Hearn, H.C., Development and application of a priming surge analysis methodology, *Proc. 41st AIAA/ASME/SAE/ASEE Joint Propulsion Conf. & Exhibit*, Tucson, AZ, pp. 1–10, July 10–13, 2005.

[4]Majumdar, A.K., Flachbart, R.H., "Numerical modeling of fluid transients by a finite volume procedure for rocket propulsion systems," *Proc. ASME FEDSM'03, 4th ASME/JSME Joint Fluids Eng. Conf.*, Honolulu, HI, pp. 1–8, July 6–10, 2003.

[5]Pinho J., Lema M., Rambaud P., and Steelant J., "Multiphase Investigation of Water Hammer Phenomenon Using the Full Cavitation Model", Journal of Propulsion and Power, Vol. 30, No. 1 (2014), pp. 105-113.

[6]Prickett, R.P., Mayer, E., and Hermel, J., "Water Hammer in Spacecraft Propellant Feed Systems", AIAA-88-2920, *Journal of Propulsion and Power*, vol. 8, no. 3, May-June 1992, pp.592–597.

[7]Lecourt R., and Steelant J. "Experimental Investigation of Water hammer in Simplified Feed Lines of Satellite Propulsion Systems", Journal of Propulsion and Power, Vol. 23, No. 6 (2007), pp. 1214-1224.

[8]Alak Bandyopadhyay and Alok Majumdar. "Network Flow Simulation of Fluid Transients in Rocket Propulsion Systems", Journal of Propulsion and Power, Vol. 30, No. 6 (2014), pp. 1646-1653

[9]Lee, N.H., "Effect of Pressurization and Expulsion of Entrapped Air in Pipelines", Ph.D. thesis, Georgia Tech., August 2005.

[10]Lee, N. H., and Martin, C. S. (1999). "Experimental and analytical investigation of entrapped air in a horizontal pipe." Proc., 3rd ASME/JSME Joint Fluids Engineering Conf., ASME, New York, 1–8.

[11]Brunone, B., Kearney, W., Mecarelli, M., Ferrante, M., "Velocity Profiles and Unsteady Pipe Friction in Transient Flow," *J. Water Resource Planning and Management,* Vol. 126, No. 4, pp. 236–244, 2000.

[12]Dehkordi, M.M., Firoozabadi, B.D., "Effects of Unsteady Friction Factor on Column Separation," *Proc. IMECE 2007*, ASME International—Mechanical Engineering Congress and Exposition, Seattle, WA, pp. 1–7, Nov. 2007

Iodine and Iodine Plasma Effects on Spacecraft Materials

Richard D. Branam[1]
University of Alabama, Tuscaloosa, AL 35487

Iodine as a propellant will allow volume-constrained, micro-satellites to reach the Moon and other near Earth objects. Current electric satellite thrusters employ xenon propellant stored in high pressure tanks limiting the amount of total impulse available to the satellite. Iodine is stored as a solid (no high pressure vessels), at density three times those of xenon (impulse density two to three times). Iodine presents unique challenges, though. This research is addressing the impact of using iodine as a propellant on solar panel surfaces, spacecraft structures, sensitive instruments on board satellites and the propulsion system. The current effort is quantifying material compatibility and sputter/erosion interactions of iodine and the iodine plasma. The compatibility of iodine effort is initially considering reactivity processes (physical properties, chemical kinetics and thermodynamics) with various spacecraft surfaces. Progress to date includes exposing several materials to iodine at low and moderate pressures and the construction of an iodine plasma chamber. While this effort is still in-progress, initial results are proving valuable to the NASA Iodine Satellite Demonstration mission. As an example, tungsten and tantalum are not as resistant to iodine as they are to oxygen.

Nomenclature

A	=	cross sectional area
C_X	=	capacitance of x capacitor
d	=	diameter: plasma sheath subscript s, orifice substrict
f	=	frequency
I	=	current
l	=	length of coil
L	=	inductance
k	=	Boltzmann constant
m_e	=	mass of an electron
N	=	number of coil turns
n_e	=	electron number density
Q	=	volumetric flow rate
P	=	pressure
T_e	=	electron temperature
T_r	=	reduced temperature
T_s	=	saturation temperature
V	=	voltage potential
v	=	velocity, subscript r relative, subscript o is thermal
X_L	=	reactance of inductor (L) or capacitor (C)
λ_d	=	debye length
μ	=	magnetic permeability
ζ	=	temperature dependent viscosity

I. Introduction

Iodine introduces a reactivity issue when being used as a rocket propellant. Reactivity is affected by physical properties (i.e. surface properties) thermodynamics (free energy) and kinetics (valance bond theory). In pure substances, increased exposure (surface area) will result in increased reactivity. Thermodynamically, the chances of a

---

[1] Assistant Professor, Department of Aerospace Engineering and Mechanics, University of Alabama, AIAA Associate Fellow.

reaction of two substances increases if the final products have a lower free energy. According to valance bond theory, the outer shell electrons can help explain the probability of a reaction. The focus of this research is defined by the expected environment found on a satellite with a Hall Effect thruster (physical, kinetic and thermodynamic) and focused on the specific materials used in satellite manufacture.

II. Iodine Plasma

Iodine is commonly a negative ion in the monatomic state as is typical with halogens. The proven ionization process used by space propulsion devices introduces high energy electrons. These electrons do influence the diatomic iodine to disassociate and create a negative ion in some instances. Negatively charged ions hurt the performance and efficiency of the thruster as the electric field attempts to accelerate negative charges in the wrong direction. Electronegativity describes the amount of energy needed for the monatom or diatom to capture an electron. The electronegativity of iodine is 2.5 eV for the diatom and 3.0 eV for the monatom, a low number compared to the ionization energies (10.4 eV monatom and 9.4 eV diatom).[1] The iodine is likely to capture electrons and become negative ions. The electric field in the thruster will then force the negative ions in the same direction as the electrons: into the thruster. The Hall Effect will not significantly influence the negative ions due to their larger relative mass as compared to the swirling electrons. The negative ions will head directly for the anode. By design, the energy of the majority of electrons influencing ionization is significantly more than the electron affinity of iodine. These electrons have too much energy to be captured, reducing the probability of negative ionization. Iodine can potentially outperform the conventional xenon thruster but definitely will require the propulsion device to operate under specific appropriate conditions.

Additionally, the effect of iodine ionizing as a diatom will significantly increase the performance (thrust) as propellant atomic mass increases to 254 amu.[2] 5 The differences in dissociation energy and ionization energy suggest that monatomic ions will be more prevalent: 1.5 eV to dissociate the diatom and 9.4 eV to ionize the diatom.[3] The expectation is to see some diatomic ionization, though.[2]

A. Satellite Environment

The iSAT Project is the maturation of iodine Hall technology to enable high ΔV primary propulsion for NanoSats (1-10kg), MicroSats (10-100kg) and MiniSats (100-500kg) with the culmination of a technology flight demonstration.[4]

The spacecraft plume interactions with the solar panels is one major concern. The design of the iSAT has gone through several iterations to ensure the deployed solar panels do not have a direct line-of-site with the plume. The charge-exchange ions will directly impact surface with a direct line-of-sight at a higher rate than for the solar panels deployed opposite the thruster as in Figure 1. A 12U cubesat (Figure 1) with the solar panels deployed as far away as practical

Figure 1: iSAT Configuration Modeled[1]

from the thruster and the plume provides better protection for these surfaces. In modeling the iodine environment, the configuration shown in Figure 1 was used.

The neutrals were modeled as a Maxwellian distribution at 500 K with a drift velocity of 230 m/s out of the thruster. The information on the ions came from measurements of ion energy distribution and current density as a function of angle from the centerline of the thruster. The information available on the particle interactions (elastic collisions, charge-exchange collisions) are modeled using collision cross-sections and a probabilistic model (COLISEUM).[5] For xenon and iodine in a Hall thruster plume, these cross sections are typically on the order of 10^{-16} cm^2.[6]

A COLISEUM model of the BHT-200 thruster plume and resulting neutrals and ion densities surrounding the iSAT spacecraft shows where iodine and iodine plasma interactions will have the greatest impact (Figure 7). The results show we need to be concerned for any materials on the exterior of the satellite. The thruster face can see iodine and iodine plasma as high as 4.0×10^{19} impacts/m^2/s. The thruster mounted surface will be subjected to neutral iodine near 1.0×10^{17} impacts/m^2/s and 4.0×10^{18} plasma iodine impacts/m^2/s. The velocity of both the neutrals and ions impacting the surface will be moving at the thermal velocity of the neutrals. Those ions impacting the spacecraft are produced by high energy impacts of ions in the plume with neutrals. The thermal velocity is 208 m/s for I$_2$ and 284 m/s for monatomic iodine. The more severe case (higher density) will be for I$_2$. For the impact densities seen in the simulation (Figure 3), the expected exposure density for the neutrals is 4.8×10^{14} m^{-3}, for the ions 1.64×10^{16}.
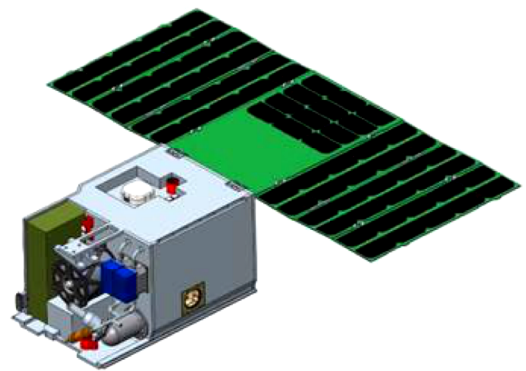
B. Condensation of Iodine on Surfaces

The spacecraft exterior will cycle between 73 K (-200°C) (radiator pointing at deep space) to 473 K (200°C) (solar panels in the sun). In order to protect the components inside the spacecraft, operating surface temperatures are nominally 298 K (25°C) (excluding the solar panels). The iodine will not condense on the surfaces at this temperature and the very low expected pressures of low Earth orbit (Figure 4).

For iodine fueled HETs, deposition is projected to be very low or non-existent.[7] Detailed modeling is required to validate this hypothesis. However, the SERT II mission already demonstrated that condensable propellants are compatible with solar electric propulsion (SEP). Mercury ion engines on SERT II were successfully fired on-orbit for 4000 hours.[8] Most spacecraft surfaces, including solar arrays, were too warm to permit

Figure 2: Coliseum Simulation Grid and Thruster Plume

Hg condensation and showed no evidence of condensate.[9] This bodes well for iodine, which has a much higher vapor pressure than mercury.
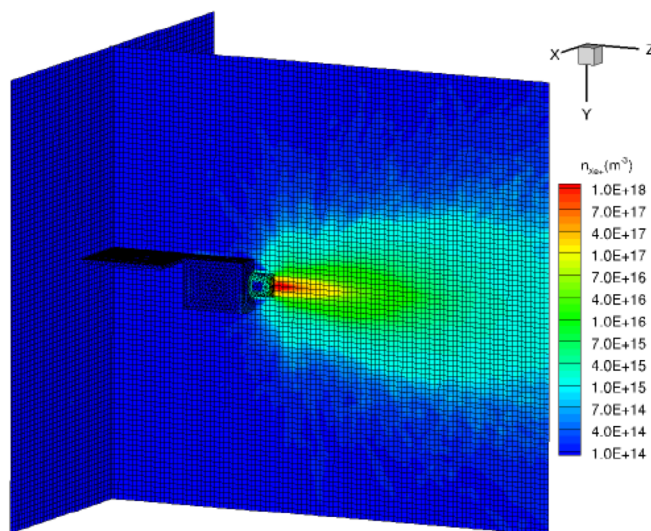

Figure 3: iSAT Plume Interaction**Error! Bookmark not defined.**

C. Busek BHT-200 Watt Hall Effect Thruster

The BHT-200 thruster developed by Busek Co. was used in this experiment both for the iodine and xenon operation. The BHT-200 is a well-known, highly characterized thruster proven in space missions. The xenon nominal operating condition is 250 volts and 800 milliamps discharge. It was used with a BHC-1500 hollow cathode mounted in standard configuration. The models of the plume provide the expected iodine interactions with the external surfaces. The most extreme environment is characterized, though, by taking a look at the internal flow path of the cathode.

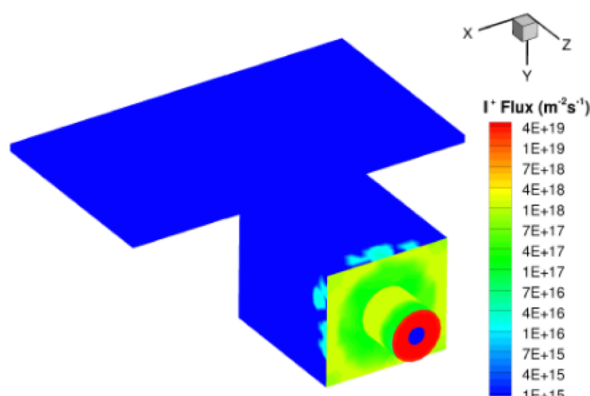Cathodes have three commonly utilized insert materials in current state-of-the-art cathodes. Lanthanum hexaboride (LaB6) and cerium hexaboride (CeB6) have bulk work functions near 2.7 eV and 2.5 eV, respectively.[10],[11] Barium-impregnated porous tungsten (BaO-W) has a work function of 2.1 eV.[10] To start the cathode, BaO-W inserts must be heated to 1300 K, and LaB6 inserts to 1900 K.[10] A room-temperature, stable electride (12CaO*Al2O3:(4e-)) has shown in testing the ability to produce electrons while resisting any corrosion or interaction from the iodine and iodine plasma. The CSU electride produced current as high as 0.15 A/m^2, temperature of 50 °C.[12] The work function for this material was calculated at 0.76 eV.

The inserts are shielded from direct contact with the barrel (Figure 5) using graphite. The insert materials will migrate into the molybdenum or tantalum barrel. The barrel orifice is often made from thoriated or lanthanated tungsten.
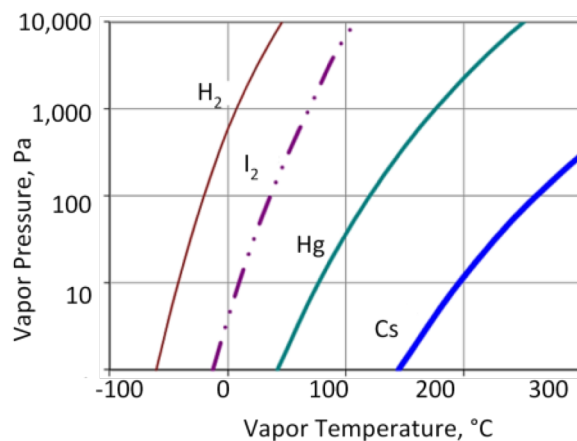

Figure 4: Vapor Pressure of I_2 and Other Electric Propulsion Propellants[1]

Some applications replace this expensive material with tantalum as seen in Figure 5. The keeper (graphite, molybdenum or steel) needs to be electrically isolated from the insert. The separation between the keeper and barrel allows for the plasma to migrate toward the heater and shielding. The heater is typically covered with alumina (Al_2O_3) or magnesia (MgO). These ceramics are expected to be fairly resistant to the reactive iodine and iodine plasma. The tantalum heat shielding, though, does react with iodine.

Determining pressure (and therefore plasma density) inside the cathode can be accomplished using Katz model.[13,14]
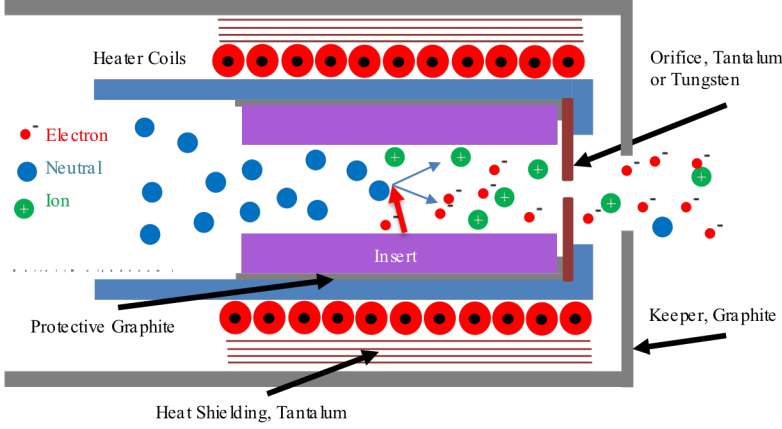

Figure 5: Hollow Cathode Configuration

Equations 2 through 4 provide the relationships to determine pressure and plasma density. These equations are results from the continuity equation and Poiseuille flow relationships. Equation 2 is the temperature dependent viscosity. The constants in this equation are for xenon.

The relative temperature (T_r) is given by $T_r = T/289.7K$, units are Pa-s.[15] Neutral gas temperatures in the insert region are heated by charge exchange. The increase in temperature increases the viscosity. The temperature in equation 2 can be determined from measuring the wall temperature and using the relationship equation 3. Gas temperature can be estimated as three times the wall temperature.[12] The measured wall temperature for our research is 1106 K.

$$\zeta = 2.3x10^{-5}T_r^{\,0.965} \qquad T_r < 1$$
$$\zeta = 2.3x10^{-5}T_r^{\left(0.71+\frac{0.29}{T_r}\right)} \quad T_r > 1 \tag{1}$$

$$T = T_{wall} + \frac{M}{k}\left[(fv_r)^2 + v_0^2\right] \tag{2}$$

The pressure is then determined from the pressure drop across the orifice (Poiseuille flow) using viscosity, temperature and flow rate.

$$P = \sqrt{0.78Q\zeta T_r\left(\frac{l_{orifice}}{d_{orifice}^4} + \frac{L_e}{d_{i,barrel}^4}\right)} \tag{3}$$

The ion density can be determined by the energy lost in the insert, equation 3.[14] For our test conditions, the resulting pressure and ion density are 300 Pa, $2.50 \text{ xv}10^{20}$ ions/m^3.

$$n_e = \frac{RI_e^2 - \left(\frac{5}{2}T_{eV} - \phi_s\right)I_e}{\left(f_nT_{eV}\sqrt{\frac{eT_{eV}}{\pi m}}eAe^{\frac{-\phi_s}{T_{eV}}} + n_0e\langle\sigma_i v_e\rangle V(U^+ + \phi_s)\right)} \tag{4}$$

III. Experimental Setup

From previous environmental modeling and empirical results, the following four spacecraft environments of interest are defined.

1. Inside cathode
2. Exhaust plume
3. Spacecraft exposure
4. Iodine feed system

The main parameters needed to be established the exposure environments are pressure, iodine density, iodine plasma density and test article temperature. The following table provides a summary of these parameters, based on the previous information

Table 1: Material Testing Environments

	Pressure (Pa)	Iodine Density $(\#/m^3)$	Iodine Plasma Density $(\#/m^3)$	Test Article Temperature
Inside cathode	301	6.58×10^{21}	2.5×10^{20}	1900 K (LaB_6)
Exhaust plume	0.1	10^{14}	10^{18}	500 K (cathode tip is hotter)
Spacecraft exposure	0.001	10^{14}	1.64×10^{16}	298 K (248 to 473 K)
Iodine feed system	10,000 Pa	2.63×10^{22}	N/A	473 K

A. Plasma Chamber

The following description focuses on the specific experimental setup at NASA/MSFC facility. Similar components are being utilized at the University of Alabama. The experiment is constructed beneath a fume hood. A water cooled cylindrical quartz tube serves as the plasma confinement tube and is inserted into a Mellen NACCI tube furnace. A coil (RF antenna) is placed around the quartz tube on one end. The tube is sealed by a vacuum flange assembly. In order to provide RF shielding, the frame of a metal box was constructed and placed over the antenna end of the tube. The inside and outside of the box was wrapped in silver coated FEP Teflon®. The other end of the quartz tube was connected via a vacuum sealing flange assembly to flexible wire reinforced PVC vacuum line. This line was connected to a water-cooled cold trap to prevent iodine vapor from escaping and damaging the vacuum pump. The vacuum line is connected to the vacuum pump via an oil trap placed on the vacuum pump intake port. In addition to the oil mist filter, a charcoal exhaust filter is installed on the vacuum pump exhaust port to further reduce the potential of iodine exhaust contamination. This exhaust is pumped into the fume hood.
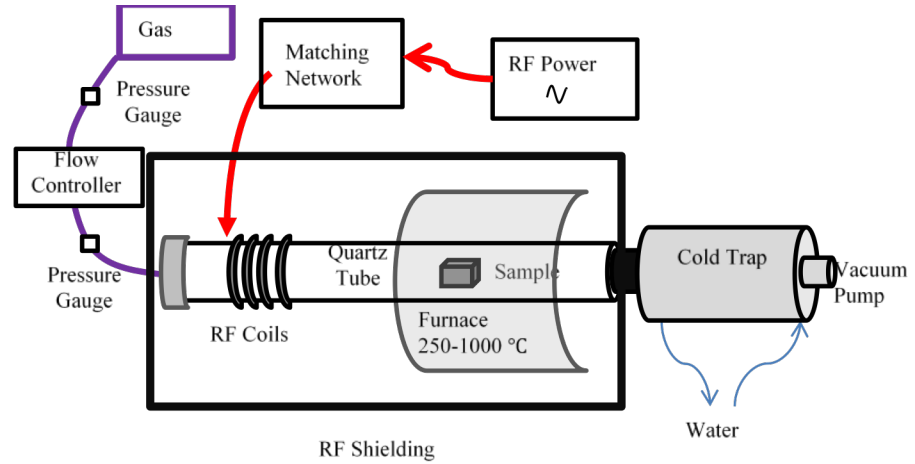

Figure 6: Test Setup, Plasma Source

Total pressure is measured accurately of 0.1 Pa at NASA/MSFC (Inficon PCG554, Pirani and capacitance diaphragm gauge) and with an accuracy of 1.0×10^{-4} Pa at the University of Alabama (Oerlikon Leybold PTR 90N, cold cathode ion gauge). Temperatures are monitored at several locations in the test setup using thermocouples and IR sensors: iodine entering the chamber, the test article, quartz tube, exhaust, RF antenna.

B. Iodine Feed System

The iodine feed system has already demonstrated operation at NASA/MSFC. Components are on hand and ready to integrate at the University of Alabama.

Iodine flow testing conducted at NASA/MSFC (Dr. Gregory Jerman) used a standard quartz vacuum tube furnace at a pressure of 10,000 Pa to simulate low pressure iodine vapor exposure in a vacuum. The furnace hot zone temperature set point was 473 K (200 ˚C), the maximum temperature expected for the iodine feed system. Iodine vapor was generated by heating solid iodine to 348 K (75˚C) in an argon atmosphere. The iodine vapor pressure is approximately 2,000 Pa when mixed with argon at 200,000 Pa.[16] The combined iodine vapor and argon gas then flowed through a flow control valve that regulated the pressure in the vacuum tube furnace to 10,000 Pa. The flow control valve and connected tubing were heated to 373 K (100˚C) to minimize condensation of iodine during test operations.

The experimental feed system can accurately control the iodine density and pressure expected by the spacecraft propellant feed system. Argon will not be available on the spacecraft. Parameters of interest with respect to the feed system include iodine flow rate, exposure time, and sample temperature. Two test conditions have been demonstrated for the current results: flow exposure → 10,000 Pa at 373 K for extended exposure times (30 days) and bath exposure → 100,000 Pa at 373 K for seven days.
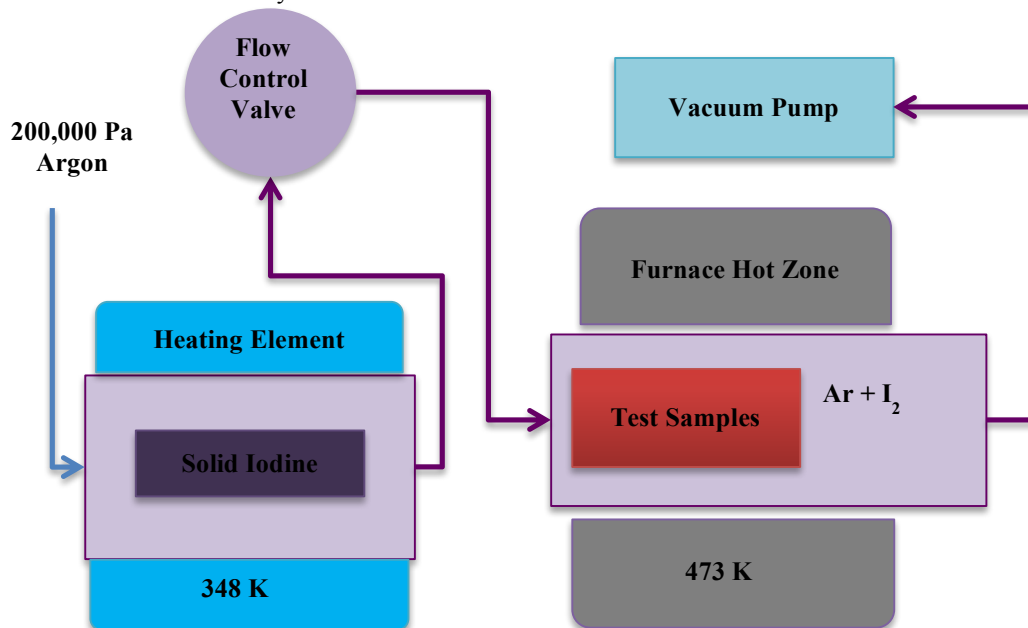

Figure 7: Iodine Flow Exposure Test Setup

C. Plasma Generation

The RF coils in Figure 6 deliver the radio frequency energy to the mass inside the quartz tube. In order to efficiently deliver the RF energy from the RF power supply, an adjustable matching network was constructed. The available RF power supplies currently provide 13.56 MHz, 600 W (NASA/MSFC) and 2.0 MHz, 1000 W (University of Alabama). In order to deliver maximum power, the power source and RF coil impedance must match. The differing RF frequencies required the matching network to have a wide range of operability.

Matching networks are used extensively to match power source impedance with the load (antenna for this research). The impedance is the effective resistance (composed of both ohmic resistance and reactance) of an electric circuit or component to alternating current. Inductors and capacitors are reactive components and are often employed for matching. In order to determine the needed values for the capacitors and inductor in the matching network, values for
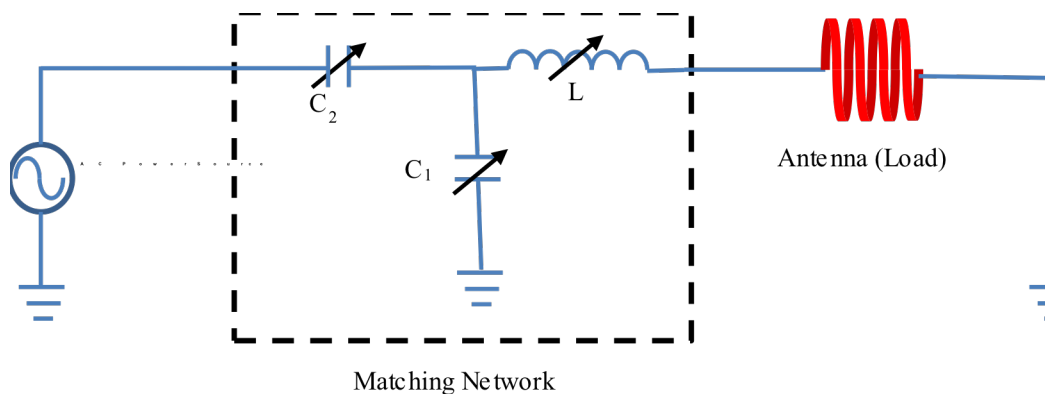

Figure 8: T Matching Network, Inductor Facing Load

the impedance of the antenna and source were needed. Typically, cables and power supplies are designed to be a specific impedance to facility matching (in this case, 50 Ω).

The antenna acts like an inductor in the circuit. The inductance is calculated from equation 6.   The reactance (impedance) of the antenna can then be calculated using equation 7. The antenna used for this effort has four loops (N), 75 mm diameter (A) and a length of 35 mm (l): 2.54 µH. The expected impedance at 1.0 MHz was then 32 Ω.

$$L = \frac{\mu N^2 A}{l} \qquad\qquad [5]$$

$$X_L = 2\pi f L \qquad\qquad [6]$$

The T matching network has only one capacitor leg to ground and acts like a low-pass or high-pass filter, depending on the location of the inductor. The circuit flows through both a capacitor and inductor (LCC circuit commonly used). The inductor is placed facing (closest) the lower impedance in order to match the circuit. For our research, the antenna proved to be at a lower impedance (Figure 8)

The matching network has a narrow target frequency, making it difficult to accurately match impedance and allow the source frequency to pass simultaneously without using variable capacitors and inductors. The transfer function (V_L/V_s) for our matching network tuned to a frequency of 1.0 MHz shows how the low-pass filter attenuates the signal but lets the target frequency to pass ().

D. Measuring Plasma Density
In order to characterize the performance of our ion source, we will need to measure the ion density being generated. We will use a Langmuir probe to characterize the environment inside the test chamber. This kind of probe can be used to determine electron temperature, plasma potential, floating potential, and number densities.

The probe is typically a small tungsten wire (~0.1 mm outside diameter, 2 - 3 mm exposed length). A ceramic insulator isolates the probe tip. Langmuir probes collect current by applying a voltage to the probe wire. This voltage typically starts at a negative value (~-10 V) and linearly increases to a positive value (~40 V).

In the ion saturation region of the curve (negative potential relative to the voltage of the plasma), the probe is at a sufficient negative voltage to repel all of the electrons in the plasma and saturates itself with ion current. Ion current, number density, and flux can be determined from the saturation region. The floating potential is the voltage when the ion and electron flux is equal. Theory developed by Laframboise is used to calculate ion number density. This theory accounts for the sheath that develops around the probe.[17]

$$d_s \cong \lambda_d \sqrt{\left|\frac{V - V_p}{kT_s}\right|} \qquad [7]$$

V is the applied voltage to the probe, d_s is the sheath width, and λ_d is the Debye length. Laframboise developed a family of curves, showing the relationship between ion current, a range of Debye lengths, and probe radii. The sheath thickness expands with probe potential and

Figure 9: Matching Network Transfer Function[1]

the collection "area" effectively increases. Without considering the sheath expansion, the current collected would be higher or lower than the true current. For this research, the Langmuir probe diameter is larger than the Debye length of the plasma. With a sufficiently large probe diameter, the sheath around the probe is thin and the ion current saturates well.

The electron retardation region of the I-V curve is physically when the electrons with enough energy to overcome the potential barrier of the probe are collected. Assuming thermal equilibrium for the electron distribution, the electron current grows exponentially relative to the probe voltage. The electron retardation region is used to calculate the electron temperature (Equation 7)
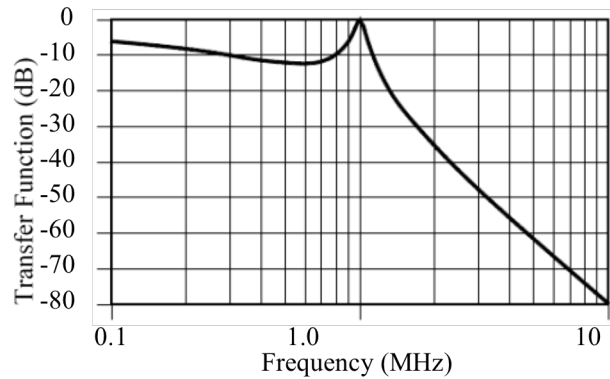
$$\frac{I(V_p)}{\int_{V_f}^{V_p} I(V)dv} = \frac{1}{kT_e} \qquad [8]$$

In the electron saturation region, just after the "knee" in **Error! Reference source not found.**, the probe is at a higher potential than the plasma and becomes saturated with electrons. Plasma potential is calculated from the slope of this region and the electron retardation region. Using the method of intersecting slopes, lines drawn along the slope of the 2nd and 3rd regions of the curve, the plasma potential is determined; the point of intersection of the straight lines. At the knee of the curve, the probe potential equals the plasma potential. Any current drawn in this region results from slow thermal electrons and ions. With the plasma potential determined, the electron number density can be determined (Equation 8).

$$n_e = \frac{I(V_p)}{A} \sqrt{\frac{2\pi m_e}{e^2 kT_e}} \qquad [9]$$

E. Material Samples

Samples will be identified and indexed to try and make measurements in the same locations before and after the exposure to iodine plasma. Measurable features will be repeated enough times to determine average values with at least a 95% confidence, where appropriate (i.e. surface roughness).

The samples will be prepared and indexed appropriately so verifiable measurements can be made and comparisons are being made accurately. In preparation, all samples will go through the same cleaning process: cleaned with alcohol and sealed. Metal samples will be micro indented to provide an easily identifiable reference when viewed under a Scanning Electron Microscope (SEM).

Table 2: Spacecraft Materials to be Tested

Material	Typical Application	Satellite Environment	Plasma
Alumina	Isolator, insulator, low erosion surface	Inside Cathode, Exhaust Plume	Yes
Aluminum, 6061	Structure	Spacecraft Exposure	
BaO-W insert	Cathode emitter	Inside Cathode	Yes
Hasteloy C-22 (Ni-56%:Cr-22%:Mo-13%)	Structure	Spacecraft Exposure	
Magnesium Fluoride (MgF2)	Solar panels	Spacecraft Exposure	
Molybdenum	Cathode	Inside Cathode	Yes
Molybdenum TZM (0.50% Ti, 0.08% Zr, 0.02% C, balance Mo)	Propellant supply junction	Spacecraft Exposure	
Moly-Manganese Metallized Surface	Metalized alumina ceramic prior to braze	Spacecraft Exposure	
PTFE (Teflon)	Supply tubing, valves	Iodine Feed System	
Stainless Steel 304 (Fe-74%:Cr-18%:Ni-8%)	Thruster structure	Spacecraft Exposure	
Tantalum	Cathode heat shield	Inside Cathode	Yes

Since iron reacts with air after being exposed to iodine plasma, these samples will be handled in an inert environment from the plasma chamber to the SEM chamber. One of the primary goals is to determine the impact iodine is having on the reactivity of iron with air. The following table identifies a sampling of the materials to be exposed to iodine and to iodine plasma. The complete list has 72 materials to be tested.

IV. Results

Results from exposing the materials to iodine are available. For this aspect of the research, the thickness of each test specimen was measured before and after iodine exposure with a digital micrometer to an accuracy of ±0.001 mm.

Corrosion rates of millimeters per year were derived from thickness changes over the tested time. The accuracy of each measurement is determined by the ±0.001 mm accuracy of the digital micrometer and the test length normalized to one year. For the thirty-day iodine flow exposure, the accuracy of each corrosion rate was 0.012 mm/year. The results of the seven-day iodine bath exposure had an average uncertainty of each corrosion rate of 0.052 mm/year.

The iodine exposure showed iron and copper allows as having the highest corrosion rates. Surprisingly, tantalum and titanium also demonstrated high rates in iodine, especially at higher pressures (Bath Exposure). The expectation was for these metals to exhibit the same low corrosion rates they have with oxygen. Nickel alloys prove to be the most resistant to iodine reactivity.

The plasma chamber has been constructed. Plasma has been generated. The next step is to characterize the chamber (pressure, temperature, etc.) and then measure/control the plasma properties in the chamber.

Table 3: Corrosion Rates when Exposed to Iodine Gas

Alloy	Flow Exposure, Corrosion Rate (mm/year)	Bath Exposure, Corrosion Rate (mm/year)
6061 Aluminum	0.147	0.209
110 Copper	0.606	
304 Stainless Steel (Iron)	1.055	0.261
Hastelloy C-22 (Nickel)	0.019	0.052
Pure Tantalum		0.834
Commercially Pure Titanium	0.037	0.782
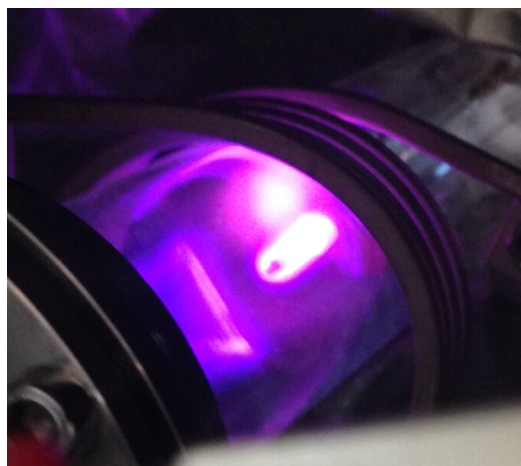
Figure 10. Plasma Sheath on Langmuir Probe, RF 2.0 MHz at 250W

Acknowledgments

References

[1]CRC *Handbook of Chemistry and Physics*, 83rd Edition, CRC Press LLC, Boca Raton, FL, 2002.

[2]Hillier, A.C., "Revolutionizing Space Propulsion Through the Characterization of Iodine as Fuel for Hall-Effect Thrusters," M.S. Thesis, Department of Aeronautics and Astronautics, Air Force Institute of Technology, Dayton, OH, March 2011.

[3]Dressler, R., Chiu, Y., and Levandier, D., "Propellant Alternatives for Ion and Hall Effect Thrusters," *38th Aerospace Sciences Meeting and Exhibit*, 2000.

[4]Dankanich, J., Polzin, K., Calvert, D., Kamhawi, H., "The Iodine Satellite (iSAT) Hall Thruster Demonstration Mission Concept and Development," *50th AIAA/ASME/SAE/ASEE Joint Propulsion Conference*, July 28-31, 2014.

[5]Spicer, R. L. "Validation of the Draco Particle-In-Cell Code Using Busek 200W Hall Thruster Experimental Data," M.S. Thesis, Department of Aerospace and Ocean Engineering, Virginia Polytechnic Institute and State University Blacksburg, 2007.

[6]Ali, A and Kim, Y., "Ionization Cross Sections by Electron Impact on Halogen Atoms, Diatomic Halogen and Hydrogen Halide Molecules," *Journal of Physics B: Atomic, Molecular, and Optical Physics*, Vol. 41, 2008 pp. 145202 -145214.

[7]Szabo, J., Robin, M., Paintal, S., Pote, B., Hruby, V., Freeman, C., "Iodine Plasma Propulsion Test Results at 1-10 kW," *IEEE Transactions on Plasma Science, Special Issue – Plasma Propulsion*, Vol. 43, No. 1, 2015, pp. 141-148.

[8]Kerslake, W., and Ignaczak, L. "Development and Flight History of SERT II spacecraft,", *28th AIAA/SAE/ASME/ASEE Joint Propulsion Conference and Exhibit*, AIAA-92-3516, July 1992.

[9]Hall, D., Newnam, B, Womack, J., "Electrostatic Rocket Exhaust Effects on Solar-Electric Spacecrafts," *Journal of Spacecraft*, Vol. 7, No. 3, March 1970, pp. 305-312.

[10]Goebel, D., Watkins, R. and Jameson, K., "LaB6 Hollow Cathodes for Ion and Hall Thrusters," *Journal of Propulsion and Power*, Vol 23, Issue 3, 2007, pp. 552-558.

[11]Warner, D. J., Branam, R.D. and Hargus, W.A., "Ignition and Plume Characteristics of Low-Current Cerium and Lanthanum Hexaboride Hollow Cathodes," *Journal of Propulsion and Power*, Vol. 26, Issue 1, 2010, pp. 130-134.

[12]Rand, L.P., "A Calcium Aluminate Electride Hollow Cathode," Ph.D. dissertation, Colorado State University, Fort Collins, CO, 2014.

[13]Katz, I., Anderson, J. Polk, J., and Brophy, J., "One-Dimensional Hollow Cathode Model," *Journal of Propulsion and Power*, Vol. 19, No. 4, 2003, pp. 595–600.

[14]Goebel, D. and Katz, I., *Fundamentals of Electric Propulsion: Ion and Hall Thrusters*, John Wiley & Sons Inc., Hoboken, NJ, 2008, Ch. 5.

[15]Reid, R. C., Prausnitz, J. M., and Sherwood, T. K., *The Properties of Gases and Liquids*, 3rd ed., McGraw–Hill, New York, 1977, pp. 402, 403.

[16]Lync, C. T., *CRC Handbook of Materials Science*, Vol. 1, p. 79, CRC Press Inc., Boca Raton, FL, 1974.

[17]Chen, Francis F. "Langmuir Probe Diagnostics" Mini-Course on Plasma Diagnostics, *IEEE-ICOPS Meeting*, June 2003.

Performance Characterization of Sun Sensor and Inertial Measuring Unit for the Near Earth Asteroid Scout Mission

D. Bullock[1]
Department of Electrical Engineering, Arkansas Tech University, Russellville, AR, 72801

D. Edberg[2]
Aerospace Engineering Department, California State Polytechnic University, Pomona, CA, 91768

A. Heaton[3]
NASA Marshall Space Flight Center, Huntsville, AL, 35812

B. Stiltner[4]
Qualis Corporation, Huntsville, AL, 35812

C. Becker[5]
NASA Marshall Space Flight Center, Huntsville, AL, 35812

B. Diedrich[6]
Dynamic Concepts Inc., Huntsville, AL, 35812

J. Orphee[7]
Aerodyne Industries, Huntsville, AL, 35812

At the beginning of its 2018 mission, NASA's Near Earth Asteroid Scout (NEA Scout) mission must perform two critical maneuvers shortly after separating from its SLS launch vehicle. The first maneuver is to stop all of the spacecraft's rotation rates that may occur during its separation from the launch vehicle, using angular rate data from an on-board microelectromechanical (MEMS) inertial measuring unit (IMU). Next, the spacecraft will use its on-board sun sensors to locate the sun and carry out its next maneuver: to orient the spacecraft such that the plane of its photovoltaic array is perpendicular to the sun, so that it may charge its batteries. In this report, we provide a detailed description of testing and a summary of the performance characteristics of the sun sensor array and the IMU.

I. Introduction

THE Near Earth Asteroid Scout (NEA Scout) spacecraft is a 6U CubeSat scheduled for launch on the Space Launch System (SLS) EM-1 in 2018. The objective of the 2.5-year NEA Scout mission is to demonstrate the use of a large, 86 m^2 solar sail for primary propulsion system, to rendezvous with a near earth asteroid, and gather photographic and other scientific information such as its size and spin rate. The NEA Scout spacecraft has an onboard science

---

[1] Faculty Fellow, Associate Professor of Electrical Engineering, Electrical Engineering, Arkansas Tech University.
[2] Faculty Fellow, Professor of Aerospace Engineering, Aerospace, 3801 W. Temple Ave., Pomona, CA 91768.
[3] NEA Scout G&C Lead, EV42, NASA-MSFC Building 4600/4212, Huntsville, AL 35812.
[4] NEA Scout GN&C Engineer, NASA-MSFC Building 4600/4215, Huntsville, AL 35812.
[5] Guidance, Navigation & Mission Analysis Engineer, NASA-MSFC Building 4600/4416, Huntsville, AL 35812.
[6] NEA Scout GN&C Engineer, NASA-MSFC Building 4600/4213, Huntsville, AL 35812.
[7] Multi-body Dynamics Engineer, NASA-MSFC Building 4600/4429, Huntsville, AL 35812.

camera that will be used take detailed images of the asteroid's surface features in hopes of identifying possible landing sites in support of a future manned mission to the asteroid.

The Planetary Systems Corporation's canisterized satellite dispenser (CSD) system that deploys NEA Scout from the SLS may induce rotational rates as high as 10°/sec in multiple axes. Therefore, spacecraft must perform two maneuvers that are critical to the success of the mission. The first maneuver is to detumble itself after deployment. After the NEA Scout has detumbled, it must locate the sun in order to successfully point the photovoltaic (PV) array that will be used to charge its batteries that provide power to the guidance and navigation system, communications equipment, and scientific instruments. If these early maneuvers are not successful, the mission will likely fail. Both the detumbling and sun-pointing maneuvers use dedicated sensors to achieve the maneuvers' goals. Since the performance characteristics of these sensors have not been studied, we provide a thorough description of the characterization of the performance of the inertial measuring unit (IMU) and sun sensors in this report.

The NEA Scout uses measurements provided by a Sensonor STIM 300 IMU [1] in order to detumble the CubeSat after deployment. This IMU is a strapdown, microelectromechanical (MEMS) system that contains a three-axis gyroscope for measuring angular rates, a three-axis accelerometer for measuring linear accelerations, and a three axis inclinometer for measuring inclination angles. MEMS-based IMUs are typically small, lightweight, and have minimal power requirements. The STIM 300 footprint is roughly 40 mm × 45 mm × 22 mm, masses 55 grams, and consumes 1.5 watts of power. One drawback of MEMS-based IMUs is that they do suffer from a lack of sensitivity at low rotational rates and small accelerations, when compared to high precision fiber optic gyros. For detumbling, the flight computer reads the rotational rates (~10°/sec per axis after ejection from the CSD system) from the IMU, and then uses a cold-gas thruster system to slow its rotation until the spacecraft is stabilized with negligible rates. One possible problem that may occur during the detumbling maneuver is that although the *initial* rotational rates are expected to be well within the capabilities of the STIM 300, as the thrusters gradually decrease the rates, they will eventually be slow enough that the IMU no longer gives useful information. At this time, the NEA Scout's star tracker will serve as the spacecraft's primary inertial sensor after the system has been stabilized.

For the sun-pointing maneuver, the NEA Scout employs three sun sensor packages attached on three different spacecraft surfaces. Each sun sensor package has a set of four silicon (Si) photodiodes that are optimized to be sensitive to wavelengths within the visible spectrum [2]. Each of the four photodiodes produce an electrical signal relative to the intensity of the light that strikes the face of the device. The relative strengths of the signals are then used to calculate a sun vector, which is used to point the photovoltaic array towards the sun in order to charge the onboard batteries.

II.   Experimental Setup

IMU Test Setup

The IMU tests were conducted in the Guidance, Navigation, and Control Laboratory facility at the NASA-Marshall Space Flight Center, Huntsville, AL. The test utilized the facility's Contraves Goerz Corp. high precision three-axis rotational rate table. The three-axis rotational rate table is vibrationally isolated from the building by resting on an independent concrete foundation that is separate from the building's foundation. The rate table allows the user to program angular rates of up to ±200°/sec for each axis, with an angular rate precision of ±0.00001°/sec.

To test the Sensonor STIM 300 IMU, a custom mounting plate was fabricated by 3D printing to allow the device to be mounted to the center of the rate table. After mounting the device, the appropriate electrical connections were made. In order to communicate with the IMU, a special RS-422 to USB cable was purchased from Sensonor. The USB-RS422 converter cable is a USB to RS-422 levels serial UART converter cable, incorporating FTDI's (Future Technology Devices International) FT232RQ USB to serial UART interface IC device that handles all the USB signaling and protocols [3]. The cable provides a fast, simple way to connect the IMU module with a RS422 interface to USB. The cable provides both communication and power from a connected laptop that is secured to the top of the rate table. Data were captured and stored using the Sensonor STIM 300 EVK software which allows the user to configure the IMU as well as graphically display gyroscope, accelerometer, and inclinometer data and export the raw data as a text file.

To measure the performance characteristics of the IMU under rotational rates similar to those that will be encountered during the NEA Scout mission, several tests were designed. For each test, carried out in ambient conditions, the IMU was configured to collect gyroscope, accelerometer, and inclinometer data for each axis. To measure the IMU bias, two tests were performed. First, the device was placed on a non-rotating rate table and data were collected from the IMU for 10 seconds, after which the IMU's power was cycled off and then on. Another bias test was performed for a one hour duration. Subsequent testing measured the run-to-run bias repeatability.

The testing matrix, shown in Table 1, describes the battery of tests that was designed, and each test's current status. It includes tests for bias, run-to-run bias repeatability, and IMU sensitivity at slew rates that will be experienced on the NEA Scout spacecraft. Additional tests were also designed to measure the IMU's performance characteristics during multi-axis rotations.

Table 1. **Sensonor STIM 300 IMU Test Matrix**

Test Name	Roll (°/sec)	Pitch (°/sec)	Yaw (°/sec)	Description	Status
Bias Offset	0	0	0	Measure initial bias offset. Two test were run one for 10 seconds and the other for an hour.	Completed
Run-to-Run Bias: Power cycle IMU	0	0	0	Measure run-to-run bias offset	Completed
Detumble – Roll	±10	0	0	Measure IMU performance at tumbling rate.	Completed
Detumble – Pitch	0	±10	0		Completed
Detumble – Yaw	0	0	±10		Completed
Min slew rate – Roll	0.01	0	0	Measure IMU performance at the minimum slew rate.	Completed
Min slew rate – Pitch	0	0.01	0		Completed
Min slew rate – Yaw	0	0	0.01		Completed
Max slew rate before sail deployment – Roll	1	0	0	Measure IMU performance at the maximum slew rate prior to solar sail deployment.	Completed
Max slew rate before sail deployment –Pitch	0	1	0		Completed
Max slew rate before sail deployment–Yaw	0	0	1		Completed
Max slew rate with sail deployed – Roll	0.04	0	0	Measure IMU performance at the maximum slew rate with the solar sail deployed.	Completed
Max slew rate with sail deployed – Pitch	0	0.04	0		Completed
Max slew rate with sail deployed – Yaw	0	0	0.04		Completed
Min rate for navigational stability – Roll	0.0001	0	0	Measure IMU performance at the minimum slew rate for navigational stability.	Pending
Min rate for navigational stability – Pitch	0	0.0001	0		Pending
Min rate for navigational stability – Yaw	0	0	0.0001		Pending
Multi-axis rotation performance–Roll+Pitch	10	10	0	Measure IMU performance during multi-axis rotation at detumble rotational rates.	Pending
Multi-axis rotation performance–Roll+Yaw	10	0	10		Pending
Multi-axis rotation performance Pitch+Yaw	0	10	10		Pending
Multi-axis rotation perf. – Roll+Pitch+Yaw	±10	±10	±10		Pending

To perform this test, the IMU was power cycled and data was taken on the stationary rate table for 10 seconds after the system was rebooted (note the STIM 300 reboot time specification is 0.3 seconds). This test was repeated twenty times in order to obtain an adequate sample size to measure run-to-run bias repeatability. Additional tests were designed to measure the IMU's sensitivity at the minimum and maximum slew rates for the spacecraft in different configurations: solar sail stowed versus deployed. Further tests were also designed to test the IMU's performance during multi-axis rotation.

As designated in the right-hand column of Table 1, many of the planned tests were completed. However, due to a critical malfunction of the rate table, not all of the proposed tests were completed. The authors plan to complete the remainder of the testing once the rate table is functional again. According to the point-of-contact for the lab, the timeline for repair may be several months.

Sun Sensor Test

The NEA Scout utilizes three sun sensor modules composed of four Hamamatsu S7686 Si photodiodes that are sensitive in the visible spectrum from 480 nm to 660 nm with the peak sensitivity occurring at 550 nm. The four photodiodes are each mounted at angles of 25° from vertical and produce an electrical current when light containing wavelengths within the photodiode's spectral response range strikes its face.

The sun sensor module was tested using a sun simulator that incorporated a 500 W mercury bulb. The sun simulator was mounted on a tripod that allowed for adjustments of height, vertical angle, and azimuthal angle. Additionally, the light intensity was adjusted by connecting the simulator to a variable autotransformer. The sun simulator was configured to measure the performance of the sun sensor array at 0°, 45°, and 90° from vertical. At each vertical

position the intensity of the sun simulator was adjusted to mimic the sun light intensity at one Astronomical Unit by measuring the optical power at the face of the photodiode array with a Thor Labs PM100D optical power meter connected to an S130C optical sensor. The sensor is sensitive to wavelengths from 400 nm – 1100 nm, similar to the optical sensitivity of the Si photodiodes.

The sun sensor array was mounted on a 3D printed replica the portion of the NEA Scout body where the sun sensor is to be mounted. To mimic the reflectance of the aluminum body of the CubeSat, the 3D printed replica piece was wrapped with household aluminum foil. The entire assembly was then mounted on a rotation table that allowed for 360° azimuthal rotation. For each sun simulator angle (0°, 45°, and 90° from vertical), the sun sensor data was taken for azimuthal angles from 0° to 180° in 10° increments. The experimental setup is shown schematically in Figure 1.
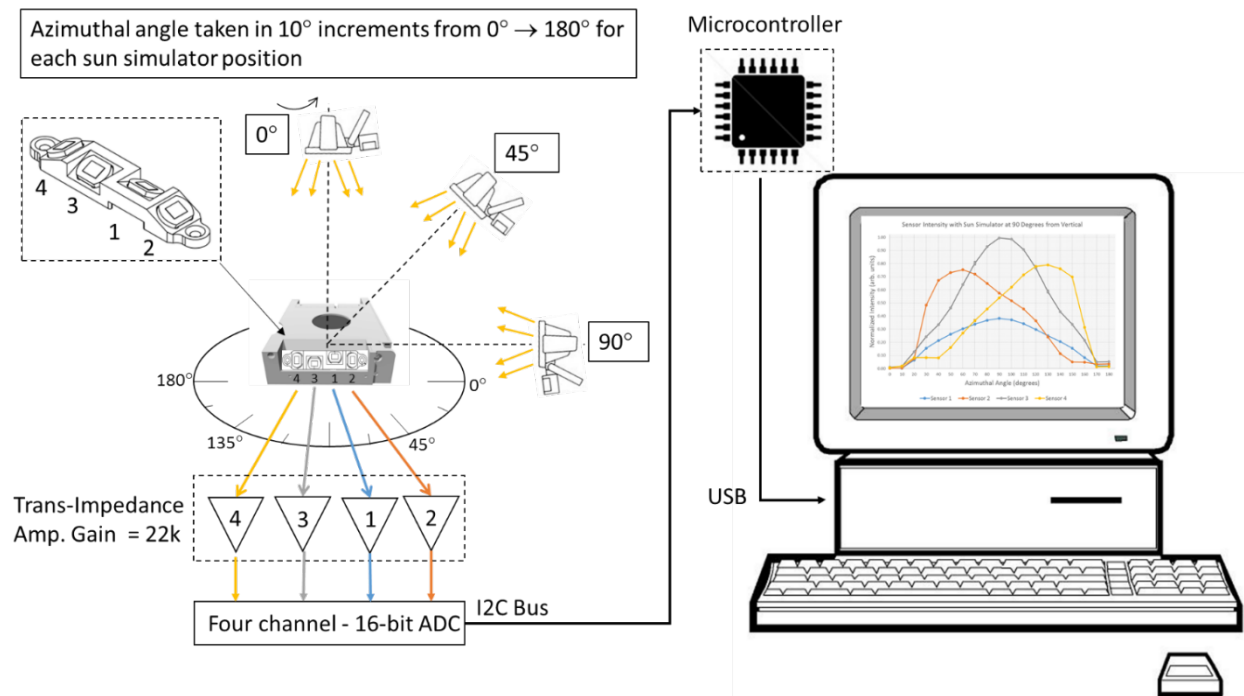

Figure 1. Illustration of the experimental setup. Data are taken by rotating the azimuthal angle from 0° to 180° in 10° increments for three different sun simulator angles (0°, 45°, and 90°). The currents generated in the photodiodes are then connected to trans-impedance amplifiers (TIAs) that produce an output voltage proportional to the input currents. The output voltages are then connected to a four channel, 16-bit analog to digital converter that are then sent to a microcontroller on the I2C bus. The microcontroller is then interfaced with a PC to capture the data.

The electronics on the NEA Scout convert the currents produced by each photodiode into a count that is proportional to the current. To mimic the flight electronics, a circuit was built that converts the current into a voltage using a trans-impedance amplifier (TIA). The TIA is an operational-amplifier (op-amp) based inverting amplifier. In this application each photodiode's cathode (negative terminal) is connected to the inverting input of an LM324 op-amp (the non-inverting input is grounded). A feedback resistor is connected between the output of the LM324 and the inverting input. This feedback controls the gain of the amplifier. The value of the feedback resistor (22 kΩ) was chosen such that at maximum intensity the voltage output would be below the saturation levels (+5 VDC) of the amplifier. The output voltage is equal to the product of the photodiode current and the feedback resistor.

The output voltage from each photodiode is connected to a four channel, 16-bit analog to digital converter (ADC). In this experiment, the ADS1115 was chosen as the ADC. The ADC was powered with +5 VDC which resulted in a 0.125 mV per bit resolution [4]. The ADC was then connected to a microcontroller using the I2C bus. The microcontroller also configured to communicate with a PC using USB port. Data was collected at a rate of 1 Hz. For each angle, 10-20 data points were taken for each of the four photodiodes in the sun sensor array. The data was then averaged, normalized, and plotted.

III. Results

IMU Test Results

At the writing of this paper, the data collection process is still ongoing. Some preliminary data have been collected regarding the bias, run-to-run bias repeatability, and sensitivity at operational slew rates.

Sun Sensor Test Results

Figures 2A, 2B, and 2C show the results from the sun sensor tests with the simulator at 0°, 45°, and 90° from vertical respectively.

In Figure 2A the sun simulator was placed directly above the sun sensor assembly. Photodiode sensor 1 shows the strongest signal followed by sensors 2 and 4 that have roughly the same signal intensity, and signal 3 that has the lowest intensity. As expected, the relative intensity levels remain fairly constant as the sensor is rotated through the different azimuthal angles. However, the signal intensity for all for sensors rapidly decreases at the 180° data point. This is attributed to a slight misalignment error in mounting the sun sensor to the rotational table.

Figure 2B shows the data with the sun simulator at 45° from vertical. These data show that sensors 2 and 4 have the highest relative intensities at 60° and 120° respectively. Also, sensors 1 and 3 reach their maximum values at the same azimuthal angle of 90°.

In figure 2C, sensors 1 and 3 reach their relative maxima at the same azimuthal angle of 90°, while sensors 2 and 4 reach their maxima at 60° and 130° respectively.

IV. Discussion

The IMU data generated from the rate-table tests will help in characterizing the performance of the device while undergoing rotational rates similar to those that the NEA Scout will experience. The data will yield some important error constants that relate to bias, bias instability, and random walk noise that will be used in a Simulink/MATLAB® model of the IMU currently under development. Additionally, the STIM 300 is scheduled to fly on another mission to the International Space Station (ISS), and the data gathered from the rate-table tests will be shared with the group planning that mission.

The results from the sun sensor test will aid in building a model that can be utilized to ensure the sensor provides correct data to assist the NEA Scout in sun pointing. Additional testing using the current setup will further examine the effects of spurious reflections off of nearby spacecraft components.

Acknowledgments
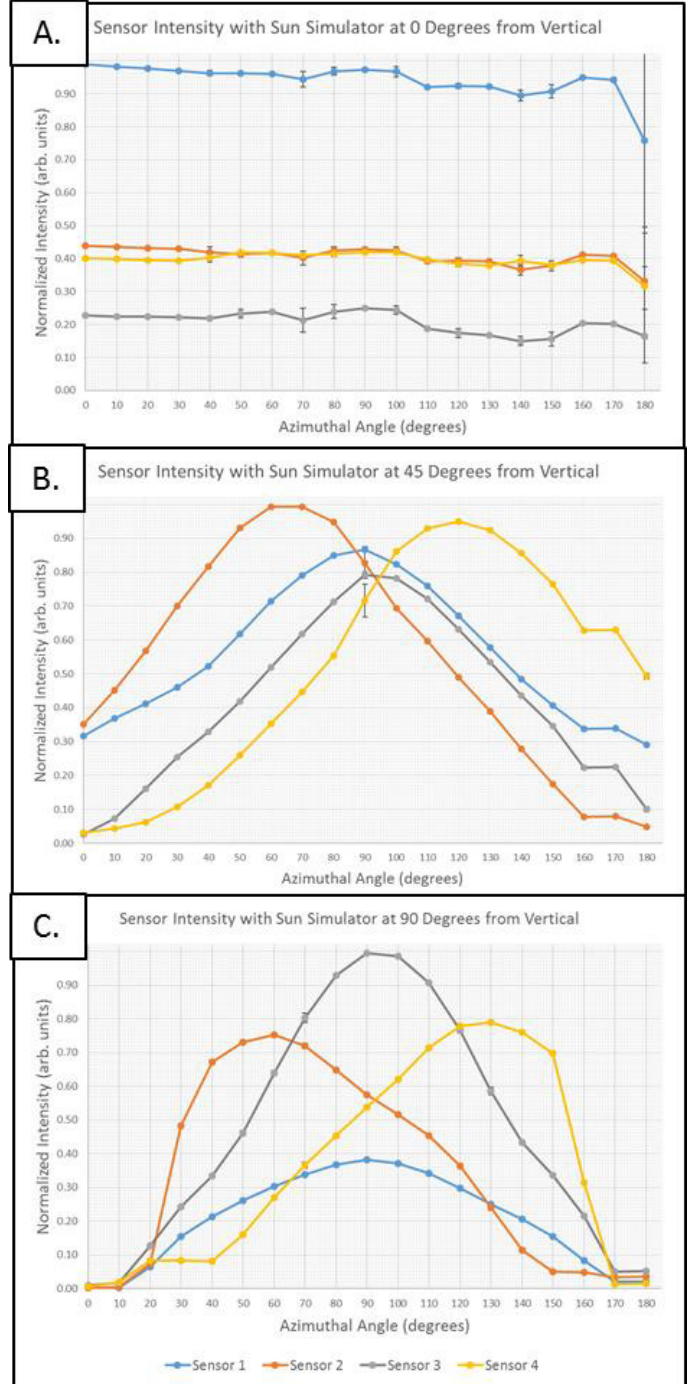
Figure 2 Normalized sun sensor data for vertical sun simulator angles of 0° (A), 45° (B), and 90° (C).

References

[1] Sensonor, "STIM300 Inertia Measurement Unit," STIM300 datasheet, Oct. 2015 [TS1524 rev.20].

[2] Hamamatsu, "Si photodiode S768," S7686 datasheet, Oct. 2002.

[3] Sensonor, "User Manual STIM210/STIM300 Evaluation Kit," manual, 2015 [DOK412 rev.0].

[4] Texas Instruments, "Ultra-Small, Low-Power, 16-Bit Analog-to-Digital Converter with Internal Reference," ADS1115 datasheet, May 2009 [Revised Oct. 2009].

Selected On-Demand Medical Applications of 3D-Printing for Long-Duration Manned Space Missions

Andres L. Carrano[1]
Auburn University. Auburn, AL 36849. USA.

    Recent technological advances in the area of Additive Manufacturing (i.e. 3D printing) allow for exploration of their use within long-duration manned space missions. Among the many potential application domains, medical and dental fabrication in support of crew health is of interest to NASA's Advanced Exploration Systems directorate. A classification of medical events with their associated response timeline discern between those applications where current 3D printing technologies can provide adequate support. Products and devices that require on-demand fabrication (due to the high level of personal customization) but that can wait for a reasonable (e.g. few hours) fabrication time are the most promising areas. Among these non-emergency, on-demand applications, two were identified for further investigation: dental health and pharmaceutical drugs. A discussion on the challenges presented by a microgravity operational environment on these technologies is provided.

I. Introduction

Current logistics operations for Low Earth Orbit (LEO) systems, such as the International Space Station (ISS), rely on regular resupply missions from earth. As NASA continues to advance human exploration beyond LEO, especially within the framework of the Evolvable Mars Campaign (EMC) and its strategic objective of expanding human presence to the surface of Mars, mission durations in the range of 2-3 years will need to be Earth-independent from a logistical standpoint. The baseline logistics design requires anticipated needed materials to be stowed on-board at the beginning of any space exploration missions. Under current logistics approaches, the extended mission durations will require transfer vehicles to carry very large amounts of materials which in turn will place severe constraints and trade-offs on mission payloads. This is aggravated by the inability to abort or resupply. Consequently, developing in-space manufacturing capabilities is a necessary step that has been identified as a key enabler for a sustainable human presence in space and a means to achieving truly earth-independent human spaceflight[1].

As part of the Advanced Exploration Systems (AES) directorate, the mission of NASA's In-Space Manufacturing (ISM) initiative (MSFC-ZP30) is to identify, design, and implement on-demand, sustainable manufacturing solutions for fabrication, maintenance and repair during exploration missions. The ability to produce parts and components on-demand while in space has the potential to impact both mission logistics (through payload mass reduction) and supportability (through risk reduction and increased ability to addressed unforeseen needs). Specifically, in-space manufacturing will provide the crew with various capabilities during long-duration exploration missions, including the following:

- the ability to carry and keep raw materials as undifferentiated stock, thus maximizing commonality.
- the ability manufacture spare parts and components for existing designs.
- the ability to manufacture new designs as well as redesign alterations.
- an enhanced ability to adapt to unexpected circumstances encountered during flight.
- the ability to repair damage components.

In addition to the primary objectives of reducing resupply weight and mass, and increasing mission supportability, there are secondary benefits of an on-demand fabrication capability. This includes the ability to supply items required to meet any scheduled or unexpected medical or dental need.

---

[1] Associate Professor, Department of Industrial and Systems Engineering, Auburn University.

The purpose of this report is to perform a review of current ground technologies and investigate their potential and challenges for health applications while operating in a microgravity environment. This is accomplished by: (*i*) proposing a classification of the potential application domains for 3D printing in support of crew health; and (*ii*) identifying two of the most promising applications and documenting their current ground capabilities, materials and products. Also, a discussion of the challenges of current ground-based technologies under microgravity environment as well as with regards to the introduction of potential hazards is provided.

II.   Potential in-space applications of 3D printing in support of crew health

The mission durations being considered for deep space explorations can very well extend into several years. This essentially means that all medical events that occur on the ground, can conceivably arise during a space mission in such span of time. Thus contingency plans for all these events will need to be developed both for when these events arise while in transit and during planetary residency. The space, crew time, and materials constraints while on planetary low gravity habitats can be significantly different thus are not considered here. The scope of this report aimed at microgravity applications within crew transfer vehicles.

With respect to the application domains, one approach is to characterize these into emergencies and non-emergency events. While the space context can cause ambiguity on the differentiation between the two categories (and most events can certainly evolve into an emergency over time), the real constraint will be on the response time for the support 3D printing system to such events. Figure 1 depicts the potential for a 3D printing platform with regards to the speed of response.
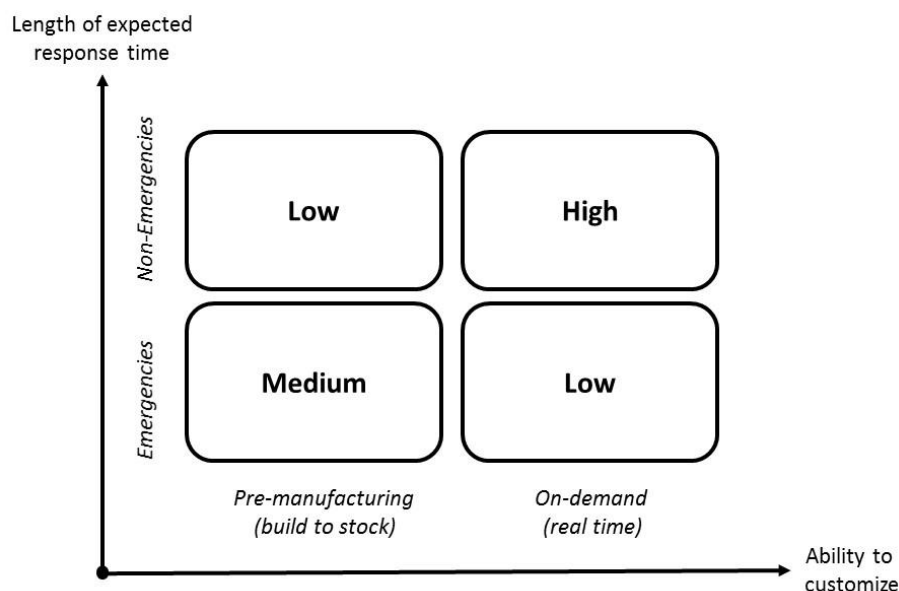

Figure 1: Potential impact of a 3D-printing supported response to in-flight medical events

In figure 1, pre-manufacturing refers to the fabrication of the device or product needed to treat a condition ahead of the event taking place. Of course, this fabrication is meant to fill an inventory stock in anticipation of a demand. The most significant advantage is the responsiveness attained by having supplies readily available. The main drawback is the inability to accurately predict events and the ensuing commitment of materials to a specific product or purpose. On-demand (real time) manufacturing refers to the fabrication of the device or product immediately after the need arises. Because 3D printing is not an instantaneous process, with fabrication taking anywhere between 15 minutes and several hours (including setup, post processing and sterilization), this is not feasible for a suite of applications in which time is of essence. For example, when it comes to emergencies, where a response in a matter of seconds or minutes is critical, current on-demand 3D printing is too slow and unlikely to be the solution.

However, when it comes to a dental event, such as a crown replacement (where a highly customized part is needed), fabricating such in a matter of few hours might be acceptable.

A. Non-emergency events

Because of careful astronaut selection, rigorous medical screening, and short mission durations, there is very little data available on non-emergency events during spaceflight. Nonetheless, issues will arise due to the extended time under microgravity conditions as well as because of other risks. For example, it is expected that prolonged absence of weight loading combined with sharp limitation of motor activity (hypokinesia) in weightlessness environments will results in muscle atony, which in turn might increase the likelihood of muscle and bone injury. Some of the potential applications for non-emergency events that can be supported with current ground 3D-printed technologies are presented in Table 1:

Table 1: Potential applications of 3D printing for non-emergency medical events

Applications	Examples
• Dental	Crowns, abutments, bridges, drill guides, aligners, bite guards.
• Orthotics and prosthetics	Flexible splints, calipers, braces, custom casts, foot inserts.
• Ear	Specula, custom hearing aid shells.
• Pharmaceutical drugs	Custom compounded, quick dissolving tablets.
• Medical instruments and utensils	Tissue forceps, clamps.
• Vision	Contact lenses.

B. Emergency events

Some of the medical emergencies that have previously arisen help illustrate the likelihood and nature of such during longer exploration missions. To date, there have been over 400 astronauts and cosmonauts involved in more than 60 person-years of manned spaceflight[2]. From 1961 until 1999, there have been 17 nonfatal emergencies in the general areas of trauma (2), cardiopulmonary (6), internal medicine (3) and genitourinary (5)[3]. Some models estimate the emergency incidence rate on orbit by approximating that to the rate of the general population on the ground[3,4]; usually about 0.06 events per person-year. For a 7-person crew and a 2.4 year mission duration to Mars, it can be expected to have 1 emergency per mission. However, given the strict medical screening of crew members, it can be argued that this incidence rate is unrealistically high. Another study[5] estimated the occurrence, type and severity of the incidents among the astronaut population while they were not on active duty. It classified these incidents into either emergencies that would have warranted evacuation or into incidents that would have been managed by the health maintenance facility at the ISS. From this study, a medical evacuation incidence rate of 0.02 events per person-year was found. Others[6,7], cited epidemiologic studies on incident rates in analogous populations in US Navy submarines and Antarctica stations and found equivalent rates for space missions events that would require medical evacuation because of minor surgical diseases (one event in 3-6 years for a 6-person crew) or acute appendicitis (1-2 cases in 45 years for 6-person crew).

Admittedly, every possible emergency that can arise in the ground, can also occur on orbit. In addition, there are medical risks and conditions that are associated with the microgravity environment and spacecraft restrictions. These include radiation and toxic gas exposure, increased fracture and dislocation risk due to bone demineralization and confined spaces, muscle and ligament injury due to muscle atony, blunt and penetrating injuries during space construction and EVAs, infectious diseases due to confinement, among others.

Some of the applications for emergency events that can potentially be supported with current ground 3D-printed technologies include:

- *Orthopedics for trauma*: it is well documented that significant bone demineralization occurs while under extended microgravity conditions; a situation that is expected to worsen in prolonged flights. Although no fractures, dislocations or other muscle/ligament injuries have been reported to date, if any were to occur, the slow healing in microgravity environments would likely require counterforces by restraining devices (e.g. splints)[3]. There is evidence that bone healing at the cellular level is delayed in space[8] and that muscle atrophy from deconditioning could also affect fracture healing by not providing sufficient fracture site impaction force. For non-invasive procedures in closed fractures, 3D printing offers the opportunity to

fabricate custom designed restraining devices (such as flexible aluminized or ABS splints) that are well adapted to the anatomy of the astronaut and specific to the type of injury. For invasive procedures, custom orthopedic implants, such as hip replacement cups or craneo-maxillofacial plates with designed porosity, have been manufactured terrestrially with electron-beam melting out of titanium alloys (Ti4Al6)[9].

- *Advanced cardiac and trauma life support*: in the event that medical resuscitation takes place, advanced life support will likely be needed. One of the most common advanced life support procedures include chest-tube insertion and tracheostomy. Devices that support such advanced function, like a laryngeal mask airways, could potentially be fabricated (and even customized) in anticipation of these events with multi-material 3D printing technologies.
- *Surgical instruments*: A wide arrangement of instruments can be fabricated with current ground technologies. These include scalpels, clamps, and hemostats, among others.

Because of the nature of the medical events reviewed in this section, the type of response needed, and the current capabilities of the 3D printing technologies commercially available, the most promising domain of applications is in support of non-emergency events, specifically those that require a high level of patient customization. Two of such applications (dental health and pharmaceutical drugs) are further explored in this report.

III. Dental Health Applications

Manufacturing of dentures, crowns and appliances using 3D Printing has been around for more than a decade. The technologies being used for terrestrial dental applications, especially those for polymers, are fairly mature and have been used for many other applications. Thus, the use of these technologies for in-space manufacturing as it pertains to dental health is a promising extension. However, it should be noted that the applicability of such technologies will require a more complex human skill set and training among the astronauts to both manufacture the needed product and to complete the dental treatment.

When it comes to anticipating the type and frequency of dental needs, there is no available data during spaceflight to estimate the incident rates for dental emergencies. This is because of a combination of the typically low incident rates of such events on the ground coupled with short mission durations, rigorous astronaut selection and strict pre-flight medical screening processes. In the only documented episode of a dental event[2], Soviet cosmonaut Yuriy Romanenko experienced a toothache during a 96-day flight of Salyut-6 in 1978. Since the Soviet space program had no contingency plans for dental emergencies back then, the cosmonaut had to endure the condition for two weeks until the Salyut 6 returned on schedule. Since this episode went unaddressed for two weeks, it raised significant awareness for the need of contingency plans for dental emergencies. A NASA informal account describes a temporary in-flight repair of a crown displacement by a crewmember with onboard supplies and without any complications[10]. Several Russian cosmonauts have also reported lost fillings and crowns in-flight that were likely dislodged by launch vibrations. Despite the lack of data, it is conceivable that dental emergencies will occur during longer space exploration missions and that in-flight treatment will be needed.

Previous studies on similarly isolated populations, such as the crews in submarine patrols, provide some insights on the incident rates and types of dental emergencies[11,12], Others attempt to do so by extending the period of pre-flight observation for astronauts[10]. Of interest among the findings, dental emergencies accounted for 6.9 − 9.3% of all medical evacuations from submarines in the U.S. Atlantic fleet between 1991 and 1999; the fifth highest cause. Another study[13] reported that tooth restoration accounted for 2% of all procedures performed in 136 submarine patrols between 1997 and 1998. Data acquired from the astronaut population that includes preflight events establishes the incidence rates of certain events at: 0.3% (caries), 0.02% (pulpitis), 0.003% for avulsion and 0.005% for crown replacement[10]. The same study reports that he MIR program had 304 medical events between 1987 and 1996 with only one event related to a dental caries. This results on an incidence rate of 0.01% per 100 days.

Augmenting the importance of properly addressing dental emergencies in space is an unanswered question: does exposure to microgravity result in the loss of mineral density in alveolar bone?. Although loss of minerals in load-bearing bones has been well documented, microgravity may well play a role on increasing tooth disease in long duration exploration missions.

The following table shows the types of pre-flight events that have been documented[10] among the astronaut population, as well as other applications that have not been reported (but appear promising). It also attempts to characterize the likelihood that 3D printing would have played a significant support role in their treatment.

Table 2: Dental events among astronaut population (preflight period) and potential for 3D printing intervention.

Events and Applications	Potential for in-space 3D-printing supported intervention
In-flight reported events[10]	
• Pulpitis	No
• Crown (dislodged, broken)	Yes
• Tooth fracture	Maybe
• Abscess (root canal)	No
• Caries (fillings)	Maybe
Other potential applications	
• Braces	No
• Dental Trays / full mouth cases	Yes
• Full and partial dentures	Yes
• Veneers	Yes
• Aligners	Yes
• Night guards bite splints	Yes
• Surgical guides / drilling guides	Yes
• Orthodontic appliances	Yes
• Abutments/ dental bridges/ bars	Yes

While there are many companies in the secondary market offering dental products and services, there is only a few technology providers, essentially offering variation of a couple of proven 3D printing principles. An overview of the current processes, materials and applications are summarized in figures 2 and 3. The sources for the commercial technologies and materials are provided in the reference section[14-28]
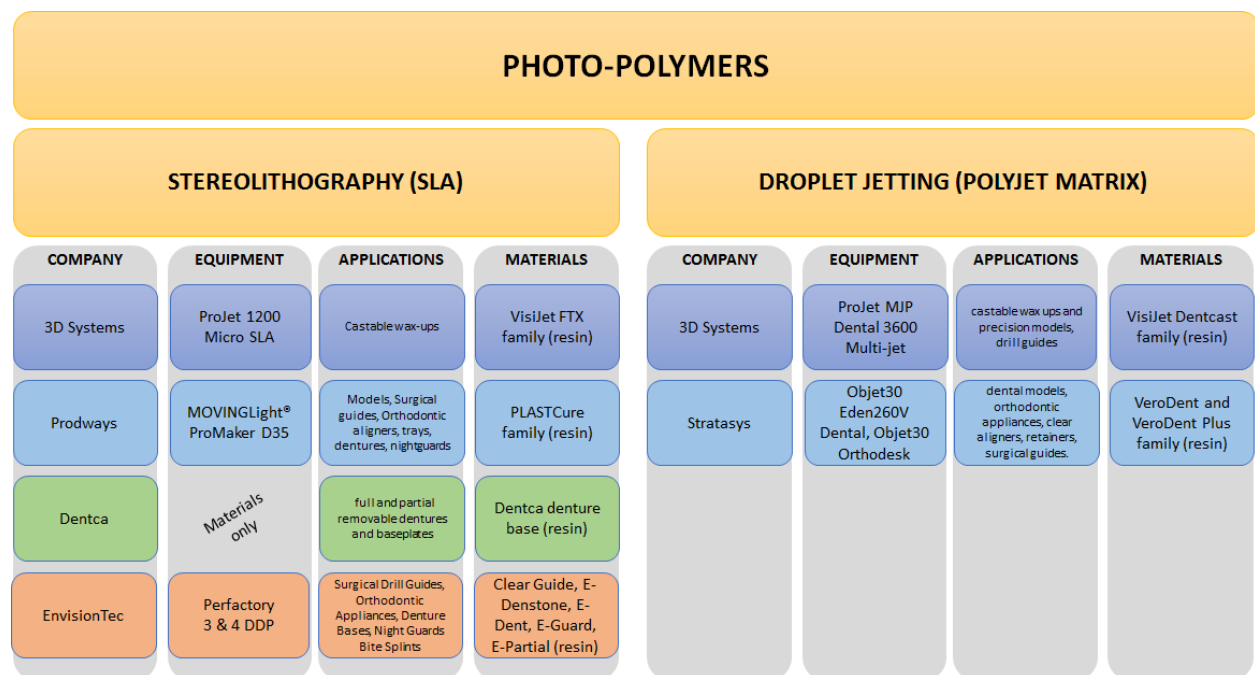

Figure 2: Overview of current technologies and materials for dental applications (polymers)

METALS

HYBRID
(POWDER BED FUSION/CLADDING + PRECISION MILLING)

COMPANY	EQUIPMENT	APPLICATIONS	MATERIALS
DMG Mori	Lasertec 65 3D	Not specialized on dental	Stainless steel, Inconel, Chrome cobalt, others.
Renishaw	Renishaw AM250	Abutments	Cobalt chromium (powder)
Hybrid Manufacturing Technologies	Retrofit of CNCs with cladding head	Not specialized on dental	Various (powder)

POWDER BED FUSION

COMPANY	EQUIPMENT	APPLICATIONS	MATERIALS
EOS	EOS M100 Direct Metal Laser Sintering	Dental models, removable partial dentures, crowns and bridges.	EOS Cobalt Chrome SP2
ConceptLaser	Mlab LaserCUSING	crowns, caps, model castings and secondary structures	Cobalt chrome, titanium, precious-metals alloys

Figure 3: Overview of current technologies and materials for dental applications (metals)

Out of the many dental treatments, the most promising appear to be those supported by the manufacturing of products such as crowns, bite guards, aligners, dentures, surgical/drilling guides, and some orthodontic appliances. Other products, such as abutments, bridges and other structures may be possible but likely limited by the human skill set needed to complete the treatment as well as the ability to manufacture load-bearing components and to post-process them to acceptable tolerances.

With respect to polymer-based fabrication of dental products, two technologies are predominant: Stereolithography (SLA) and Droplet Jetting. Both technologies are mature and have the resolution and capability needed to produce ready-to-use dental products. Both boast layer thicknesses in the order of 16-30 µm which result in excellent surface finish. The interlayer bonding and densification of both technologies is such that the resulting mechanical properties are adequate for the dental products being manufactured and do not typically need post processing. The equipment used in SLA has a smaller footprint and much lower energy consumption when compared to the analogous metal-based equipment. Some of the challenges include the use of an open vat for resin (SLA), and the generation of resin waste (both processes). Droplet jetting also employs a liquid resin but it is contained in a closed system. However, its operating principle could be affected by microgravity so testing is required to understand this effect on machine performance. Also, the droplet jetting machines tend to generate more waste (due to resin confinement) and have a larger footprint (though energy consumption remains relatively low).

With respect to metal fabrication, two fundamental technologies are predominant: laser-based powder bed fusion and laser-based cladding. Hybrid systems that combine these with precision milling have started to become available. These systems use principles that have been proven in other application domains and are capable of manufacturing structural parts (such as abutments and implants) that can withstand higher loads and stresses. However, there are some barriers for their use for in-space manufacturing of dental products. Current technologies are not capable of achieving the resolution and surface finish needed for dental products so significant post finishing (likely precision milling and polishing) is needed. This post processing will likely remove material in the form of metal chips and thus pose a risk of cabin contamination. It will also require cutting fluids and coolants which aggravate the situation. Also, the raw material for these metal processes is fine powders (24-200 µm) which will be very difficult to handle and contain in microgravity. Finally, because of the physical principles governing the sintering and melting of metals, these machines possess a large footprint and invoke significant amounts of energy during operation.

While current 3D printing technologies have been successfully been employed for terrestrial dental applications, their use for in-space manufacturing of dental needs is not without its challenges nor is it directly transferrable. These challenges will need to be addressed or alternative principles will need to be developed before a solution can be implemented in microgravity.

IV. Pharmaceutical Drug Applications

Pharmaceutical drug manufacturing is one of the latest applications of 3D printing. Lee Cronin's visionary TED talk in 2012 predicted that doctors will no longer write prescriptions but will instead provide algorithms so patients can print the drugs at their homes. The first FDA-approved 3d printed drug was announced in August 2015 [29] and made commercially available to the U.S. market in the first quarter of 2016 [30]. The company at the forefront of this application (Aprecia® Pharmaceuticals) currently uses a proprietary technology called ZipDose® to manufacture a porous formulation that quickly disintegrates with a sip of liquid, thus enhancing the patient experience. More drug applications can be expected in the near future, as they have three other products in the approval pipeline.

Table 3: Advantages of on-demand 3D printed pharmaceutical drugs

Advantages		Terrestrial	In-space
	Enables the packing and delivery of high drug load into a single dose.	Yes	Yes
	Allows for compounding of several formulations (previously taken as separate) into one.	Yes	Yes
	Requires very small amounts of liquids for delivery of high drug loads and quick disintegration.	Yes	Yes
	Helps overcome swallowing disorder.	Yes	Maybe
	Helps enforce adherence to dose protocol by simplifying it.	Yes	Yes
	Allows for taste masking capability thus enhancing the experience	Yes	Yes
	Allows for customization of doses based on patient's characteristics (e.g. weight, height, etc.).	Maybe	Maybe
	Pharmaceutical drugs that might have limited shelf life (once compounded) may have extended shelf life (if kept separate).	Maybe	Maybe
	Allows for keeping undifferentiated stock of pharmaceutical drugs that will maximize commonality and allow for flexibility in formulations	Maybe	Yes
	Allows for telemedicine	Yes	Yes
	Addition of compositional or structural features into each slice might allow for customization of time-release profile or other.	Maybe	Maybe

The technology used to manufacture these oral drugs, called ZipDose®, is based on a modified powder-liquid 3-dimensional printing developed by MIT in the 1980's [31]. The principle relies on a layer of compressed powder upon which a liquid binder is precisely applied to form a 2D layer contour. Repeating this process forms a three-dimensional object. There can be implications on the use of this technology while on orbit during long-duration exploration missions and during which operation under microgravity conditions might pose certain challenges. Some of these are summarized below in Table 4.

Table 4: Challenges for current powder-liquid binder 3DP technology for adaptation to microgravity environments

Disadvantages	Terrestrial	In-Space
Issues with handling of powder raw stock (including contamination)	No	Yes
Issues with compounding principle (requires gravity-assisted powder pressing).	No	Yes
Issues with process volumes (currently geared towards higher volumes/mass production)	No	Yes
Highly porous structures with seemingly weaker bonds (designed to quickly breakdown) may be challenging to manufacture.	No	Maybe
Aqueous binder might introduce resolution issue under microgravity	No	Maybe
Risk of erroneous compounding (sub or super potent), incorrect loading/dosing, contamination or adulteration (human or machine error).	Unlikely	Maybe

The ability to 3D print pharmaceutical drugs on the ground currently exist. The most promising aspects for long-duration space missions are: the flexibility gained by stockpiling raw materials for later custom compounding, the potential for extending shelf life of certain drug ingredients, as well as the reduced requirement of intake fluids. However, the current operating principle relies on gravity-assisted powder handling as well as aqueous application of binder materials. While the later can likely be overcome in the near term, the powder form of the drug ingredients might require a paradigm shift on the operating principle (e.g. "pre-pressed powder tablets" upon which the binder can be selectively applied as opposed to a layer of powder) as well as containment for this to work. For example, a new startup company[32] from Germany proposes using an edible filament process to print tablets. This process, though promising, is still in its infancy.

V. Other Considerations

In order for 3D printing technologies and systems to adequately support medical (and other) applications while in space, there are a series of considerations and requirements that must be considered. These include restrictions on space available for the installation (likely to be constrained to an EXPRESS Rack payload volume), operational complexity and crew time requirements, process capabilities, material recyclability, safety, etc., among others. One of the most important aspects in space mission design is safety. The introduction of 3D printing technology onboard must not introduce any unsafe conditions or risks to the crew and mission. One aspect that is critical is that the system must not introduce any harmful contaminants into the crew cabin at any concentration. All materials (fluids, powders and gasses) must be contained at all times and appropriately handled. This in itself is a challenge for current technologies since prevalent processes (i.e. droplet jetting, SLA and SLS/DMLS) used in dental applications employ either liquid resins or powder metals. Any hybrid technology that incorporates precision milling coupled with 3D printing will likely make use of cutting fluids and will generate metal chips. Two separate studies[33,34] investigated and characterized the particle emissions from various types of printers and materials, finding a presence of PM10 (10 μm) in the vicinity of the printer. Ultrafine particulate emissions could present some inhalation hazards to the crew but larger particles can pose a contamination risk across the board. These risks will need to be characterized and mitigated before these technologies become mainstream for space manufacturing.

VI. Conclusions

The technological advances in the area of 3D printing allow for investigation of their use within long-duration manned space missions. Among the potential application domains, medical and dental fabrication in support of crew health is investigated. A classification of medical events with their associated response timeline discern between those applications where current 3D printing technologies can provide adequate support. Products and devices that require on-demand fabrication (due to the high level of personal customization) but can wait for a reasonable (e.g.

few hours) fabrication time are the most promising areas. Among these non-emergency, on-demand applications, two were identified for further investigation: dental health and pharmaceutical drugs. Dental health products and appliances have been manufactured using 3D printing for many years. However, there are significant challenges related to the three predominant approaches with respect to operation in microgravity: stereolithography (open resin vat), droplet jetting (liquid resin), hybrid (machine size, energy consumption, powder metals and milling chips). With respect to 3D printing of pharmaceutical drugs, while the technology has existed for a while, the application to drug manufacture has just been approved by the FDA. This also presents significant challenges, as the process relies on gravity-assisted layers of powders and a liquid binder to solidify the compound. These challenges would need to be addressed before an in-space implementation is deemed feasible.

Acknowledgments

References

[1] Owens, A., "In-space manufacturing utilization study: Task 3" Exploration Mission and Logistics Assessment. NASA Marshall Flight Space Center. Huntsville, Alabama. 2016. (unpublished).

[2] Ball, J. R., and Evans, C. H. (2001). Committee on Creating a Vision for Space Medicine During Travel Beyond Earth Orbit, Board on Health Sciences Policy, Institute of Medicine. In *Safe Passage: astronaut care for exploration missions.* URL: http://www.ncbi.nlm.nih.gov/books/NBK223786/ [cited 19 July 2016].

[3] Summers, R. L., Johnston, S. L., Marshburn, T. H., and Williams, D. R. (2005). Emergencies in space. *Annals of emergency medicine*, 46(2), 177-184.

[4] Billica, R. D., Simmons, S. C., Mathes, K. L., McKinley, B. A., Chuang, C. C., Wear, M. L., and Hamm, P. B. (1996). Perception of the medical risk of spaceflight. *Aviation, Space, and Environmental Medicine*, 67(5), 467-473.

[5] Peterson, L. E., Pepper, L. J., Hamm, P. B., and Gilbert, S. L. (1993). Longitudinal study of astronaut health: mortality in the years 1959-1991. *Radiation Research*, 133(2), 257-264.

[6] Campbell, M. R. (2002). A review of surgical care in space. *Journal of the American College of Surgeons*, 194(6), 802-812.

[7] Stewart, L. H., Trunkey, D., and Rebagliati, G. S. (2007). Emergency medicine in space. *The Journal of Emergency Medicine*, 32(1), 45-54.

[8] Kirchen, M. E., O'Connor, K. M., Gruber, H. E., Sweeney, J. R., Fras, I. A., Stover, S. J., and Marshall, G. J. (1995). Effects of microgravity on bone healing in a rat fibular osteotomy model. *Clinical Orthopaedics and Related Research*, 318, 231-242.

[9] Arcam Orthopaedic Implants. http://www.arcam.com/solutions/orthopedic-implants/ [accessed 9 August 2016].

[10] Menon, A. (2012). Review of Spaceflight Dental Emergencies. NASA Technical Report. NASA/TM-2012-217368.

[11] Deutsch, W. M. (2008). Dental events during periods of isolation in the US submarine force. *Military Medicine*, 173 (Supplement 1), 29-37.

[12] Sack, D. 1998. Total Atlantic Fleet Medical Evacuations from Submarines, 1993–1996. Presentation at *Undersea and Hyperbaric Medicine Meeting*, Seattle, Washington.

[13] Thomas, T. L., Hooper, T. I., Camarca, M., Murray, J., Sack, D., Molé, D., and Garland, F. C. (2000). A method for monitoring the health of US Navy submarine crewmembers during periods of isolation. *Aviation, Space, and Environmental Medicine*, 71(7), 699-705.

[14] Dentca CAD/Cam Dentures. URL: http://dentca.com/. [accessed 2 August 2016].

[15] DENTCA Receives FDA Approval for World's First Material for 3D Printed Denture Bases. URL: https://3dprint.com/87913/dentca-fda-3d-print . [cited 2 August 2016].

[16] Dental Materials: Advanced materials for superior digital dentistry and orthodontics. URL: http://usglobalimages.stratasys.com/Main/Files/Material_Spec_Sheets/MSS_PJD_DentalMaterials.pdf?v=635785180466728444 [cited 2 August 2016].

[17] Javelin Dental. URL: http://www.javelin-tech.com/3d-printer/stratasys-printers/dental-series . [accessed 2 August 2016].

[18] EnvisionTec: Professional grade printing solutions. URL: http://envisiontec.com/dental-industry . [accessed 2 August 2016].

[19] Renishaw Laser Abutments. http://www.renishaw.com/en/laserabutments--24225 . [accessed 2 August 2016].

[20] Prodways: A new way of producing. URL: http://www.prodways.com/en/industrial_segment/dental . [accessed 2 August 2016].

[21] 3D Systems: Solutions for Surgeons. URL: http://www.medicalmodeling.com/solutions-for-surgeons/tactile-medical-imaging/accudental-sup-reg-sup-validation-models . [accessed 3 August 2016].

[22]3D Systems Projet 1200: URL: http://www.3dsystems.com/3d-printers/professional/projet-1200. [accessed 3 August 2016].

[23]Dentwise. URL: http://www.dentwise.eu/ . [accessed 3 August 2016].

[24]EOS: e-manufacturing solutions. URL: http://www.eos.info/dental. [accessed 3 August 2016].

[25]ConceptLaser: LaserCUSING is revolutionasing the dental industry. URL: http://www.concept-laser.de/en/industry/dental.html . [accessed 3 August 2016].

[26]Hybrid: manufacturing technologies: URL: http://www.hybridmanutech.com/technology.html. [accessed 3 August 2016].

[27]DMG Mori. URL: http://us.dmgmori.com/products/lasertec/lasertec-additivemanufacturing/lasertec-65-3d. [accessed 3 August 2016].

[28]DMG Mori: All-in-one laser deposition welding and milling: Additive manufacturing for quality finished parts. URL: http://us.dmgmori.com/blob/354972/d7a3183a57062104c9ab543ea54ca110/pl0us15-lasertec-65-3d-pdf-data.pdf. [cited 3 August 2016].

[29]FDA Approves the First 3D Printed Drug Product: Aprecia introduces its First Product Using the ZipDose® Formulation platform. URL: https://www.aprecia.com/pdf/2015_08_03_Spritam_FDA_Approval_Press_Release.pdf . [cited 1 August 2016].

[30]First FDA-Approved Medicine Manufactured Using 3D Printing Technology Now Available. URL: https://www.aprecia.com/pdf/ApreciaSPRITAMLaunchPressRelease__FINAL.PDF . [cited 1 August 2016].

[31]Three Dimensional Printing Lab at MIT. http://www.mit.edu/~tdp/index.html . [accessed 1 August 2016].

[32]German Company Aims to Sell 3D Printed Drugs and A 3D Drug Printer. https://3dprint.com/87977/3d-printed-drugs-2. [accessed 2 August 2016].

[33]Stephens, B., Azimi, P., El Orch, Z., and Ramos, T. (2013). Ultrafine particle emissions from desktop 3D printers. *Atmospheric Environment*, 79, 334-339.

[34]Zhou, Y., Kong, X., Chen, A., and Cao, S. (2015). Investigation of Ultrafine Particle Emissions of Desktop 3D Printers in the Clean Room. *Procedia Engineering*, 121, 506-512.

Determination of Leakage and Crack Growth Rates in a Layered Pressure Vessel

Cameron W. Coates[1]
Armstrong State University, Savannah, GA, 31419

ABSTRACT

The shell section of an AO Smith Layered Pressure Vessel (LPV) built in the 1960's and in prior service at the NASA Marshall Space Flight Center is evaluated for crack instability, leakage rates and related growth rates. The objectives of this project were: (i), to determine limiting flaw sizes for various crack sizes in the shell layer, (ii), to apply an analytical model which approximates leakage rates due to various cracks with and without interlayer gaps and (iii), to calculate related crack growth rates for typical in service cycles of the AO Smith LPV. Limiting flaw sizes for axial and circumferential cracks in the shell layer were first determined in accordance with the API 579-1 standard. Leakage rates were then calculated incorporating compressibility and frictional effects. A first approximation analytical method was also developed in order to model the effect of interlayer gaps on leakage rates. This model applied the isentropic compressible flow relationships while accounting for friction using the Darcy-Weisbach friction factor. A fatigue crack growth analysis was also performed using the Barsom equation for crack growth. The aspect ratios of the circumferential surface cracks at their limiting flaw size were found to be approximately 20% of the aspect ratio of axial surface cracks at comparable sizes. Leakage rates for axial through cracks were higher than those for circumferential through cracks of the same aspect ratio. The interlayer gap length was found to be inversely proportional to leakage rate, however frictional effects decreased with increasing crack size. Fatigue crack growth analysis indicated that neither axial nor circumferential cracks will be unstable for typical service pressure cycles, for sizes below their respective LFS. Recommendations for methods to monitor crack sizes in the shell layer of the LPV while in service are also provided.

Nomenclature

K_{IC}	=	Plane Strain Fracture Toughness (ksi√in)
a	=	half crack length (in)
c_d	=	discharge coefficient
Q	=	Mass Flow Rate (lbm/hr)
L	=	Through-crack length (in)
ρ_1	=	gas density in vessel (lbm/ft^3)
f	=	friction factor
F	=	Friction number
d	=	crack divergence parameter
D	=	crack depth (in)
W	=	mean crack height (in)
R_A	=	roughness (in)
h	=	roughness height (in)
d_H	=	Hydraulic Diameter (in)
P_1, P_2	=	Pressure inside, outside vessel (psig)

---

[1] Professor and Engineering Studies Program Coordinator, Engineering Studies Program, Armstrong State University, Savannah, GA 31419.

k	=	Ratio of specific heat capacities of an ideal gas
M_a	=	Mach number at crack exit
T^*	=	Temperature at sonic speed location (^{0}R)
A^*	=	Cross sectional area of sonic speed location (in^2)
R	=	Specific Gas Constant (ft-lbf/slug ^{0}R)
Re	=	Reynolds number

I. Introduction

The National Aerospace and Space Administration (NASA) Marshall Space Flight Center has approximately 170 layered pressure Vessels (LPV's) currently in service. The majority of these vessels were built in the 1950's and 60's, prior to the development of ASME code for construction and fabrication of LPV's. These vessels therefore do not currently satisfy any ASME construction or fabrication standards. For the majority of these LPV's, their material property records are inaccessible due to proprietary rules at the time of manufacture. Within the last two decades, cracks have been found in similarly constructed LPV's in the oil, gas and agricultural industries. Several of these have failed catastrophically, resulting in mass evacuations, loss of life, environmental damage and destruction of adjacent systems and property. Current Non-Destructive Evaluation (NDE) methods are unable to effectively detect and/or characterize cracks due to the material discontinuities at the layer interfaces. The ability of Phased Array Ultrasonics (PAUT) to successfully detect flaws within head to shell and shell to shell welds for layered metal plates has been recently demonstrated[1]. So far PAUT has not been able to detect flaws running parallel to the weld seam, transverse to the weld direction or those embedded in the layered plate material. PAUT is also currently unable to interpret transitional wall thicknesses and sloped surfaces between head and shell.

It is imperative that methodologies be devised that will allow the determination of LPV material properties, crack growth rates and their associated stability. This research outlines methods to determine limiting flaw sizes, leakage and crack growth rates for cracks of various sizes within the shell layer for an AO Smith MV-50288-34 LPV, manufactured in 1962. NDE techniques for the detection of crack growth within the LPV shell layer and inner layers have thus far, either been unsuccessful or marginally successful. The correlation of leakage rates with crack sizes may augment LPV maintenance by being incorporated into a health monitoring program for crack growth and stability. LPV's have very small blind holes on the surface (4-6 per cylindrical shell), which end in different layers in order to allow air to be released or taken in due to compression and expansion of the material (breathing) while in service. Some weep holes end in the gap between the shell and the first layer. Flow rates or pressure changes could be monitored using these weep holes in order to determine whether cracks exist in the inner layer as well as their approximate sizes. Recently, Prossner[2] noted that an advantage of LPV construction was that vent holes could be drilled through all of the layers except the inner shell of the vessels, ensuring that pressure did not build up between layers and also providing a means of detecting leakage, noting that the monitoring of these holes could indicate inner shell failure before catastrophic rupture of the vessel.

The AO Smith MV-50288-34 LPV was given the designation V032 at the NASA MSFC. V032 was removed from service for experimental testing and evaluation, as well as to support the development of analytical or computational approaches for LPV crack growth and life assessment evaluations. The working fluid for this type of vessel may be air, gaseous nitrogen (GN$_2$) or gaseous hydrogen (GH$_2$). This work addresses the V032 shell layer (1146a material) only and accomplishes the following considering these three working fluids within the LPV:

- Provides the Limiting Flaw Size (LFS) for Axial and Circumferential Through Cracks in the V032 shell (SFS software)
- Provides geometrical bounds for the LFS for elliptical inner/outer axial and circumferential cracks (SFS software)
- Provides expected leakage rates for crack sizes as a fraction of their respective LFS's
- Provides expected leakage rates assuming that a 0.05″ gap exists between the shell and 1st layer
- Provides recommendations for further work

An operating temperature of 77^{0}F was used in the development of all results provided.

II. Previous Work

Southwest Research Institute (SwRI)[3] recently conducted Fatigue Crack Growth (FCG) testing and fractographic analysis for an 1146a section of an AO Smith LPV previously used in service at the NASA Ames facility. FCG testing was performed at a load ratio, R, (ratio of minimum to maximum load) of 0.15 and at RT. Crack growth rate estimates obtained from striation spacing ranged from 7.2×10^{-6} inch/cycle near the notch to 1.8×10^{-5} inch/cycle adjacent to the transition to fast fracture. Fractographic analysis of crack notches revealed primarily transgranular fracture with isolated regions of intergranular fracture. Secondary (out of plane) cracking was also evident. Plane strain fracture toughness testing was also performed in accordance with ASTM E399 for the A-225 Grade B head material while plane stress fracture toughness was conducted in accordance with ASTM E5671 for the AO Smith 1146a. Reported plane stress fracture toughness values for 1146a ranged between 86ksi√in at -20⁰F to 92ksi√in at room temperature. Hudson et al[4] also conducted experiments to determine fracture toughness, fatigue-crack growth, sustained-load flaw growth, and impact properties on three pressure vessel steels: A. O. Smith VMS 5002, VMS 1146A, and ASTM A-225 Gr.B. These authors found that the elastic fracture toughness of all three steels did not decrease significantly with decreasing temperature from room temperature to about -20° F. Charpy impact energies were found to decrease with decreasing temperature in the nominal temperature range from room temperature to -20° F. The Ductile to Brittle Transition temperatures of VMS 5002 and A- 225 Gr.B were found to be -10° F and -25° F, respectively.

III. LPV Design

The AO Smith vessel is composed of an inner cylindrical shell and concentric layers of thin plates wrapped around the inner shell with longitudinal welds. The AO Smith LPV inner and outer shell are made from AO Smith 1146a steel, while the head is made from ASTM A225 Grade B Firebox steel. Geometric and Material Properties are provided in Tables 1 and 2, respectively. Full penetration welds (i.e. welds which fuse all layers together) connect a layered section to either the solid vessel heads (head-to-shell weld) or to an adjacent shell section (shell-to-shell weld)[5]. Smith initially pre-stressed the vessel using the "auto-frettage," or Keplar, method. In this method, a relatively incompressible fluid was injected into the completed vessel under high pressure. The inner shell and the few adjacent layers would expand beyond their elastic limits while outer layers expand but remain within their elastic limits. Once the internal pressure is removed, the outer layers would exert a compressive load on the plastically deformed inner layers. There are also wrapping pre-stresses in each layer due to transverse contraction of the longitudinal seam welds and circumferential contraction of the circumferential welds.

There are several advantages expected due to the presence of multiple layers. If a crack develops in any layer, it is unlikely that it will transfer to adjacent layers due to the material discontinuity. The local area around the crack may be relieved and the load transferred to other layers before it reaches critical crack length. Similarly, man-made surface flaws such as scratches due to tooling impact, would likely remain on the outer layer only[6]. Thin plates exhibit better mechanical properties than thick plates and only the inner shell needs to be made from process resistant material[7]. The principal stresses produced in the wall of the shell due to internal pressure are circumferential (hoop), longitudinal and radial.

Table 1. Vessel V032 Geometric Properties

Shell:	
Length	14.125 ft. (tangent to tangent)
Shell Inside Diameter	20 in
Inner Shell Thickness	0.5 in.
Layers	5
Layer Thickness	0.25 in.
Outer Shell Thickness	1.250 in.
Total Thickness	1.750 in.
Head:	
Radius	10 in.
Thickness	1.438 in.
Corrosion Allow.	0.00 in.

Table 2. Vessel V032 Material Properties

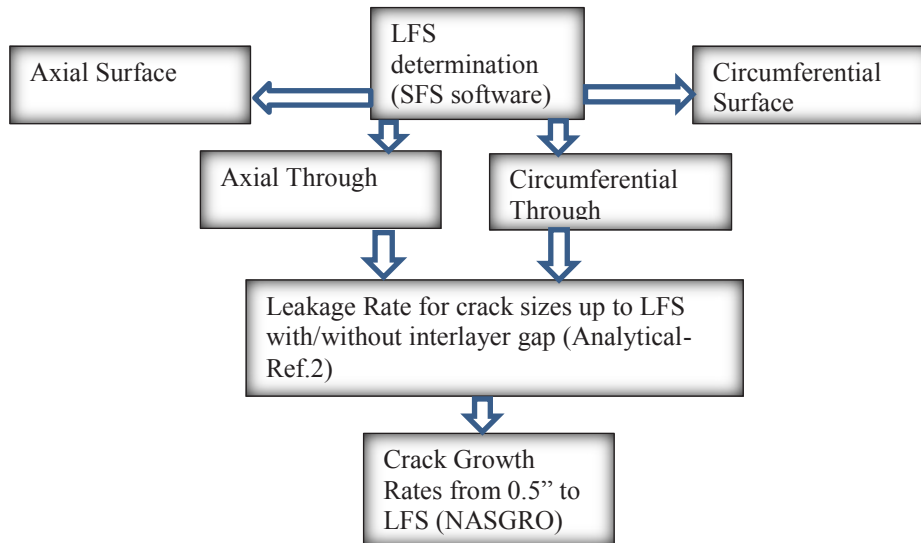| Property	Inner (1146a)	Outer (1146a)	Head (ASTM-225)
UTS (ksi)	105	105	75
YS (ksi)	75	75	43
S (ksi)	35	35	25
Fracture Toughness $(ksi\sqrt{in})$*	82	82	76
Young's Modulus(ksi)	30	30	**

*Ref. 4

IV.   Method

The task sequence of the project is shown in Figure 1. The LFS for surface and through axial/circumferential cracks, for the inner cylindrical layer of vessel V032 were first determined in accordance with API-579-1, section 9.4.3.3. This was done using Signal-Fitness for Service (SFS) software[8]. Plots of the LFS for surface cracks (axial and circumferential) are provided in the results section.

The SFS input data are provided in Table 2, an operating temperature of 77^0F was assumed. A linear hoop stress distribution across the thickness was input based on results from a Finite Element (FE) model of the vessel. This hoop stress distribution was

$$\sigma(psi) = 41,000 - 2000\left(\frac{x}{t}\right) \tag{1}$$

where x is the radial distance starting from the inner wall and t is the shell thickness. The model predicted an axial stress of 16,000 psi, constant through the thickness. FE stress predictions were consistent with closed form solutions using the thick walled cylinder formulae. Wrapping pre-stresses (compressive) would reduce the magnitude of the

```
                        LFS
Axial Surface  <====  determination  ====>  Circumferential
                   (SFS software)               Surface

        Axial Through      Circumferential
                              Through

          Leakage Rate for crack sizes up to LFS
          with/without interlayer gap (Analytical-
          Ref.2)

                 Crack Growth
                 Rates from 0.5" to
                 LFS (NASGRO)
```

Figure 1. Task Sequence

hoop stress, however this influence is also affected by the size of any gaps, as well as the thermal and creep relaxation properties for both the 1146a steel and the longitudinal weld material. Since these vessels are over 50 years old, it is reasonable to assume that creep relaxation has negated any service stress reduction effects due to pre-stress. Additionally, the thermal and creep properties for 1146a are not published in the literature. Therefore the wrapping pre-stresses were ignored in the FE model.

The leakage rates for various through crack sizes for axial and circumferential cracks up to the LFS were then determined. The leakage rates were calculated for axial through-crack sizes as a fraction of the LFS (0.25-0.9). The physical sectioning of V032 and similar vessels revealed interlayer gaps of various sizes. Leakage rates for the inner shell assuming an interlayer gap exists were therefore also determined. The largest gap found among the sectioned pieces was 0.05″ in height and 7″ wide. These dimensions were therefore used as a conservative estimate for gap size. Table 3 provides leakage rates for axial and circumferential through-cracks for the cylindrical portion of the V032 vessel with and without a 0.01 inch interlayer gap assumption. Note that the pressure drops substantially as the working fluid flows through the interlayer gap, therefore the distance from the weep hole (where pressure might be measured) to the crack will significantly affect pressure measurements. Leakage rates (with interlayer gap assumption) for which the shell crack may be located 2, 4 and 6 feet longitudinally from the weep hole exit were therefore also provided.

A. Leakage Rate Model

The American Petroleum Institute code API-579-1 recommends that leakage rates be calculated using methods developed by Ewing[9]. Ewing developed closed form formulae for single flow rates through cracks based on a generalization of previous work by Button et al[10]. These formulae predicted flow rates to within 12% of those found by numerically integrating the governing equations for diverging cracks. There was less agreement with the numerical solution for converging cracks, however tables of correction factors were developed. The assumed crack geometry is that of the trapezoidal prism shown in Figure 2. Three flow regimes were identified:

I- Very low friction: choked flow occurs at entry and the flow is independent of friction;
II- Intermediate friction: choked flow occurs at exit;
III- Sufficiently high friction: choked flow does not occur at all.
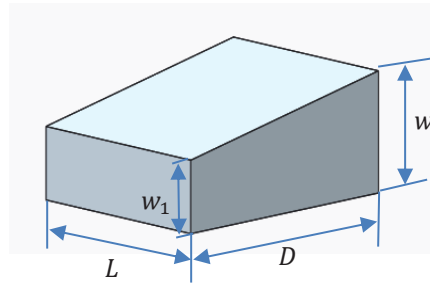

Figure 2. Assumed Crack Geometry

Knowing the inner and outer radius to thickness ratios for the cylinder, Crack Opening Areas (COA) for various crack configurations were determined using methods recommended in API 579-1/ASME FFS-1 section K.3, utilizing tables K.1 through K.4. These areas were then used to determine the crack heights w_1 and w_2, for a given input crack length, L.

The leak rate can then be calculated using Eqn. (2),

$$Q = c_d L W \sqrt{P_1 \rho_1} \qquad (2)$$

In order to determine the flow regime for a specific scenario, it is necessary to determine the friction number, F. The friction number is given by

66

$$F = \frac{fD}{W} \tag{3}$$

The friction factor f depends on the hydraulic diameter, the surface roughness, and on whether flow is laminar or turbulent (i.e. Reynolds number). There is no consensus in the literature regarding appropriate fiction factor values for flow through crack. The friction factor empirical equation is of the general form

$$f = \left[a \log \frac{d_H}{R_A} + b \right]^{-2} \tag{4}$$

Where a and b are constants which slightly differ depending on the author[11,12]. There is reasonable agreement in the literature on a lower bound value for f, which assumes turbulent flow on a hydraulically smooth surface, given by

$$f = 0.079 Re^{-0.25} \tag{5}$$

Chivers[13] reviewed data on flow rates through idealized and real crack geometries and found that, if $f < 1$, the data supported use of Eqn. (4) to determine flow rate bounds for the fully rough regime. If $f > 1$, the database is less precise, however $f \approx 4$ appears to be an upper bound. It was noted that $f = 4$ applied to a geometry that was not representative of a real crack surface, and that previous maximum values for f ranged between 0.7 and 0.8. It was recommended that in practice f be chosen not to exceed unity in the absence of information on $\frac{d_H}{R_A}$. Ref. 9 also recommended unity as an upper bound on f. Additionally, an intermediate value of 0.25 was suggested if Eqn. (4) yields a value for f which exceeds 0.25. For this project, Eqn. (4) was used to determine f ($a = 4.5, b = -2.5$) using an assumed roughness of 10 microns (recommended by Ref. 9). Due to the very small pressure ratios, turbulent flow can be expected. The hydraulic diameter, d_H, was approximated by $d_H \approx 2W$.

The crack divergence parameter, d, is defined as

$$d = (w_2 - w_1)/2W \tag{6}$$

The flow regime dictates the form of c_d, the discharge coefficient, which accounts for pressure losses. c_d was determined by either Eqn.(7a), Eqn.(7b) or Eqn.(7c), depending on the flow regime:

$$c_d = 0.4(1 - d) \qquad\qquad F < F_1 \qquad (7a), \text{ flow regime I}$$

$$c_d = (1 - d^2) / \left(1 + \sqrt{(1 + 1/n)F} \right) \qquad F_1 < F < F_2 \qquad (7b), \text{ flow regime II}$$

$$c_d = \frac{(1 - d^2)\sqrt{\left(1 - (P_2/P_1)^{\frac{n+1}{n}} \right)}}{1 + \sqrt{(1 + 1/n)F} - k} \qquad F > F_2 \qquad (7c), \text{ flow regime III}$$

where k is chosen to make solutions match at $F = F_2$. For the isothermal case

$$k = (1 - d) \left[(P_1/P_2) - \sqrt{(P_1/P_2)^2 - 1} \right] \tag{8}$$

The flow regime bounding parameters F_1, F_2 are given by:

$$F_1 = \frac{n}{n + 1} (1.5 + 2.5d)^2 \tag{9}$$

$$F_2 = \left[(1 - d)(P_1/P_2)^{\frac{n+1}{2n}} - \sqrt{n} \right]^2 / (n + 1) \tag{10}$$

Note that Ref. 9 obtained Eqn's 7 through 10 with an initial assumption of polytropic behavior, hence the presence of the polytropic index, n. However, the solution may be applied to the adiabatic case if n is related to the ratio of specific heat capacities by Eqn. (11),

$$n = (3k - 1)/(k + 1) \tag{11}$$

B. A First Approximation Model for the Effect of Imperfect Contact between Adjacent Layers

In practice, imperfect rolling or plate thickness variation may result in gaps between the layers. Thermal expansion or contraction may also affect the gap size. Imperfect contact between layers reduces wrapping pre-stress. When the vessel is subjected to an internal pressure, it expands and the gaps close. There is therefore an additional circumferential stress developed in these layers that is required to close these gaps. Consider a weep hole that ends at the outer surface of the shell layer. If a through crack develops in the shell layer, the leakage rate through the weep hole will be influenced by any space which exists between the shell layer and the first layer. After exiting the crack in the shell layer, the working fluid will flow into this interlayer gap prior to entering the weep hole. Frictional effects will result in a pressure drop across the gap between where the flow enters from the crack exit to where it exits to the weep hole. In order to include the interlayer gap contribution to the leakage rate, the pressure reduction due to an interlayer gap was estimated, and then incorporated in Eqn. (1). Vessel V032 was dissected and gap sizes were measured during an earlier investigation. The gap spacing reported ranged from 0.005″ to 0.05″, with gap widths ranging from 1″ to 7″. As a worst case scenario, the gap was modeled using the largest dimensions found, i.e. 0.05″ in height and 7″ in width. As the interlayer gap height to width ratio is very small (<1%), the gap geometry was simplified to that of a triangular prism. An interlayer gap picture of a V032 section is shown in Figure 3.

The gap now acts as a diverging converging nozzle after the flow has left the crack exit. The choked location was therefore assumed to be at the weep hole base along the interlayer gap outer surface. The isentropic flow relationship in Eqn. (12) allows the determination of the Mach number at the crack exit, since the ratio of the area of the crack exit to the area of the weep hole (0.25" diameter) is known.

$$\frac{A}{A^*} = \frac{1}{M_a}\left[\frac{2}{k+1}\left(1 + \frac{k-1}{2}M_a^2\right)\right]^{(k+1)/[2(k-1)]} \tag{12}$$

All other properties within the flow can then be determined using compressibility tables or the related isentropic flow formulae for compressibility. At the crack exit, the speed of the flow v may be found from

$$v = M_a\sqrt{kRT^*} \tag{13}$$

Since the flow is choked at the crack exit, T^* is found from the stagnation temperature T_o using Eqn. (11):

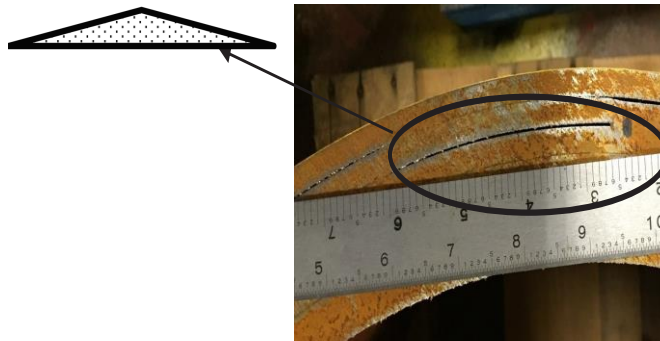$$\frac{T^*}{T_o} = \frac{2}{k+1} \tag{14}$$

Figure 3. Interlayer Gap Modeled as a Triangular Prism

The Darcy-Weisbach equation, Eqn. (15), was used to determine the pressure drop for flow through the triangular prism,

$$\Delta P = \gamma \frac{\rho \Delta L v^2}{2 d_H} \qquad (15)$$

while the Darcy friction factor γ was approximated using the Blasius equation

$$\gamma = (100 Re)^{-0.25} \qquad (16)$$

The hydraulic diameter d_H was found using the standard formula for a triangular cross section.

In order to determine leakage rates, ΔP was then subtracted from the initial pressure and this new value used in Eqn. (2) for values of ΔL= 2, 4, and 6 feet.

C. Fatigue Crack Growth

For air, the maximum pressure fluctuation in one day is one cycle from 3,225 psig to 1,200 psig and then back to 3,225. For GH_2, the maximum pressure fluctuation in one day is one cycle from 5,000 psi to 2,500 psi and then back to 5,000 psi. The GN_2 system is presently operating from 3,500 to 2,500 psi with no weekend operation. For the GH_2 ETA system, the hydrogen has been pressurized on the average less than three times per week. The maximum pressure fluctuation would be from 4,400 psig down to 2,000 psig and back up to 4,400 psig. The GH_2 WIA system undergoes 10 pressurizations per year, from 3,000 psig to 1,500 psig and back to 3.000 psig.

NASGRO v8.1[14] was used to perform a Fatigue Crack Growth (FCG) analysis in the V032 shell layer. Axial and Circumferential cracks were evaluated under all operating cycles and pressures previously provided. The T07 through crack (axial) in a hollow cylinder and T08 through crack (circumferential) in a thin cylinder were used. An initial flaw size (2c) of 1.0 inch was used in the analysis. The constants from the Barsom equation, shown below in Eqn. (17), were used as input for the NASGRO.

$$da/_{dN} = 3.6 \times 10^{-10} (\Delta K)^{3.0} \qquad (17)$$

Ref. 3 found that while this model gave less conservative results compared to a curve fit from experimental crack growth data, crack growth predictions using the Barsom equation more closely matched experimental results. The material data input screen used in the NASGRO model is provided in Figure 6 Appendix B. The material was user defined and assigned the properties shown in Table 2, crack closure was not suppressed.

V.   Results

Figures 4a and 4b provide the LFS for axial inner and outer surface cracks, respectively, in the V032 shell. Figures 5a and 5b provide the LFS for circumferential inner and outer surface cracks, respectively, in the V032 shell. The limiting flaw size for axial through cracks in the V032 shell layer was 1.541 inches while the LFS for circumferential through cracks in the shell layer was 6.74 in. For discussion purposes, leakage rates for air flowing through various crack sizes as a fraction of their LFS values for axial and circumferential cracks are shown in Table 3. Circumferential crack size values were chosen such that leakage rates could be compared with those of axial cracks. Leakage rates for the other two working fluids, GH2 and GN2 are provided Tables 4 and 5 in Appendix A. The FCG analysis indicated that neither axial nor circumferential cracks below their respective LFS, within the shell layer, would grow under service load cycles.

VI.   Discussion

Some inferences of surface crack general behavior can be made based on their behavior at their limiting size. For both the axial and circumferential cases, in transitioning from a surface crack to a through crack, there is little difference in aspect ratios for the cracks growing from the outside compared to those growing from the inside. The aspect ratios of the circumferential cracks at their limiting size are however approximately 20% of the aspect ratio of

axial cracks at comparable stages. This indicates that circumferential cracks will grow much wider (smaller a/c ratio) than axial cracks before they become through cracks.
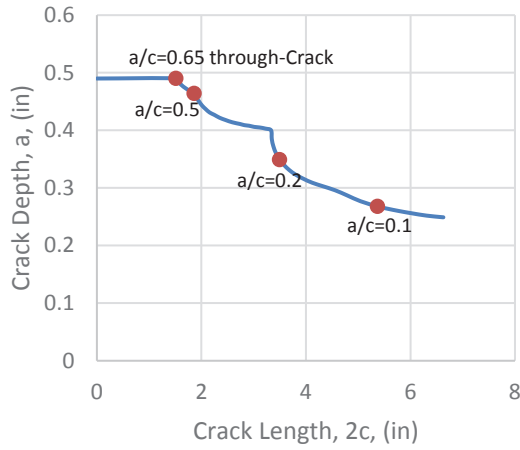

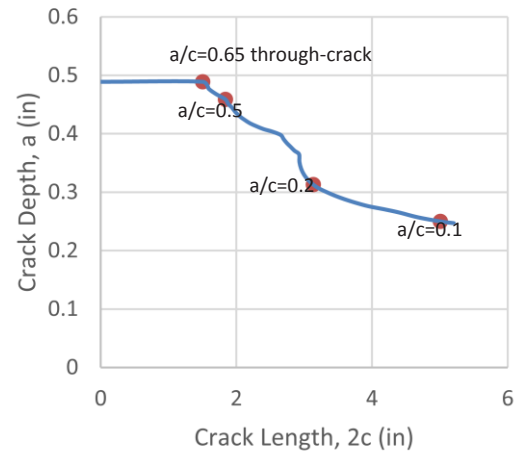Figure 4a. Axial LFS Shell Inner Surface

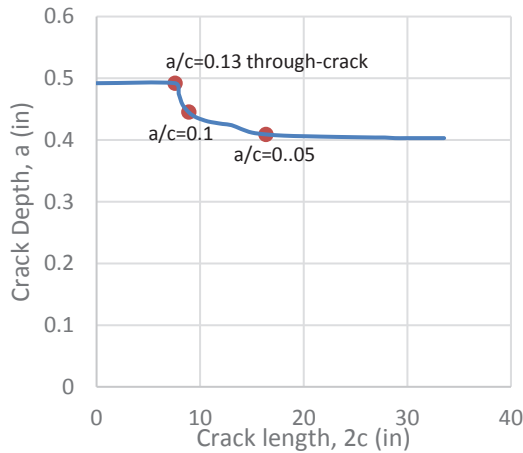Figure 4b. Axial LFS Shell Outer Surface
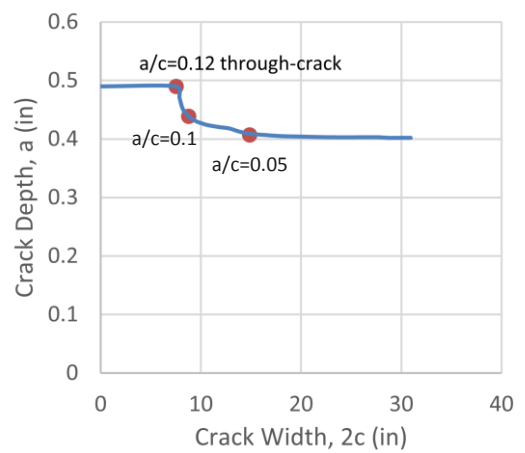

Figure 5a. Circumferential LFS Shell Inner Surface

Figure 5b. Circumferential LFS Shell Outer Surface

Working fluid leakage rates increase with increasing density: GH2, GN2, air. Since the LFS for a circumferential through crack is much greater than the LFS for an axial through crack, circumferential through crack leakage rates were also much greater than axial through crack leakage rates at equivalent fractions of their LFS. However for the same crack width (2c), circumferential leakage rates were less than axial crack leakage rates. In the development of this method, the authors (Ref. 9) assumed an energy loss of half a velocity-head occurs on entering the channel. Additionally, these authors recommended that a sensitivity study be done regarding the effect of the friction coefficient assumed on any calculated leakage rates. The friction factor was therefore varied between recommended limits, i.e. 0.01 to 4. Leakage rates did not change with this variation in friction factor.

Since surface roughness is finite, friction will have some upper bound value. As flow rate increases with increasing crack size, there will be a specific rate magnitude for which friction will attain its maximum value. As the flow rate increases beyond this value, frictional effects will have less significance on the flow. The data in Table 3 shows that the effect of interlayer gap friction on leakage rate diminishes as crack size increases, this behavior is consistent with theoretical predictions regarding fluid behavior and friction. As interlayer gap length increases, the effect of friction

Table 3. Leakage Rates for various crack sizes in V032 Shell with and without Interlayer Gap; working fluid: air

%LFS	Crack length (2c) in.	Leakage Rate (lbm/hr)	Leakage rate (lbm/hr) with 0.05" x 7" interlayer gap for various lengths		
			2ft	4ft	6ft
Axial Crack					
0.25	0.38	44.59	35.96	24.46	N/A
0.5	0.77	217.69	214.79	211.84	208.86
0.75	1.16	582.05	580.25	578.45	576.63
0.9	1.39	920.40	918.97	917.54	916.11
Circumferential Crack					
0.06	0.38	30.97	24.98	16.99	N/A
0.1	0.72	109.89	108.42	106.93	105.43
0.16	1.05	239.76	239.02	238.28	237.53
0.2	1.39	423.46	422.80	422.14	421.48

on flow rate increases. Overall the effect of friction within the interlayer gap on leakage rate is relatively small (1-6 lbm/hr) and as crack size increases up to 1.38″, friction becomes less and less influential on leakage rate. As interlayer gap length increases, the head loss increases, thereby reducing the leakage rate. However in the case of the densest fluid in this study, air, leakage rates decreased by approximately 4% for a 6 ft. interlayer gap length. The effect of interlayer gap length also decreases as crack size increases and/or fluid density decreases.

VII. Conclusion

At the LFS, circumferential surface cracks will be at least five times wider than axial surface cracks at the transition point before becoming through cracks. The LFS assessment predicts that the LFS for axial through cracks in the shell layer for 1146a material will be 16% less than then LFS for a circumferential through crack.

Leakage rates have been determined for the V032 LPV with and without interlayer gaps, based on API recommended literature as well as modifications incorporating isentropic flow theory for compressible gases. Leakage rates increase with increasing density of the working fluid and/or increasing interlayer gap length. As crack sizes increase, leakage rates become less sensitive to interlayer gap length. For a crack size beyond 0.5", an interlayer gap length of 6 ft. reduces leakage rate by only 3%. A sensitivity study indicated that variations of the friction number between 0.01 and 4 does not change calculated leakage rates. This however is case dependent, the friction number value will influence the type of flow regime, which in turn, influences leakage rate. The friction number should therefore be calculated when estimating leakage rate for other cases (if using the method provided). The discharge coefficient solution is valid only for steady state fluid flow under adiabatic conditions. If a replenishing source does not exist, fluid flow will not be steady. The occurrence of substantial heat transfer would accelerate the flow and invalidate the application of the method described in this report.

Analysis of fracture growth using NASGRO, indicates that neither axial nor circumferential cracks at sizes below their respective LFS will be unstable for the pressure cycles currently being used at MSFC. The least conservative empirical constants available from the literature were used in the NASGRO analysis. The NASGRO model also assumes the vessel is thin walled. While residual stresses were ignored, it is difficult to assess how creep relaxation may have reduced or eliminated these stresses. It is possible that wrapping pre-stresses still exist within the shell layers. The typical LPV shell has many layers wrapped around it, therefore the likelihood of through crack instability may be reduced by interlayer contact forces and residual compressive (wrapping) stresses.

VIII. Recommendations for Future Work

An experimental program is recommended in order to provide outcomes that may corroborate or invalidate analytical predictions of leakage rates. Experiments could be performed to measure leakage rates of artificial cracks machining in the shell layer of a small scale LPV. Additionally various sensor networks may be researched and tested in order to evaluate their potential for large scale health monitoring applications of LPV's at MSFC. These sensors would have to be robust to environmental influences, require low energy and low maintenance. It would also be beneficial to experimentally and/or analytically investigate whether stresses would indeed be transferred to another layer before a crack reaches its critical value in an adjacent layer.

Current NDE techniques have thus far proven ineffective in detecting and characterizing cracks (size, stability) within the inner layers of LPV's. The monitoring of leakage rates has the potential to be a low cost practical solution that may prevent structural failure due to crack instability (stand alone or combined with other methods). There is a dependency of leakage rates on the presence and size of interlayer gaps. While gap sizes between 0.01 and 0.05" have relatively insignificant effects, a very small interlayer gap (<0.005") could dissipate the airflow proceeding to the weep hole. For this case, leakage rate measurements would not detect the presence of a crack. However, over time, the high internal pressure may force expansion of the adjacent layer and widen this gap, thereby allowing leak detection.

An analytical investigation regarding load transfer to an adjacent layer before an axial crack in the layer reaches its critical length or after an axial crack has extended to the circumferential welds, would be beneficial to the establishment of appropriate failure criterion.

While the theoretical fatigue model predicts that no crack growth will occur if similar LPV's are subject to the typical in service pressures for the V032 shell, there is still very limited data regarding the material properties. It is therefore recommended that fatigue crack growth tests be performed on shell and head material samples in accordance with ASTM E647, at a variety of R values, with cycles consistent with service load cycles at NASA MSFC. Results could then be used to determine the empirically derived NASGRO equation coefficients and provide data for comparison with NASGRO fatigue life predictions.

Appendix A

Table 4. Leakage Rates for various crack sizes in V032 Shell with and without Interlayer Gap; working fluid: GH2

%LFS	Crack length (2c) in.	Leakage Rate (lbm/hr)	Leakage rate with 0.05" x 7" interlayer gap for various lengths		
			2ft	4ft	6ft
Axial Crack					
0.25	0.38	43.85	35.32	23.93	**
0.5	0.77	214.06	211.19	208.28	205.33
0.75	1.16	572.33	570.55	568.77	566.98
0.9	1.39	905.02	903.61	902.20	900.78
Circumferential Crack					
0.06	0.38	30.46	24.54	16.63	**
0.1	0.72	108.07	106.62	105.15	103.66
0.16	1.05	235.80	235.06	234.33	233.59
0.2	1.39	416.46	415.81	415.16	414.51

Table 5. Leakage Rates for various crack sizes in V032 Shell with and without Interlayer Gap; working fluid: GH2

%LFS	Crack length (2c) in.	Leakage Rate (lbm/hr)	Leakage rate with 0.05" x 7" interlayer gap for various lengths		
			2ft	4ft	6ft
Axial Crack					
0.25	0.38	11.76	8.42	1.84	**
0.5	0.77	57.43	56.35	55.26	54.15
0.75	1.16	153.54	152.88	152.21	151.55
0.9	1.39	242.80	242.27	241.75	241.22
Circumferential Crack					
0.06	0.38	8.17	5.85	1.28	**
0.1	0.72	28.99	28.45	27.89	27.33
0.16	1.05	63.25	62.98	62.70	62.43
0.2	1.39	111.71	111.46	111.22	110.98
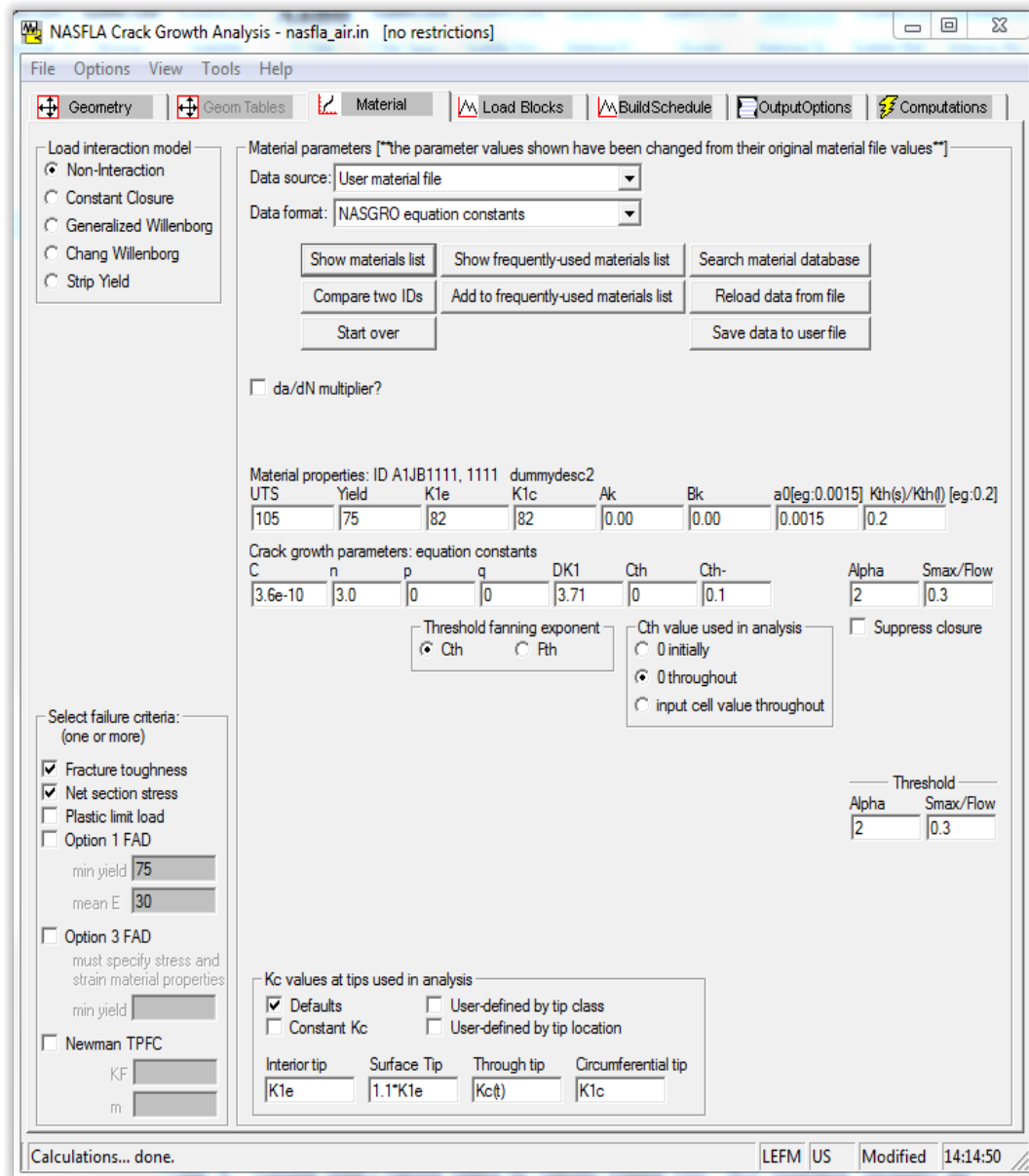
Figure 6. NASGRO GUI with NASGRO equation inputs and Relevant Material Properties

References

[1] Furr, P., "Final Report NASA MSFC – Layered Vessel Demonstration Block," Davis NDE Inc. Contract: Bastion-BPO-140096-CO1, Birmingham, AL, March 13, 2015.

[2] Prosser, W.H. (NESC), "Evaluation of Agency Non-code Layered,," NASA/TM2014-218505/Volume I, NESC-RP-13-00852, Langley Research Center, Hampton, VA, 2014.

[3] J. W. Cardinal, C. F. Popelar and R. A. Page, "Multilayer Pressure Vessel Materials Testing and Analysis NASA/CR2014-218157," Southwest Research Institute , San Antonio, Texas, 2014.

4 Hudson, C., Newman, J.J.C., and Lewis, P.,"An Investigation of Fracture Toughness, Fatigue Crack Growth, and Impact Properties of Three Pressure Vessel Steels," NASA TM X-3316, NASA LaRC, Hampton, VA,, 1975.

[5] NASA Technical Report PVS-15-015, "MSFC Layered Pressure Vessel (LPV)," NASA, Huntsville, 2015.

[6] Pierce, W., "Strength Comparison of Flawed Single-Layer and Multi-Layer AIS1 301 at Cryogenic Temperatures," NASA TN D-2949, Lewis Research Center, Cleveland, OH, 1965.

[7] Rasty, J. and Sabbaghian, M., "Effect of Imperfect Contact between Adjacent Layers on The Integrity of Wrapped Vessels," *Journal of Pressure Vesssels,* vol. 110, no. 3, pp. 247-254, 1988.

[8] Quest Integrity Group, "Signal TM Fitness-for-Service," Quest Integrity Group, Seattle, WA, Version 2012.1017.

[9] Ewing, D., "Simple Methods For Predicting Gas Leakage Flows Through Cracks," Central Electricity Research Laboratories, Leatherhead, Surrey, KT22 7SE, 1989.

[10] Button, B., Grogan, A., Chivers, T. and Manning, P., "Gas Flow Through Cracks," *ASME Trans. J. Fluids Engr.,* vol. 100, pp. 453-458, 1978.

[11] Wilkinson, J., Spence, G. and Chandler, R., "Leakage Flow Through Small Cracks-Report of Second Stage of Experimental Work," AEA Technology, Report FMWG/P(91) 123D, Risley, UK, 1991.

[12] Gardiner, G. and Tyrell, R.J., "The Flow Resistance of Experimental Models of Naturally Occurring Cracks," *Proceedings of the Institute of Mechanical Engineers,* vol. 200, no. C4, 1968.

[13] Chivers, T, "Asessment of Fluid Friction Factors in Leak Rate Calculations," Nuclear Electric TC-Berkely Technology Center, Berkely, Glosgow, UK, 2002.

[14] NASGRO(R) v8.10 (NASA/ESA/FAA version) NASA Johnson Space Center and Southwest Research Institute, San Antonio, TX.

Advanced Equations of State in Loci-THRUST

Eric M. Collins [*]

Mississippi State University, Mississippi State, MS 39762

A new framework for handling advanced equation of state (EoS) models has been developed within the context of a high-order accurate, modal discontinuous Galerkin (DG) solver known as Loci-THRUST. Design considerations and implementation details are provided as well as preliminary results for verification test cases. A new mixed variable reformulation of the DG solver is also presented in which only the mean values of the conservative variables are advanced in time along with higher-order moments for the primitive variables. In conjunction with the new EoS framework, this approach has the potential to improve the ability of the Loci-THRUST solver to efficiently handle more complex fluid dynamics problems.

Nomenclature

e	Internal fluid energy per unit volume
e_0	Total fluid energy per unit volume
h	Fluid enthalpy per unit volume
G	Mixed variable representation
P	Fluid pressure
Q	Conservative variable representation
R	Specific gas constant ($R = \mathcal{R}/\omega$)
R	Vector of residual values
$\mathcal{R}$	Universal gas constant
t	Time
U	Primitive variable representation
u, v, w	Cartesian components of fluid velocity
x, y, z	Cartesian spatial coordinates
ρ	Fluid density
ω	Fluid molecular weight
Subscripts	
i, j	Index into the array of polynomial coefficients for each solution variable approximation and the corresponding polynomial basis functions
ref	Indicates reference conditions for a given fluid

I. Introduction

The ability of computational fluid dynamics (CFD) solvers to accurately and efficiently handle complex equations of state is critical to their practical utility to the aerospace engineer. Within the last two decades, the discontinuous Galerkin (DG) method has shown great promise for providing high-order accurate CFD solutions. Although this greater accuracy comes with a significant computational cost, the method itself permits many potential avenues for improving the performance of numerical DG solvers. Exactly which of these avenues are pursued often depends on the specific capabilities of the solver and the requirements for resolving the relevant physical phenomena.

---

[*]Assistant Research Professor, Center for Advanced Vehicular Systems, Mississippi State University

In the present work, we are concerned with the ability of a specific DG solver, Loci-THRUST, to handle more complex fluid physics through the use of advanced equation of state (EoS) implementations. In Section III. we describe the development of a framework which will allow multiple EoS models to be incorporated into Loci-THRUST. Two specific EoS models have been implemented using this framework and some preliminary numerical verification work is presented in Section V.

The cost of using more advanced EoS models in the context of a DG solver is not insignificant. The DG solver makes extensive use of numerical quadrature rules to perform the required spatial integrations. The use of quadrature rules dramatically increases the number of evaluations of the solution state and the associated EoS queries needed to advance the solution in time. The sheer number of these queries that need to be made in each cell, and at multiple instances per time step, can easily come to dominate the overall computational effort of the solver. In Section IV, we describe a novel mixed variable formulation that may have the potential to reduce a significant part of the overhead incurred when making EoS queries.

II.   Background

Loci-THRUST is a first through fourth-order accurate, density-based flow solver for the inviscid Euler equations. The higher-order accuracy of the solver provides lower numerical dissipation and dispersion than typically found in second-order finite volume solvers. This highly desirable feature has lead to the use of Loci-THRUST as a computational aeroacoustics (CAA) solver.

Recently, the Loci-THRUST solver was coupled to the Loci-Chem solver for the purposes of performing acoustic simulations of NASA's Space Launch System (SLS) launchpad environment.[3] The high-order accuracy of the solver has proven to be a practical choice for propagating the acoustic source terms over the hundreds of meters of the domain of interest. Since both solvers have been implemented in the Loci computational framework, the integration of their respective rule sets can be managed directly by the Loci scheduler. Thus the two solvers run fully coupled with the added benefit of Loci's facilities for automatic parallelization and load balancing, as well as proper assurances that the specified data dependencies will be satisfied.

In the coupled approach, Loci-Chem provides the acoustic source terms from its detailed simulation of the plume gases from the SLS engines. At a prescribed standoff distance from the plume, an overset approach is used to transfer the fluid state from Loci-Chem into the Loci-THRUST solver. If sufficient mesh conditions are met, then the transferred solution can capture the details of the Loci-Chem solution at the order of accuracy prescribed by the Loci-THRUST solver.

While the acoustic simulation of the launch pad environment is a very useful capability, it currently only capable of simulating thermally and calorically perfect, single species fluids. This restriction prevents the solver from adequately resolving the complex acoustic environment that results when the exhaust products from the rocket engines combine with the water suppression system on the pad. In order to accurately predict the launchpad acoustic environment, the effects of these complex fluid interactions need to be properly modeled and simulated.

To that end, we have begun the process of upgrading the Loci-THRUST solver to support the simulation of multi-species real fluid flows. The first stage of these upgrades was undertaken as part of the ten week NASA Faculty Fellowship at Marshall Space Flight Center (MSFC) during the summer of 2016. This report provides details of this work, demonstrates some preliminary verification results, and discusses some proposed modifications designed to improve the overall performance of the solver when using complex equations of state.

III.   Equation of state framework

To support more advanced fluid physics simulations, the Loci-THRUST solver first had to be refactored to support more complex thermodynamic equation of state models. The thermally and calorically perfect Euler solver was used as a starting point for the current work. It was first necessary to identify all of the code that made explicit use of these thermodynamic assumptions in the form of inline formulas for computing primitive variables and other derived quantities. These hard-coded formulas were removed and replaced with explicit calls for the desired variable from an `eos` object.

The next task was to design a modular framework that would allow multiple equation of state models to be used interchangeably in the context of the DG Euler solver without requiring any modifications to the

core of the solver code base as new EoS models are added. Loci-Chem has a similar framework already in place, and much inspiration was derived from the software architecture found therein.

In our implementation, a delegate `EOS` object is created which can be accessed from any Loci rule within the solver. This delegate object provides an application programming interface (API) through which various thermodynamic queries can be made using whatever state information is currently available. Behind the scenes, these API calls are dynamically routed to the associated methods in the appropriate EoS model.

In addition to the delegate object and the supporting EoS modules, a handful of user accessible helper objects were also created. These objects are used to transfer whatever local state variables are available into the EoS module when performing queries for other state variables. Table 1 lists the helper classes and the values that they hold.

Helper	State Variables
`RHO_RHOU_RHOE`	density, momentum, total energy
`RHO_U_P`	density, velocity, pressure
`RHO_U_T`	density, velocity, temperature
`P_U_T`	pressure, velocity, temperature
`RHO_P`	density, pressure
`RHO_T`	density, temperature
`P_T`	pressure, temperature

Table 1. EoS helper classes and state variables encoded within.

Each of the helper classes have a number of constructors which allow them to be instantiated with whatever set of data values is most convenient. The use of these helper classes allows the delegate object to select the proper methods in the EoS models to properly resolve a specific query in the most efficient manner possible given the provided input.

By way of example: If the conservative variables are available and the corresponding fluid pressure needs to be computed, then any one of the following calls to the EoS delegate, `$eos`, can be made:

```
$eos.pressure(RHO_RHOU_RHOE(rho, rhou, rhov, rhow, rhoE));
$eos.pressure(RHO_RHOU_RHOE(rho, rhoU, rhoE));
$eos.pressure(RHO_RHOU_RHOE(Q));
```

However, if only density and temperature were known, then this call would be used:

```
$eos.pressure(RHO_T(rho, T));
```

Here, `rho`, `rhou`, `rhov`, `rhow`, `rhoE`, and `T` are all `double` values, `rhoU` is a `vect3d` type, and `Q` is a pointer to an array of `double` values in the same order as the arguments to the first version. These helper classes are also first class Loci objects so they can be used in `param`, `store`, and `storeVec` data stores as inputs and outputs of Loci rules. Table 2 provides a list of the quantities which can be queried from the EoS delegate object. It should be noted that not all of the queries are available for all types of input. For some queries the velocity, momentum, or total energy must be known.

III.A.   Thermally and calorically perfect fluid model

The first EoS model to be developed using this new framework was the same thermally and calorically perfect fluid model that was previously available in Loci-THRUST. We refer to this model as the *ideal gas* model. For calorically perfect fluids, the specific heats at constant pressure, c_p, and at constant volume, c_v, are assumed to be constant. Thus, the adiabatic exponent (ratio of specific heats), $\gamma = c_p/c_v$ is also held constant. The thermally perfect assumption implies that internal energy and enthalpy are functions of temperature only.

$$e(T) \;=\; e_{ref} + \int_{T_{ref}}^{T} c_v \; \mathrm{d}\tau = e_{ref} + c_v(T - T_{ref}) \tag{1}$$

$$h(T) \;=\; h_{ref} + \int_{T_{ref}}^{T} c_p \; \mathrm{d}\tau = h_{ref} + c_p(T - T_{ref}) \tag{2}$$

EoS Query	Returned value
`density`	fluid density (ρ)
`pressure`	fluid pressure (P)
`temperature`	fluid temperature (T)
`energy`	internal fluid energy per unit mass (ρe)
`specificEnergy`	internal fluid energy per unit volume (e)
`totalEnergy`	fluid total energy per unit mass (ρE)
`enthalpy`	enthalpy per unit mass (ρh)
`specificEnthalpy`	fluid enthalpy per unit volume (h)
`totalEnthalpy`	total enthalpy per unit mass (ρH)
`soundSpeed`	fluid sound speed (a)
`soundSpeedSq`	fluid sound speed squared (a^2)
`specificVolume`	volume per unit mass ($\nu = \rho^{-1}$)
`specificGasConstant`	specific gas constant (R_s)
`specificHeat_p`	specific heat at constant pressure (c_p)
`specificHeat_v`	specific heat at constant volume (c_v)
`adiabaticExponent`	ratio of specific heats ($\gamma = c_p/c_v$)
`drho_dT`	derivative of density w.r.t. temperature (ρ_T)
`drho_dP`	derivative of density w.r.t. pressure (ρ_P)
`inviscidFluxTensor`	conservative variable inviscid flux terms (F_i)

Table 2. Thermodynamic queries supported by the EoS delegate object.

Internal energy can also be computed from the conservative variables by subtracting the kinetic energy of the flow from its total energy.

$$e(\mathbf{Q}) = \frac{\rho e_0}{\rho} - \frac{1}{2}\frac{\rho\vec{u} \cdot \rho\vec{u}}{\rho^2} \tag{3}$$

Finally, pressure, temperature, and density are related through the expression:

$$P = \rho R T, \tag{4}$$

and sound speed is given by:

$$a = \sqrt{\gamma R T} \tag{5}$$

One final operation that is often necessary is obtaining temperature from the conservative variables. Combining Eqs. (1) and (3),

$$T(\mathbf{Q}) = T_{ref} + \frac{1}{c_v}\left(e(\mathbf{Q}) - e_{ref}\right) \tag{6}$$

The development of this model helped to mature the design of the framework as well as provided a practical means of testing the correct implementation. Solutions computed with the new EoS module was frequently compared against similar solutions generated by the previous solver version. Results obtained from the final EoS module implementation were effectively indistinguishable from those generated by the previous solver version. In Section V, comparisons are made to solutions generated by the Loci-Chem solver operating on the same mesh and using an equivalent EoS model.

III.B. Thermally perfect, calorically imperfect fluid model

The second module to be implemented was a thermally perfect, calorically imperfect equation of state model. For these models, the specific heat at constant pressure, c_p, is provided as a power series polynomial expression along with values for the molecular weight, ω, and reference conditions (T_{ref}, P_{ref}, h_{ref}, s_{ref}).[4]

$$c_p(T) = \sum_k \alpha_k T^k \tag{7}$$

Here, the α_k are the power series polynomial coefficients for c_p. From this data, R, $c_v(T)$, $h(T)$, and $e(T)$ can all be derived.

$$R = \frac{\mathcal{R}}{\omega} \tag{8}$$

$$c_v(T) = c_p(T) - R \tag{9}$$

$$h(T) = h_{ref} + \int_{T_{ref}}^{T} c_p(\tau) \, \mathrm{d}\tau \tag{10}$$

$$e(T) = e_{ref} + \int_{T_{ref}}^{T} c_v(\tau) \, \mathrm{d}\tau \tag{11}$$

The reference energy is given by: $e_{ref} = h_{ref} - RT_{ref}$. Since $c_p(T)$ is given as a simple power series polynomial, evaluating the integrals analytically is trivial. Evaluating these quantities when temperature is known is straight-forward; however, we typically have evaluations of the conservative variables as our starting point. We can still make use of Eqn. (3) to obtain the specific internal energy of the fluid, but Eqn. (6) must now take into account the fact that c_v is no longer constant. Since c_v is now a non-linear function of temperature, we perform a Newton search to identify the temperature, T, that corresponds to the specific internal energy computed from the conservative variables, $\mathbf{Q}$, such that $e(T) = e(\mathbf{Q})$ is satisfied. The following pseudocode provides a rough outline of the search algorithm.

```
T = Tref
de = e(Q) - e(T)
while ( |de| > tol ) {
    T += de/Cv(T)
    de = e(Q) - e(T)
}
```

A similar algorithm can be used to determine temperature from queries from $c_p(T)$ and $h(T)$.

IV. Mixed conservative-primitive variable formulation

As we examine the process that the solver takes to update the solution at each time step, we make several observations:

- Integrations are accomplished through numerical quadrature, which requires a large number of evaluations of flux terms at multiple locations within the cell and on its faces.

- Nearly all of the inviscid flux terms require the primitive variables and other EoS dependent quantities to be evaluated.

- Many of the EoS dependent quantities rely on pressure and/or temperature, or can be rewritten to evaluate more efficiently as a function of pressure and/or temperature.

- The use of the Newton search to obtain temperature from conservative variables has the potential to make this evaluation one of the most expensive parts of any EoS query.

- Although conservation requires that the conservative variables (density, momentum, total energy) must be advanced in time, the modal DG method used by Loci-THRUST only requires the first order moments for the conservative variables to maintain consistency with the governing equations.

This last observation is key to overcoming the performance penalties imposed by the previous observations. Rather than storing high-order approximations to the conservative variables, we can keep only their first-order moments (the mean values) in each element, and then store and advance higher order moments for the primitive variables instead. Let the conservative variable vector, $\mathbf{Q}$, and primitive variable vector, $\mathbf{U}$, be given as:

$$\mathbf{Q} = [\rho, \rho u, \rho v, \rho w, \rho e_0]^T, \tag{12}$$

$$\mathbf{U} = [P, u, v, w, T]^T \tag{13}$$

A mixed variable formulation is now proposed in which the mean values of the conservative variables are advanced in time along with the higher-order moments of the primitive variables. We begin by noting that the polynomial approximations can be broken down into mean value and higher-order contributions simply by isolating the first order moments.

$$\mathbf{Q} = \bar{\mathbf{Q}} + \tilde{\mathbf{Q}} = Q_0\phi_0 + \sum_{i=1}^{n} Q_i\phi_i \tag{14}$$

$$\mathbf{U} = \bar{\mathbf{U}} + \tilde{\mathbf{U}} = U_0\phi_0 + \sum_{i=1}^{n} U_i\phi_i \tag{15}$$

The first order basis function is a constant, often set to one. The rest of the polynomial can be considered to be a perturbation about the mean value. The high-order basis functions are selected so that their integrals over a given element are identically zero. Our mixed variable solution vector can now be written as:

$$\mathbf{G} = \left[\begin{array}{c} \bar{\mathbf{Q}} \\ \tilde{\mathbf{U}} \end{array} \right] = [\bar{\rho}, \bar{\rho}u, \bar{\rho}v, \bar{\rho}w, \bar{\rho}\bar{e}_0, P_1, u_1, v_1, w_1, T_1, P_2, \cdots, P_n, u_n, v_n, w_n, T_n]^T \tag{16}$$

In general, the governing equations for the conservative variables have the following form:

$$\frac{\partial \mathbf{Q}}{\partial t} = \mathbf{R}(\mathbf{U}) \tag{17}$$

where $\mathbf{R}$ is a vector of conservative variable update terms (residuals). To obtain a similar update expression for the primitive variables, we have to transform deltas in the conservative variables into deflections in the primitive variables. Equation (18) shows the Jacobian of the transformation between conservative and primitive variable deflections.

$$\mathcal{A} = \frac{\partial \mathbf{Q}}{\partial \mathbf{U}} = \left[\begin{array}{ccccc} \rho_P & 0 & 0 & 0 & \rho_T \\ \rho_P u & \rho & 0 & 0 & \rho_T u \\ \rho_P v & 0 & \rho & 0 & \rho_T v \\ \rho_P w & 0 & 0 & \rho & \rho_T w \\ (\rho e_0)_P & \rho u & \rho v & \rho w & (\rho e_0)_T \end{array} \right] \tag{18}$$

Here, ρ_P, ρ_T, $(\rho e_0)_P$ and $(\rho e_0)_T$ are the derivatives of density and total energy with respect to pressure and temperature. The forms of the derivatives for density are often equation of state dependent, but for thermally perfect fluids they can be obtained from: $\rho = P/RT$.

$$\rho_P = 1/RT \tag{19}$$
$$\rho_T = -P/RT^2 \tag{20}$$

Expressions for the derivatives for total energy can also be derived.

$$(\rho e_0)_P = h_0\rho_P + T\rho_T/\rho \tag{21}$$
$$(\rho e_0)_T = h_0\rho_T + \rho c_p \tag{22}$$

Here, $h_0 = e_0 + P/\rho$, is the total enthalpy of the fluid per unit volume. Now we can derive the update expressions for the primitive variables by utilizing the chain rule:

$$\frac{\partial \mathbf{U}}{\partial t} = \frac{\partial \mathbf{U}}{\partial \mathbf{Q}} \frac{\partial \mathbf{Q}}{\partial t} = \mathcal{A}^{-1}(\mathbf{U})\mathbf{R}(\mathbf{U}) \tag{23}$$

Using these expressions, we can obtain the update expressions for the polynomial coefficients in the mixed variable solution vector.

$$\int_\Omega \frac{\partial \mathbf{G}}{\partial t}\phi \, d\Omega = \left[\begin{array}{c} \int_\Omega \frac{\partial \bar{\mathbf{Q}}}{\partial t}\phi_0 \, d\Omega \\ \int_\Omega \frac{\partial \tilde{\mathbf{U}}}{\partial t}\phi_j \, d\Omega \end{array} \right] = \left[\begin{array}{c} \int_\Omega \mathbf{R}(\mathbf{U})\phi_0 \, d\Omega \\ \int_\Omega \mathcal{A}^{-1}(\mathbf{U})\mathbf{R}(\mathbf{U})\phi_j \, d\Omega \end{array} \right] \quad \forall j \in [1, n]$$

Finally, these continuous expressions are discretized over elements and the integrals approximated by the appropriate numerical quadrature rules.

This mixed variable formulation has not yet been evaluated. It's proper implementation will require considerable refactoring of the Loci-THRUST solver. Coding of the necessary changes has already been started. We anticipate being able to verify the validity and efficacy of this approach in the near future.

V. Results

The new equation of state framework was tested on a slice of space shuttle main engine (SSME) nozzle geometry with hot steam as the working fluid. This particular configuration was chosen due to the considerable fluid temperature variations experienced within the nozzle (1600 Kelvin), which would allow a fairly wide range of the energy-temperature curve to be tested. The computational domain consists of a single layer of hexahedral cells along with a single row of prisms along the axis of the nozzle. The geometry and resolution of the mesh are shown in Fig. 5 and Fig. 6.

For verification purposes, the first through fourth order solutions produced by Loci-THRUST were compared against first and second order solutions generated by Loci-Chem using similar equation of state models. Loci-Chem is a second order finite volume solver, but it can be run in first order mode by selecting `zero` as the active slope limiter.

V.A. Ideal gas

For the thermally and calorically perfect EoS (ideal gas) model, the molecular weight of the fluid was set to 0.0180153 kg/mol, and the adiabatic exponent to 1.3333333.

The results computed from the ideal gas EoS model are compared with first order solutions in Fig. 1 and second order solutions in Fig. 2. These plots show general agreement in the distribution of pressure temperature and mach number across the radial direction of the nozzle. However, we should expect to see much better agreement, especially for the first order runs.

A representative slice through the first and second order Loci-Chem solutions and first through fourth order Loci-THRUST solutions is shown in Fig. 5. From this comparison, we can see that the Loci-THRUST solver obtains nearly identical distributions for its second through fourth order solutions. This may indicate that Loci-THRUST is able to resolve the dominant flow physics on this coarse mesh with second order or higher solutions while Loci-Chem is not quite able to obtain similar convergence. If that is the case, then the current mesh may be inadequate for comparing the two solver implementations. More work will be required to adequately verify that this EoS implementation is correct.

V.B. Perfect gas

For the thermally perfect, calorically imperfect EoS (perfect gas) model, a piecewise fifth order power series polynomial was used to specify the specific heat at constant pressure, c_p, as a function of temperature. The coefficients used in Eq. (7) for the polynomial segments are given in Table 3 along with their valid temperature ranges.

T	α_0	α_1	α_2	α_3	α_4
200 K – 1000 K	34.9088	-0.0169315	$5.42126 \cdot 10^{-5}$	$-4.56286 \cdot 10^{-8}$	$1.47328 \cdot 10^{-11}$
1000 K – 3500 K	25.2255	0.0180995	$-1.36415 \cdot 10^{-6}$	$-8.06836 \cdot 10^{-10}$	$1.39847 \cdot 10^{-13}$

Table 3. Piecewise polynomial expression for the specific heat at constant pressure of hot steam.

The results computed from the perfect gas EoS model are compared with first order solutions in Fig. 3 and second order solutions in Fig. 4. The first order plots show much better agreement in the distribution of pressure temperature and mach number across the radial direction of the nozzle; however the second order solutions still show some discrepancies. The pronounced ringing in the second order DG solution is most likely due to poor limiter performance. This will be examined closely to determine the source of the spurious oscillation.

The fact that the two methods agree so closely in the first order solutions appears to indicate that both solvers are using fundamentally equivalent EoS implementaions. This suggests that the deviations in the second order runs may be due to the numerical differences in the solvers on such a coarse mesh.

A representative slice through the first and second order Loci-Chem solutions and first through fourth order Loci-THRUST solutions is shown in Fig. 6. Again we see that the second through fourth order solutions from Loci-THRUST are effectively converged. It should also be noted that the ringing present in the second order solutions are not present in the higher order solutions. This might indicate that the DG solver is capable of adequately resolving the shock at higher order.

VI.   Conclusion

The new equation of state framework is in place and has been used to sucessfully implement two EoS models into the Loci-THRUST solver. The preliminary comparisons with Loci-Chem look promising; however the models will need to undergo more rigorous testing to complete their verification.

The hybrid conservative-primitive variable formulation described in this report has the potential to improve the efficiency of the solver when evaluating the pressure-temperature based lookups required in some of the more advanced equation of state models.

VII.   Future work

The updates to the Loci-THRUST solver described in this report are part of an ongoing effort to make the high-order accurate DG method capable of simulating more advanced fluid physics problems. The near term objective of these enhancements is to create the capability to perform multi-species simulations capable of accurately propagating acoustics effects through mixed species fluids.

The development of the EoS framework within the Loci-THRUST solver will make it possible to implement other advanced EoS models as modules which can be loaded into the solver at run time. The tabular equation of state recenetly developed for the Loci-Chem solver[2] will be given a high priority for inclusion in the Loci-THRUST solver.

The mixed variable formulation will be implemented and tested. Once it has been verified to solve the governing equations at the prescribed order of accuracy, we will begin profiling the implementation to determine the overall effectiveness of this method for reducing the computational overhead associated with making EoS queries.

Acknowledgments

References

[1]E. Collins, *On Mesh Quality Considerations for the Discontinuous Galerkin Method*, Ph.D. Dissertation, Mississippi State University, 2009

[2]E. Collins, E. Luke, "Fast Evaluation of Complex Equations of State", *Electronic Journal of Differential Equations*, vol. 20, pp. 27-37, 2013

[3]R. Harris, E. Collins, E. Luke, A. Sescu, "Coupled Overset Unstructured Discontinuous Galerkin Method for Launch Environment Acoustics Prediction", *AIAA Journal*, vol. 54, no. 6, pp. 1932-1952, 2016

[4]E. Luke, X. Tong, J. Wu, P. Cinnella, R. Chamberlain, "CHEM 3.3: A Finite-Rate Viscous Chemistry Solver - The User Guide", Mississippi State University, pp. 88, 2016
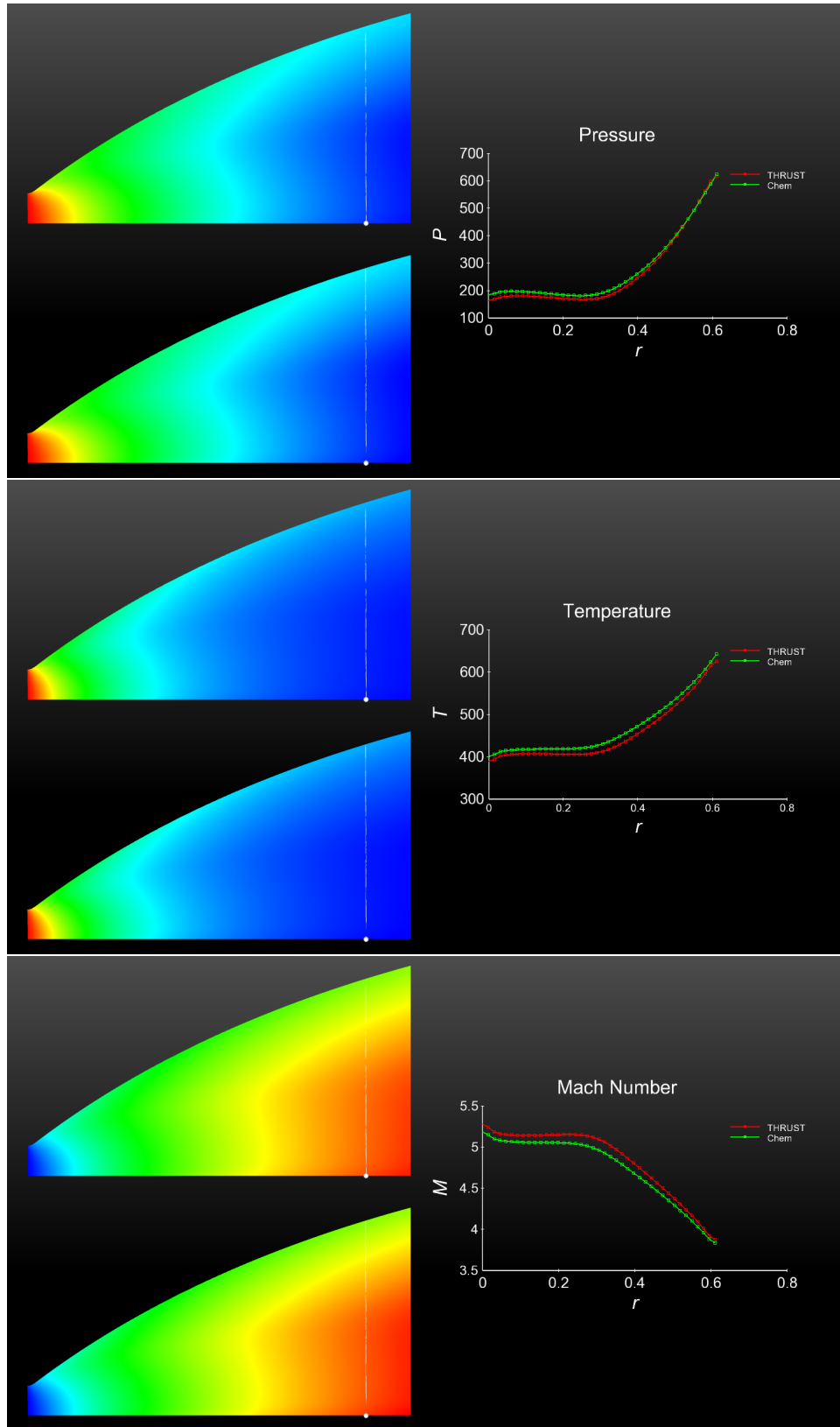
Figure 1. Comparison of ideal gas pressure, temperature, and mach number distributions in an SSME nozzle geometry from first order solutions generated by Loci-Chem (top) and Loci-THRUST (bottom)
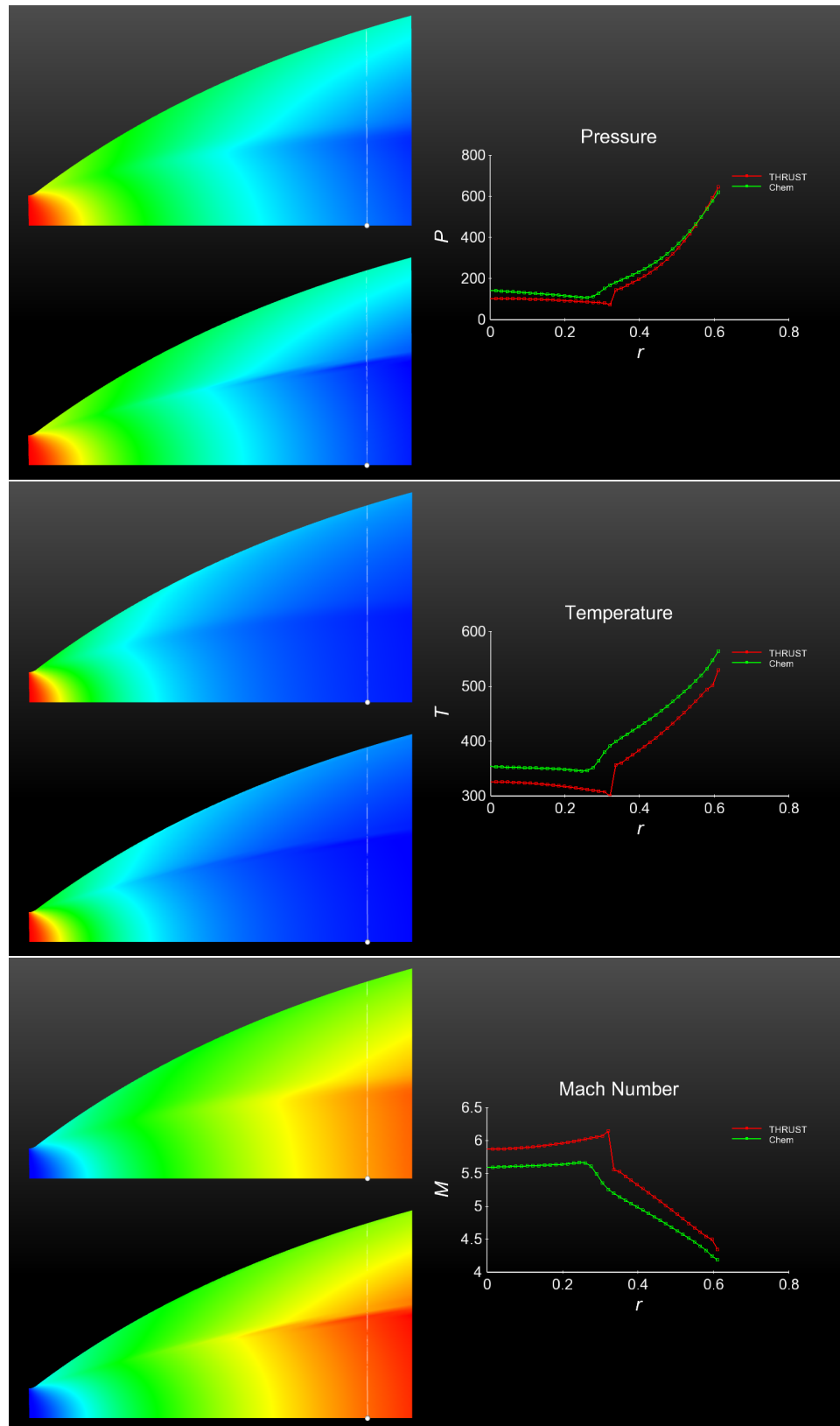
Figure 2. Comparison of ideal gas pressure, temperature, and mach number distributions in an SSME nozzle geometry from second order solutions generated by Loci-Chem (top) and Loci-THRUST (bottom)
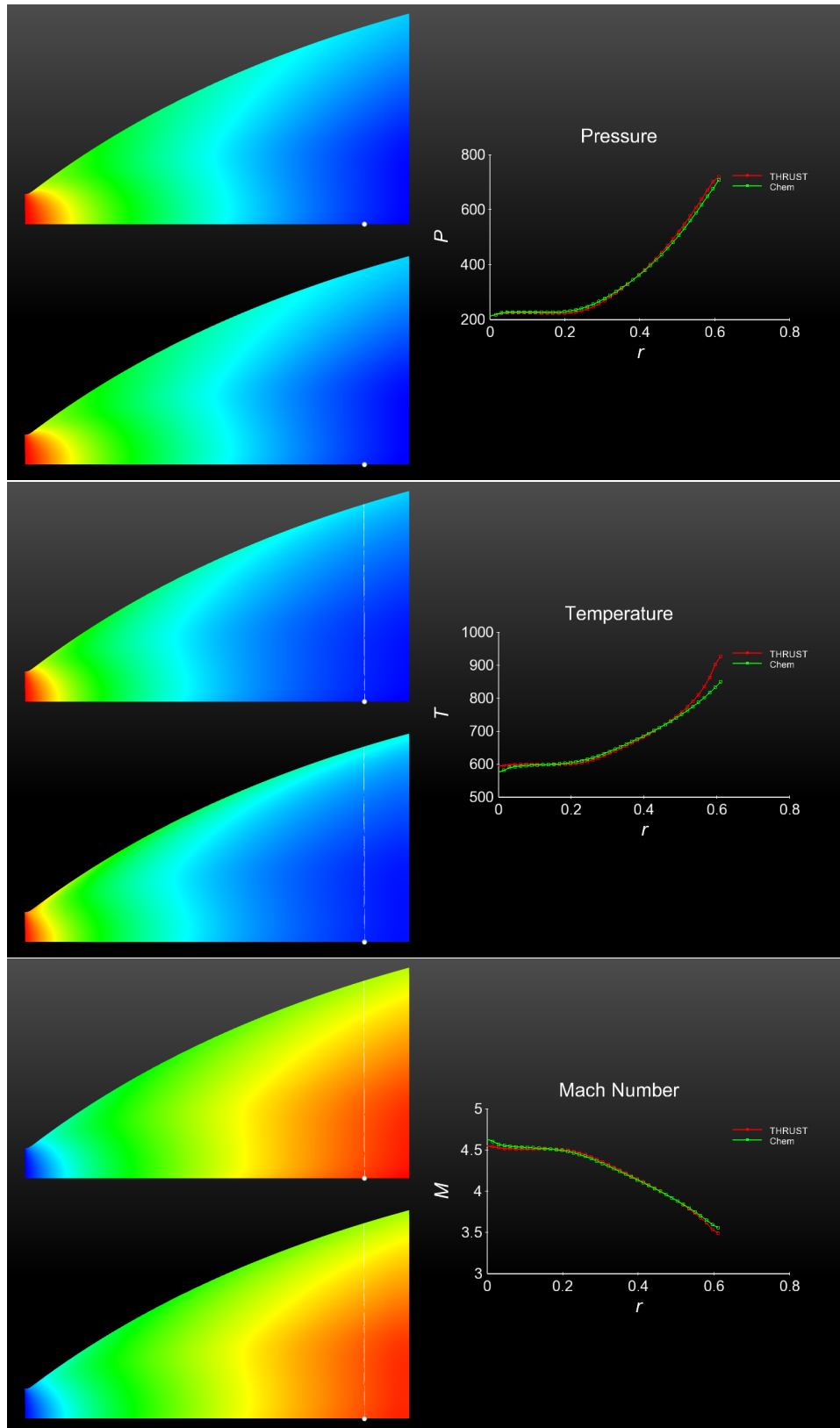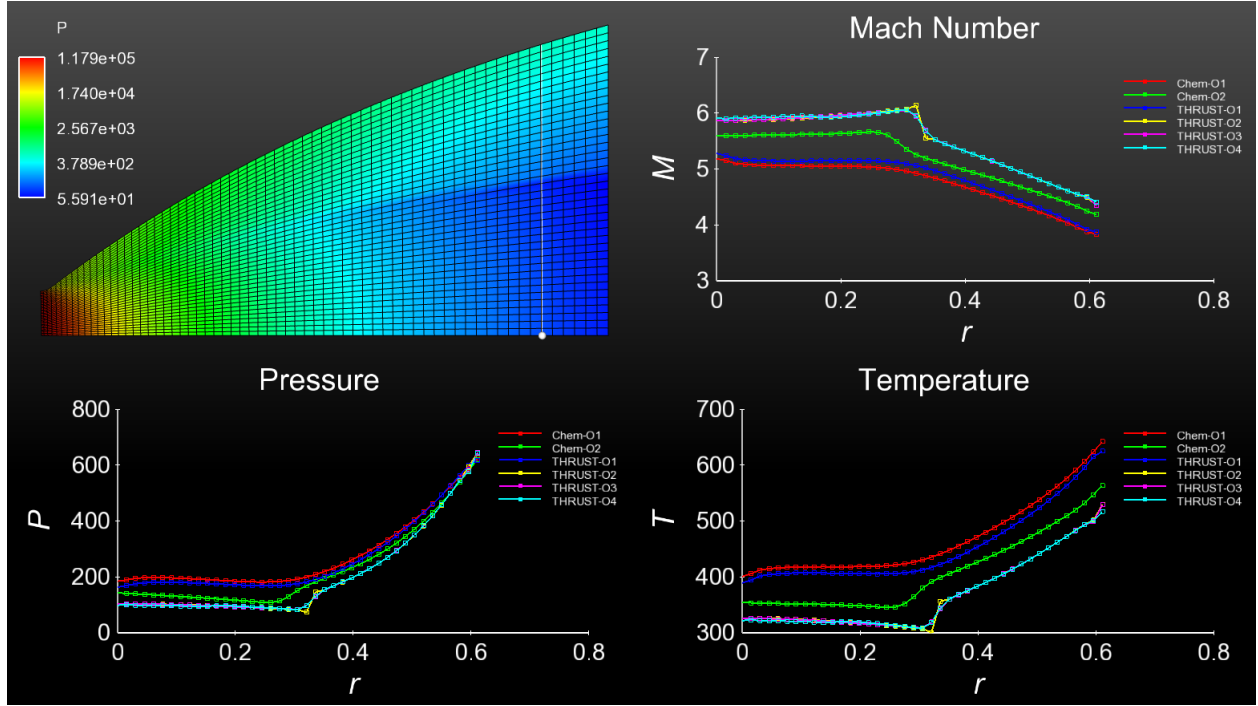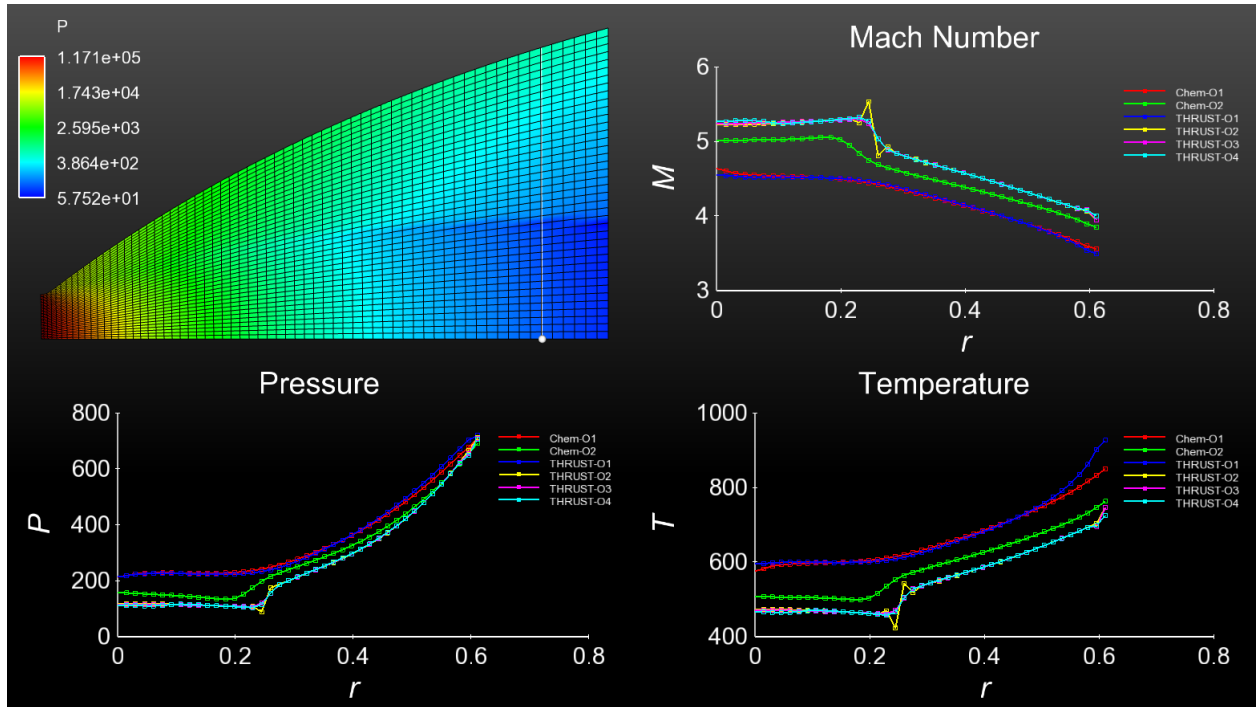
Figure 3. Comparison of perfect gas pressure, temperature, and mach number distributions in an SSME nozzle geometry from first order solutions generated by Loci-Chem (top) and Loci-THRUST (bottom)
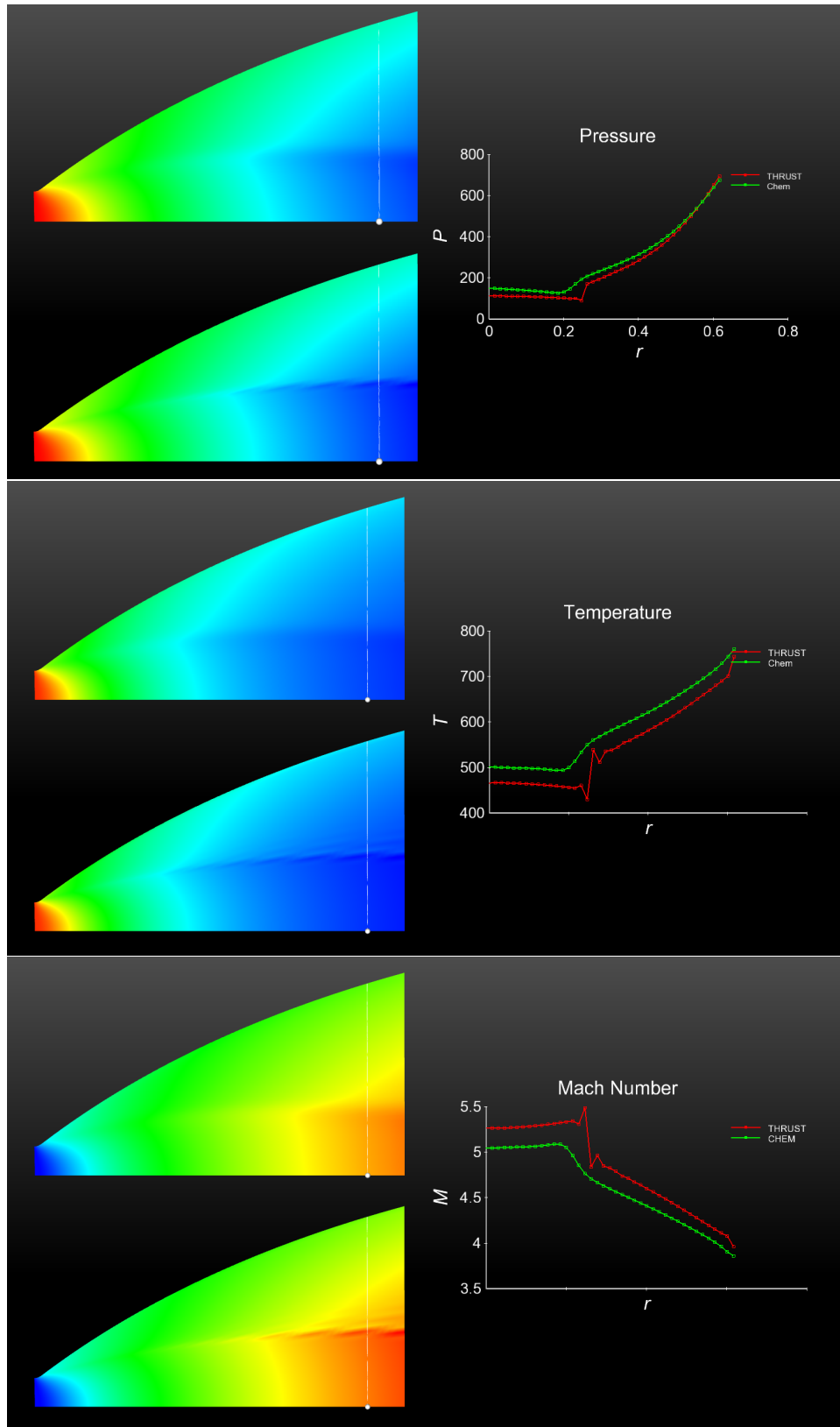
Figure 4. Comparison of perfect gas pressure, temperature, and mach number distributions in an SSME nozzle geometry from second order solutions generated by Loci-Chem (top) and Loci-THRUST (bottom)

Figure 5. Comparison of ideal gas pressure, temperature, and Mach number distributions in an SSME nozzle geometry for first and second order solutions from Loci-Chem and first through fourth order solutions from Loci-THRUST.

Figure 6. Comparison of perfect gas pressure, temperature, and Mach number distributions in an SSME nozzle geometry for first and second order solutions from Loci-Chem and first through fourth order solutions from Loci-THRUST.

Design Concepts for Bubble Transport Simulation Experiment

Z.T. Deng[1]

Mechanical Engineering, Alabama A&M University, Huntsville, AL 35762

Heath Martin[2], Alicia Turpin[3], Alok Majumdar[4], Jonathan Stephens[5],and Stanley Tieman[6]
NASA Marshall Space Flight Center, Huntsville, Alabama

Abstract: The understanding of the bubble formation and transport in propellant is essential for in-space propulsion system applications. When cryogenic fluid propellant is transported through a pipe, gas bubble may be generated due to heat transfer. The system level simulation tool, GFSSP, needs to expand its capability to accurately model the two-phase separated flow. A bubble transport simulation experiment was previously proposed. It uses a single experimental setup to investigate multiple fluid bubble transport inside a pipe with/without heat transfer. The experiment was aimed to provide the critical correlation coefficients to GFSSP and to expand its capability to compute the two–phase separated flow. This study analyzes the design concept of the bubble transport simulation experiment. Preliminary hydrodynamic flow analysis on the pipe configuration, the pipe inlet pressure, the side injection air pressure and onset nucleate boiling length with heating source were presented.

I. Introduction

Understanding of bubble formation and dynamics in propellant transport is essential for in-space missions, where vapor can lead to unknown conditions within ducts, lines, acquisition devices creating operational issues. It is challenging to transport the cryogenic liquid propellant from a propellant storage tank in space where the tank is undergoing uneven space radiation heat transfer. It is critical to provide vapor-free liquid propellant at the tank outlet and the accurate and reliable measurements of cryogenic liquid mass in low-gravity transport line.

The transport of cryogenic liquid propellant in a pipe involves complicated hydrodynamics and forced convection boiling heat transfer process. Vapor bubble formed at the inner surface of the pipe where the cryogenic fluid is flowing. The existence of the bubble formation, the bubble growth, and the bubble separation significantly affect the hydrodynamics of the two-phase fluid flow pattern. The typical flow regimes are the bubbly flow, the slug-flow, the annular flow, and the mist-flow regime. The two-phase flow regime is also strongly influenced by the flow velocity. The hydrodynamic coefficients and heat transfer coefficients for single phase fluid flow can be obtained from the traditional fluid mechanics and heat transfer experiment. However, when forced convection boiling occurs, the single phase fluid flow correlations and the homogeneous treatment of the two-phase fluid flow become inadequate.

The GFSSP, developed by NASA MSFC, is a powerful computational tool for analyzing steady state and time-dependent flow rates, pressures, temperatures, and concentrations in a complex flow network. The program is capable of modeling real fluids with phase changes, compressibility, mixture thermodynamics, conjugate heat transfer between solid and fluid, fluid transients, pumps, compressors, flow control valves, and external body forces such as gravity and centrifugal [1]. The GFSSP program has been extensively validated with experimental data and has been widely used in propulsion system analysis for tank pressurization, internal flow of rocket engine, the chill-down of cryogenic

---

[1] Professor, Marshal Space Flight Center Faculty Fellow, Mechanical Engineering, Alabama A&M University.
[2] Thermal Analyst, Jacob Engineering, Collaborator, ER 43, NASA Marshall Space Flight Center.
[3] Branch Chief, Collaborator, ER 43, NASA Marshall Space Flight Center.
[4] Collaborator, ER 43, NASA Marshall Space Flight Center.
[5] Collaborator, ER 24, NASA Marshall Space Flight Center.
[6] Division Chief, Collaborator, ER 40, NASA Marshall Space Flight Center.

tanks and transfer lines, and many other applications of gas-liquid systems involving fluid transients and conjugate heat and mass transfer. Many NASA programs including SSME have been benefited from the GFSSP. The execution of the GFSSP program requires the theoretically or experimentally validated correlations for hydrodynamics and heat transfer coefficients for various flow regimes. For two-phase flow, the GFSSP assumes that the fluid flow is homogeneous. The homogeneous mixture modeling technique for two-phase flow assumes that the two phases (vapor and liquid) are well mixed and have the same velocity at any location [2]. It then considers the two-phase flow as a single phase flow having average fluid properties depending on flow quality. Thus, the frictional pressure drop is calculated by assuming a constant friction coefficient between the inlet and outlet sections of the pipe. To expend the capability of the GFSSP for analysis in separated two–phase flow, it is necessary to conduct a series of experiment to measure the flow coefficients in various two-phase separated flow regimes. Multiple materials such as liquid water, cryogenic liquid Nitrogen and glycerin as working fluid with wide range of working temperature have to be investigated.

The challenges in the system level software like GFSSP, are how to accurately represent the gas-liquid two phase flow quality in the flow. The prediction of the pressure change in the transport line (pipe), the liquid and vapor mass flow rate in the transport line (pipe), and the heat transfer through thermal insulation in the transport line are required output of the simulation program. With forced convection boiling, it become extremely complicated because the bubble nucleation, detachment, shape, transport, rising velocity, the interaction between bubbles, and the interphase mass and heat transfer all depend dramatically on the density and viscosity of the liquid, heat transfer mode, and wall contact angle. These critical information can only be provided by experiment.

A series of bubble transport simulation experiments were proposed to experimentally investigate the separated two-phase fluid bubble transport dynamics (formation, detachment and transportation) in a pipe. The experimental data will be used to develop correlation models within GFSSP and expand its capability in prediction of forced convection boiling separated two-phase flow [3]. The expected output of the experiment are: mass flow rate (both liquid and vapor), the heating power, the flow regime (Flow Quality), the pressure drop, and the temperature distribution in the fluid. These data will then be used to provide the correlation of flow coefficients, the friction coefficients, flow quality and the heat transfer coefficients, as function of pipe inlet pressure and heat flux from the wall.

The proposed experiment was designed to investigate two modes of operation covering convective and stagnant conditions for saturated/near saturated fluids. The single test setup consist of a pipe configuration with or without bends and or flow obstructions, the gas (vapor) injection, and a wall heating source. The proposed experiment will examine multiple fluids include water, liquid Nitrogen and glycerin. The experiment configuration [3] is shown in Figure 1. Four possible configurations was proposed to conduct the multi-materials (fluid) experiment. In this test setup, a near saturated subcooled liquid with variable pressure is pumped into a horizontal or a vertical pipe of 2-4 inch equivalent diameter for square cross section. The pipe was made of a transparent material which allows for the observation of the formation of the vapor bubble and transport. The pipe may have a 90 degree bend or obstructions inside to allow for the examination of interactions. The test configuration also include a variable pressure side air
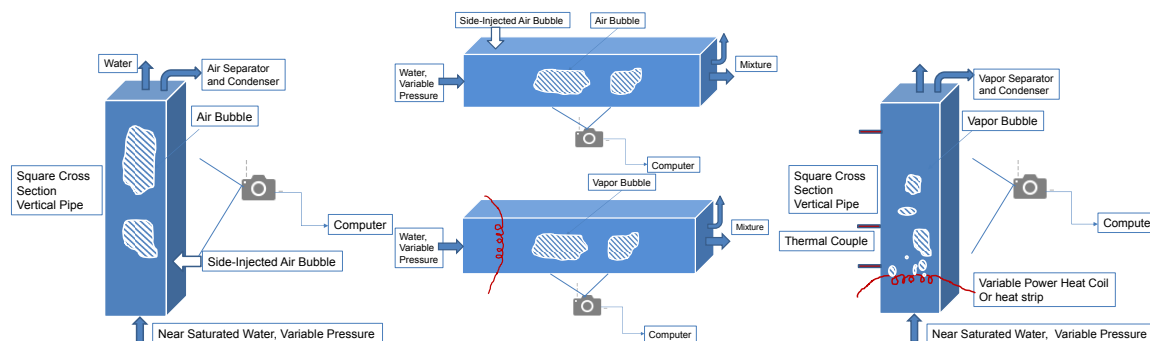

Figure 1. Proposed single test setup with four configurations.

injection for cold flow simulation experiment. The bubble formation, grow and transport dynamics will be captured through high speed and resolution video camera.

The objective of the current work is to conduct preliminary hydrodynamic and on-set boiling heat transfer analysis for the proposed test configurations and to evaluate the bubble transport simulation design concept in terms of pipe dimensions, materials, pump pressure, flow rate, side injection pressure, two-phase flow regimes and heating power.

II. Hydrodynamics and On-Set Boiling Heat Transfer Considerations

A. Hydrodynamics and Thermal Considerations

When near saturated subcooled liquid enters the pipe, the viscus effects between the liquid and the pipe wall will create a hydrodynamic and thermal entry region, before the fluid become fully developed. In the hydrodynamic entry region, the fluid velocity profile changes along the direction of the stream while in the fully developed region, the velocity profile of the liquid is no longer changing in the direction of the flow. From a pure hydrodynamic consideration, it is necessary for the test setup to cover the entire flow region including hydrodynamic entry and fully developed regions. The thermal entry region exists where the thermal boundary layer begins to develop, the temperature profile changes along the stream direction. The shape of the temperature profile in the thermally fully developed region differs according to the thermal boundary conditions of the wall. Therefore the minimum length of the pipe in the experimental setup has to be greater than the entry length (more importantly momentum entry length) with given flow conditions. For single phase fluid flow, the hydrodynamic entry length, x, compared to the equivalent pipe diameter D, can be estimated as in [4],

$$10 \leq \frac{x}{D} \leq 60, \text{ for Reynolds number } R_{eD} \geq 10,000, \text{ (Turbulent Flow)}$$
$$\frac{x}{D} \approx 0.05 \, R_{eD}, \text{ for Reynolds number } R_{eD} \leq 2300, \text{ (Laminar Flow)}$$

The thermal entry length $x_{thermal}$ can be estimated as a function of Reynolds number R_{eD} and fluid Prandtl number P_r,

$$\frac{x_{thermal}}{D} \approx 0.05 \, R_{eD} P_r, \text{ for laminar flow,}$$

For turbulent flow, conditions are nearly independent of the Prandtl number, and it is generally assumed that

$$\frac{x_{thermal}}{D} \approx 10.$$

For large Prandtl number fluid, the hydrodynamic boundary layer develops more rapidly than the thermal boundary layer and for fluid with the small Prandtl number, it is reversed. For a 2" x 2" rectangular cross section pipe, the equivalent diameter of the pipe is

$$D = \frac{4 \times Flow \; Cross \; Sectional \; Area}{Wetted \; Perimeter} = 2 \text{ (inch)},$$

and the minimum pipe length to achieve the fully developed laminar flow is 230 inches. When Reynolds number increased to 10,000, the entry length decreased to 20 inches. Therefore, it is reasonable to suggest that the pipe length be 80 inches, so that a fully developed flow can be reached.

B. Heat Transfer Considerations:

When subcooled liquid flow inside a pipe with higher temperature, the heat transfer occur. This is more important when cryogenic fluid is transported inside a pipe which was exposing to the warm surroundings. The subcooled liquid absorbs the heat from the wall and boiling may occur if the temperature difference between the wall and fluid reaches critical threshold. Experimental observation [4] indicated that the free convection pool boiling will occur when the temperature difference between the surface of the wall and the saturation temperature of the fluid, $(T_s - T_{saturation}) \leq 5$ °C. The nucleate boiling will occur when 5°C $\leq (T_s - T_{saturation}) \leq 30$ °C. The transition boiling will occur when 30°C $\leq (T_s - T_{saturation}) \leq 120$ °C, and the film boiling will occur when $(T_s - T_{saturation}) \geq 120$°C. The critical heat flux required to reach the nucleate pool boiling of water [4] is estimated as a function of the surface tension coefficient, σ, the latent heat, h_{fg} and the density difference between vapor and liquid.

$$q''_{critical} = 0.149 \, h_{fg}\rho_v \left[\frac{\sigma g(\rho_l - \rho_v)}{\rho_v^2}\right]^{0.25}$$

For example, @ 290 K, the latent heat for water is $h_{fg} = 2461 \frac{kJ}{kg}$, $\rho_v = 0.014 \frac{kg}{m3}$, $\rho_l = 999.0 \frac{kg}{m3}$, $\sigma = 0.0737 \frac{n}{m}$, the critical heat flux can is estimated as $q''_{critical} = 22 \frac{kW}{m2}$.

Experimental results on constant heat flux water flow inside a vertical pipe [2] suggested that in forced convection boiling, the on-set nucleate boiling length depends on the wall heat flux, the pressure, the flow Reynolds number, and the pipe contact surface perimeter. With a given constant wall heat flux q''_W, and liquid pressure, P, the liquid mass flow rate $\dot{m}_L$, the Onset Nucleate Boiling (ONB) length, Z_{ONB}, can be solved by combining the following equations.

$$n = 0.463 \, P^{0.0234}, \quad (T_W - T_{sat})_{ONB} = 0.556 \left[\frac{q''_W}{1082 \, P^{1.156}}\right]^n$$

$$Nu_D = \frac{H_{L0}D}{k_L} = 0.023 \, Re_L{}^{0.8} Pr^{0.4}, \qquad q''_W = H_{L0}(T_W - T_L)_{ONB}$$

$$\dot{m}_L Cp_L\left(T_{L\,ONB} - T_{L\,IN}\right) = Contact\ Surface\ Area \, * \, q''_W * Z_{ONB}$$

C. Two-Phase Flow Hydrodynamics Regimes

For flow in a vertical pipe, the two-phase flow regimes can be classified [5] as in Figure 2. It involves bubbly, slug, churn, annular, and disperse flows. The flow regimes depend on the flow geometry, the flow quality and the flow rate. The flow quality is defined as the ratio of the vapor mass flow rate to the overall mass flow rate, as $x = \frac{\dot{m}_v}{\dot{m}_v + \dot{m}_L}$. At low flow quality and low flow rate, the two-phase flow is in the bubbly flow regime. At intermediate flow rate and intermediate flow quality, the two-phase flow is in slug flow regime. It was observed that the flow quality and flow rate are critical in determining the two-phase flow regimes. If one can measure the flow quality and flow rate, it is possible to predict the frictional pressure drop in two-phase flow by empirical correlations. The prediction of void fraction in two-phase flow can also be achieved by empirical correlations.
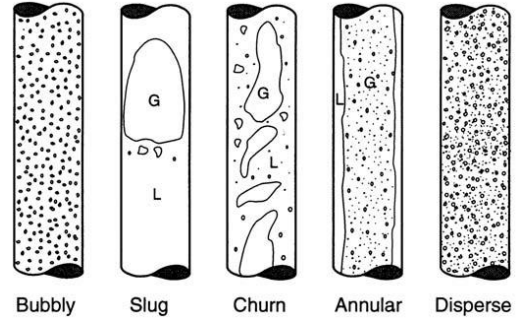
Figure 2. Two-phase Flow Regimes [5].

D. Two-Phase Flow Experiment Control Variables

Dimensionless groups are useful in arriving at key basic relations among system variables that are valid for various fluids under various operating conditions. . The use of the dimensionless groups is important in obtaining correlations for pressure drop in two-phase flow, and other different parameters in two-phase flow. For boiling heat transfer, there are eight critical dimensionless parameters, explained in the following.

1). the Archimedes number: $A_r = \frac{\rho_l(\rho_l - \rho_g)gD^3}{\mu_l^2}$, which represents the ratio of gravitational force to viscous force. It is used to determine the motion of fluids due to density differences;

2). the Bond Number: $B_0 = \frac{gD^2(\rho_l - \rho_g)}{4\sigma}$, which represents the ratio of gravitational and surface tension forces;

3). The Jacob Number: $J_a = \frac{C_p \Delta T}{h_{lg}}$, which represents the ratio of the sensible heat for a given volume of liquid to heat or cool through the temperature difference in arriving to its saturation temperature to the latent heat required in evaporating the same volume of vapor;

4). the Prandtl number, Pr

5). the Grashof Number: $G_{rL} = \frac{g\beta(T_S - T_\infty)L^3}{\left(\frac{\mu}{\rho}\right)^2}$, $\quad \beta = -\frac{1}{\rho}\left(\frac{\partial \rho}{\partial T}\right)_p \approx -\frac{1}{\rho}\left(\frac{\rho_\infty - \rho}{T_\infty - T}\right)$ and

6). the Boiling Number: $K_f = \frac{q}{Gh_{lg}} = \frac{heat\ flux}{mass\ flux\ *laten\ heat}$.

Combining with convection, where the Reynolds number and the Nusselt number have to be considered,

7). Reynolds Number: $R_e = \frac{\rho U_{average} L}{\mu}$, where L is the characteristic length,

8). The Nusselt number, $N_{UL} = \frac{hL}{K}$.

For forced convection two-phase flow with boiling, the boiling effects due to natural buoyancy 1), 2) and 5) are small, the heat flux for Boiling number 6) and Jacob number 3) are inter-related, the Prandtl number is fixed for given fluid, therefore, the Nusselt number is directly linked to a the fundamental two dimensionless parameters, heat flux and Reynolds number.

$$\text{Nusselt Number: } N_{UL} = f\left(J_a,\ R_e\right)$$

It seems that the convection boiling can be defined as a system with three degree of freedom. There are 14 physical variables that can influence the value of the aforementioned dimensionless parameters for forced convection boiling vertical pipe experiment, 1) the liquid thermal conductivity K_L, 2) liquid heat capacity C_P, 3) liquid density ρ_L, 4) liquid surface tension σ_L, 5) liquid viscosity μ_L, 6) liquid Latent Heat H_{LG}, 7) liquid flow Reynolds number R_{EL}, 8) liquid Prandtl number Pr_L, 9) liquid flow quality, 10) vapor density ρ_G, 11) wall temperature (Heat Flux) q_W'', 12) saturation temperature T_{sat}, 13) saturation pressure P_{sat}, and 14) the fluid pressure P. For a pre-defined flow geometry and given fluid, it is quite possible to obtain the experimental correlation coefficients for pressure, mass flow rate and heat transfer in the two-phase forced convection flow with boiling by simply control three variables, such as the Reynolds number, the heat flux and the liquid pressure.

III. Parametric Flow Studies on Test Setup

Parametric studies for flow inside a horizontal and a vertical pipe with side air injection were conducted using GFSSP. The flow geometry include both circular and rectangular cross sections. Figure 3 shows the flow geometry used in the GFSSP simulation and GFSSP network for the flow configuration. The rectangular pipe has a dimension of 2x2x78 inches, while the circular pipe has the diameter of 1 - 2.25 inch. For GFSSP simulations, the flow network is defined as in Figure 3, where node 1 represents the inlet, with 2.25" circular diameter, or with 2"x2" rectangular cross section, or with 1" circular diameter pipe. The 60°F water is flowing into the pipe from node 1 with pressure ranges from 15 to 20 psi. High pressure air is injected from the Node 7, through a replaceable orifice. The air pressure ranges from 20 to 100 psi. The orifice has a diameter of 0.25" to 1". The injection port is located 8" from the pipe inlet. The air and water starts to mix at 8" from the pipe inlet. All pipes are considered to have a small roughness, which introduces pressure drop due to friction. The fluid mixture leaves the pipe at Node 6, where the ambient pressure is 14.7 psi. The mixture exit is 78.74" from the inlet.

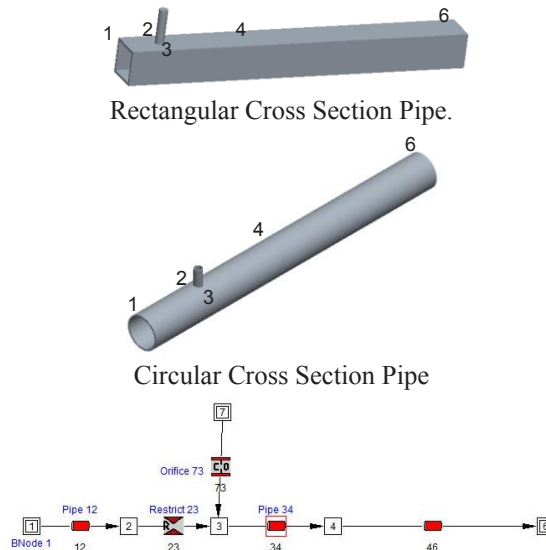Rectangular Cross Section Pipe.

Circular Cross Section Pipe

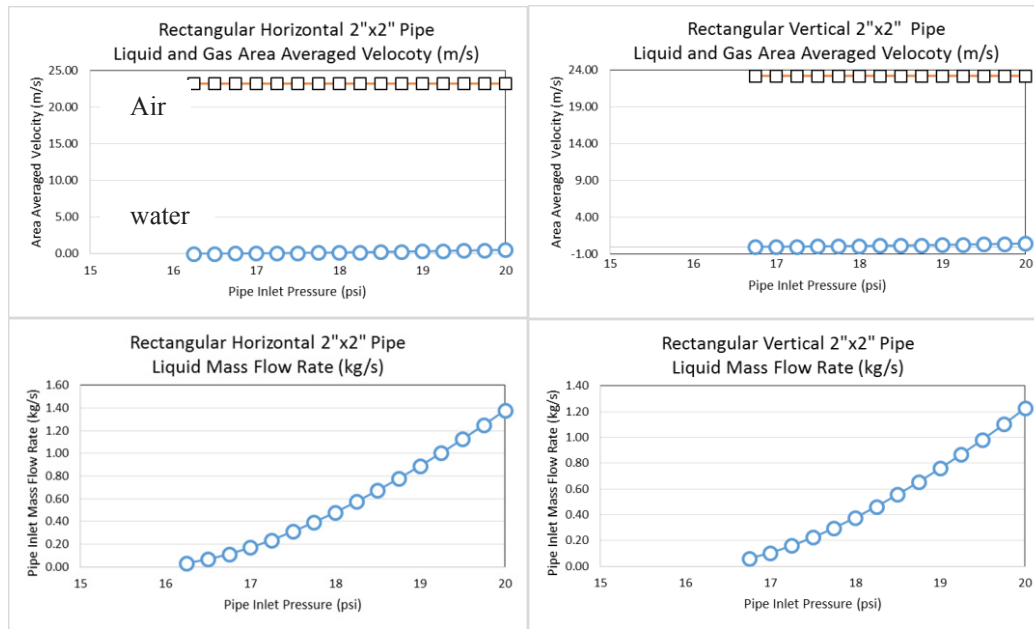Figure 3. Flow geometry configuration for GFSSP simulation.
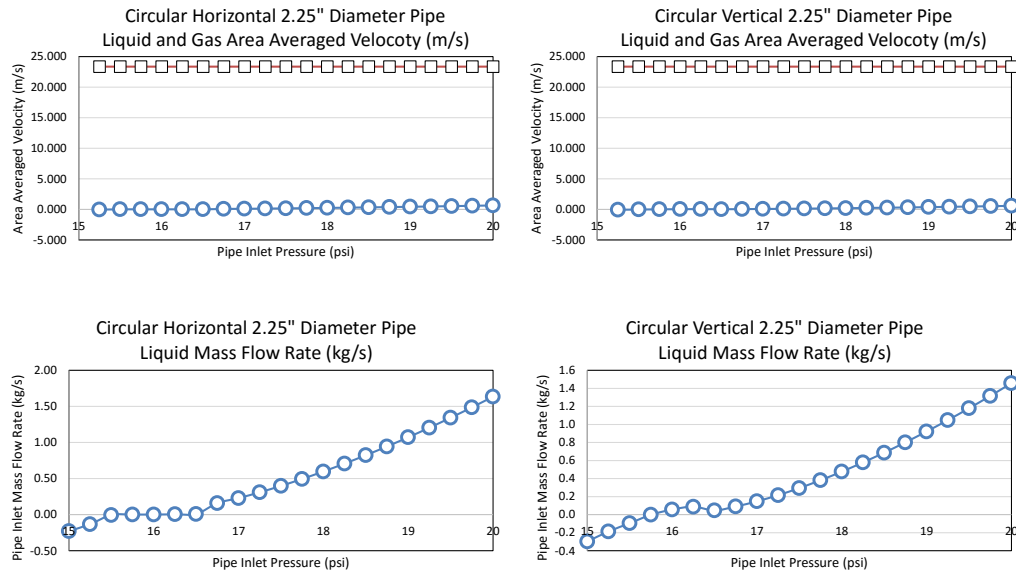

Figure 4. Area averaged "superficial" velocity of liquid and gas and liquid mass flow rate for horizontal and vertical pipe.

Figure 4 shows the GFSSP results for flow inside a 2" x 2" rectangular cross section pipe. The pipe is configured with horizontal and vertical setup. The side air injection has a pressure of 100 psi with 1" diameter orifice. The air is chocked when leaving the orifice with sonic speed. The mass flow rate of the air entering the pipe is fixed at 100 psi injection pressure. The flow quality is relatively high. For the horizontal pipe setup, the flow quality is 0.745 when pipe inlet water pressure is 17 psia, and 0.265 when inlet water pressure reaches 20 psia. For the vertical pipe setup, the flow quality reaches 0.826 when water inlet pressure is 17 psia, and 0.289 when water inlet pressure reaches 20 psia. Figure 5 shows the GFSSP results for flow inside a 2.25" diameter circular pipe. Both horizontal and vertical setup were calculated. The side air injection has 100 psi pressure with 1" diameter orifice. The air entering the pipe is also chocked with high mass flow rate. For the horizontal pipe setup, the flow quality is 0.616 when pipe inlet water pressure is 17 psia, and 0.234 when inlet water pressure reaches 20 psia. It is slightly smaller than the flow quality of rectangular pipe. For the vertical pipe setup, the flow quality reaches 0.771 when water inlet pressure is 17 psia, and

0.255 when water inlet pressure reaches 20 psia. The superficial velocity of liquid ranges from Liquid: 0.02- 0.48m/s, Gas: 23 m/s.

Figure 5. Area averaged "superficial" velocity of liquid and gas and liquid mass flow rate for horizontal and vertical pipe.

Notice that the flow quality is high for all above cases. When side air injection orifice area is reduced to 0.25" in diameter, significant reduction of the flow quality can be obtained. Figure 6 show the significant difference (10 times higher!) in averaged liquid velocity comparing to the 1" orifice results for 2"x2' cross section pipe.
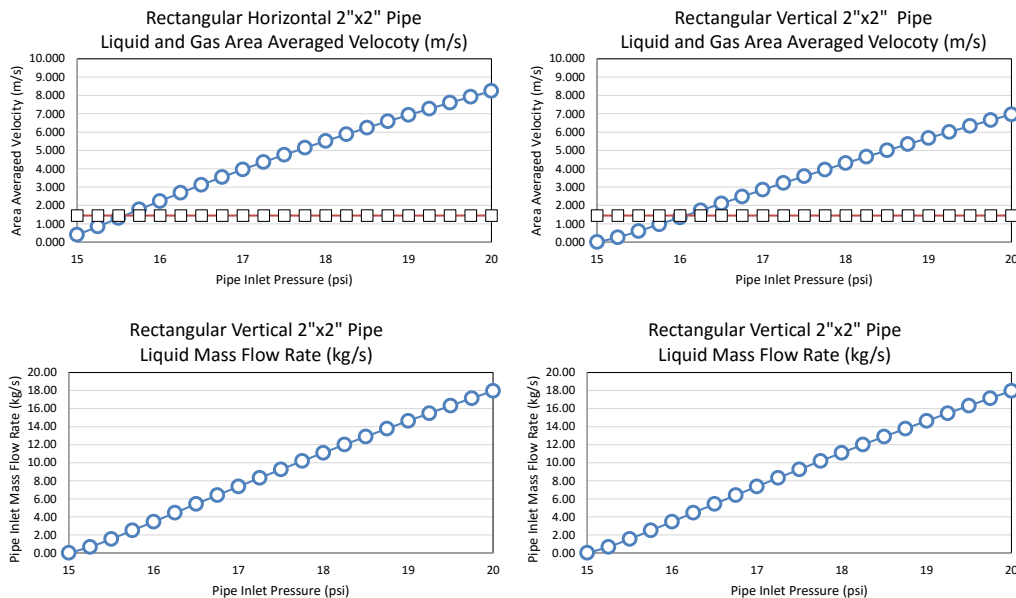
Figure 6. Rectangular 2" x2" pipe, 100 psi side air injection with 0.25" diameter orifice.

The flow quality ranges from 0.004-0.003 at 17 psi inlet pressure and 0.002-0.001 at 20 psi inlet water pressure. It is reasonable to think that the smaller orifice will provide smaller air mass flow rate so that the flow quality can be significantly reduced. As a result, the two-phase flow will not be dominated by the air. Table 1 shows the computed Onset Nucleate boiling length with constant heat flux wall for water flow inside a 2"x2" rectangular pipe. The

Reynolds number was computed from water inside a rectangular pipe with side air injection, and the orifice diameter is 0.25". In order to reach Onset Nucleate boiling, the minimum pipe length should be 78 inches.

Table 1. Computed Onset Nucleate Boiling Length for Water inside a 2"x2" Pipe with constant Heat Flux.

Heat Flux Q" (Flux) (W/m2)	Inlet PressureP1 (psi)	Mass Flow Rate (kg/s)	REYNOLD_L	ONB Length Z_ONB (m)
3.000E+05	16.250	4.442	8.790E+04	1.426
3.500E+05	16.500	5.421	1.072E+05	1.771
4.000E+05	16.750	6.396	1.265E+05	1.938
4.500E+05	17.000	7.357	1.456E+05	1.959
5.000E+05	17.250	8.314	1.645E+05	1.886

IV. Design Concept Discussion and Recommendation

Figure 7 shows the suggested experiment setup for the bubble transport simulation experiment. A circular thick aluminum pipe with 1" inside diameter, 80 inch length. The inlet of the pipe is connected to a variable pressure liquid supply tank, with regulated 15 to 20 psia pressure. A liquid flow meter is installed about 2 inch downstream of the pipe inlet to measure the fluid mass flow rate. High pressure air is injected from an interchangeable area orifice with
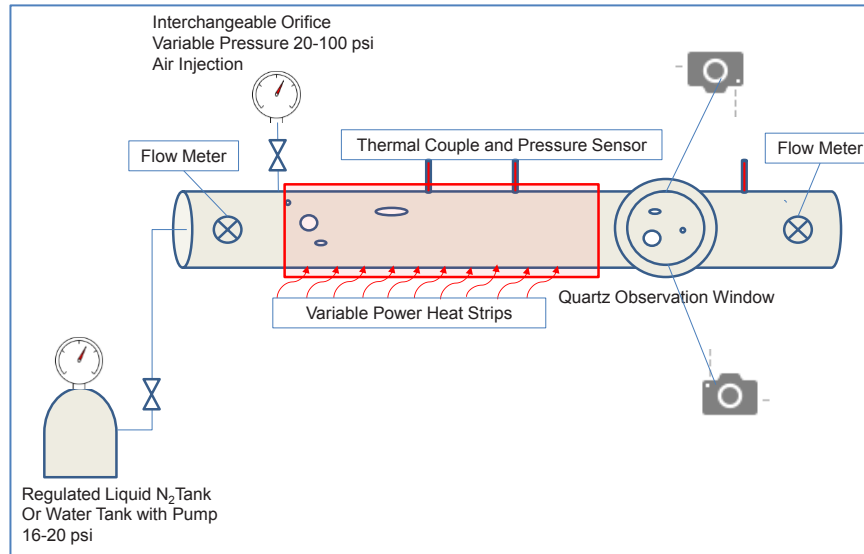
Figure 7 Suggested bubble transport simulation experiment setup.

variable regulated pressure from 20 to 100 psia. The injector port is located 8" from the pipe inlet. Variable power heat strips with variable length is used to provide uniform heat flux to the pipe. The starting location of the heat strip is floating depending on the individual heat flux power requirement. The starting location of the heat strip can be determined by the flow quality requirement through trial and error observation. A Quartz glass observation window is installed near the exit of the pipe to make sure the wide range of flow quality can be detected by imaging system. On the side surface of the pipe, multiple thermos-couples and pressure sensors are installed to measure the temperature and the pressure distribution along the pipe stream direction. A two-phase flow meter at the exit of the pipe is installed to measure two-phase flow liquid mass flow rate. The pipe exit should have space to connect to another pipe with a 90 degree bend.

Pipe Material Selection: In order to configure a single test setup for multiple fluid including water, liquid Nitrogen and glycerin, the pipe has to be able to sustain the large variation of fluid temperature, especially at cryogenic temperature near 77K. The thick aluminum can be used to construct the pipe since it has a better thermal conductivity

than the stainless steel. The plexi glass tends to be very brittle at 80K temperature, where liquid Nitrogen vaporizes. To heat the subcooled water, it requires a significant amount of heat flux to create the 373K boiling water vapor. Since the water is moving inside the pipe with relatively high speed, the heat transfer residence time is very short, hence the pipe material has to be very conductive. The aluminum also perform better than the plexi glass.

Pump: Variable power (pressure). It should be able to provide water pressure 16-20 psia with a minimum 0.25 psia increment, with variable flow rate, up to 30 kg/s.

Pipe: 1" Circular thick aluminum pipe with minimum of 80" length is recommended. A 2" x 2" x 80" transparent rectangular plexi glass pipe may be used to prove the similarity criteria between the liquid water and the cryogenic liquid Nitrogen. If similarity criteria works, the experimental setup will be extremely easy and the liquid Nitrogen test may not be needed and it will only be used to verify the similarity criteria. Further studies on similarity criteria are required.

Pipe Configuration: Horizontal and vertical configuration is possible if a single test setup is configured. The pipe inlet water pressure ranges from 16 psi - 20 psi, with 0.25 psi increment.

Side Air Injection: The side air injection should provide controllable air mass flow rate into the pipe where liquid is flowing. The interchangeable area orifice with varying pressure ranges from 20-100 psi, (0.25" Diameter pipe) is recommended in order to observe wide ranges of hydrodynamic flow regimes.

Camera: The imaging system should be able to capture the bubble nucleation, formation, motion and velocity. Two camera system with phase angle change is recommended.

Instrumentation: The key to the bubble transport simulation experiment is to provide correlation coefficients to enhance the two-phase separated flow capability for GFSSP. The correlation coefficients depends on the flow quality, the Reynolds number, and the heat flux. Therefore, the instrumentation system is recommended to measure liquid and gas mass flow rate, pressure, temperature, and the velocity of the liquid and gas.

Heating Element: For the forced convection boiling two-phase flow, the heat strips should be able to produce variable and controllable high heat flux. The recommended variable heat flux ranges from 2×10^4 to 5×10^5 $\frac{Watts}{m^2}$.

Acknowledgments

References

[1]Majumdar, A.K., LeClair, A.C., Moore, R. and Schllhorn, P.A., "Generalized Fluid System Simulation Program (GFSSP), Version 6," AIAA 2015 Joint Propulsion Conference, https://gfssp.msfc.nasa.gov/pdf/GFSSP_Version_6_AIAA_JPC_2015.pdf

[2]Ghiaasiaan, A. M., "Two-Phase Flow, Boiling, and Condensation in Conventional and Miniature Systems," Cambridge University Press, 2008.

[3]Turpin, A., "Bubble Transport Simulation Experiment," Internal Presentation, NASA-MSFC, December 2015.

[4]Incropera, F.P. and DeWitt, D. P., "Fundamentals of Heat and Mass Transfer," Fifth Edition, Wiley, 2002.

[5]Abdulmouti, H., "Bubbly Two-Phase Flow: Part I- Characteristics, Structures, Behaviors and Flow Patterns
 American Journal of Fluid Dynamics, 2014; 4(4): 194-240

Consultation for NASA Marshall Space Flight Center: Performance Characterization of *NEA Scout* Inertial Measuring Unit, *iSAT* Mission Planning, and SLS Structural Uncertainty Studies

D. Edberg[1]
Aerospace Engineering Department, California State Polytechnic University, Pomona, CA, 91768

D. Bullock[2]
Department of Electrical Engineering, Arkansas Tech University, Russellville, AR, 72801

A. Heaton[3]
NASA Marshall Space Flight Center, Huntsville, AL, 35812

J. Bush [4]
NASA Marshall Space Flight Center, Huntsville, AL, 35812

D. Sanders[5]
NASA Marshall Space Flight Center, Huntsville, AL, 35808

This paper summarizes work performed by the principal author as a visiting Faculty Fellow at NASA Marshall Space Flight Center (MSFC). The principal author's work encompassed three areas: support for MSFC's Near Earth Asteroid Scout (NEA Scout); MSFC's Iodine Satellite (iSAT) project; and the Space Launch System (SLS) program.

NASA's Near Earth Asteroid Scout (NEA Scout) mission must perform critical maneuvers after separating from its launch vehicle using angular rate data from an on-board inertial measuring unit (IMU). In this report, we provide a detailed description of testing and a summary of the performance characteristics of the IMU.

The author also participated in mission planning exercises for the Iodine Satellite (iSAT) project. This spacecraft is to fly on a U.S. national security mission in late 2017, manifested as a secondary payload to the primary mission.

A third program that that author contributed to was the Space Launch System (SLS) development program. This is NASA's flagship launch vehicle program that is scheduled to make its first flight in 2018.

I. Introduction: NEA Scout

THE Near Earth Asteroid Scout (NEA Scout) spacecraft is a 6U CubeSat scheduled for launch on the Space Launch System (SLS) EM-1 in 2018. The objective of the 2.5-year NEA Scout mission is to demonstrate the use of a large, 86 m^2 solar sail for primary propulsion system, to rendezvous with a near earth asteroid, and gather photographic and other scientific information such as its size and spin rate. The NEA Scout spacecraft has an onboard science camera that will be used take detailed images of the asteroid's surface features in hopes of identifying possible landing sites in support of a future manned mission to the asteroid.

The Planetary Systems Corporation's canisterized satellite dispenser (CSD) system that deploys NEA Scout from the SLS may induce rotational rates as high as 10°/sec in multiple axes. Therefore, spacecraft must perform two maneuvers that are critical to the success of the mission. The first maneuver is to detumble itself after deployment. After the NEA Scout has detumbled, it must locate the sun in order to successfully point the photovoltaic (PV) array that will be used to charge its batteries that provide power to the guidance and navigation

---

[1] 2016 Faculty Fellow, AIAA Associate Fellow, Professor of Aerospace Engineering
[2] 2016 Faculty Fellow, Associate Professor of Electrical Engineering, Arkansas Tech University.
[3] NEA Scout G&C Lead, Guidance, Navigation, & Mission Analysis (EV42), NASA-MSFC, Huntsville, AL 35812
[4] Control System Engineer, EV41, NASA-MSFC, Huntsville, AL 35812
[5] Aerospace Engineer, Guidance, Navigation, and Mission Analysis (EV42), NASA-MSFC, Huntsville, AL 35812

system, communications equipment, and scientific instruments. If these early maneuvers are not successful, the mission will likely fail. Both the detumbling and sun-pointing maneuvers use dedicated sensors to achieve the maneuvers' goals. Since the performance characteristics of these sensors have not been studied, we provide a thorough description of the characterization of the performance of the inertial measuring unit (IMU) and sun sensors in this report.

As mentioned in a companion paper by D. Bullock et al [1], the NEA Scout utilizes measurements provided by a Sensonor STIM 300 IMU [2]. This IMU is a strapdown, microelectromechanical (MEMS) system that contains a three-axis gyroscope for measuring angular rates, a three-axis accelerometer for measuring linear accelerations, and a three-axis inclinometer for measuring inclination angles. MEMS-based IMUs are typically small, lightweight, and have minimal power requirements. The STIM 300 footprint is roughly 40 mm × 45 mm × 22 mm, masses 55 grams, and consumes 1.5 watts of power. One drawback of MEMS-based IMUs is that they do suffer from a lack of sensitivity at low rotational rates and small accelerations, when compared to high precision fiber optic gyros.

In order to detumble the NEA Scout after deployment, the flight computer receives the rotational rates (which are expected to be as high as ~10°/sec per axis after ejection from the CSD system) from the IMU, and then uses a cold-gas thruster system to slow its rotation until the spacecraft is stabilized with negligible rates. One possible issue that may occur during the detumbling maneuver is that although the *initial* rotational rates are expected to be well within the capabilities of the STIM 300 IMU, as the thrusters gradually decrease the rates, they will eventually be small enough that the IMU will no longer properly sense them. At this time, rates are expected to be low enough that the NEA Scout's star tracker will be able to serve as the spacecraft's primary inertial sensor and complete the stabilization process.

II. IMU Experimental Testing

IMU Test Results

The IMU tests were conducted in the Guidance, Navigation, and Control Laboratory facility at the NASA-Marshall Space Flight Center, Huntsville, AL. The test utilized the facility's Contraves Goerz Corp. high precision three-axis rotational rate table. The three-axis rotational rate table is isolated from the building, resting on a seismic-stable concrete foundation that is separate from the building's foundation. The rate table allows the user to program angular rates of up to ±200°/sec for each axis, with an angular rate precision of ±0.00001°/sec.

The Sensonor STIM 300 IMU was attached to a custom 3D-printed mounting plate and fastened to the center of the rate table. The first setup attempted to communicate with the IMU using wiring that passed from the center of the rate table to the outside gimbal of the table. This meant passing USB signals through several meters of wiring within the arms and gimbals of the rate table. This wiring included three slip rings, each slip ring passing signals from the platform "inside" to the platform "outside" while allowing motions of the gimbals to occur. After constructing the appropriate patch cords from IMU to inner table, and from outer table to PC, communication could not be made. The resistance from outer to inner via the various slip rings was 1.75 Ω, meaning about 3.5 Ω for both sides of a USB cable. This resistance, coupled with the IMU's 0.5 amp at 5 volts required power supply through the USB interface, along with the circuitous cable routing described above, prevented USB communications from occurring.

Next, a USB-RS422 converter cable from Sensonor was used to directly communicate with the IMU. The cable incorporates FTDI's (Future Technology Devices International) FT232RQ USB to serial UART interface IC device that handles all the USB signaling and protocols [3] and provides a fast, simple way to connect the IMU module's RS422 interface to USB. The cable provides both communication and power from a recording laptop computer. To minimize cabling, the recording laptop was secured to the top of the rate table using elastic cables and elastomeric padding underneath. Data were captured and stored on a HP laptop using the Sensonor STIM 300 EVK software that allows the user to configure the IMU, as well as graphically display gyroscope, accelerometer, and inclinometer data, and export the raw data as a text file. The experimental setup is shown in Figure 1.
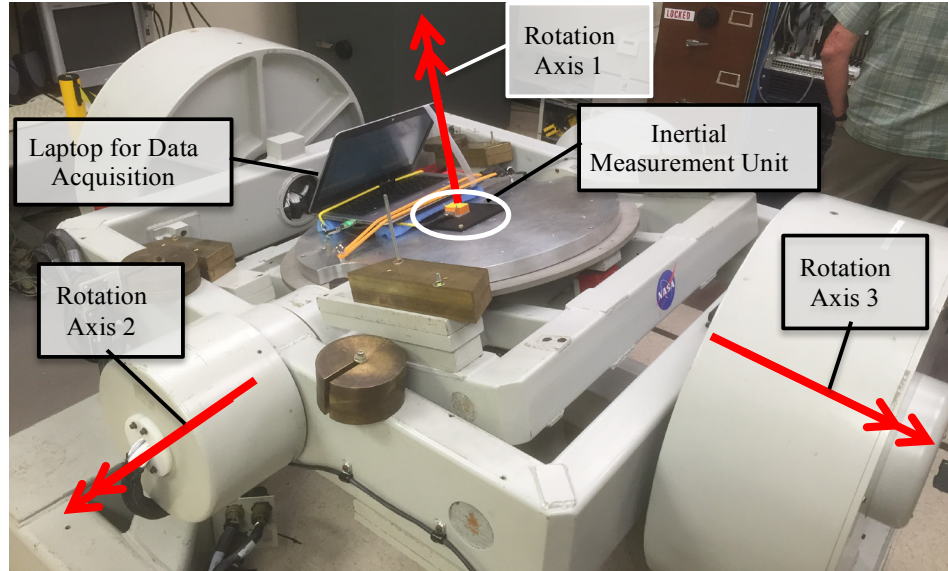
Figure 1. Experimental setup: the IMU (circled) was mounted at the center of the three-axis rate table at the Guidance, Navigation, and Control Laboratory facility, Bl. 4487, at MSFC. One, two, or three axes of the table may be actuated; table rotation axes are shown as double-headed arrows. Data were recorded by the laptop strapped to the inner circular table.

Table 1. **Sensonor STIM 300 IMU Test Matrix**

Test Name	Roll (°/sec)	Pitch (°/sec)	Yaw (°/sec)	Description	Status
1. Bias Offset, rate table locked, 10 seconds	0	0	0	Measure mounting misalignment	Complete
2. Run-to-Run Bias: Power cycle IMU 20 times, operate 10 sec each cycle.	0	0	0	Measure run-to-run bias by cycling power.	Complete
3. Static test, 60 minutes, rate table locked				Long run to measure bias.	Complete
4. Detumble – Roll positive direction	+10	0	0		Complete
5. Detumble – Roll negative direction	−10	0	0		Complete
6. Detumble – Pitch positive direction	0	+10	0	Measure IMU performance at tumbling rate, single axis.	Complete
7. Detumble – Pitch negative direction	0	−10	0		Complete
8. Detumble – Yaw positive direction	0	0	+10		Complete
9. Detumble – Yaw negative direction	0	0	−10		Pending
10. Detumble – roll + pitch axes simultaneously	10	10	0	90 sec duration	Pending
11. Detumble – roll + yaw axes simultaneously	10	0	10	90 sec duration	Pending
12. Detumble – Pitch + yaw simultaneously	0	10	10	90 sec duration	Pending
13. Detumble – roll+pitch+yaw simultaneously	10	10	10	90 sec duration	Pending
14. Detumble – (-roll-pitch-yaw) simultaneously	−10	−10	−10	90 sec duration	Pending
15. Minimum spacecraft slew rate – Roll	0.01	0	0	Measure IMU performance at the minimum slew rate.	Complete
16. Minimum spacecraft slew rate – Pitch	0	0.01	0		Complete
17. Minimum spacecraft slew rate – Yaw	0	0	0.01		Complete
18. Max slew rate before sail deployment, Roll	0.04	0	0	Measure IMU performance at the maximum slew rate after solar sail deployment.	Complete
19. Max slew rate before sail deployment, Pitch	0	0.04	0		Complete
20. Max slew rate before sail deployment, Yaw	0	0	0.04		Data lost
21. Max slew rate with sail deployed – Roll	1	0	0	Performance at max SS slew rate.	Complete
22. Max slew rate with sail deployed – Pitch	0	1	0		Complete
23. Max slew rate with sail deployed – Yaw	0	0	1		Complete
24. Min rate for navigational stability – Roll	0.0001	0	0	Measure IMU performance at the minimum slew rate for navigational stability.	Pending
25. Min rate for navigational stability – Pitch	0	0.0001	0		Pending
26. Min rate for navigational stability – Yaw	0	0	0.0001		Pending

A number of tests were planned in order to measure the performance characteristics of the IMU under rotational rates similar to those that are anticipated during the NEA Scout mission. The testing matrix, shown in Table 1, describes the battery of tests that was designed, and their status at the time of this writing. Proposed testing included tests for bias, run-to-run bias repeatability, and IMU sensitivity at slew rates that are expected to be experienced by the NEA Scout spacecraft. Additional tests were also designed to measure the IMU's performance characteristics during multi-axis rotations and to measure the IMU's sensitivity at the minimum and maximum expected slew rates

for the spacecraft in its two configurations: stowed and deployed solar sail. Further tests were also designed to test the IMU's performance during multi-axis rotation.

For each test, carried out at room-temperature ambient conditions, the data collection system was configured to collect three axes of gyroscope, accelerometer, and inclinometer data at a rate of 125 sets of data per second, the minimum allowed by the Sensonor STIM 300 EVK software.

To measure the IMU bias, two tests were performed. First, the device was placed on a static rate table and data were collected from the IMU for 10 seconds, after which the IMU's power was cycled off and then on. Another bias test was performed for a one-hour duration. Subsequent testing measured the run-to-run bias repeatability.

III.   Results

IMU Test Results

As indicated in the table, the testing that was completed provided a wealth of data regarding the bias, run-to-run bias repeatability, and sensitivity at operational slew rates. A description of the test data obtained is provided below. The preliminary analysis of the data and some conclusions are presented in the following section.

Figure 2 shows the data taken during Test 1, a ten-second run under ambient (no rotation) conditions. To perform this test, the IMU's power was cycled and data were taken on the stationary rate table for 10 seconds after the system was rebooted (note the STIM 300 reboot time is specified to be 0.3 seconds).
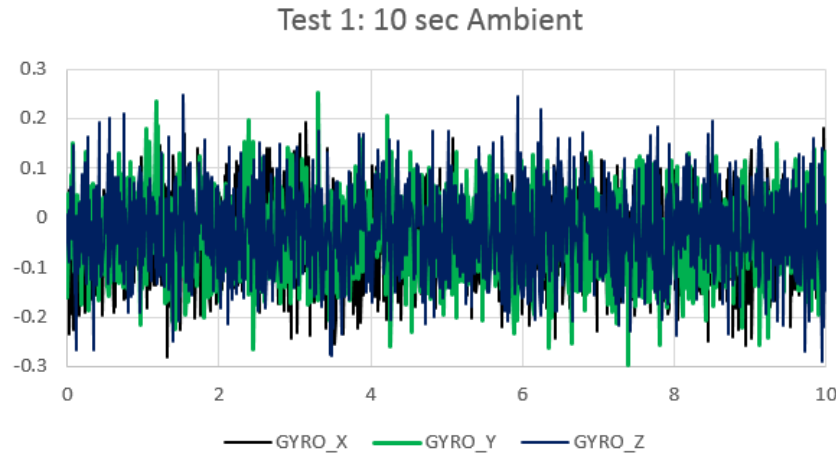
Figure 2. Data obtained from the IMU's gyros during a ten-second period with rate table not rotating.

Test 2 consisted of twenty repetitions of runs similar to Test 1, where the ten-second run under ambient conditions was repeated in order to obtain an adequate sample size to provide run-to-run bias repeatability. The measured data plots were similar to those presented in Figure 2 and will not be shown here.

Figure 3 shows the data taken during Test 3, a one hour (3600 second) run under ambient (no rotation) conditions.
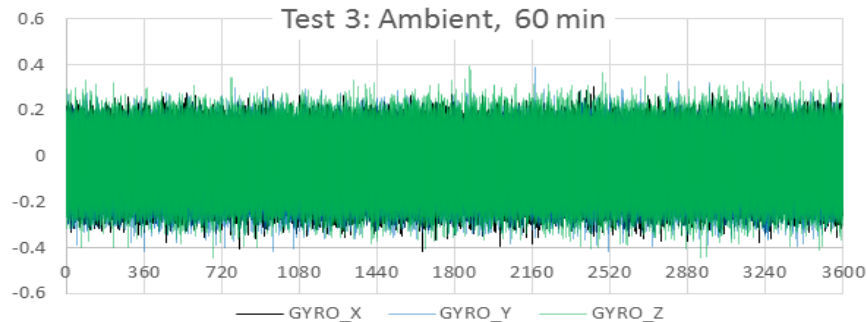
Figure 3. Data obtained from the IMU's gyros during a 60-minute period with no rotation of rate table.

Test 4 was the first application of defined table motion. Here a rate of 10° per second was applied to the IMU, and data were taken for 60 seconds. Figure 4 shows the data recorded, which confirm the prescribed rate being felt by the X-gyro, and no rate being felt by the Y- and Z-gyros.
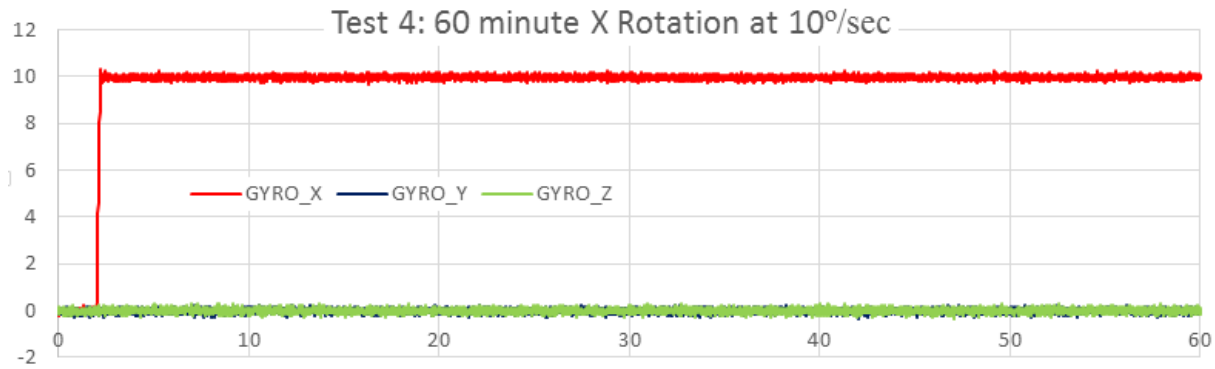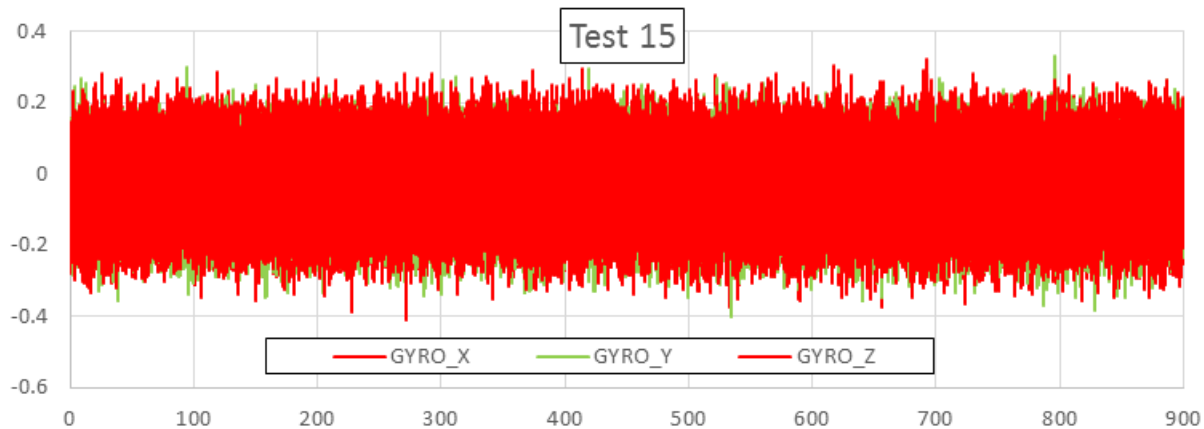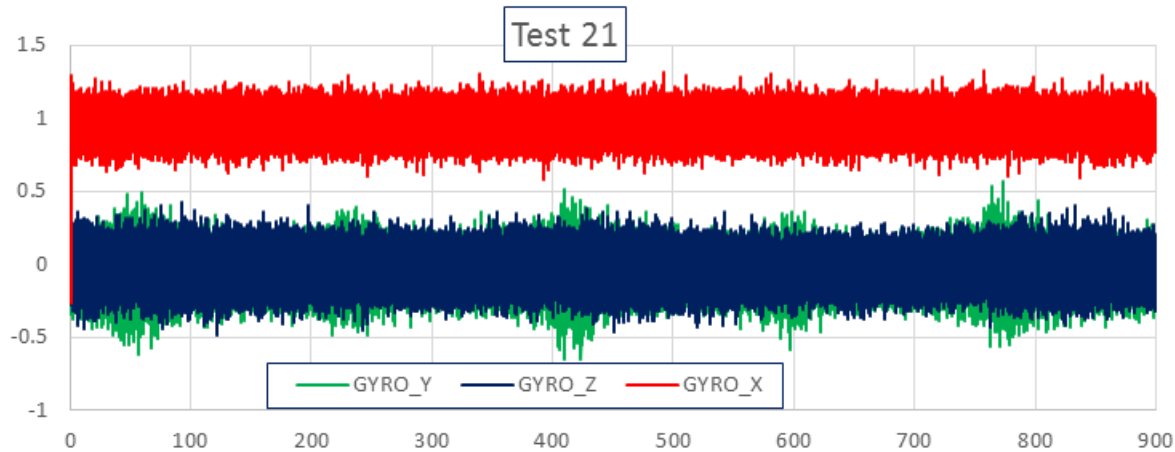
Figure 4. Test 4 provided data from the IMU's gyros during a 60 minute period with rate table rotating at +10°/second in the X-axis. Tests 5 – 9 provided data for similar rotations in the –X, ±Y, and Z directions.

During Tests 5, 6, 7, 8, and 9, the applied rotation tests were repeated with –X rotation, +Y and –Y rotations, and +Z and –Z rotations. The measured data resembled those shown in Figure 4 and will not be shown here.

Tests 10 through 14 were not executed due to difficulties with multiple simultaneous rotation axes on the rotation table.

Tests 15 through 20 provided a simulation of the environment at lower rotation rates. The first three tests, nos. 15, 16, and 17, were at the expected minimum slew rate of 0.01°/second. Test 15 is shown in Figure 5, with 0.01°/second rotation in the gyro-X direction. Tests 16 and 17 were the same rate about the gyro-Y and –Z directions.

Figure 5. Test 15 provided data from the IMU's gyros during a 15 minute period with rate table rotating at +0.01°/second in the X-axis. Tests 16 – 20 provided data for similar rotations in the –X, ±Y, and ±Z directions.

The second three tests, 18, 19, and 20 were at an applied rate of 0.04°/second, to simulate the predicted maximum slewing rate with the solar sail deployed.

Tests 21-23 imposed a rotation rate of 1°/second in the three gyro directions. Figure 6 shows the recorded data for Test 21, rotation at 1°/second about the Gyro-X direction. Tests 22 and 23 repeated this for the –Y and –Z directions, and will not be shown here as they are very similar to Figure 6.

102

Figure 5. Test 15 provided data from the IMU's gyros during a 15 minute period with rate table rotating at +0.01°/second in the X-axis. Tests 16 – 20 provided data for similar rotations in the –X, ±Y, and ±Z directions.

Referring to Figure 5, the reader may have noticed an increased level of "noise" in the green trace, which represents gyro-Y measurements, while the IMU is rotating at 1°/sec about the gyro-X direction (red trace). This noise is not steady and only appears during certain periods of the time history. To look further into this, the plots of accelerations from the IMU taken during the same test are shown in Figure 6. Because the higher noise levels seem to correspond only to orientations of the rate table (apparently around ±45° rotation about the Y and Z directions), it seems possible that particular orientations of rate table may provide increased rotational "noise," perhaps due to the gravitational preload provided by the weight of its gimbals on its gear trains, or something similar.
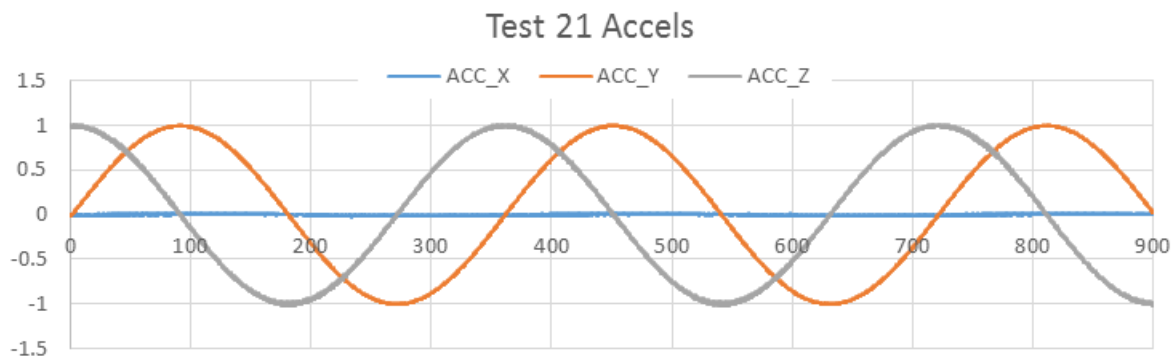
Figure 6. The accelerations measured during test 15 indicates that the position of the rate table may provide increased noise in certain positions. The noise appears to increase when both Y and Z positions are in the vicinity of ±45° slant at times of approximately 50, 230, 410, 590, and 760 seconds after start.

IV. Discussion

In the following section, we discuss the data and provide numeric in summary tables. Test 1 indicates that the gyros in the IMU have a noise level that is significant. The results shown in Table 2 indicate that the standard deviation in the ambient measurements is enough to mask rotation rates on the order of a third of a degree per second. This is not surprising for an IMU that is intended to measure rotational rates in the hundreds of degrees per second. Therefore, one conclusion that can be made is that the IMU rate measurements will not be helpful for nulling out rotational rates that are relatively small. In order to deal with such motions, another measurement scheme will be needed. It has been suggested that the NEA Scout's star sensor will be able to operate fast enough to help damp out the lower rotational rates without using the IMU.

Table 2. Averaged Results from Test 1 of IMU Unit

Test 1: Ten Sec, Ambient	Gyro X	Gyro Y	Gyro Z
Average	-0.0470	-0.0388	-0.0253
Standard Deviation	0.0785	0.0788	0.0845

As mentioned earlier, Test 2 was a compilation of ten-second runs taken at ambient conditions. The procedure was to turn the IMU's power on, take ten second of data, turn power off, and repeat. The variation of the average values and the standard deviations would give an idea of the repeatability of the IMU's operation under repeated power cycling. The data obtained are provided in Table 3.

Table 3. Data from 21 Runs during Test 2

Run #	Average for Gyro X	Average for Gyro Y	Average for Gyro Z	Run #	Average for Gyro X	Average for Gyro Y	Average for Gyro Z
1	-0.04807	-0.05141	-0.03339	12	-0.04444	-0.04416	-0.03531
2	-0.03953	-0.04785	-0.03175	13	-0.04812	-0.04405	-0.03061
3	-0.04461	-0.04599	-0.03316	14	-0.04522	-0.04771	-0.02666
4	-0.04497	-0.04634	-0.03098	15	-0.04584	-0.04303	-0.03421
5	-0.04220	-0.04567	-0.03292	16	-0.04574	-0.04070	-0.02704
6	-0.04811	-0.05037	-0.03223	17	-0.04092	-0.04991	-0.03752
7	-0.04181	-0.04804	-0.03363	18	-0.04581	-0.04409	-0.03455
8	-0.04255	-0.04709	-0.03302	19	-0.04663	-0.04386	-0.03569
9	-0.04603	-0.04680	-0.02886	20	-0.04409	-0.04627	-0.03312
10	-0.04444	-0.04854	-0.03664	21	-0.04348	-0.04988	-0.03112
11	-0.04626	-0.04758	-0.03143				

Next, we took the data from Table 3 and considered the average of the average values for gyro-X, gyro-Y, and gyro-Z. These data are shown in Table 4. In addition, we calculated the standard deviation of the averages listed in Table 3. A small value for these standard deviations would indicate that the IMU's sensitivity would be stable despite repeated on-off cycles. Since the multi-run standard deviations of the individual averages are a factor of twenty or more less than the single-run standard deviations, the IMU's sensitivity can be concluded to be consistent and stable.

Table 4. Averaged Data from 21 Runs in Table 3

	Gyro X	Gyro Y	Gyro Z
Average	-0.0447	-0.0466	-0.0326
Standard Deviation	0.0023	0.0026	0.0027

The results from numerical analysis of Test 3, shown in Figure 3, are provided in Table 5. Averages and standard deviations are close to those in Tests 1 and 2, indicating temporal stability. In addition, we plotted moving averages of the data, sampling 50 samples behind and ahead, and still the data showed randomness.

Table 5. **Averaged Results Over 60 Minutes from Test 3 of IMU Unit**

Test 3: 60 minutes, ambient	Gyro X	Gyro Y	Gyro Z
Average	-0.044	-0.047	-0.030
Standard Deviation	0.078	0.081	0.088

Tests 4 through 8 data analyses are summarized in Table 6. Now we see that the magnitude of the moving axes (shown as gray shading in the table) is able to discern the rotational motion, since the magnitude of the 10°/second rotational rate signals is well above the standard deviation. This indicates that the IMU will be useful to provide the signals needed to de-tumble the spacecraft, at least at the higher rates expected at the beginning of the ejection maneuver.

Table 6. Summary of ±10°/sec Rotational Testing (rotating direction shaded yellow)

±10°/s Testing	X output average (Standard dev.)	Y output average (Standard dev.)	Z output average (Standard dev.)
Rotate about X	9.975/-10.07 (0.081/0.080)	-0.026/-0.075 (0.084/0.082)	-0.01/-0.061 (0.093/0.104)
Rotate about Y	0.041/-0.111 (0.081/0.079)	9.970/-10.068 (0.084/0.086)	-0.015/-0.057 (0.104/0.108)
Rotate about Z	-0.068/-0.017 (0.079/0.079)	-0.067/-0.031 (0.081/0.082)	9.978/-10.042 (0.109/0.106)

Tests 15 through 20 provide imposed rotation rates of 0.01 and 0.04°/second. It is clear that the high ambient noise level, as demonstrated by the calculated standard deviations of the data, that the IMU cannot resolve these

lower rotation rates from the noise present. The data are summarized in Table 7, where again the direction with the non-zero rotation rate is shaded gray.

Table 7. Summary of ±0.01°/sec Rotational Testing (rotating direction shaded yellow; -Z not tested)

±0.01°/s Testing	X output average (Standard dev.)	Y output average (Standard dev.)	Z output average (Standard dev.)
Rotate about X	0.034/-0.042 (0.077/0.079)	-0.043/-0.055 (0.080/0.081)	-0.034/-0.033 (0.086/0.088)
Rotate about Y	-0.042/-0.002 (0.082/0.079)	-0.045 /-0.045 (0.093/0.081)	-0.022/-0.032 (0.101/0.096)
Rotate about Z (-Z not tested)	-0.042/NA (0.080/NA)	-0.086/NA (0.082/NA)	-0.032/NA (0.093/NA)

Run 21-23 calculations are provided in Table 8. The 1° per second rotation rate is large enough to be visible over the ambient noise, as shown by the figures in the shaded areas of the table versus the non-shaded ones.

Table 8. Summary of 1°/sec Rate Rotational Testing (rotating direction shaded yellow)

1°/s Testing	X output average (Standard dev.)	Y output average (Standard dev.)	Z output average (Standard dev.)
Rotate about X	0.959 (0.084)	-0.055 (0.115)	-0.031 (0.104)
Rotate about Y	-0.048 (0.080)	-1.015 (*0.195*)	-0.035 (0.107)
Rotate about Z	-0.042 (0.081)	-0.046 (0.086)	0.968 (0.105)

As shown in the right-hand column of Table 1, many of the planned tests were completed. However, due to difficulties with operation of the rate table, not all of the proposed tests were completed. The authors hoped to complete the remainder of the testing when the rate table became functional again. According to the point-of-contact for the lab, the timeline for repair may be several months, so a completion date is not known at the time of this writing.

The IMU data generated from the rate-table tests will help in characterizing the performance of the device while undergoing rotational rates similar to those that the NEA Scout will experience. The data will yield some important error constants that relate to bias, bias instability, and random walk noise that will be used in a Simulink/MATLAB® model of the IMU currently under development. Additionally, the STIM 300 is scheduled to fly on another mission to the International Space Station (ISS), and the data gathered from the rate-table tests will be shared with the group planning the latter mission.

V. Space Launch System

Space Launch System Description

NASA's Space Launch System, or SLS, is its newest heavy-lift launch vehicle, designed to provide human and heavy cargo transportation to space, including both Earth orbit and missions to the Moon, nearby asteroids, and beyond. Shown in Fig. 7, the Core Stage, main engines, and solid rocket boosters are derived from heritage Space Transportation System (STS, or Space Shuttle) hardware. The Interim Cryogenic Propulsion Stage is derived from a United Launch Alliance (ULA) Delta Cryogenic Second Stage (DCSS), and the remaining hardware is newly developed.

SLS Analytical Model Development

The SLS program currently does not plan to carry out an "all-up" dynamic test. Such a test is normally used to obtain whole-vehicle natural vibration characteristics, which are critical to the design of its flight control system, because control inputs at the engines can interfere destructively with the flexibility in the structure. Instead of an all-up test, the program plans to implement the 'building block' approach in which all of its major components (the solid rocket boosters, the core stage, the upper stage, etc.) are tested individually.

SLS Uncertainty Study

Because of uncertainties in the modeling of these components as well as the conditions at the joints or interfaces between them, the program has begun a statistical study wherein the inertial and/or elastic properties are randomly varied within a range of ±20%, and the resulting variations in all-up model structural frequencies are obtained. By executing a sufficient number of the statistical variations, it is possible to show that the probability of any

unexpected variations causing a control-structure interaction problem is minimally small, and gain confidence that the component testing method is adequate even in the presence of the uncertainties mentioned earlier. For the case of the SLS program, a total of 2000 cases with random statistical variations in 20 different inertial + elastic parameters has been run, and the resulting frequencies and mode shapes recorded. What remains is a means to evaluate the mode shapes' sensitivities to the 20 variables.
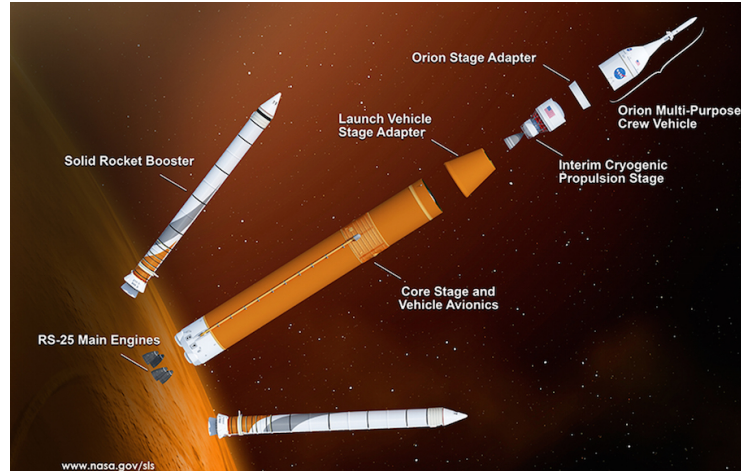

Figure 7. NASA's Space Launch System has many components that are derived from the retired Space Shuttle program, including its main engines, external tank, and solid rocket boosters. Courtesy NASA.

A MATLAB® toolbox program to handle this problem, fitChiSquare.m, was found online and appears to be able to perform this estimation [4]. The SLS team needs to provide the raw data (which includes the variation in synthetically-assembled structural parameters) to get the needed sensitivity parameters. The routine appears suitable to accept all 2000 SLS parameter variation cases and the resulting frequency data variations, and will estimate the best chi-square fit for the data and provide an estimate of all 20 sensitivity derivatives and their uncertainty as its results.

The principal author is not proficient with MATLAB®, and neither his NASA-supplied PC nor his campus PC was able to run the program. The data analysis will therefore have to wait until the NASA SLS organization is able to supply a specialist to carry out the data reduction.

The principal author also researched the structural modeling techniques used to couple small support structure to the main structure for the SLS vehicle. The research revealed an apparent error in the modeling of the isogrid structure used for tank and adaptor walls – rather than using the entire composite plate properties (outside sheet metal combined with the isogrid ribs), the report [5] only documented the milled-out ribbed portion of the isogrid, apparently omitting the outside sheet metal. After some investigation, it was determined that the analysis had been done correctly, however those responsible for documentation had omitted the outside sheet metal's properties from their report – but not from the actual modeling effort.

VI. Iodine Satellite Work

iSAT Description

The use of iodine propellant for Hall thrusters has been studied due to the potential mission benefits over xenon. In 2013, MSFC selected a project to demonstrate an iodine flight propulsion system through its Technology Investment Program. The spacecraft, launched as a secondary payload on a national security mission, is intended to demonstrate the efficacy of iodine propulsion by using it as a main propulsion system to lower its orbital periapsis and end the mission by atmospheric entry. The use of iodine as a propellant has many advantages over the traditional xenon gas, including a reduction of up to 80% of mass and volume.

The Iodine Satellite (iSAT) spacecraft is a 12U CubeSat manifested for launch as a secondary payload on a U.S. National Reconnaissance Office Falcon 9 flight scheduled for fall 2017 [6]. Its one-year mission objectives are to operate its iodine propulsion system in low Earth orbit and use the system's retro-thrust (thrust in the negative orbital velocity direction) to hasten orbit's decay, as well as to gather orbital information using GPS tracking data to estimate thrust and quantify the iodine propulsion system's propulsive performance. Its goal is to reach an orbital altitude that allows a 90 day decay of orbital operations, causing the iSAT to ultimately burn up in the Earth's atmosphere. A view of the design for iSAT and its internal components are shown in Fig. 8.
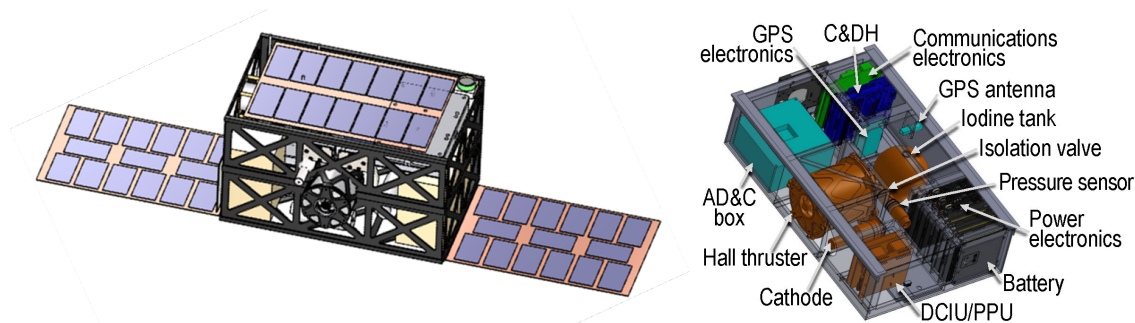
Figure 8. NASA's iSAT will demonstrate a 200 W iodine electric thruster in its compact 12U CubeSAT envelope. Courtesy NASA.

The iSAT's mission is complicated by its compact design and geometry. Its small size and mass limits the size of solar arrays that can power the spacecraft. Since the iodine engine consumes 200 watts (a considerable amount of power for such a small spacecraft), the spacecraft must spend a significant amount of time with the solar arrays aligned perpendicular to the sun's direction vector to recharge the batteries. Since that direction is not generally the same as the orbital velocity vector, the spacecraft must alternate between a sun-pointing attitude and a retro-orbit attitude. In addition, the spacecraft must periodically download its collected information to a ground station. This provides a third pointing requirement, making mission operations somewhat complex.

iSAT Mission Planning

Author DE was tasked with assisting in mission planning and in verification and validation, both associated with the planned iSAT control system hardware and software. The mission planning involved determination and specification of the spacecraft's operational modes and each mode's associated orbital attitude (with respect to sun vector and velocity vector), control system operational mode, as well as what type of operations would be happening (thrusting using the iodine thruster, battery charging via solar array, communicating with ground, etc.).

Verification and validation, or V&V, is important in that it provides a means of checking many aspects of a system's operation before flight. For this, author DE revised and outlined some changes to a draft V&V plan to better carry out a complete review of the iSAT's control system development, including software, hardware, simulation, and testing.

Acknowledgments

References

[1] Bullock, D., et al, **Performance Characterization of Sun Sensor and Inertial Measuring Unit for the Near Earth Asteroid Scout Mission**, Summer 2016 Faculty Fellow Session, submitted Aug. 2016, to be published.

[2] Sensonor, "STIM300 Inertia Measurement Unit," STIM300 datasheet, Oct. 2015 [TS1524 rev.20].

[3] Sensonor, "User Manual STIM210/STIM300 Evaluation Kit," manual, 2015 [DOK412 rev.0].

[4] MATLAB® software toolbox "fitChiSquare.m," available on-line (accessed 27 August 2016) from
https://www.mathworks.com/matlabcentral/fileexchange/9592-generalized-nonlinear-non-analytic-chi-square-fitting/content/fitChiSquare.m

[5] Report SLS-RPT-233-01, **Space Launch System (SLS) Loads Analysis Report Volume 1: Block 1 Finite Element Models**, 31 Aug. 2012 (ITAR-controlled)

[6] Retrieved 05 Sept. 2016 from
http://www.nasa.gov/directorates/spacetech/small_spacecraft/iodine_satellite.html

Vision-Based Small Satellite Formation Control - A Feasibility Analysis

Farbod Fahimi[*]

University of Alabama in Huntsville, Huntsville, AL 35899

During the 10-week faculty fellowship of the author, a vision based formation and attitude controller has been derived and simulated for the formation keeping of two 3U CubeSats. Four markers are installed on the leader CubeSat. Two cameras are installed on the follower CubeSat. The Mirage vision based pose estimation method, originally developed by the author's research team, is used to estimate the pose of the follower CubeSat with respect to the leader CubeSat. A Higher-Order Sliding Mode (HOSM) exact differentiator with finite-time convergence is derived to estimate the rate of the follower's pose parameters. The follower's pose and its time rate are fedback to HOSM formation and attitude controllers to correct any gradual drift in formation and pose of the follower. The simulations show the effectiveness of the approaches. It is worthy to note that, for the purpose of certification, equivalent gain and phase margins can be found for HOSM controllers.

I. Introduction

NASA Goddard Space Flight Center has been studying and designing and testing tools that enable the use of constellations of nano or micro satellites [1]. There are several projects at NASA that can strongly benefit from the utilization of multiple satellites in orbit. Examples of these projects are: Global Precipitation Measurement (GPM) Constellation, Leonardo-BRDF, GPS Occultation Constellation, Magnetospheric Constellation, Global Ionosphere-Thermosphere-Mesosphere (ITM) Constellation, and so on [1].

Conventionally, single satellites have been used to carry out different missions. A single satellite has to carry all the needed internal components and sensors for a successful mission. That is why single satellites are normally large and heavy and expensive to launch. Also, if one of the so many components on the single satellite fails, the whole satellite can be rendered useless.

A new approach is using multiple cooperative satellites, also known as constellation of satellites. Each satellite of the constellation can be smaller and carry part of the sensors and needed instruments. They are lighter and less expensive to launch, and if one satellite fails it can be replaced with less cost. However, using multiple satellites creates new challenges in formation flying, GN&C (Guidance, Navigation, and Control), remote sensors, communications, and inter-satellite ranging.

Close and accurate formation flying is one of the challenges of realization of constellation of satellites. For some applications, the accuracy of GPS position and velocity measurements are not adequate for close formation flying. Also, more accurate and robust control methodologies are required to control the formation correction maneuvers.

In this research, to address the GN&C needs of close formation flying of small satellites, a vision based control methodology combined with robust Higher-Order Sliding Mode (HOSM) controllers is explored. In the following, a vision based pose estimation method, originally developed by the author's research team at UAH, is briefly introduced. Then, a HOSM exact differentiator with finite-time convergence is explained. Next, a HOSM formation controller and a HOSM attitude controller are presented. Finally, the vision system is integrated with the controllers and the performance of the whole system is shown via simulations.

II. Mirage Vision Based Pose Estimation Method - A Summary

The leader and follower CubeSats are shown in Fig. 1. There are two poses shown for the follower. One (on the left) is the desired position of the follower CubeSat with respect to the leader CubeSat. The *desired pose* of the follower is represented by a spatial frame $\{f^d\}$. However, the follower has drifted away from its desired pose with respect to the leader. The *actual pose* of the follower after the drift is denoted by a spatial frame $\{f\}$.

Note that the desired pose of the follower with respect to the leader CubeSat is defined by a user. Therefore, the 4×4 homogeneous transformation matrix $\mathbf{T}_r^{f^d}$ between the frames $\{f^d\}$ and $\{r\}$ is known. If one can determine
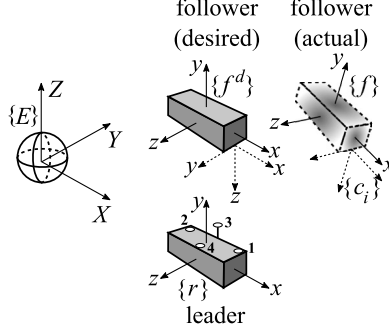
Figure 1. The leader and follower CubeSats with body frames

the transformation between the frames $\{f\}$ and $\{f^d\}$ (i.e., the 4×4 matrix $\mathbf{T}_{f^d}^f$), then, the actual relative pose of the follower $\{f\}$ with respect to the leader $\{r\}$ can be determined by the following simple transformation.

$$\mathbf{T}_f^r = (\mathbf{T}_{f^d}^f \mathbf{T}_r^{f^d})^{-1} \tag{1}$$

The Mirage pose estimation method directly calculates the elements of matrix $\mathbf{T}_{f^d}^f$ via an analytical linear non-iterative solution, when two cameras are used.

The calculation of $\mathbf{T}_{f^d}^f$ involves the comparison of two images: the *desired image* and the *actual image*, which are defined in the following. Four non-planar markers (with known geometry) are installed on the leader (Fig. 1). Two cameras are installed on the follower, but only one of them, represented by frame $\{c_i\}$, is shown in Fig. 1. The camera $\{c_i\}$ ($i = 1, 2$) generates images of the markers. The image seen by the camera when the follower is at its desired pose is called the *desired image*. On the other hand, the image that the camera sees when the follower is in its actual pose is called the *actual image*.

The difference in the pixel coordinates of marker j ($j = 1, ..., 4$) in the actual and desired images of camera c_i ($i = 1, 2$) is a function of $\mathbf{T}_{f^d}^f$. This difference in pixel coordinates is denoted by the following equation.

$$\mathbf{e}_j^{c_i} = \begin{bmatrix} x_{p_j} - x_{p_j}^d \\ y_{p_j} - y_{p_j}^d \end{bmatrix}_{c_i} \tag{2}$$

where (x_{p_j}, y_{p_j}) and $(x_{p_j}^d, y_{p_j}^d)$ are the pixel coordinates of marker j in camera i in the actual and desired image, respectively. Note that both pixel coordinates are known, therefore, the pixel error $\mathbf{e}_j^{c_i}$ is known. If a relation between the pixel error $\mathbf{e}_j^{c_i}$ and the transformation matrix $\mathbf{T}_{f^d}^f$ is established, that relation can be used to solve for the elements of $\mathbf{T}_{f^d}^f$. The derivation of such a relation is explained in the following.

First, the *actual* and the *desired* 3D projection of marker j in the camera space $\{c_i\}$ are denoted.

$$(\mathbf{p}_{c_i})_j = \begin{bmatrix} p_{c_i x} \\ p_{c_i y} \\ p_{c_i z} \end{bmatrix}_j \quad , \quad (\mathbf{p}_{c_i}^d)_j = \begin{bmatrix} p_{c_i x}^d \\ p_{c_i y}^d \\ p_{c_i z}^d \end{bmatrix}_j \tag{3}$$

The pixel error $\mathbf{e}_j^{c_i}$ can be calculated based on the coordinates in the 3D camera space.

$$\mathbf{e}_j^{c_i} = \begin{bmatrix} x_{p_j} - x_{p_j}^d \\ y_{p_j} - y_{p_j}^d \end{bmatrix}_{c_i} = \begin{bmatrix} \frac{p_{c_i x}}{p_{c_i z}} - \frac{p_{c_i x}^d}{p_{c_i z}^d} \\ \frac{p_{c_i y}}{p_{c_i z}} - \frac{p_{c_i y}^d}{p_{c_i z}^d} \end{bmatrix}_j = \begin{bmatrix} \frac{p_{c_i x} p_{c_i z}^d - p_{c_i x}^d p_{c_i z}}{p_{c_i z} p_{c_i z}^d} \\ \frac{p_{c_i y} p_{c_i z}^d - p_{c_i y}^d p_{c_i z}}{p_{c_i z} p_{c_i z}^d} \end{bmatrix}_j \tag{4}$$

The components of $(\mathbf{p}_{c_i})_j$ and $(\mathbf{p}_{c_i}^d)_j$ in Eq. (4) are related to the Euclidean position of marker j. This relation is derived in the following.

The *known* Euclidean position vector of marker j with respect to the origin of $\{r\}$ is denoted by $(\mathbf{r}_r)_j = [r_x, r_y, r_z, 1]_j^T$. The *actual* 3D projection of marker j in the camera space $(\mathbf{p}_{c_i})_j$ is found by a series of transformation applied to the vector $\mathbf{r}_r$.

$$(\mathbf{p}_{c_i})_j = \mathbf{K}_{c_i} \mathbf{T}_f^{c_i} \mathbf{T}_r^f (\mathbf{r}_r)_j \tag{5}$$

where the 4×4 matrix $\mathbf{T}_f^{c_i}$ transforms any vector from frame $\{f\}$ to frame $\{c_i\}$, and the 3×4 matrix $\mathbf{K}_{c_i}$ contains the intrinsic camera parameters (focal length, principle points and distortion parameters), which are available a priori via camera calibration. Similarly, for the *desired* 3D projection of marker j in the camera space $(\mathbf{p}_{c_i}^d)_j$ is written.

$$(\mathbf{p}_{c_i}^d)_j = \mathbf{K}_{c_i} \mathbf{T}_{f^d}^{c_i} \mathbf{T}_r^{f^d} (\mathbf{r}_r)_j \tag{6}$$

Equation (5) is rewritten by incorporating the fact that $\mathbf{T}_r^f = \mathbf{T}_{f^d}^f \mathbf{T}_r^{f^d}$ and $\mathbf{T}_f^{c_i} = \mathbf{T}_{f^d}^{c_i}$.

$$(\mathbf{p}_{c_i})_j = \mathbf{K}_{c_i} \mathbf{T}_f^{c_i} \mathbf{T}_{f^d}^f \mathbf{T}_r^{f^d} (\mathbf{r}_r)_j \tag{7}$$

Note that there are no unknowns in Eq. (6) and the only unknowns in Eq. (7) are the *twelve* elements of the matrix $\mathbf{T}_{f^d}^f$.

$$\mathbf{T}_{f^d}^f = \begin{bmatrix} t_1 & t_4 & t_7 & t_{10} \\ t_2 & t_5 & t_8 & t_{11} \\ t_3 & t_6 & t_9 & t_{12} \\ 0 & 0 & 0 & 1 \end{bmatrix} \tag{8}$$

Equation (8) is substituted in Eq. (7). The result of the substitution and Eq. (6) are expanded to obtain the components of $(\mathbf{p}_{c_i})_j$ and $(\mathbf{p}_{c_i}^d)_j$. The resulting components are substituted in Eq. (4). After very involved manipulations, which can be found in [2], the following relation is found between the pixel error $\mathbf{e}_j^{c_i}$ and the elements of $\mathbf{T}_{f^d}^f$.

$$\mathbf{e}_j^{c_i} = \mathbf{V}_j^{c_i} \mathbf{t}_{f^d}^f + \mathbf{Y}_j^{c_i} \tag{9}$$

where $\mathbf{V}^{c_i}$ is a 2×12 matrix and $\mathbf{Y}^{c_i}$ is a 2×1 vector with known values. For the detailed formulation of these parameters, see [2]. The 12×1 vector $\mathbf{t}_{f^d}^f$ contains all 12 unknown elements of the transformation matrix $\mathbf{T}_{f^d}^f$.

$$\mathbf{t}_{f^d}^f = [t_1, t_2, t_3, t_4, t_5, t_6, t_7, t_8, t_9, t_{10}, t_{11}, t_{12}]^T \tag{10}$$

Note that Eq. (9) includes 2 equations and 12 unknowns and cannot be solved it its current form. However, this equation is valid for camera c_i ($i = 1, 2$) and marker j ($j = 1, ..., 4$). Therefore, Eq. (9) can be easily rewritten for a combination of cameras and markers, which add more to the number of equations. In the following, the usage and solution procedure for this equation is explained for the dual-camera case with 4 markers.

For this case, Eq. (9) is written 8 times, covering the combinations of 2 cameras c_1 and c_2 and 4 markers.

$$\begin{bmatrix} \mathbf{e}_1^{c_1} \\ \mathbf{e}_2^{c_1} \\ \mathbf{e}_3^{c_1} \\ \mathbf{e}_4^{c_1} \\ \mathbf{e}_1^{c_2} \\ \mathbf{e}_2^{c_2} \\ \mathbf{e}_3^{c_2} \\ \mathbf{e}_4^{c_2} \end{bmatrix} = \begin{bmatrix} \mathbf{V}_1^{c_1} \\ \mathbf{V}_2^{c_1} \\ \mathbf{V}_3^{c_1} \\ \mathbf{V}_4^{c_1} \\ \mathbf{V}_1^{c_2} \\ \mathbf{V}_2^{c_2} \\ \mathbf{V}_3^{c_2} \\ \mathbf{V}_4^{c_2} \end{bmatrix} \mathbf{t}_{f^d}^f + \begin{bmatrix} \mathbf{Y}_1^{c_1} \\ \mathbf{Y}_2^{c_1} \\ \mathbf{Y}_3^{c_1} \\ \mathbf{Y}_4^{c_1} \\ \mathbf{Y}_1^{c_2} \\ \mathbf{Y}_2^{c_2} \\ \mathbf{Y}_3^{c_2} \\ \mathbf{Y}_4^{c_2} \end{bmatrix}, \quad \text{or} \quad \mathbf{e} = \mathbf{V} \mathbf{t}_{f^d}^f + \mathbf{Y} \tag{11}$$

Equation (11) forms a linear system of 16 equations in terms of 12 unknown elements of $\mathbf{t}_{f^d}^f$, which can be easily solved in the Least-Square sense.

$$\mathbf{t}_{f^d}^f = (\mathbf{V}^T \mathbf{V})^{-1} (\mathbf{V}^T (\mathbf{e} - \mathbf{Y})) \tag{12}$$

Now that the vector $\mathbf{t}_{f^d}^f$ is calculated, the transformation matrix $\mathbf{T}_{f^d}^f$ is found. Next, this matrix is used to calculate the pose of the follower satellite ($\mathbf{q} = [x, y, z]^T$ and $\mathbf{\Phi} = [\phi, \theta, \psi]^T$).

III.   Higher-Order Sliding Mode Differentiator

The pose vector $\mathbf{Q} = [\mathbf{q}, \mathbf{\Phi}]^T$ is not sufficient for feedback control. The rate of the pose vector $\dot{\mathbf{q}}$ is also required. The conventional differentiators provide asymptotic convergence. When the rate of a vector changes rapidly with time, the asymptotic convergence causes a phase lag, which is not good for robust control.

Here a Higher-Order Sliding Model (HOSM) differentiator is introduced that provides *finite-time* (as opposed to asymptotic) convergence to the *exact* derivative (in the absence of measurement noise). The HOSM differentiator is obtained as follows.

The time variable measured signal $\mathbf{Q}(t)$ is considered. It is desired to calculate $\dot{\mathbf{Q}}(t)$ in real-time. A real-time estimate of the measured signal is defined as $\tilde{\mathbf{Q}}(t)$. At any given time the estimation error is defined.

$$\mathbf{y}_Q = \tilde{\mathbf{Q}}(t) - \mathbf{Q}(t) \tag{13}$$

The derivative of the estimation error is given as follows.

$$\dot{\mathbf{y}}_Q = \dot{\tilde{\mathbf{Q}}} - \dot{\mathbf{Q}} \tag{14}$$

The rate of the estimated measurement $\dot{\tilde{\mathbf{Q}}}$ is considered as a control input that affects the dynamics of the estimation error $\mathbf{y}_Q$.

$$\mathbf{v} = \dot{\tilde{\mathbf{Q}}} \tag{15}$$

Therefore, the dynamics of the estimation error is obtained.

$$\dot{\mathbf{y}}_Q = -\dot{\mathbf{Q}} + \mathbf{v} \tag{16}$$

A control law for $\mathbf{v}$ is desired such that it can drive both $\mathbf{y}_Q$ and $\dot{\mathbf{y}}_Q$ to zero in finite-time. If both $\mathbf{y}_Q$ and $\dot{\mathbf{y}}_Q$ are driven to zero in finite-time, then, $\tilde{\mathbf{Q}} \to \mathbf{Q}$ and $\dot{\tilde{\mathbf{Q}}} \to \dot{\mathbf{Q}}$, at which point the exact derivative of $\mathbf{Q}$ is obtained.

The following control law achieves the goal.

$$\mathbf{v} = \lambda_1 \,\mathrm{sign}(\tilde{\mathbf{Q}} - \mathbf{Q})^T |\tilde{\mathbf{Q}} - \mathbf{Q}|^{\frac{1}{2}} + \mathbf{q}_1 \tag{17}$$

with

$$\dot{\mathbf{q}}_1 = -\lambda_2 \,\mathrm{sign}(\tilde{\mathbf{Q}} - \mathbf{Q}) \tag{18}$$

The differentiator is used as follows. The initial value of the measured signal $\mathbf{Q}(0)$ is known. The initial value of the estimated measured signal is set to $\tilde{\mathbf{Q}}(0) = \mathbf{Q}(0)$. The control signals $\mathbf{q}_1$ and $\mathbf{v}$ are found by integrating Eq. (18) and calculating Eq. (17), respectively. The control signal $\mathbf{v}$ is applied to the dynamic system in Eq. (15), which is integrated to obtain $\tilde{\mathbf{Q}}$. The obtained $\tilde{\mathbf{Q}}$ is fedback for control in Eqs. (17) and (18), and the process continues in time. In the meantime, the control signal $\mathbf{v}$ is the estimated derivative of the measured signal.

IV. HOSM Formation Controller

A. Governing equations of the leader-follower relative motion

The coordinate axes shown in Fig. 1 are considered. Let $\mathbf{x}_r^r$ and $\mathbf{x}_f^r$ denote the position of the leader and the follower satellites with respect to the geocentric system (X, Y, Z), but expressed along the moving axes (x, y, z) at the location of the leader satellite. Note that axes $x, y,$ and z are radial, along track, and cross-track directions, respectively, defined by Hill and used in [3]. The acceleration of the follower satellite can be written in terms of the acceleration of the leader satellite.

$$\ddot{\mathbf{x}}_f^r = \ddot{\mathbf{x}}_r^r + \dot{\boldsymbol{\omega}}_r^r \times \mathbf{q} + \boldsymbol{\omega}_r^r \times (\boldsymbol{\omega}_r^r \times \mathbf{q}) + 2\boldsymbol{\omega}_r^r \times \dot{\mathbf{q}} + \ddot{\mathbf{q}} \tag{19}$$

where $\mathbf{q}$ is the relative distance of the follower with respect to the leader along the moving axes (x, y, z), and $\boldsymbol{\omega}_r^r$ is the instantaneous rate of rotation of the leader around the Earth.

Here, *to achieve a precise formation, the relative position of the follower with respect to the leader* will be controlled. Therefore, the dynamic equations of motion must be written as a relation between $\ddot{\mathbf{q}}$ and the control forces from the follower's thrusters $\mathbf{u}_f$.

It is known that the effect of $\mathbf{u}_f$ on the acceleration of the follower $\ddot{\mathbf{x}}_f^r$ is described by the follower's equation of the motion.

$$m_f \ddot{\mathbf{x}}_f^r = \mathbf{F}_{Ef}^r - \mathbf{F}_{fr}^r + \mathbf{u}_f^r + \mathbf{F}_{df}^r \tag{20}$$

In this equation, m_f is the mass of the follower satellite; $\mathbf{F}_{Ef}^r$ is the pulling force from the Earth on the follower satellite; $\mathbf{F}_{fr}^r$ is the pulling force from the follower satellite on the leader satellite; and $\mathbf{F}_{df}^r$ is the resultant perturbing forces on the follower satellite. All vectors have a superscript r, which indicates that they are written along the axes of the moving coordinate (x, y, z). For the derivation of the controller, the "nominal" situation is used, in which the resultant perturbing forces on the follower satellite are neglected ($\mathbf{F}_{df}^r = \mathbf{0}$) and the nominal mass of the satellite is used ($\hat{m}_f$).

Equation (20) is substituted in Eq. (19), and the result is solved for $\ddot{\mathbf{q}}$. The following is obtained

$$\ddot{\mathbf{q}} = \hat{\mathbf{f}}_x + \hat{b}_x \mathbf{u}_f^r \tag{21}$$

where

$$\hat{\mathbf{f}}_x = -(\ddot{\mathbf{x}}_r^r + \dot{\boldsymbol{\omega}}_r^r \times \mathbf{q} + \boldsymbol{\omega}_r^r \times (\boldsymbol{\omega}_r^r \times \mathbf{q}) + 2\boldsymbol{\omega}_r^r \times \dot{\mathbf{q}}) + (\hat{\mathbf{F}}_{Ef}^r - \hat{\mathbf{F}}_{fr}^r)/\hat{m}_f, \quad \hat{b}_x = 1/\hat{m}_f \tag{22}$$

in which $\hat{\mathbf{F}}_{Ef}^r$ and $\hat{\mathbf{F}}_{fr}^r$ are calculated using $\hat{m}_f$.

Equation (21) describes the direct effect of the follower's thrust $\mathbf{u}_f^r$ on the relative motion of the follower with respect to the leader ($\mathbf{q}$). This equation will be used for derivation of the formation controller.

B. Implementation notes

A controller that is derived based on Eq. (21) will need the measurement of the realtime acceleration of the leader ($\ddot{\mathbf{x}}_r^r$), the relative position of the follower with respect to the leader ($\mathbf{q}$), and its rate ($\dot{\mathbf{q}}$). The acceleration $\ddot{\mathbf{x}}_r^r$ can be measured by an accelerometer on board of the leader satellite, and can be broadcast to the follower satellite. The relative position $\mathbf{q}$ can be measured by the vision system, and its rate $\dot{\mathbf{q}}$ can be observed by the HOSM differentiator.

C. The HOSM control law

Higher-Order Sliding Mode (HOSM) controllers have the same features of conventional sliding mode controllers, without the potential for chattering. Here, since the equation of relative motion (21) is a second-order equation, a second-order sliding mode (also known as 2-sliding mode) controller is derived. The methodology is presented in detail in [4] and [5]. Here, the final result of the derivations are presented for this particular application to formation control.

First, the control problem is defined as follows. The second-order nominal system (21) is rewritten as follows.

$$\ddot{\mathbf{q}} = \hat{\mathbf{f}}_x + \hat{b}_x \mathbf{u}_f^r \tag{23}$$
$$\mathbf{y} = \mathbf{q} - \mathbf{q}^d \tag{24}$$

In these equations, $\mathbf{y}$ is the controller output, and $\mathbf{q}^d$ is the user-defined desired relative distance between the leader and follower satellites in the formation. A 2-sliding control law for $\mathbf{u}_f^r$ must be derived to take and hold $\mathbf{y}$ and $\dot{\mathbf{y}}$ to zero vectors in finite time.

The controller also needs to address the uncertainty in the dynamic parameters of the system and the bounded external disturbances. The uncertain system has the following form

$$\ddot{\mathbf{q}} = \mathbf{f}_x + b_x \mathbf{u}_f^r \tag{25}$$

where

$$\mathbf{f}_x = -(\ddot{\mathbf{x}}_r^r + \dot{\boldsymbol{\omega}}_r^r \times \mathbf{q} + \boldsymbol{\omega}_r^r \times (\boldsymbol{\omega}_r^r \times \mathbf{q}) + 2\boldsymbol{\omega}_r^r \times \dot{\mathbf{q}}) + (\mathbf{F}_{Ef}^r - \mathbf{F}_{fr}^r + \mathbf{F}_{fd}^r)/m_f, \quad b_x = 1/m_f \tag{26}$$

Here, m_f is the real (unknown) mass of the satellite and $\mathbf{F}_{fd}^r$ is the unknown external disturbance.

The HOSM control law that covers uncertainty in the system is as follows.

$$\mathbf{u}_f^r = \hat{b}_x^{-1}(-(\hat{\mathbf{f}}_x - \ddot{\mathbf{q}}^d) + \hat{\mathbf{w}} + \tilde{\mathbf{w}}) \tag{27}$$

The term $\hat{\mathbf{w}}$ is called "the nominal control," whose components are calculated as follows.

$$\hat{w}_j = -\sum_{i=1}^{2} k_{ij} \, \text{sign}(z_{ij})|z_{ij}|^{v_{ij}}, \quad j = 1, 2, 3 \tag{28}$$

In the above equations, $v_{1j} = 3/5$ and $v_{2j} = 3/4$. The control gains k_{ij} are found such that the following characteristic polynomial is Hurwitz.

$$p^2 + k_{2j}p + k_{1j} = 0, \quad j = 1, 2, 3 \tag{29}$$

For the purpose of the formation control, a critically damped system, with different natural frequencies (rate of approach) has been used. In that case, the control gains are selected as

$$k_{2j} = 2\zeta\omega_n, \quad k_{1j} = \omega_n^2 \tag{30}$$

where $\zeta = 1$ and ω_n takes different values during tunning of the controller. And z_{ij} ($i = 1, 2$ and $j = 1, 2, 3$) are the components of the following vectors.

$$\mathbf{z}_1 = \mathbf{q} - \mathbf{q}^d \tag{31}$$
$$\mathbf{z}_2 = \dot{\mathbf{q}} - \dot{\mathbf{q}}^d \tag{32}$$

The term $\tilde{\mathbf{w}}$ in Eq. (27) is calculated as shown below.

$$\tilde{\mathbf{w}} = -G \operatorname{sign}(\mathbf{s}) \tag{33}$$

where

$$\mathbf{s} = \mathbf{z}_2 + \mathbf{z}_{\text{aux}} \tag{34}$$

and $\dot{\mathbf{z}}_{\text{aux}} = -\hat{\mathbf{w}}$. The gain G must satisfy the following condition [4].

$$G \geq \frac{(1 - \alpha)\|\hat{\mathbf{w}}\| + \rho + \eta}{\alpha} \tag{35}$$

where $\eta > 0$ and ρ and α, the bounds of uncertainty, are defined using the following relations.

$$\|\tilde{\mathbf{f}}_x - \tilde{b}_x \hat{b}_x^{-1}(\hat{\mathbf{f}}_x - \ddot{\mathbf{q}}^d)\| \leq \rho \tag{36}$$

$$\|\tilde{b}_x \hat{b}_x^{-1}\| \leq 1 - \alpha \tag{37}$$

In the above equations, $\tilde{\mathbf{f}}_x$ and $\tilde{b}_x$ define the difference between the nominal and uncertain systems.

$$\tilde{\mathbf{f}}_x = \mathbf{f}_x - \hat{\mathbf{f}}_x \tag{38}$$

$$\tilde{b}_x = b_x - \hat{b}_x \tag{39}$$

V. HOSM Attitude Controller

A. The rotational dynamic model

Equations (40) and (41) are the complete dynamic model of the CubeSat and reaction wheels as a system. At any simulation step, the reaction wheel driving moments are known. One can calculate the CubeSat's angular acceleration vector $\dot{\boldsymbol{\omega}}_B$ using Eq. (40). Also, the reaction wheel driving moments and the CubeSat's angular acceleration vector $\dot{\boldsymbol{\omega}}_B$ just obtained from Eq. (40) can be used with Eq. (41) to calculate the reaction wheel's angular acceleration $(\ddot{\theta}_1, \ddot{\theta}_2, \ddot{\theta}_3)$. Integrating these angular accelerations will provide $\boldsymbol{\omega}_B$ and $(\dot{\theta}_1, \dot{\theta}_2, \dot{\theta}_3)$ for the next time step. The integration can go on by repeating the above steps.

$$(\mathbf{I}_B + \sum_{i=1}^{3} \mathbf{B}_i \mathbf{I}_i)\dot{\boldsymbol{\omega}}_B = \begin{bmatrix} \tau_{1x} \\ \tau_{2y} \\ \tau_{3z} \end{bmatrix} - \boldsymbol{\omega}_B \times \mathbf{I}_B \boldsymbol{\omega}_B - \sum_{i=1}^{3} \mathbf{B}_i(\boldsymbol{\omega}_B \times \mathbf{I}_i \boldsymbol{\omega}_i) + \boldsymbol{\tau}_D \tag{40}$$

$$\begin{bmatrix} I_{1xx}\ddot{\theta}_1 \\ I_{2yy}\ddot{\theta}_2 \\ I_{3zz}\ddot{\theta}_3 \end{bmatrix} = - \begin{bmatrix} \tau_{1x} \\ \tau_{2y} \\ \tau_{3z} \end{bmatrix} - \sum_{i=1}^{3} \mathbf{A}_i(\mathbf{I}_i \dot{\boldsymbol{\omega}}_B + \boldsymbol{\omega}_B \times \mathbf{I}_i \boldsymbol{\omega}_i) \tag{41}$$

B. The HOSM control law

For control derivations, Eq. (40) is matched with the following kinematic equation.

$$\dot{\boldsymbol{\Phi}} = \begin{bmatrix} 1 & \sin\phi \tan\theta & \cos\phi \tan\theta \\ 0 & \cos\phi & \sin\phi \\ 0 & \sin\phi \sec\theta & \cos\phi \sec\theta \end{bmatrix} \boldsymbol{\omega}_B, \quad \dot{\boldsymbol{\Phi}} = \mathbf{E}\boldsymbol{\omega}_B \tag{42}$$

where $\boldsymbol{\Phi} = [\phi, \theta, \psi]^T$ contains the roll, pitch, and yaw angles, respectively. The following form of Eq. (40) is written that is useful for control derivation: $\dot{\boldsymbol{\omega}}_B = \hat{\mathbf{f}} + \hat{\mathbf{b}}\boldsymbol{\tau}$, where $\boldsymbol{\tau} = [\tau_{1x}, \tau_{2y}, \tau_{3z}]^T$, and

$$\hat{\mathbf{b}} = (\hat{\mathbf{I}}_B + \sum_{i=1}^{3} \mathbf{B}_i \hat{\mathbf{I}}_i)^{-1} \tag{43}$$

$$\hat{\mathbf{f}} = -(\hat{\mathbf{I}}_B + \sum_{i=1}^{3} \mathbf{B}_i \hat{\mathbf{I}}_i)^{-1}(\boldsymbol{\omega}_B \times \hat{\mathbf{I}}_B \boldsymbol{\omega}_B + \sum_{i=1}^{3} \mathbf{B}_i(\boldsymbol{\omega}_B \times \hat{\mathbf{I}}_i \boldsymbol{\omega}_i)) \tag{44}$$

are calculated using the "nominal" values of the system parameters. On the other hand, $\mathbf{b}$ and $\mathbf{f}$ will have the same form as the above equations, except they represent the real (unknown) dynamic parameters of the system.

The following notation are adopted: $\hat{\mathbf{A}} = \mathbf{E}\hat{\mathbf{f}} + \dot{\mathbf{E}}\boldsymbol{\omega}_B - \ddot{\boldsymbol{\Phi}}^d$ and $\hat{\mathbf{B}} = \mathbf{E}\hat{\mathbf{b}}$, $\mathbf{A} = \mathbf{E}\mathbf{f} + \dot{\mathbf{E}}\boldsymbol{\omega}_B - \ddot{\boldsymbol{\Phi}}^d$ and $\mathbf{B} = \mathbf{E}\mathbf{b}$. With these notations, the controller described by Eqs. (27) to (39) will also work for the attitude control, provided that $\hat{\mathbf{f}}_x - \ddot{\mathbf{q}}^d$ is replaced by $\hat{\mathbf{A}}$, $\hat{b}_x$ is replaced by $\hat{\mathbf{B}}$, $\mathbf{f}_x - \ddot{\mathbf{q}}^d$ is replaced by $\mathbf{A}$, b_x is replaced by $\mathbf{B}$, and $\mathbf{u}_f^r$ is replaced by $\boldsymbol{\tau}$. Also,

$$\mathbf{z}_1 = \boldsymbol{\Phi} - \boldsymbol{\Phi}^d, \quad \mathbf{z}_2 = \mathbf{E}\boldsymbol{\omega}_B - \dot{\boldsymbol{\Phi}}^d \tag{45}$$

VI. Implementation of the Vision-Based Formation and Attitude Control

The HOSM formation controller and the HOSM attitude controller, derived and presented in the previous reports, are combined with the Mirage vision based pose estimation method described in this report. The block diagram of the whole system is shown in Fig. 2. The part of the system that is simulated is shown in red. In the real implementation, the red blocks are replaced by the actual system. All outputs of the red blocks must be provided by sensors installed on the CubeSats. All inputs to the red blocks are applied to the actuators of the real follower CubeSat.

The black blocks in Fig. 2 are the code defining the desired formation, Mirage vision based pose estimation, HOSM differentiator, HOSM formation controller, and HOSM attitude controller. This part must be compiled and executed in real-time on the follower CubeSat's embedded computer. All inputs to the black blocks must be provided by sensors. All outputs of the black blocks must be connected to the actuators on the follower CubeSat.

The block "simulated camera" calculates the "actual pixel coordinates" of the marker j ($j = 1, ..., 4$) using the simulated pose of the follower CubeSat. First, the matrix $\mathbf{T}_r^f$ is calculated.

$$\mathbf{T}_f^r = \left[\begin{array}{c|c} \mathbf{R}_z(\psi)\mathbf{R}_y(\theta)\mathbf{R}_x(\phi) & \begin{array}{c} x \\ y \\ z \end{array} \\ \hline 0 \quad 0 \quad 0 & 1 \end{array} \right], \quad \mathbf{T}_r^f = (\mathbf{T}_f^r)^{-1} \tag{46}$$

Then, the *actual* 3D projection of marker j in the camera space is found using Eq. (5). Finally, the simulated pixel coordinates are obtained as follows.

$$\begin{bmatrix} x_{p_j} \\ y_{p_j} \end{bmatrix}_{c_i} = \begin{bmatrix} \frac{p_{c_i x}}{p_{c_i z}} \\ \frac{p_{c_i y}}{p_{c_i z}} \end{bmatrix}_j \tag{47}$$
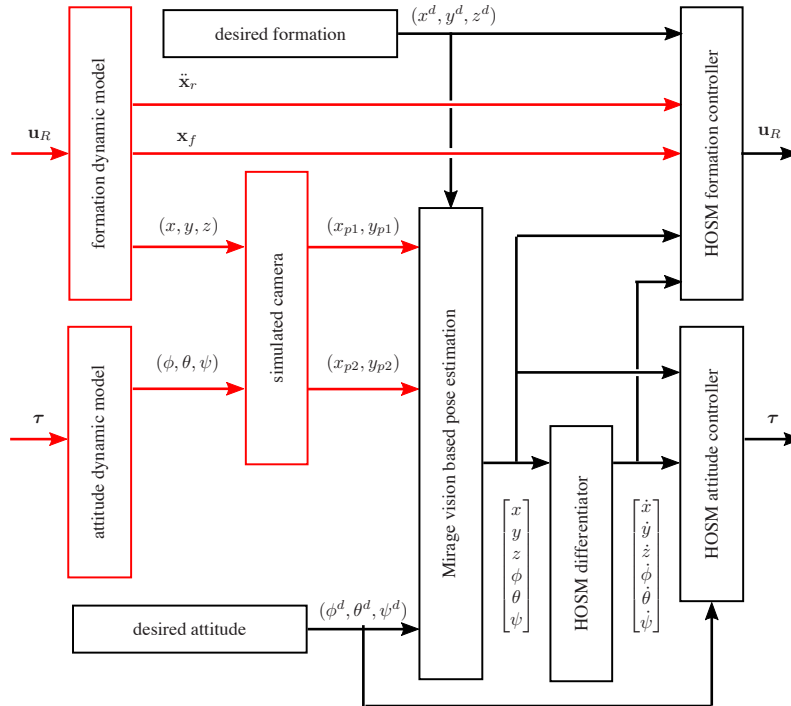
Figure 2. Block diagram of the vision based formation control implementation

VII.   Results

An in-track formation is assumed for the simulations. The desired orientation of the follower CubeSat is defined to be parallel to that of the leader CubeSat. In other words, the desired roll, pitch, yaw of the leader with respect to the follower are all zeros ($\phi^d = \theta^d = \psi^d = 0°$). However, a desired separation of $y^d = -5$ m along the y direction of the follower CubeSat is assumed, while $x^d = z^d = 0$ m.

It is assumed that when the formation/attitude correction is turned on, the follower CubeSat has an orientation defined by $\phi(0) = 5°, \theta(0) = 5°$, and $\psi(0) = -5°$. Also, it is assumed that the follower has drifted 0.5 m away in the y direction from its desired position with respect to the leader CubeSat. Therefore, $x(0) = 0$ m, $y(0) = 5.5$ m, and $z(0) = 0$ m.
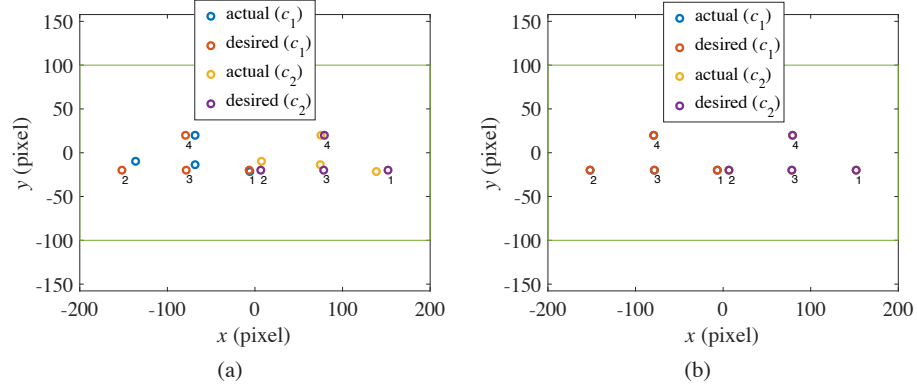
Figure 3. (a) The images of the markers in the cameras at the beginning of the simulation. (b) The images of the markers in the cameras at the end of the simulation

The images of the leader's markers in the follower's cameras at the beginning of the simulation, when the follower is not at the desired formation, are shown in Fig. 3a. It can be seen that the actual image, calculated by the simulated cameras, is different from the desired image, calculated by the internals of the Mirage vision based pose estimation algorithm. This is because at the start of the simulation, the follower CubeSat is not at the desired formation location.

The images of the leader's markers in the follower's cameras at the end of the simulation, when the follower reaches its desired formation, are shown in Fig. 3b. It can be seen that the actual image, calculated by the simulated cameras, coincides with the desired image, calculated by the internals of the Mirage vision based pose estimation algorithm. This is because at the end of the simulation, the follower CubeSat is exactly at the desired formation location.
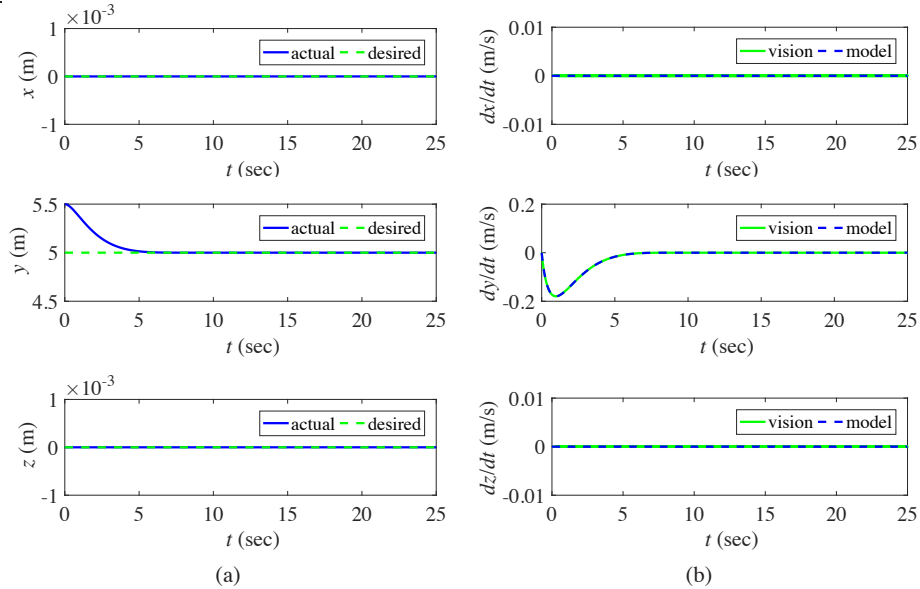
Figure 4. (a) Relative position components. (b) Relative velocity components.

The relative position components of the follower CubeSat with respect to the leader CubeSat are shown in Fig. 4a. It can be seen that the x and z components start and remain at their desired value of zero meters. The y component, which needed correction, goes from 5.5 m to the desired value of 5 m.

Figure 4b shows the velocity components of the follower CubeSat with respect to the leader CubeSat. The curves labeled "model" are the velocities that are calculated by the "formation dynamic model." The model is not part of the real world implementation and is only used for simulation purposes. The curves labeled "vision" are the output of the HOSM differentiator that calculates the numerical derivative of the vision based estimated pose. This is the signal that is used for feedback in the simulations, and must be used for feedback in the real implementation.

Figure 4b shows that the velocity estimated by the HOSM differentiator from "vision" aligns *exactly* with the simulated values by the "formation dynamic model" beginning from time zero. To achieve convergence from time zero, a correct initial condition for the differentiator must be used (see section III).

(a) (b)
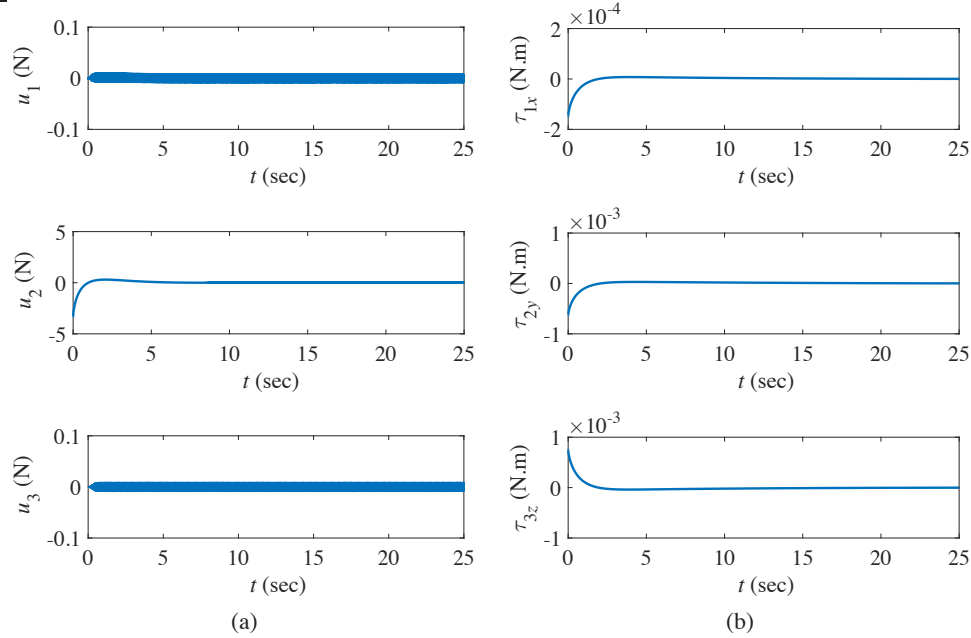
Figure 5. (a) Follower's thrust components along the radial, along track, and across track axes. (b) The follower's reaction wheel torques.

The thrust components of the follower CubeSat during the formation correction maneuver are shown in Fig. 5a. There is a small chattering in the thrust components. Figure 5b shows the torques of the follower CubeSat's reaction wheels during the attitude correction maneuver. No chattering is evident in the torques of the reaction wheels. The curves are comparable in magnitude and profile with the ones obtained in previous reports, in which the relative pose and angular velocity were fedback directly from the "attitude dynamic model."

The relative pose components of the follower CubeSat with respect to the leader CubeSat are shown in Fig. 6a. It can be seen that all components start with a $5°$ error in pose. They converge to their desired values of zero degrees. Figure 6b shows the rate of roll, pitch, and yaw angles of the follower CubeSat with respect to the leader CubeSat. The curves labeled "model" are the rates that are calculated by the "attitude dynamic model." The model is not part of the real world implementation and is only used for simulation purposes. The curves labeled "vision" are the output of the HOSM differentiator that calculates the numerical derivative of the vision based estimated pose. This is the signal that is used for feedback in the simulations, and must be used for feedback in the real implementation.

Figure 6b shows that the Euler angle rates estimated by the HOSM differentiator from "vision" aligns *exactly* with the simulated values by the "attitude dynamic model" beginning from time zero. To achieve convergence from time zero, a correct initial condition for the differentiator must be used (see section III).

VIII.   Conclusions

During the 10-week faculty fellowship of the author, a vision based formation and attitude controller has been derived and simulated for the formation keeping of two 3U CubeSats. The simulations show the effectiveness of the approaches.
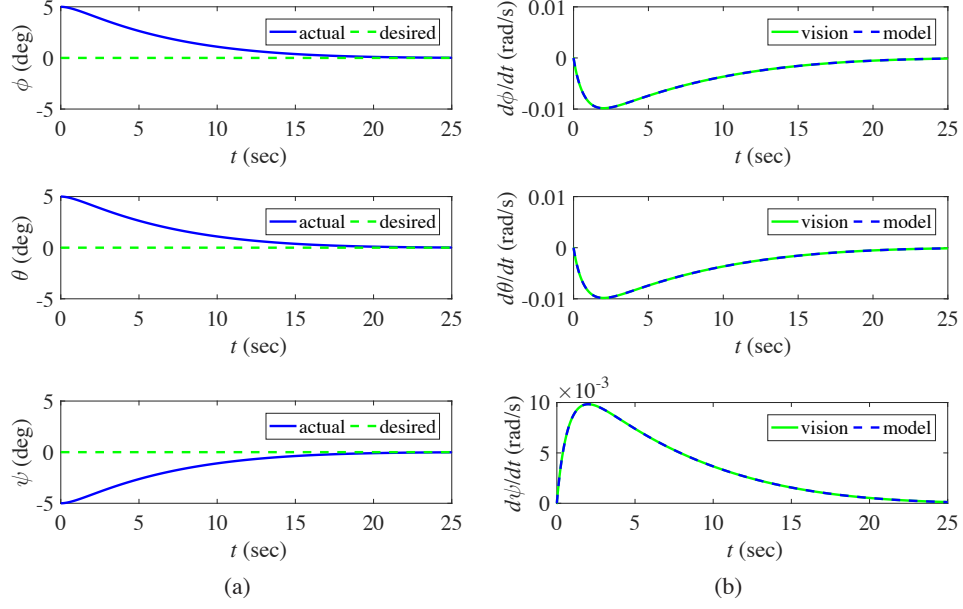
116

Figure 6. (a) Relative pose components. (b) Relative pose components' derivative.

Acknowledgements

References

[1] Esper, J., Neeck, S., Slavin, J. A., Leitner, J., Wiscombe, W., and Bauer, F. H., "Nano/micro satellite constellations for Earth and space science," *Acta Astronautica*, Vol. 52, No. 9-12, 2003, pp. 785 – 791.

[2] Dinc, S., *Mirage: A $O(n)$ time analytical multi-camera pose estimation method with application to trajectory tracking problem*, Ph.D. thesis, The Department of Computer Science, University of Alabama in Huntsville, Huntsville, AL 35899, July 2016.

[3] Sabol, C., Burns, R., and McLaughlin, C. A., "Satellite Formation Flying Design and Evolution," *Journal of Spacecraft and Rockets*, Vol. 38, No. 2, 2001, pp. 270 – 278.

[4] Defoort, M., Floquet, T., Kokosy, A., and Perruquetti, W., "A novel higher order sliding mode control scheme," *Systems and Control Letters*, Vol. 58, No. 2, 2009, pp. 102 – 108.

[5] Barbot, J. P. and Perruguetti, W., editors, *Sliding Mode Control in Engineering*, Technology & Engineering, CRC Press, New York, NY, January 2002, pp. 53 - 101.

Modeling of Inductive Coupling for Close-Proximity, Wireless Sensors

Aaron D. Mazzeo[1]
Rutgers University, Piscataway, NJ 08812, USA
Marshall Space Flight Center, Huntsville, AL 35811, USA

Patrick V. Hull[2]
Marshall Space Flight Center, Huntsville, AL 35811, USA

This paper describes general principles and a simulation-based methodology for designing and modeling inductive coils for close-proximity, wireless sensors. Measurements of impedance on a reading coil are dependent on the mutual inductance between the reading coil and a sensing coil, along with changes in electrical impedance of a battery-less, wireless sensing unit. The mutual inductance depends on both the relative position/orientation between the coils and the frequency of applied electrical power. By simulating and understanding the factors affecting mutual inductance, it will be possible to calibrate and obtain accurate measurements between a reading coil and a mounted/embedded sensing coil. The objective of this report is to document and describe a methodology for modeling and quantifying the inductive behavior between coils. The included results demonstrate how to simulate the frequency-dependent self-inductance of a single loop, mutual inductance between coaxial loops, and mutual inductance between parallel, non-coaxial loops. Comparisons to quasi-static analytical expressions also provide confidence in the described methodology, which is capable of modeling arbitrary geometries and configurations without closed-form solutions. Further efforts are necessary to improve accuracy at high frequencies and verify the methodology experimentally, but advances in simulation and optimization are paving paths toward reliable modeling of close-proximity, wireless sensing systems. Reliable modeling techniques for inductive coupling will facilitate future opportunities in structural health monitoring with intermittent and/or continuous, non-contact measurements.

I. Introduction

Inductive coupling traces its origins back to the early discoveries in electromagnetism by Faraday, Lorentz, and Maxwell. In simple terms, this coupling involves driving a wire/coil with an electrical current, which results in an oscillating magnetic field surrounding a primary wire/coil. When a secondary wire/coil is brought into close proximity of the oscillating magnetic field, there is the induction of an electromotive force (voltage) in the secondary wire/coil. The most common example is that of a transformer, which is used to step down or step up the alternating potential between a source and a load based on the square of the ratio of the number of turns in a primary coil to the number of turns in the secondary coil.

Our preliminary work on wireless structural health monitoring at the Marshall Space Flight Center uses inductive coupling with similarities to previous efforts in the academic literature[1–7]. Nonetheless, we have noticed a lack of concise, relevant background for how one might begin to model and simulate the mutual inductance between primary and secondary coils. In an effort to guide someone new to the design of inductive coupling-based sensors, we present this report. Its goal is to introduce a useful simulation-based approach that aligns well with classic analytical expressions in the literature and also represents a platform that can handle arbitrary geometries and configuration outside the scope of simple, closed-formed solutions.

---

[1] Assistant Professor, Department of Mechanical and Aerospace Engineering, Rutgers University
   Marshall Space Flight Center Faculty Fellow, ES21, Building 4487, Marshall Space Flight Center
[2] Technical Assistant, ES21, Building 4487, Marshall Space Flight Center

II. Modeling

There are many commercial and open-source packages that use finite element analysis (FEA) to solve partial differential equations numerically. For this work, we use COMSOL with the AC/DC module and online documentation[8], but the techniques we describe should be generalizable and applicable to other FEA packages. To develop confidence in the simulated results, we begin modeling simple cases and compare the results to analytical expressions. Then, we gradually progress to advanced cases that do not necessarily have straightforward analytical expressions.

A. B Field along the Vertical Axis of a Magnetostatic Loop

To start, we first model the simple case of a single loop of wire with a DC current running through it. We prescribe the radius of the loop R and consider the magnitude of the magnetic field (magnetic flux density) along an orthonormal axis running through the center of the loop. Using the Biot-Savart law, the magnetic flux density has the following analytical expression for its magnitude along this vertical axis[9,10]:

$$B = \mu_0 i R^2 / \left[2(z^2 + R^2)^{3/2}\right], \tag{1}$$

where z is the distance above the plane of the loop, μ_0 is the permeability of free space or $4\pi \cdot 10^{-7}$ H/m, and i is the current running through the loop.

To model this simple system using finite element analysis, our software solves the following pair of partial differential equations:

$$\begin{aligned}\nabla \times \mathbf{H} &= \mathbf{J} \\ \mathbf{B} &= \nabla \times \mathbf{A}\end{aligned}, \tag{2}$$

where $\mathbf{H}$ is the magnetic field intensity, $\mathbf{B}$ is the magnetic flux density and is proportional to $\mathbf{H}$ based on the permeability of the material, $\mathbf{J}$ is the current density, and $\mathbf{A}$ is the magnetic vector potential. With a static, imposed current, Figure 1 shows the resulting magnitude of the magnetic flux density and agreement with the analytical expression shown in Equation 1 for the field going through the center of the loop. For this case, the radius of the loop R was 10 mm, the diameter of the wire was 1 mm, and the vertical distance away from the plane containing the loop was z.

B. Self-inductance of a Single Loop

We often associate inductance with oscillating current, but it is also possible to describe inductance in terms of stored magnetic energy:

$$E_{mf} = Li^2/2, \tag{3}$$

where E_{mf} is the stored magnetic energy and L is the inductance. For the magnetostatic case shown in Figure 1, the calculated inductance was 42 nH with the 3D FEA-based model. Using an approximate solution, it is possible to estimate the inductance in a single loop in air with the following[11]:

$$L_{loop} \approx R\mu_0[\ln(8R/a) - 1.75], \tag{4}$$

where a is the radius of the wire. Using Equation 4, we also calculate a value of 42 nH.
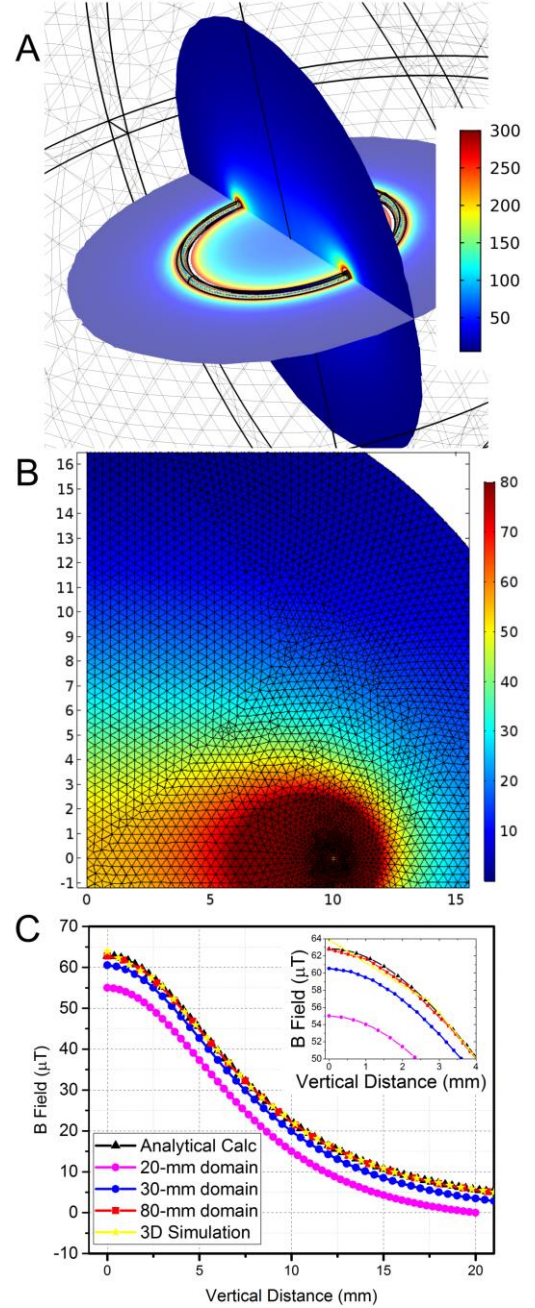
Figure 1. Magnetostatic simulations with 1 A of current running through a 20-mm diameter loop with a 1-mm wire. (a) 3D result for magnetic flux density (μT). (b) 2D axisymmetric result with color bar for magnetic flux density (μT) only up to 80 μT. (c) Magnetic flux density as a function of distance above the loop. Simulations agreed more closely with analytical expressions with increases in the radius of the surrounding domain.

C. Frequency-dependent Impedance of a Single Loop

While the magnetostatic calculations/simulations of inductance are accurate at low frequencies, the skin effect begins to play a role in lowering inductance at high frequencies. The skin effect drives the majority of the current toward the outer skin of the solid conductor, which means the effective area of the conductor decreases. With this decrease in effective area, the effective resistance of the coil increases. Thus, more of the applied power gets lost in the resistance of the coil and less goes into creating the magnetic field. Figure 2 shows resulting cross sections for the wire with dependence on frequency, along with simulated values for resistance and inductance as a function of frequency for the same 20-mm diameter loop and 1-mm diameter wire described in Figure 1. Notice how the surface current begins to move toward the outer edges and shows a propensity for the left portion of the cross section of the wire. In addition to frequency-dependent skin effect, resonance due to self-capacitance also occurs at very high frequencies greater than 1 GHz[12].

D. Mutual Inductance Between Two Coaxial Loops

For the general case of measuring the impedance across a single loop or coil to determine the impedance of a neighboring loop or coil, we refer to a circuit-based description of a transformer in terms of mutual inductance. In Figure 3A, we have two coils with inductance L_1 and L_2 connected in series with lumped elements of impedances Z_1 and Z_2. We can describe the potentials across these inductively coupled circuits with the following equations[9,10,13]:

$$v_{eff} = i_1 Z_1 + L_1 \frac{di_1}{dt} - M \frac{di_2}{dt}$$
$$v_2 = M \frac{di_1}{dt} - L_2 \frac{di_2}{dt} \quad , \quad (5)$$
$$v_2 = i_2 Z_2$$

where v_1 and v_2 are the associated electric potentials, i_1 and i_2 are currents in the separated circuits, and M is the mutual inductance
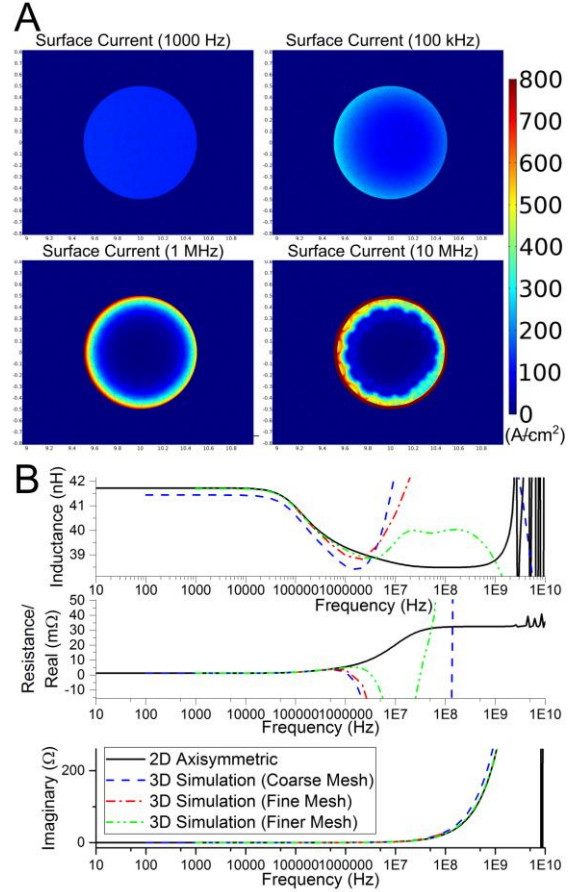

Figure 2. Frequency-dependent behavior of a single loop with a diameter of 20 mm and a wire diameter of 1 mm. (a) Surface current in the 1-mm wire as simulated with a 2D axisymmetric model. The axis of the loop is to the left of the profiles shown, and the asymmetric profile of surface current is not abnormal. (b) Inductance, resistance, and imaginary component as a function of frequency for simulations of current running through the single loop.

Figure 3. (a) Circuit diagram for inductive coupling of a sensor with variable impedance Z_2. **(b)** Circuit diagram with an open circuit to determine mutual inductance M as a function of v_2 and applied current i_1.

between the two halves of the overall circuit. In the Laplace domain, we can write the following single expression for the impedance across the left side of the circuit:

$$Z_{eff} = \frac{V_{eff}}{I_1} = Z_1 + L_1 s - M^2 s^2 / (L_2 s + Z_2). \quad (6)$$

For some wireless sensing applications, the objective is to build a transducer that effects a change in Z_2. Thus, if we know the other lumped parameters in Equation 6 and measure Z_{eff}, it will be possible to determine Z_2. While Z_1, L_1, and L_2 may have fixed characteristics for our applications, the mutual inductance M depends on the relative position between the two coils. For transformers, this positioning is static, but for some sensing platforms envisioned for intermittent measurements with a handheld reader, we do not have a static M and would like to understand how M changes as a function of relative position between the coils.

For the diagram shown in Figure 3B, mutual inductance has the following form:

$$M = V_2 / (I_1 s). \quad (7)$$

Using finite element analysis, it is possible to run frequency-dependent simulations to calculate the mutual inductance M for varied geometries, configurations, and frequencies. While there are analytical expressions for simple magnetostatic cases and

geometries[14], simulations are appropriate for irregular geometries, skin effects (frequency-dependent resistance), and high-frequency, capacitance-based resonance of the coils themselves.

Similar to our approach of comparing simulated calculations with an analytical estimate for a single conductive loop, we review an estimate for the mutual inductance between two coaxial circles. These coaxial circles are essentially loops of given radii R_1 and R_2 separated by a distance b having wires of infinitesimal diameters. Their mutual inductance is the following expression derived by Maxwell[11,15]:

$$M = -\mu_0\sqrt{R_1 R_2}\left[\left(c - \frac{2}{c}\right)F(c) + \frac{2}{c}E(c)\right],$$
$$c = 2\sqrt{R_1 R_2}/\sqrt{(R_1 + R_2)^2 + b^2} \tag{8}$$

where $F(c)$ and $E(c)$ are the first and second complete elliptic integrals, respectively, to modulus c. For two 20-mm coaxial, parallel circles separated by a distance of 3 mm, Equation 8 yields a value of 21 nH for this quasi-static case. Equation 8 also makes it clear that mutual inductance decreases as the distance between the circles increases.

Using FEA, we setup axisymmetric and 3D models to calculate the mutual inductance between two coaxial loops. For these simulations, we use the same loops described previously for determining self-inductance with a diameter of 20 mm and a wire diameter of 1 mm as shown in Figure 4A. We simulate the resulting potential across the "broken" portion of the top loop with a specified oscillating current in the bottom loop to mimic the configuration in Figure 3B. Then, we use Equation 7 to calculate the mutual inductance[8].

The simulated mutual inductances in Figure 4B show the dependence of mutual inductance on frequency and the distance between the coaxial coils. First, the values at low frequencies are of the same order of magnitude but less than the static values calculated in Equation 8. These differences
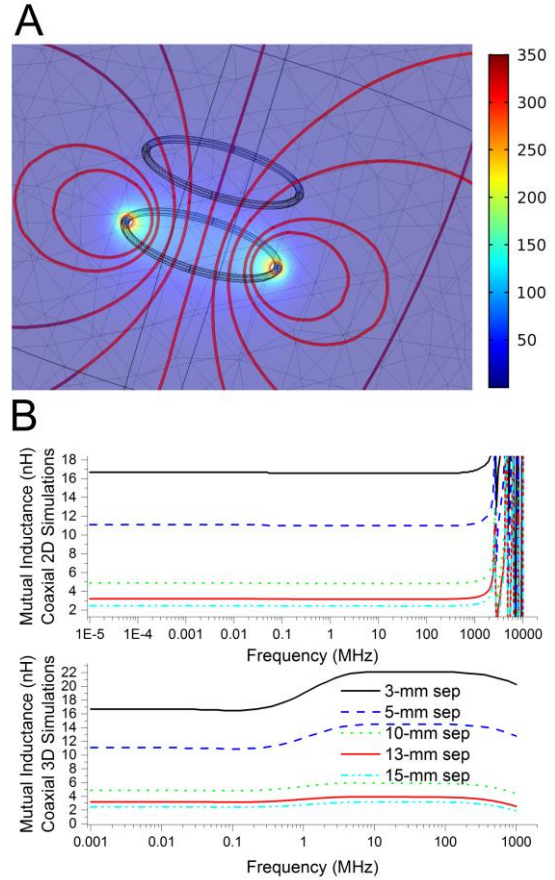
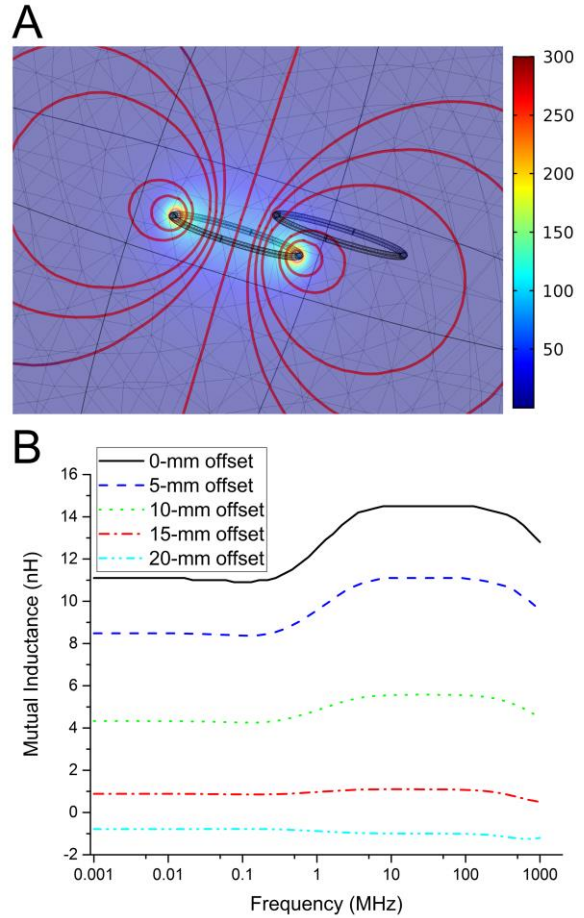**Figure 4. Frequency-dependent simulations for mutual inductance between two coaxial loops (a) Graphical result showing the magnetic flux density (μT), along with a few associated field lines. (b) Simulated mutual inductances for axisymmetric and 3D geometries.**

are not unexpected, as Equation 8 does not account for the diameter of the looped wire or the frequency of applied current on the primary coil. Second, the mutual inductances become less as the separation between the coils increases. The static calculations, 2D simulations, and 3D simulations all demonstrate this behavior. This behavior is a result of less magnetic flux density going through the second loop as the separation between loops increases. Figure 4A helps visualize this behavior as the number of streamlines going through the top loop decreases as the separation increases. Third, there is a slight reduction in mutual inductance as frequency increases until approximately 200 kHz, which is similar to the decrease in self-inductance for a single loop (see Figure 2B), which results from the increasing resistance in the coil from the skin effect. Fourth, there is disagreement in Figure 4B between the 2D axisymmetric and 3D simulations as the frequency approaches 1 MHz. At this point, we have more confidence in the axisymmetric simulations than the 3D simulations. We believe we need to refine the mesh further for the 3D cases (see Figure 2B) or revise the boundary conditions on the surfaces of the coils to improve the accuracy of the 3D simulations at high frequencies. Fifth, the axisymmetric models capture resonant behavior at very high frequencies greater than 1 GHz, which we expect as capacitive effects begin to play a dominant role.

E. Mutual Inductance between Non-coaxial, Offset Loops

While it is possible to use analytical expressions for non-coaxial, offset loops in some static cases[16–18], the calculations are complex and do not generally account for frequency-dependent physics. As the final demonstration in this article, we include simulated calculations of mutual inductance for parallel loops offset laterally from each other. In this case, it is not possible to use a 2D axisymmetric simulation, but it requires a 3D simulation as shown in Figure 5A. As such, there are still issues with mutual inductances increasing unrealistically at frequencies greater than approximately 1 MHz, but future efforts will resolve these issues with refinement and/or revised boundary conditions.

The conductive loops have the same dimensions used previously, and there is a separation of 5 mm between them and a varied lateral offset in 5-mm increments up to 20 mm. As shown in Figure 5A, the loops are asymmetric with respect to how the streamlines of constant magnetic flux density pass through the upper, secondary loop. As the offset distance increases and the integral of the magnetic flux density passing through the upper loop decreases, the mutual inductance decreases.

III. Conclusions

This report has described the basic physics and modeling of inductive coupling for close-proximity, wireless sensing systems. The sensor itself may be embeddable in a material or mountable on a structure without needing a battery or microprocessor. The electrical power comes from a reading unit with a coil or loop designed to produce an oscillating magnetic field, which drives a potential/current across a sensing unit with environment- or measurement-specific electrical impedance. As the coils couple to each other, changes in electrical impedance will be detectable by the reader. This electrical impedance will be dependent on both the electrical impedance of the embedded sensor and the relative position between the reader and the sensor.

FEA-based models are capable of quantitatively calculating the self-inductance of a coil/loop and the mutual inductance between coils. Mutual inductance is dependent on geometry of the coils, their relative position/orientation, and frequency. By using simulations, the goal is to decouple changes in relative position and changes in electrical impedance of the sensor itself. While this report demonstrates the basic approach and calculation of relevant lumped electrical parameters from electromagnetic simulations, further work is still necessary to improve the accuracy of 3D simulations and verify the calculations with experiments for this ongoing project. Overall, this report should facilitate understanding on how to model and simulate inductive coupling in close-proximity, wireless sensing systems.

Figure 5. Frequency-dependent simulations for mutual inductance between two parallel, non-coaxial loops separated by 5 mm. (a) Graphical result showing the magnetic flux density (µT), along with a few associated field lines with a lateral offset of 15 mm. (b) Simulated mutual inductances for parallel coils with varied lateral offsets.

References

[1] Ong, K. G., Grimes, C. A., Robbins, C. L., and Singh, R. S., "Design and Application of a Wireless, Passive, Resonant-circuit Environmental Monitoring Sensor," *Sensors and Actuators A: Physical*, vol. 93, Aug. 2001, pp. 33–43.

[2] Butler, J. C., Vigliotti, A. J., Verdi, F. W., and Walsh, S. M., "Wireless, Passive, Resonant-circuit, Inductively coupled, Inductive Strain Sensor," *Sensors and Actuators A: Physical*, vol. 102, Dec. 2002, pp. 61–66.

[3] Jia, Y., Sun, K., Agosto, F. J., and Quiñones, M. T., "Design and Characterization of a Passive Wireless Strain Sensor," *Measurement Science and Technology*, vol. 17, 2006, p. 2869.

[4] Loh, K. J., Lynch, J. P., and Kotov, N. A., "Inductively Coupled Nanocomposite Wireless Strain and pH Sensors," *Smart Structures and Systems*, vol. 4, 2008, pp. 531–548.

[5] Nopper, R., Niekrawietz, R., and Reindl, L., "Wireless Readout of Passive LC Sensors," *IEEE Transactions on Instrumentation and Measurement*, vol. 59, Sep. 2010, pp. 2450–2457.

[6] Salas, M., Focke, O., Herrmann, A. S., and Lang, W., "Wireless Power Transmission for Structural Health Monitoring of Fiber-Reinforced-Composite Materials," *IEEE Sensors Journal*, vol. 14, Jul. 2014, pp. 2171–2176.

[7] Focke, O., Salas, M., Herrmann, A. S., and Lang, W., "Inductive Wireless Sensor-actuator Node for Structural Health Monitoring of Fiber Reinforced Polymers by Means of Lamb-waves," *Proc. SPIE 9435*, San Diego, CA, USA: SPIE, 2015.

[8] COMSOL Documentation, *www.comsol.com*, 2016.

[9] Zahn, M., "RES.6-002 Electromagnetic Field Theory: A Problem Solving Approach," 2008.

[10] Zahn, M., *Electromagnetic Field Theory: A Problem Solving Approach (Reprint of 1979 Edition)*, Krieger Publishing Company, 2003.

[11] Rosa, E. B., and Grover, F. W., *Formulas and Tables for the Calculation of Mutual and Self-Inductance*, Bureau of Standards, 1916.

[12] Medhurst, R., "HF Resistance and Self-capacitance of Single-layer Solenoids," *Wireless Engineer*, 1947.

[13] Bitschnau, M. D., "Analysis of Quality Factor and Resonance Frequency Measurements of RFID Transponders," Bachelors of Science, FH Vorarlberg, 2016.

[14] Mohan, S. S., Hershenson, M. del M., Boyd, S. P., and Lee, T. H., "Simple Accurate Expressions for Planar Spiral Inductances," *IEEE Journal of Solid-State Circuits*, vol. 34, Oct. 1999, pp. 1419–1424.

[15] Maxwell, J. C., *A Treatise on Electricity and Magnetism (Republication of 1891 Edition from Clarendon Press)*, New York: Dover, 1954.

[16] Kim, K.-B., Levi, E., Zabar, Z., and Birenbaum, L., "Mutual Inductance of Noncoaxial Circular Coils with Constant Current Density," *IEEE Transactions on Magnetics*, vol. 33, Sep. 1997, pp. 4303–4309.

[17] Akyel, C., Babic, S. I., and Mahmoudi, M.-M., "Mutual Inductance Calculation for Non-Coaxial Circular Air Coils with Parallel Axes," *Progress In Electromagnetics Research*, vol. 91, 2009, pp. 287–301.

[18] Pankrac, V., "Generalization of Relations for Calculating the Mutual Inductance of Coaxial Coils in Terms of Their Applicability to Non-Coaxial Coils," *IEEE Transactions on Magnetics*, vol. 47, Nov. 2011, pp. 4552–4563.

Modeling the Detection of Solar Neutrinos via Inverse Beta Decay in a Space Environment

Robert McTaggart[1]

South Dakota State University 1, Brookings, SD, 57007

Abstract: The GEANT4 simulation package is used to model the response of a proposed solar neutrino detector to an isotopic background of monoenergetic particles, which will aid in the rejection of unwanted background events that mimic neutrino signals. The ability to detect neutrinos from space would facilitate observations away from the plane of the ecliptic, which may provide a unique insight on stellar fusion processes. 10 MeV protons do not reach the primary detector. The production of secondary neutrons, gammas, and positrons as a result of 10 MeV neutrons and 10 MeV gammas, while small, warrant further study because neutrino interaction rates will be small.

I. Introduction

Neutrinos are a neutral particle with almost no mass that are copiously produced by nuclear processes such as radioactive decay, nuclear fusion, supernovae, and nuclear fission. Due to their ability to oscillate between different types (or flavors) of neutrino, they may have played a role in why our universe consists of matter instead of antimatter[1].

Terrestrial neutrino experiments attempt to improve their chances of detecting the very weakly interacting neutrino by manufacturing more in an accelerator, building larger detectors, or reducing background noise that may interfere with signals resulting from neutrino events. Detector materials consisting of a liquid noble gas like liquid argon or very large tanks of water surrounded by photomultiplier tubes have been designed and/or built.

However, terrestrial detection methods are confined to the plane of the ecliptic. Angular distributions are often used to extract information regarding internal structure of particles, and the dependence of the neutrino flux on the polar angle may provide additional insight into internal solar processes[2, 3].

II. Design of the Solar Neutrino Astronomy Platform (SNAP)

Inverse beta decay is similar to a regular beta decay of a neutron, but in this case, an anti-electron neutrino emitted by the sun can interact with a proton to generate a neutron and a positron.

$$\overline{\nu}_e + p \rightarrow n + e^+ \tag{1.}$$

Thus, neutron detectors could in principle serve as indirect neutrino detectors. The Advanced Neutron Spectrometer (ANS) under development by NASA Marshall Space Flight Center[4] will monitor neutron doses in the International Space Station caused by interactions of the solar wind with the support structures of the station. It has been estimated that up to 25% of the astronaut's dose may come from secondary neutrons. The purpose of this summer study is to evaluate a design based upon the neutron detection characteristics of the ANS spectrometer for detecting neutrinos via the inverse beta decay.

---

[1] Associate Professor of Physics, Department of Physics, South Dakota State University

The GEANT4 simulation package[5, 6, 7] is copiously used in particle physics, and it was used in this analysis to evaluate the response of the detector design to isotropic protons, neutrons, and gamma rays with a kinetic energy of 10 MeV.

Because the proposed detector, the Solar Neutrino Astronomy Platform (SNAP), must be located above the plane of the ecliptic to examine the angular distribution of the neutrino flux, one cannot significantly increase the size of the detector due to the high cost of launching elements of such a large detector into space. Instead, one must place the detector closer to the sun to maximize the benefit of the inverse-square law and increase the strength of the neutrino flux.

As a result, heat shielding must be provided so that detectors may operate at maximum efficiency. While plastic scintillators are robust enough to operate in the space radiation environment and survive launch conditions, heat may liquefy the scintillator and reduce its efficiency. Heat reduction technologies have been included in the simulation because any study of the effects of background events must at least consider the impact of secondary particles arising from interactions of the infrastructure surrounding the primary particle detectors.

Two NASA projects, the Solar Probe Plus[8] mission, and the James Webb Space Telescope[9] use heat reduction technologies to maintain a high level of satellite performance. Both technologies are included in this design.

First, a layer of carbon foam similar to the Solar Probe Plus mission forms the primary heat barrier for a satellite that will be just under 4 million miles from the surface of the sun. In front of the carbon foam is a layer of gallium arsenide solar cells to produce power, and behind it lies a control module that is part aluminum and part copper. A disk of aluminum provides structural support for the carbon foam layer and acts as a reflector.

Second, three successive cones made of parallel layers of kapton, silicon, and aluminum follow the heat removal design of the Sunshield of the James Webb Telescope, which allows heat to reflect between the layers and away from the critical detector elements.

In order to reduce the background as much as possible, an anti-coincidence counter (ACC) has been integrated into the design. The ACC consists of 4 side volumes arranged in a pinwheel configuration, whereby there is some overlap with the next side. The top and bottom volumes overhang this arrangement. The overhangs are included to reduce, if not eliminate, the possibility that background candidates register signals in the primary detector without leaving a signal in the ACC. In particular for the inverse beta decay, an accidental event topology that introduces a neutron and positron with the right timing can yield a false event, and every neutrino counts.

Each side volume consists of a 5 X 5 arrangement of staggered polystyrene panels. Each panel is 40 cm square, and currently overlaps neighboring panels by 10 cm. In order to avoid physical overlaps of panels, the polystyrene panels are staggered. The first row occupy positions 1 and 3, and the next row will occupy positions 2 and 4. The program is configured that a different arrangement with different sized panels is easy to obtain. Each top or bottom volume is a similar 6 X 6 arrangement of polystyrene panels.

Roughly speaking, the outer surface of the ACC matches a cube of length 2 meters.

A layer of glass is placed at the end of each polystyrene panel to represent the behavior of a photomultiplier tube. Aluminum absorbers are placed on the outside of the glass layer. The whole combination is wrapped with a layer of Tyvek for light tightness. This layer needs to be thinner than it is currently to optimize optical physics.

Inside the ACC lies the primary detector, a 1-meter cube of polyvinyl toluene, which is the plastic scintillator used in the ANS spectrometer. A 2% mixture of Gadolinium is included throughout the cube. Isotopes of Gadolinium have high neutron absorption cross-sections, so emission of a characteristic gamma ray is a signal that a neutron has been absorbed. Areas on two sides of the cube are reserved for a layer of glass and a layer of aluminum absorber like the polystyrene panel. This assembly is also wrapped in a layer of Tyvek.

The resulting design for the Solar Neutrino Astronomy Platform (SNAP) is shown in Figure 1. The arrows in the picture represent the x, y, and z axes used by the program.

Please see the computer code that built the detector, ran the resulting simulations, and processed all of the data in the Appendix.

Figure 1: The Solar Neutrino Astronomy Platform
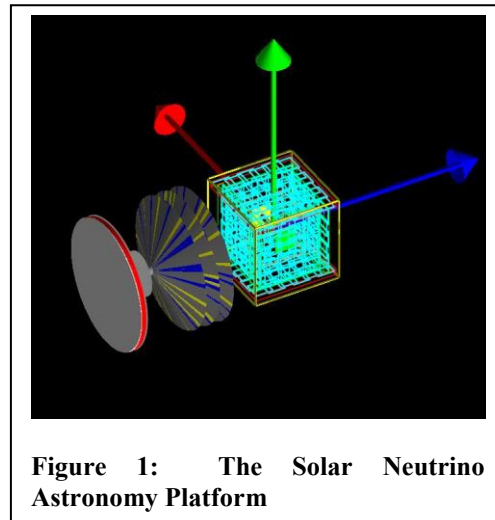
III. Simulation of an isotropic background

For each simulation, 100,000 fake events were produced. The source was the surface of a sphere with a radius of 4.5 meters that was centered about the origin, where the primary polyvinyl toluene cube was centered. This allowed for the possibility that scattering with the other infrastructure elements was possible, while reducing the number of particles that simply missed the detector altogether. Nevertheless, only about 4000 protons, 6000 neutrons, and 3000 gamma rays generated a response from any of the properties that were tracked in the program. Much of this is due to simple geometry.

If none of the variables being tracked are triggered, the zeroes for the event are not recorded. But if at least one item is triggered, data is written whether many variables are zero or not.

One of the greatest challenges of such a simulation is the generation and tracking of optical photons produced in the polyvinyl toluene and the polystyrene scintillators. However, while the program successfully generates and tracks optical photons within the scintillators, it does not currently transfer some of those photons to the glass layer which represents a window of a photomultiplier tube. Thus data are not presented for the collection of optical photons by the glass layers. Optical physics relies heavily on the properties of neighboring surfaces, and more time is necessary to understand how optical photons are behaving within the current design.

Below we present plots of interest out of the following variables tracked in the scintillators: Total energy deposited, number of secondary neutrons, number of secondary gamma rays, number of secondary electrons, number of secondary positrons, and number of optical photons. Note that all ACC plots sum the contribution of all polystyrene panels in sides, top, and bottom that were hit in an event.

A. 10 MeV Protons

3856 events were registered by the program for 10 MeV protons. Nothing really was seen by the polyvinyl toluene, but signals were seen in the ACC. We do not find evidence for extraneous neutrons or positrons in the primary detector that would interfere with an inverse beta decay process due to 10 MeV protons.

126
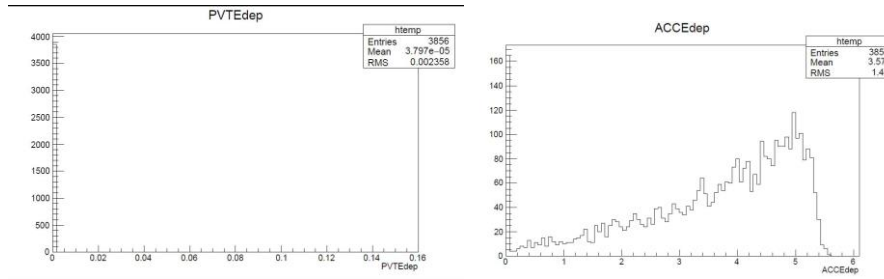
Figure 2: Total energy deposited in the PVT (left) and the ACC (right).

We note in Figure 2 that the total energy was 10 MeV, so some energy should make it past the ACC into the polyvinyl toluene (PVT). However, it is likely that the Tyvek layer is thick enough to stop the protons from entering the PVT.

No secondary neutrons resulting from proton interactions were registered. It may be the case that with a thinner layer of Tyvek and a higher proton energy, some secondary neutrons would be observed.
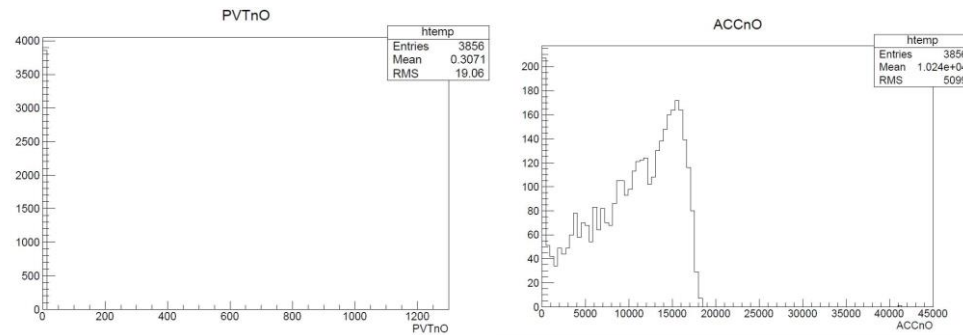

Figure 3: Optical photons produced in the PVT (left) and the ACC (right).

As can be seen from Figure 3, the program is successfully generating optical photons, but none of them are entering the glass layer at the moment.

B. 10 MeV neutrons

Tyvek is essentially a processed form of polyethylene, so it may moderate neutrons some, but it will not stop them. One can see in Figure 4 below that energy is deposited in both scintillators.

One interesting feature of the energy deposited in the polyvinyl toluene is that sometimes, more energy is deposited than the original 10 MeV. One way that this can occur is when isotopes of gadolinium absorb a neutron and emit a photon with a characteristic gamma ray. At the moment, the program does not track which gammas originate from Gadolinium, but it is not likely that conservation of energy is being violated. One is simply releasing energy that is stored in the Gadolinium.

It is possible for neutrons to be completely absorbed in either the polyvinyl toluene or the polystyrene panels. This may depend on the angle of approach permitted by the isotropic particle source.
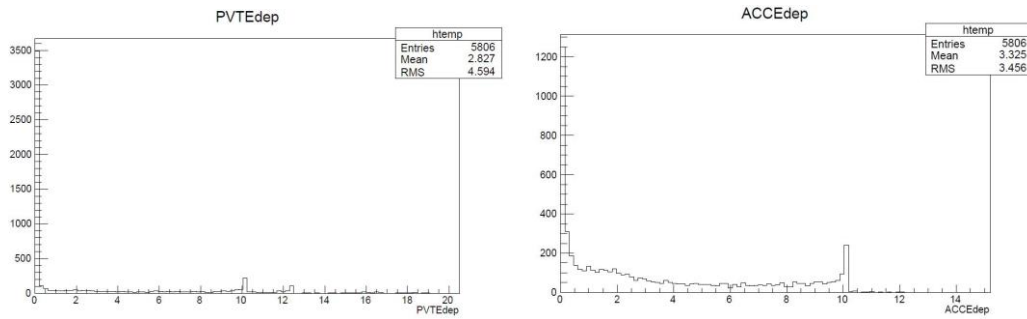
Figure 4: Total Energy Deposited by Neutrons in the PVT (left) and ACC (right)

Figure 5 shows that additional neutrons can result from interactions with a neutron or one of its secondaries. This shows that a background event can produce unwanted neutrons which may accidentally mimic an inverse beta decay.
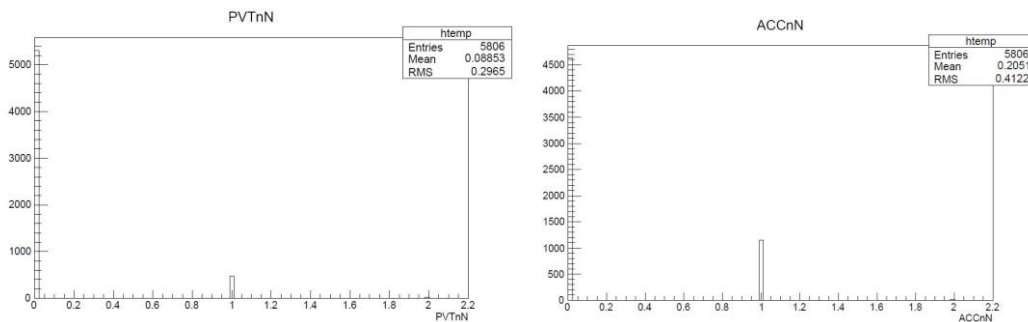
Figure 5: Secondary Neutrons in the PVT (left) and ACC (right)

Because gamma rays are neutral, discrimination between gamma rays and neutrons is often important. The simulation shows that 10 MeV neutron events can sometimes generate multiple gamma rays in the detector, some of which could result from neutron capture in Gadolinium. The PVT cube is also larger than a polystyrene panel, offering more opportunities for gamma ray generation in Figure 6.
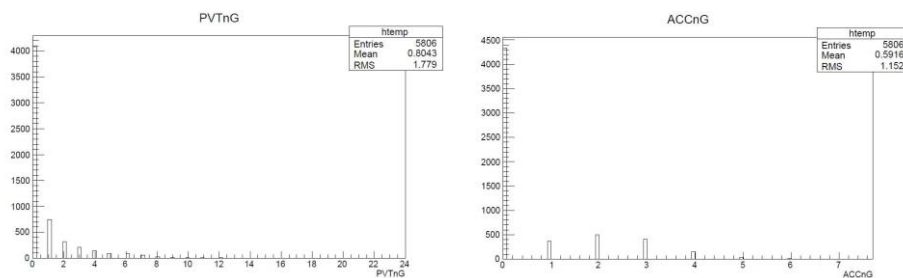
Figure 6: Secondary Gamma Rays produced in the PVT (left) and the ACC (right)

It is found that a handful of positrons are produced by 10 MeV neutrons in both types of scintillator, likely the result of pair production that can occur with gamma rays that are generated. In general, neutrons produce many more

gamma rays than other neutrons or positrons, but the latter particles that also come from inverse beta decay occur. When a revised analysis occurs with a distribution of energies, the frequency of both neutrons and positrons occurring together during the same event will be examined. Time of production or detection may allow for background cuts of such combinations.
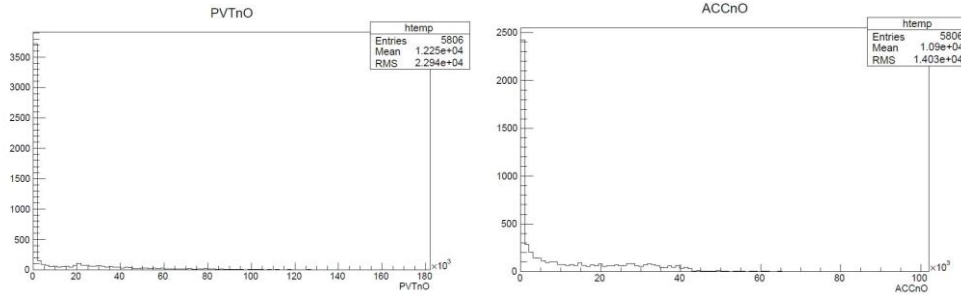
Figure 7: Optical photons generated in the PVT (left) and ACC (right) by 10 MeV neutrons

Once again in Figure 7, there is no trouble in generating optical photons in either scintillator. In a future analysis, firing optical photons only into the scintillator may allow one to better study what is actually happening to the optical photons near the boundaries with the glass layer (i.e. a photomultiplier tube window), or the Tyvek that surrounds the scintillator.

C. 10 MeV Gamma Rays

As opposed to neutrons, and particularly protons, more gamma rays seem to make it to the polyvinyl toluene cube. It is possible in Figure 8 for a gamma ray to deposit all of its energy in either scintillator, or no energy in either scintillator. Gamma rays produce an assortment of electrons like neutrons do as a result of ionization in the material.
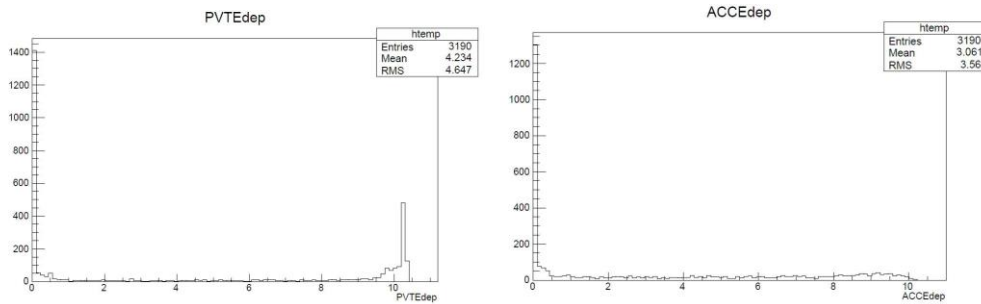
Figure 8: Total Energy Deposited by 10 MeV gamma rays in PVT (left) and ACC (right).

10 MeV gamma rays were not found to generate secondary neutrons in either scintillator, but they did produce an occasional positron. If the neutrino flux is only a few neutrinos per day and thousands of background events enter the detector, then the topology of secondary positrons warrants further study. It is believed that the positrons are a result of pair production within the scintillators, and pair production generally becomes more dominant as the photon energy increases.
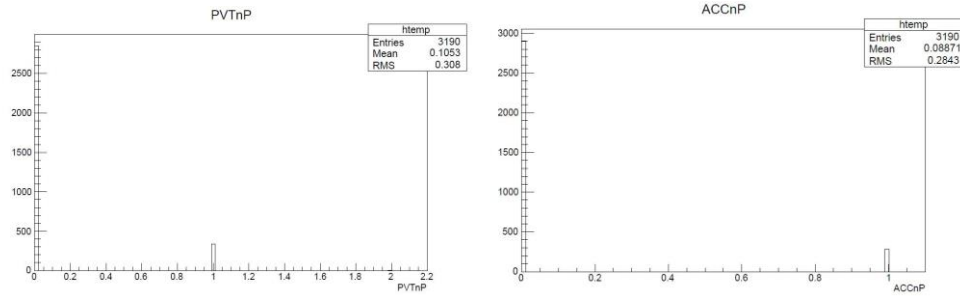
**Figure 9: Secondary positrons generated by 10 MeV gamma rays
in PVT (left) and ACC (right)**

We finally find in Figure 10 that gamma rays also copiously produce optical photons within the scintillators, but not in the glass layers right next to said scintillators. The production of optical photons and their tracking becomes an issue as the gamma ray energy increases, because the number of optical photons increases dramatically. This means that simulation of 100,000 events with 100 MeV gamma rays will take much longer than a simulation with 10 MeV gamma rays.
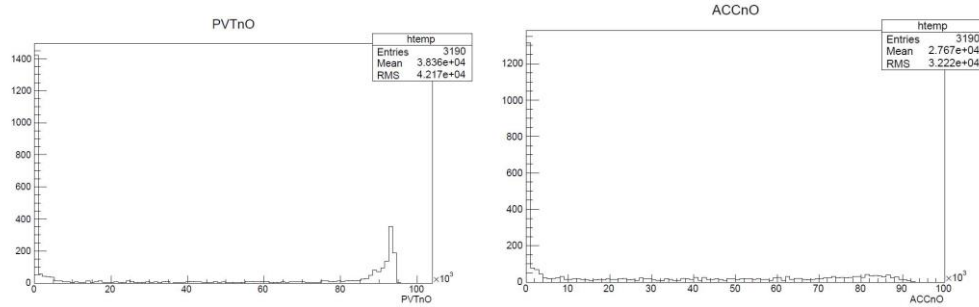
**Figure 10: Optical photons generated in PVT (left)
and ACC (right) by 10 MeV gammas**

IV. Conclusions

The Geant4 simulation package has been successfully implemented to design a prototype detector referred to here as the Solar Neutrino Astronomy Platform (SNAP). This project is a first attempt to design a space-based neutrino detection system. Integration of the full galactic background, solar particle flux, and the physics of neutrinos will be necessary, as will any future engineering analyses and design that would modify the detection of neutrinos.

Modifications to the program will be easier to make now that the program is fully functional….with the exception of the behavior of optical photons. It is important to understand what the optical photons are doing in the program and adjust geometries and surface properties as necessary.

Besides the small cross sections for neutrino interactions, the biggest challenge for this detector design is that event rates can only be increased if one moves closer to the sun because of the inverse-square law. Thus heat rejection is an issue, and the expense of launching heavy items means that increasing the detector mass to increase the event rate is inhibited.

Regarding the analysis, energy spectra that are not monoenergetic will be necessary to truly assess background sources. The rate of accidental inverse beta decay topologies needs to be compared with the number of actual events that the Sun could generate. It should be possible to generate desired neutrino events with another routine used by

130

current neutrino experiments. While Geant4 cannot process the neutrino interactions, it can certainly process the secondaries like gamma rays, electrons, positrons, etc. generated by another routine.

Several broader impacts will occur as a result of the work done with NASA on this project. The same framework can be used in many other experiments in particle physics, but it can also be used in analyses for radiation detection and radiation shielding. Geant4 allows for many different kinds of undergraduate research projects to occur in the Department of Physics at South Dakota State University, and will help train students who come to NASA Marshall for future internship and research opportunities.

It is unclear at the moment if a detector designed for neutrino detection would have a secondary use for NASA, but it could be used to augment alert systems used in protecting astronauts from radiation or protecting critical infrastructure from the impact of space weather. Solar proton events generate neutrinos, but at a different energy than the solar neutrinos. It is unclear whether the neutrino flux in a solar particle event would be suitable for such a purpose. Nevertheless, if the detector is sensitive to gammas, protons, and neutrons, a secondary use may be possible and beneficial.

Acknowledgments

References

[1] Deep Underground Neutrino Experiment, "Why neutrinos?", URL: http://www.dunescience.org/why-neutrinos/ [cited August 11, 2016].

[2] P.A. Sturrock, L. Bertello, E. Fischbach, D. Javorsek II, J.H. Jenkins, A. Kosovichev, A.G. Parkhomov, "An analysis of apparent r-mode oscillations in solar activity, the solar diameter, the solar neutrino flux, and nuclear decay rates, with implications concerning the Sun's internal structure and rotation, and neutrino processes," *Astroparticle Physics,* Vol. 42, February 2013, pp. 62-69.

[3] Shantu Desai and Dawei W. Liu, "A search for evidence of solar rotation in Super-Kamiokande solar neutrino dataset", *Astroparticle Physics*, Vol. 82, September 2016, pp. 86-92.

[4] Mark Christl, Eugeny Kuznetsov, Jeff Apple, John Watts, Brian Gibson, "Advanced Exploration Systems Radworks – Radiation Protection Technologies," NASA Technical Report 20160001286, Payload Operations and Integration Workshop, 27 Jan 2016, Huntsville, AL, NASA Marshall Space Flight Center. URL: http://ntrs.nasa.gov/search.jsp?R=20160001286 [cited August 11, 2016].

[5] S. Agostinelli et al, "GEANT4—a simulation toolkit," *Nuclear Instruments and Methods in Physics Research A,* Vol. 506, Issue 3, 1 July 2003, pp. 250-303.

[6] J. Allison et al, "Geant4 developments and applications," *IEEE Transactions on Nuclear Science*, Vol. 53, Issue 1, Feb. 2006, pp. 270-278.

[7] Geant 4, URL: www.geant4.org/geant4/ [cited August 11, 2016].

[8] "Solar Probe Plus: A NASA Mission to Touch the Sun," http://solarprobe.jhuapl.edu/ [cited August 11, 2016].

[9] "Explore James Webb Space Telescope: The Sunshield," http://jwst.nasa.gov/sunshield.html [cited August 11, 2016].

Appendix

Contact me if you are interested in the files that were used to generate this project, and could serve as examples for future researchers in the use of Geant4 for their own projects. These are separated into three groups of files essentially. Macros and data files, header files (.hh) that define variables, and files that contain all of the C++ routines (.cc) that build the detector, control Geant4, and process all of the data.

The Science Case for a Large Area Gamma-Ray Burst Polarimeter

Robert D. Preece[1]
University of Alabama in Huntsville, Huntsville, Alabama, 35809

Colleen Wilson-Hodge[2] and Jessica Gaskin[2]
NASA Marshall Space Flight Center, Huntsville, Alabama, 35809

Even after more than 40 years of observations, there are still a large number of unknowns related to the phenomenon of Gamma-Ray Bursts. Still, bursts provide a good experimental sample for the study of cosmological jets, since they are plentiful (~1 per day) and quite narrowly beamed. We describe how an instrument designed to detect gamma-ray polarization can resolve some of the long-standing issues of energization, jet structure and emission by adding a new dimension to the observations of burst properties. One such instrument is a large-area polarimeter (LEAP), to be proposed for operation on the International Space Station.

Nomenclature

A	=	total surface area of scintillators
B	=	background rate in counts/cm^2 s
BATSE	=	Burst And Transient Source Experiment (on CGRO)
CGRO	=	Compton Gamma-Ray Observatory
EGRET	=	Energetic Gamma-Ray Experiment Telescope (on CGRO)
η	=	efficiency of detection of polarization
f_c	=	statistical significance factor for confidence level C
GBM	=	Gamma-ray Burst Monitor (on Fermi)
GeV	=	billion electron volts
GRB	=	gamma-ray burst
keV	=	thousand electron volts
LAT	=	Large Area Telescope (on Fermi)
LEAP	=	LargE Area Polarimeter
MDP	=	minimum detectable polarization
MeV	=	million electron volts
M	=	modulation fraction: response of the detector to 100% polarization
S	=	GRB fluence in photons/cm^2
T	=	burst duration in s
z	=	redshift

---

[1] Associate Professor, Department of Space Science, University of Alabama in Huntsville.
[2] MSFC-ZP12.

I. Introduction

γ-ray bursts (GRBs) are one of the major outstanding puzzles in astrophysics. They are true cosmological events, with measured redshifts equal to the most distant astrophysical objects found to date ($z \sim 9$). The prompt emission (usually in an energy band of 10 keV to 1 MeV) reflects a unique capacity to efficiently produce high-energy radiation, which can last for durations of milliseconds to hours. Knowledge of the distance and the brightness observed at Earth allows the determination of the intrinsic brightness for bursts with known redshifts. This, along with opacity considerations, forces the conclusion that burst emission generally must be highly beamed in a relativistic jet toward the observer; otherwise, the energies involved would be greater than the rest mass of a typical star and the highest energies would be choked off by runaway pair production.

The study of GRBs is at a crossroads. With large data sets produced by several highly successful missions (including CGRO-BATSE[1], Swift[2] and Fermi-GBM[3]), bursts are now known to be cosmological, to have at least two viable progenitor models to address the bi-modality of durations, to have their prompt emission originate from highly relativistic outflows (usually assumed to be confined within a narrow jet) and that many GRBs have extended afterglow emission in nearly every observable energy regime from hard gamma-rays (GeV) down to radio that last from minutes to months, depending on the wavelength. We now know of several bursts that have different spectral components between the GBM and Fermi-LAT energy ranges and many more that may have several components in the prompt gamma-ray emission, observed by BATSE and GBM. What we do not know is precisely the mechanism of emission for each of these spectral components, or even in the case that only a single component is observed. There are too many possibilities that are consistent with observations and predictions from any single emission model are too ambiguous to distinguish between them. Knowing the correct emission mechanism can allow us to better determine the radiative efficiency and overall energy budget to better than current estimates that span several orders of magnitude. What is needed is a new set of observables that have the possibility to break the degeneracies between current models. A solid determination of polarization (or its absence) can do this. In this article, we discuss the capabilities of a LargE Area Polarimeter for gamma-ray bursts (LEAP).

II. GRB Observables

GRBs have been extensively investigated in both the temporal and energy domains. We focus mainly on the prompt gamma-ray emission, as it is the least understood and will benefit the most from observations of polarization. Burst durations can be anywhere between 1 ms and several hours; there is a well-supported bi-modality in the duration distribution function, with a split at 2 s dividing bursts into the only know subpopulations: 'short' and 'long'[4]. The time history of each event is unique and can be found anywhere on a scale between smooth and spiky. Recent work lends support to the concept that burst light curves are composed of individual pulses, possibly overlapping, each with a conserved shape but different time constants characterizing the pulse rise and decay[5].

The prompt emission is traditionally recorded over an energy range from $8 - 10$ keV on up. Most bursts do not have any significant emission above 1 MeV. Comprehensive analyses of BATSE and GBM data has resulted in a generally-accepted grouping of possibly four basic types of spectra prevalent in GRBs:

1) Those that fit the empirical 'Band' GRB function[6], essentially a smoothly broken power law that is usually parameterized in terms of the energy (E_{peak}) of the spectral break in the power

density $E^2 f(E)$ spectrum and low- and high-energy power-law indices, α (alpha) and β (beta), respectively.

2) Those that fit a cut-off model power-law (usually called 'COMP'). This also can be parameterized in terms of E_{peak} and the low-energy power-law index alpha. These spectra are by far the most prevalent in the BATSE[1] and GBM Spectroscopy Catalogs[3].

3) There are two-component spectra with a steep power-law (index ~ -1) that extends into the Fermi-LAT energy range (> 30 MeV), as well as a lower-energy component, best described as COMP, that dominates the GBM energy range. The two components have different temporal behaviors, with the high energy power-law growing with time and sometimes persisting for much longer than the GBM prompt signal (e.g. GRB090902B[7]).

4) Finally, there is a fairly large body of evidence for multiple-component spectra within the GBM energy range[8]. Burgess and collaborators have directly fit the spectral data with optically-thin synchrotron emission for a power-law distribution of electrons plus a blackbody[9]. The thermal spectral component peaks below the synchrotron peak. It is important to keep in mind that the same spectra are usually those that are well-fitted by the BAND or COMP functions. The physical nature of the functions employed by Burgess makes them preferable over the empirical BAND, for the same number of parameters.

Except for case 4), there is no preferred physical emission model that may be directly associated with these common spectral forms; while as stated, for case 4), a simpler empirical function can often provide a fit to the data with comparable statistics.

Polarization brings several new observables to the table. First of all, the polarization fraction can be between 0 and 100%. This value can be used in conjunction with theory to infer the magnetization of the emitting plasma. In addition, the direction of polarization, projected on the sky, can be measured, taking values from 0 to π. For GRBs, both of these, fraction and direction of polarization, can be expected to change as a function of time as well as energy. Correlation with features already known for GRBs in the time and energy domains can be especially useful.

III. Polarization Models

So, what is the case for polarization of GRB emission? Four possibilities have been discussed:

1) Synchrotron emission from a well ordered magnetic field (constant in magnitude and direction within the viewable emission region) provides the most easily testable case[10]. For power-law distributions of electrons (such as may arise as a result of one or more shock regions in the jetted outflow from a GRB progenitor), the polarization can be as much as 75%, depending on the power-law index. The lower-energy emission should be composed of synchrotron below the 'critical frequency', assuming that the particle distribution has a low-energy cutoff. In that case, the polarization fraction should approach 22%. Another possibility is that the particle distribution may be a relic thermal Maxwellian from the initial fireball. In this case, synchrotron is remarkably efficient near the peak of the Maxwellian and could be as much as 95% or so, falling with lower energies to $\sim$22% as energies approach kT (typically $\sim$30 keV)[11].

2) If the magnetic field within the viewable region is disorganized, the polarization fraction from synchrotron will be reduced, depending on the ratio of residual organized field (if any) to random field. The magnetic field may be chaotically tangled or the emission may come from several small regions at once, such as with multiple magnetic reconnection events. Truly randomized fields can regain some fraction of order by way of geometric asymmetry or relativistic aberration. Off-axis viewing of a relativistic jet is one means of accomplishing this[12].

3) Photospheric emission from the fireball itself is not likely to be polarized at all, due to the thermalization between particles and photons randomizing angles. However, as the fireball becomes optically thin, the geometric and relativistic effects mentioned above may come into play. Alternatively, if the jet is threaded by a magnetic field that is coherent in magnitude and direction within the relativistic viewing geometry, thermal synchrotron as described in section 1) above may be observed.

4) Finally, it is possible that the jet geometry favors Compton upscattering of some population of ambient photons, including the possibility to 'Compton drag' the jet's own emission. Any value of polarization fraction between 0 and 100% can be expected in this case, depending upon the jet geometry and photon energies and angular distribution[13].
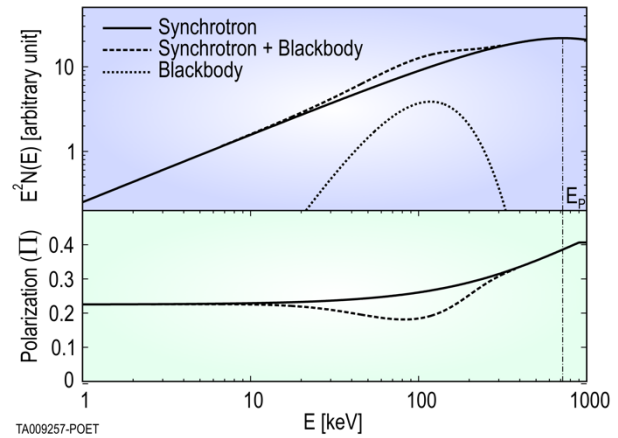
Figure 1. Two Component Spectral Model. *The polarization curve as a function of energy (lower panel) indicates a change in polarization near the peak of an added blackbody component, which will be very difficult to measure for a polarization resolution < 5%.*

IV.   Key Questions for a Gamma-Ray Polarimeter

GRBs are quite diverse in every quantifiable property; we expect no less from polarization: the current polarization results for 12 GRBs so far are inconclusive; but all of these have large uncertainties (see Fig. 2). It is very likely that the GRB polarization mechanism varies from burst to burst; we will need a large population of bursts in order to determine the relevant mechanisms. Each question that a gamma-ray polarimeter answers relates back to astrophysical jet properties:

1) Are BAND function spectra in bursts synchrotron-like? A positive result determines whether the jet is homogeneously magnetized or not on the scale of the viewable geometry. This is also an energy-domain question, as it requires bursts bright enough to detect slight (5%) changes in polarization above and below E_{peak}.

2) Are cut-off power-law spectra (COMP) thermal or magnetic in origin? If these are thermal: expect close to or identical to 0 pol.; need excellent resolution in the polarization fraction to distinguish 0% from small but finite polarization. In the magnetic case, expect to observe synchrotron from relic thermal electrons: Π = 95% – 22%. This can discriminate between jet emission that arises in optically thick or thin plasma.

3) Can we detect a difference in polarization for composite spectra? Composite spectra imply that the jet emission originates in more than one zone: the photosphere and the Band component observed as being coincident in time. Again, this is an energy domain question; the photosphere component may have small polarization fraction, while higher energies have large polarization.

4) Do GRB pulses have constant polarization degree and direction? If pulses are the basic components of the burst lightcurve, expect properties to vary from pulse to pulse: implies 'mini-jet' model of emission, rather than internal shocks. This is an investigation that must be performed in the time domain: for this to be practical, we need to split multi-pulse

GRBs in time while maintaining sufficient significance to constrain the polarization fraction in each segment.

The key questions that need to be addressed require good precision: it is relatively easy to resolve between individual bursts with 75% and 0% polarization. Determining differences of on the order of 5% as a function of energy (as in the figure) or time is much more difficult. In many cases, it will be difficult to distinguish between the different models, so a guaranteed population of bright bursts will be required. We use the Minimal Detectable Polarization (MDP) as a figure of merit to predict how many bursts will be observable for each level of precision.

V. MDP as a Science Driver

As in Ref. 13, we can determine the Minimum Detectable Polarization (MDP) as a figure of merit to explore the capabilities of proposed polarimeter designs. We have interpreted their expression for the MDP as appropriate for a gamma-ray burst detector by expressing the source counts as the burst fluence and the background counts as a rate times the burst duration. The resulting MDP is calculated as given in Eq. 1.

$$MDP = \frac{3\sqrt{2}}{MA\eta(S \cdot 0.75)} \sqrt{A\eta(S \cdot 0.75 + B \cdot T)} \times 100\% ,$$

(1)

where:
- A = surface area of scintillators
- η = efficiency of detection of polarization (here, assumed to be 20%)
- M = Modulation fraction: response of the detector to 100% polarization (assumed to be 44%)
- S = GRB fluence in photons/cm^2
- B = Background rate in counts/cm^2 s (non-coincidence rate; must be corrected by η)
- T = Duration of GRB in s
- 0.75 = Average of source-to-zenith angle cosine
- $f_C = a_C\sqrt{N}$ = Statistical significance factor (Weisskopf 2010) for confidence level C:
  e.g.: for $C = 1\% \Rightarrow f_C = 4.29$

In this study, we calculated the MDP for every GRB in the BATSE Spectroscopy Catalog[1], which has durations and photon fluences for 2145 GRBs. Once these have been sorted, we use the MDP formula to calculate how many bursts lie below a given value of MDP; these are the brighter GRBs. The MDP becomes an estimate of the worst uncertainty on the polarization measurement of a BATSE-like detector with total area A. An estimate made by inverting the MDP formula suggests that the BATSE fluence distribution peaks near ~15% MDP and thus there is a large population of bursts with good significance for determining the polarization. The estimate assumes a constant 4 count/cm^2 background and that the duration is proportional to the fluence, which is generally true.

We must scale the BATSE number to account for the difference in sky coverage and baseline mission lifetime of our proposed detector. A simple estimate can be constructed as follows: BATSE saw 2/3 of the sky above the Earth's limb; LEAP will see ¼ of the sky, assuming an acceptance angle of 60° from zenith; the BATSE mission lifetime = 9 yr, while the LEAP mission lifetime = 2 yr. The conversion factor is the product: ¼ / 2/3 • 2/9 = 1/12. Note: Both BATSE and LEAP turn off during passage through the SAA. A further reduction would account for turning off at certain high latitude locations with high flux.

A. Trade Study of Confidence Levels

Using the BATSE Catalog values, we calculate an MDP for each burst, assuming a total scintillator area of 5000 cm^2, times 20% efficiency for polarization. This corresponds to a notional design for the LEAP detector. We count the number of BATSE GRBs below each MDP limiting value, then divide that number by 12 to obtain an estimate of LEAP GRBs at each level. We then vary the background rate between an estimated equatorial value and a higher latitude value and tabulate the number of expected bursts for 4 MDP values (5%; 10%; 15%; 20%) and 3 MDP measurement confidence levels (90%; 95%; 99%). The results are shown in Table 1.

B. What kind of Science can LEAP do?

As can be seen in the Table, there are sufficient bright bursts for all assumptions that we can perform quite useful threshold science. For example, there are 12 bursts with < 5% MDP (B = 2.6 count/cm^2/s; 99% confidence). One bright burst with Π > 10% would answer the question, "Do GRBs have polarization?" with good confidence. All 12 bursts could be used to answer the question, "Is the average polarization different from burst to burst?" with good confidence. The bursts with the highest fluences can be divided up into several slices in either the time or energy domains to address some of the issues presented above.

Table 1. Numbers of expected GRBs for varying assumptions

Background	Confidence	N_{LEAP} < 5%	N_{LEAP} < 10%	N_{LEAP} < 15%	N_{LEAP} < 20%
B = 4 cnt/cm²s	90% (f_C = 3.03)	17	45	69	89
	95% (f_C = 3.46)	14	39	61	80
	99% (f_C = 4.29)	10	29	47	65
B = 2.6 cnt/cm²s	90%	21	55	83	101
	95%	18	46	73	92
	99%	12	36	59	78

C. Modeling Polarization Classes

Clearly, there will be a lot of fainter bursts with decent MDP levels. Next, we should consider if these can be used to address the numbers of bursts that correspond with each emission class or jet geometry. This will constitute the baseline science for the instrument. Following Ref. 15, the expected average polarization measures of a diverse population of GRBs can be plotted against the spectroscopically-determined value of E_{peak}, since many of the models predict different polarization fractions above and below this value. A simulation based upon 242 GRBs from the HETE-II experiment[15] is shown in Figure 2. Each of the four different polarization models discussed in section III above were constructed from the known parameters of the HETE-II bursts: red – ordered synchrotron (SO); green – random synchrotron (SR); blue – Compton drag (CD); and magenta – thermal synchrotron (TS). In black, the 21 known polarization observations have been plotted with uncertainties and the energy coverage of the observing detector. The key parameter is E_{peak}, since this is the only observable characteristic energy that could be associated with an energy in the models. As E_{peak} moves down through the 50 to 300 keV region (used for determining the polarization), more of the high-energy polarization enters into the average. Thus, the average changes between the low- and high-energy behaviors. The can be seen most dramatically with the downward slope in the red (SO) points in Figure 2.

From Table 1, we can expect to observe ~60 GRBs with better than 15% MDP in the nominal two-year mission of LEAP. We would like to know whether this number of events is sufficient to determine the relative distribution of bursts in each class of polarization model from the observations. One method might be to divide the polarization fraction (the vertical axis on Figure 2) into several bins and determine the relative fractions of the different models in each bin. Taking 15% bins (0 – 15%; 15 – 30%; 30 – 45%; and 45+%), for 60 LEAP GRBs we have:

SO: 7, 16, 36, 2
SR: 50, 8, 2, 0
CD: 45, 5, 4, 5
TS: 0, 1, 7, 52

Figure 2. Simulations of GRB Polarization. *Based on Ref. 15. Includes 12 bursts with detected polarization (see text for guide to colors).*

The bins were chosen to maximize the differences between the model predictions; SR and CD are the two most indistinguishable in the set. We can simulate how well we can distinguish the models by creating 10,000 random Poisson-deviate realizations of the SO distribution, for example, and compare it with the others using chi-square (χ^2) as a figure of merit. As may be expected, if the model is assumed to be SR or CD, their χ^2 distributions overlap considerably; however, neither distribution overlaps the narrow distribution of the correct model, which peaks near 1 (see Figure 3). The SR and CD peaks are at 17 and 26, respectively, so their probabilities to be the correct model are vanishingly small. Now, suppose the 'true' GRB model is an equal mix of SR and SO. In that case, simulations show that the χ^2 distributions for the single models (including SR and SO separately) do not overlap significantly with the one arising from the correct model. A four-parameter least-squares fit should be sufficient to unravel the different components with good significance, with a baseline LEAP detector.

VI. Caveats

Because of the changing background rate with latitude, we should really average smoothly between low and high background burst rates; an investigation into the high latitude background rate is ongoing. We will have to turn the instrument off during SAA and possibly at the highest Geomagnetic latitudes during peak particle precipitation 'seasons'. No effort was made to model the fall-off of efficiency with zenith angle (only the average angle was used). All of these effects only decrease the numbers of bursts in these estimates.

Acknowledgments

References

[1]Goldstein, Adam, Preece, Robert D., Mallozzi, Robert S., Briggs, Michael S., Fishman, Gerald J., Kouveliotou, Chryssa, et al., "The BATSE 5B Gamma-Ray Burst Spectral Catalog", *The Astrophysical Journal Supplement Series*, Vol. 208, Aug. 2013, p. 21.

[2]Lien, Amy, Sakamoto, Takanori, Barthelmy, Scott D., Baumgartner, Wayne H., Cannizzo, John K., Chen, Kevin, et al., "The Third Swift Burst Alert Telescope Gamma-Ray Burst Catalog", *The Astrophysical Journal* (accepted for publication), arXiv:1606.01956.

[3]Gruber, David, Goldstein, Adam, Weller von Ahlefeld, Victoria, Narayana Bhat, P., Bissaldi, Elisabetta, Briggs, Michael S., et al., "The Fermi GBM Gamma-Ray Burst Spectral Catalog: Four Years of Data", *The Astrophysical Journal Supplement Series*, Vol. 211, Mar. 2014, p. 12.

[4]Kouveliotou, Chryssa, Meegan, Charles A., Fishman, Gerald J., Bhat, Narayana P., Briggs, Michael S., Koshut, Thomas M., et al., "Identification of two classes of gamma-ray bursts", *The Astrophysical Journal Letters*, Vol. 413, Aug. 1993, pp. 101, 104.

[5]Hakkila, Jon and Nemiroff, Robert J., "Testing the Gamma-ray Burst Pulse Start Conjecture", *The Astrophysical Journal*, Vol. 705, Nov. 2009, pp. 372, 385.

[6]Band, D., Matteson, J., Ford, L., Schaefer, B., Palmer, D., Teegarden, B., et al., "BATSE observations of gamma-ray burst spectra. I - Spectral diversity", *The Astrophysical Journal*, Vol. 413, Aug. 1993, pp. 281, 292.

[7]Abdo, A. A., Ackermann, M., Ajello, M., Asano, K., Atwood, W. B., Axelsson, M., et al., "Fermi Observations of GRB 090902B: A Distinct Spectral Component in the Prompt and Delayed Emission", *The Astrophysical Journal Letters*, Vol. 706, Nov. 2009, pp. 138, 144.

[8]Ryde, Felix, "Is Thermal Emission in Gamma-Ray Bursts Ubiquitous?", *The Astrophysical Journal Letters*, Vol. 625, June 2005, pp. 95, 98.

[9]Burgess, J. M., Preece, R. D., Connaughton, V., Briggs, M. S., Goldstein, A., Bhat, P. N., et al., "Time-resolved Analysis of Fermi Gamma-Ray Bursts with Fast- and Slow-cooled Synchrotron Photon Models", *The Astrophysical Journal*, Vol. 784, Mar. 2014, p. 17.

[10]Rybicki, George B. and Lightman, Alan P., *Radiative Processes in Astrophysics*, Wiley-Interscience, New York, 1979.

[11]Pandya, Alex, Zhang, Zhaowei, Chandra, Mani, and Gammie, Charles F., "Polarized Synchrotron Emissivities and Absorptivities for Relativistic Thermal, Power-law, and Kappa Distribution Functions", *The Astrophysical Journal*, Vol. 822, May 2016, p. 34

[12]Lundman, C., Pe'er, A., and Ryde, F., "Polarization properties of photospheric emission from relativistic, collimated outflows", *Monthly Notices of the Royal Astronomical Society*, Vol. 440, June 2014, pp. 3292, 3308.

[13]Lazzati, Davide, Rossi, Elena, Ghisellini, Gabriele, and Rees, Martin J., "Compton drag as a mechanism for very high linear polarization in gamma-ray bursts", *Monthly Notices of the Royal Astronomical Society Letters*, Vol. 347, Jan. 2004, pp. 1, 5.

[14]Weisskopf, Martin C., Elsner, Ronald F., & O'Dell, Stephen L., "On understanding the figures of merit for detection and measurement of x-ray polarization", *Space Telescopes and Instrumentation 2010: Ultraviolet to Gamma Ray*, SPIE Proceedings, Vol. 7732, July 2010, pp. 77320

[15]Toma, Kenji, Sakamoto, Takanori, Zhang, Bing, Hill, Joanne E., McConnell, Mark L., Bloser, Peter F., et al., "Statistical Properties of Gamma-Ray Burst Polarization", *The Astrophysical Journal*, Vol. 698, June 2009, pp. 1042, 1053.
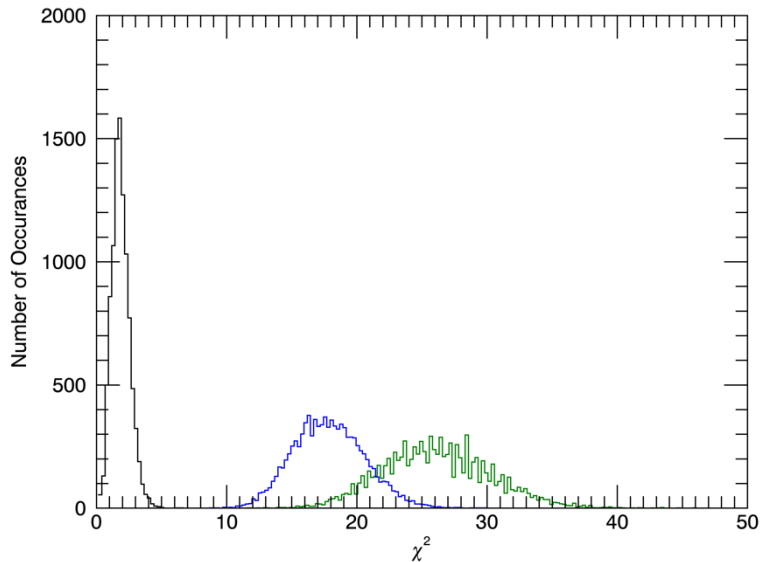
Figure 3. Chi square distributions for 10,000 simulated bursts. *Colors correspond with Figure 2; correct model in black.*

Origins of Line Defects in Self-Reacting Friction Stir Welds and Their Impact on Weld Quality

Judy Schneider, Professor
University of Alabama in Huntsville, Huntsville, Al 35899

Arthur C. Nunes, Jr., Weld Theoretician
NASA, Marshall Space Flight Center, Al 35812

Nomenclature

AA	aluminum alloy
AS	advancing side
Cu	copper
C-FSW	conventional friction stir welding
EDS	energy dispersive x-ray spectroscopy
FSW	friction stir welding
HAZ	heat-affected zone (of a weld)
MSFC	Marshall Space Flight Center
NASA	National Aeronautics and Space Administration
ROD	residual oxide defect
RT	Room Temperature (22°C)
RS	retreating side
SEM	scanning electron microscopy
SR-FSW	self-reacting friction stir welding
TEM	transmission electron microscopy
UTS	Ultimate Tensile Strength
V	travel velocity of the friction stir welding tool
ω	angular velocity of friction stir welding tool

Abstract

Friction stir welding (FSWing) is a solid state joining technique which reduces the occurrence of typical defects formed in fusion welds, especially of highly alloyed metals. Although the process is robust for aluminum alloys, occasional reductions in the strength of FSWs have been observed. Shortly after the NASA-MSFC implemented a variation of FSW called self-reacting (SR), low strength properties were observed. At that time, this reduction in strength was attributed to a line defect. At that time, the limited data suggested that the line defect was related to the accumulation of native oxides that form on the weld lands and faying surfaces. Through a series of improved cleaning methods, tool redesign, and process parameter modifications, the reduction in the strength of the SR-FSWs was eliminated. As more data has been collected, the occasional reduction in the strength of SR-FSW still occurs. These occasional reductions indicate a need to reexamine the underlying causes.

This study builds off a series of self reacting (SR)-FSWs that were made in 3 different thickness panels of AA2219 (0.95, 1.27 and 1.56 cm) at 2 different weld pitches. A bead on plate SR-FSW was also made in the 1.56 cm thick panel to understand the contribution of the former faying surfaces. Copper tracer studies were used to understand the flow lines associated with the weld tool used. The quality of the SR-FSWs was evaluated from tensile testing at room temperature. Reductions in the tensile strength were observed in some weldments, primarily at higher weld pitch or tool rotations.

This study explores possible correlations between line defects and the reduction of strength in SR-FSWs. Results from this study will assist in a better understand of the mechanisms responsible for reduced tensile strength and provide methodology for minimizing their occurrence.

I. Introduction

I-1   Joint line indications

When weld strength is reduced in FSWing, the seam trace is investigated for clues since the actual solid state joining takes place between the faying surfaces which form the weld seam. Aluminum and its alloys are known to form a native, protective oxide on the surface. It is reported that if these native surface oxides are not sufficiently broken up during the FSW process, they remain in the FSW interior, resulting in a weakened bond strength. This type of linear indication has been referred to as a lazy "S", lazy "Z", joint line defect, kissing bond, or residual oxide defect[1-9]. Inadequate dispersion of the native oxide remaining in the weld nugget was initially identified as the cause of the "joint line remnant" shown in Figure 1. The joint line remnant was believed to be comprised of an array of oxides observed in the macrostructure at very low magnifications. Typically this correlation was made by anodizing the faying surfaces and inspecting the macrograph[9]. No detailed microscopy or elemental analysis was reported in these early studies[6-9]. Ultimately these linear indications were mitigated by modification of the process parameters, such as increased tool rotation rate, which causes a finer breakup of the native oxide particles[9].

| (a) | (b) |
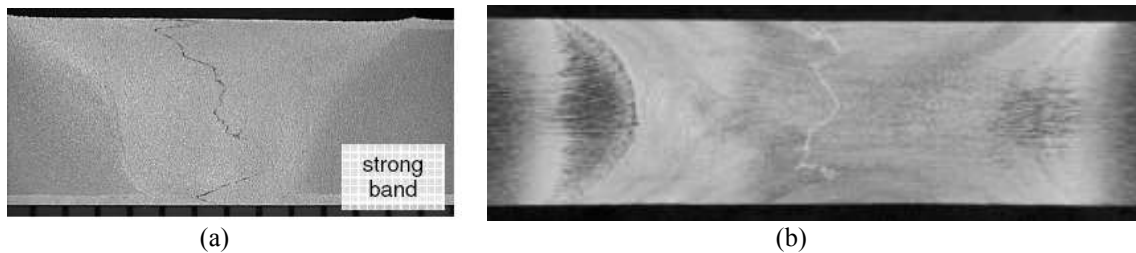
Figure 1. Metallographic images (a) of a C-FSW[10] and (b) a SR- FSW showing a typical joint line remnant feature[9]. The faying surfaces of the panels shown in the macrograph in (b) were anodized prior to the SR-FSW process.

Models of the C-FSW process have promoted the understanding that the joint is formed as the rotation of the pin surface shears the metal thereby exposing fresh un-oxidized surfaces which bond under the resulting load as the tool advances[11, 12]. The resulting fragmented Al_2O_3 particles are theorized to flow collectively during the FSW process and, if of sufficient size, accumulate in the lazy S feature reported. Since the amount of material flow increasingly varies from the root to the crown in C-FSW, most remaining oxide particles are expected to be near the root region[13]. Offsetting the pin to the retreating side (RS) is expected to reduce the size of the oxide to the point of no detection[12] due to the increasing amount of shearing strain.

Studies on AA2xxx series alloys have also reported agglomeration of Al_2Cu particles within the weld nugget. Cao and Kou[14] did a study on the agglomeration of Al_2Cu particles in a C-FSW nugget, and found they tended to form near the former weld seam and near the weld tool. Reynolds, et al.,[15] reported that the agglomeration of particles in the wake of the weld in AA2024 is responsible for the banding features observed. Sherman[16] reported on additional studies of Al_2Cu agglomeration in AA219 and found that the extent of agglomeration tended to increase as the ratio of travel velocity (V) to tool rotation (ω) decreased. The agglomeration was observed near the tool threads and on the root side of a C-FSW with porosity present in the Cu rich region.

There are very few detailed metallurgical studies in the literature on particles present in the FSW nugget. In a study by Sato[13], TEM studies of the particles along the remnant line were found to be amorphous Al_2O_3. This indicated that the oxides were not subjected to high temperatures for any length of time. Because of the amorphous nature, the oxides were attributed to native oxide films on the aluminum surfaces prior to the FSW. Findings in a study by Li et al.[1] contrast the results of Sato[13] and reported the presence of coarsened precipitates of Al_2Cu in the region around a kissing bond defect. Thus this study suggested higher temperatures occurred resulting in the coarsening. No information was provided on identification of any oxide phases present.

Most studies indicate that the joint line remnant can be eliminated by proper selection of FSW parameters of tool rotation, travel, and tilt[1, 4, 9, 17, 18]. In many studies, the remnant line was only visible when the workpiece surfaces were anodized prior to either the SR or C-FSW[3, 9]. Thus these studies indicate that the joint line remnant is

not an indication of inadequate cleaning or extended delay between pre-weld cleaning and the FSW, but rather an indication of non-optimized FSW parameters.

I-2   Aluminum Oxidation

Most theories and studies which regard the oxidation of solid aluminum, consider the first monolayer of oxidation to be virtually instantaneous, and only dependent on the arrival rate of oxygen. This monolayer develops into an amorphous layer whose rate of oxidation is dependent upon both the oxygen arrival rate and the rate of diffusion through the existing oxide layer. Earlier studies published the stable oxide layer at thickness of 2-3 nm[19-21]. Later studies found that the crystalline structure and orientation[22] affected the oxidation rate expanding the thickness range from 0.5 nm[22] to 4 nm[23].

The rate of oxidation for aluminum is reported to be influenced by both temperature and moisture[24]. The kinetics of aluminum oxidation follows a parabolic law in the temperature range 350 to 475ºC, reaching an equilibrium thickness rapidly. At low temperatures (<300º C) the oxide film growth rate is considered to be very fast initially, followed by an abrupt and drastic reduction to virtually zero, or self-limiting, within less than 250 s[25, 26]. At higher temperatures (> 500º C), the oxidation rate changes to linear and the oxide layer can reach a greater thickness which stabilizes at approximately 200 nm[25, 26]. The native oxide layer is amorphous, but can crystallize at elevated temperatures[22]. The kinetic rate is reduced as the oxide layer changes from amorphous to crystalline.

Based on a review of the literature, the concern regarding initial oxidation films on the workpiece would not be expected to be affected by delays between cleaning and FSWing. The initial stable oxide layer would not be expected to increase in thickness as a function of additional time at room temperature. As a stable oxide layer of 1-2 nm is noted to form within 250 s, any delays between cleaning and welding would not be expected to result in thicker oxide layers. Even in the presence of high humidity, a stable layer is still expected to form within seconds. However the noted change in oxidization rates at temperatures greater than 500ºC, suggest that the linear indications have no correlation with the native oxides on the surface of the aluminum workpiece prior to welding, but instead occur during the FSW process. Thus the occurrence of joint line remnants or line indications may correlate with FSW temperature due to weld parameters as they influence the FSW temperature and resulting weld microstructure[13, 14].

Rather than considering the native oxide responsible for internal oxidation within a FSW, it is possible that the heated material is oxidized during the FSW process. Krishnan[11] commented on the report of oxides in a manuscript by Larsson[29] and speculated that oxides could form along the layers of metal as they are sheared and consolidated in the wake of an aluminum alloy FSW. Speculation was made that at some point, purge gases might be required to avoid oxidation. Since then various studies have investigated the effect of the joint line remnant on mechanical properties and have found no detrimental effect in C-FSWs[1-5, 13].

Another source of in process oxidation could be related to the heat zone around the root and shoulder crown. If the foot print of this heat zone is larger than the foot print of the shoulder, it could experience increased oxidation in advance of the weld tool which could be stirred into the weld nugget.

I-3   Aluminum alloy 2219

The elemental composition of aluminum alloy 2219 is summarized in Table I[30]. It can be represented by the Al-Cu binary phase diagram shown in Figure 2 with the dashed line representing the elemental composition of AA2219. The alloy is age hardened with the precipitation sequence given in eq. (1). After a solutionizing heat treatment, the GPI and II phases precipitate out to strengthen the alloy. θ is the equilibrium phase and has the elemental composition of Al_2Cu. As can be observed from the phase diagram, 2219 will have some excess θ phase since its elemental composition range is higher than the maximum solubility. Due to the elemental range acceptable for Cu in 2219, the excess θ could vary.

Table I. Elemental composition of AA2219[30].

Aluminum, Al	91.5 - 93.8 %
Copper, Cu	5.8 - 6.8 %
Iron, Fe	<= 0.30 %
Magnesium, Mg	<= 0.02 %
Manganese, Mn	0.20 - 0.40 %
Other, each	<= 0.05 %
Other, total	<= 0.15 %
Silicon, Si	<= 0.20 %
Titanium, Ti	0.02 - 0.10 %
Vanadium, V	0.05 - 0.15 %
Zinc, Zn	<= 0.10 %
Zirconium, Zr	0.10 - 0.25 %
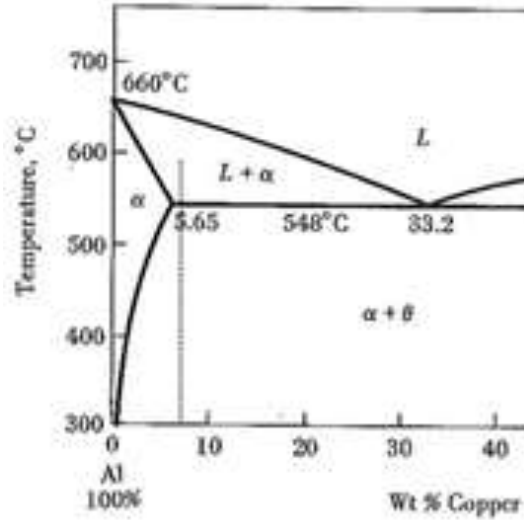
Figure 2. Binary phase diagram for Al-Cu.
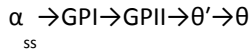
$$\alpha_{ss} \rightarrow GPI \rightarrow GPII \rightarrow \theta' \rightarrow \theta \qquad\qquad [eq. 1]$$

II. Experimental Procedures

This study builds off a series of SR-FSWs made in 3 different thicknesses of panels of AA2219-T87 that were nominally 10 cm wide by 61 cm long. Panel thicknesses used were 0.95, 1.27, and 1.59 cm. All welds were made in the butt weld configuration using the ESAB LEGIO machine at the NASA-Marshall Space Flight Center operated in load control. An additional bead on plate (BOP) weldment was made in the 1.59 cm thick panel to evaluate the effect of the weld seam. The BOP on plate weld length was shorter as 3 weld pitches were used on one panel; therefore the overall weld length of approximately 18 cm long was lower than the butt welded configurations. A threaded pin with 3 flats was used with scrolled shoulders. All panels were stitch tacked prior to the SR-FSW process using a conventional FSW tool with a shortened pin.

The weld parameters are summarized in Table II along with the logged torque for the shoulder and the pin. The LEGIO configuration independently drives the upper shoulder from the pin and lower shoulder. Thus there is a separate torque measurement associated with the upper shoulder, and another torque measurement associated with the pin and lower shoulder. Because of the combined drive of the pin and the lower shoulder, the pin/lower shoulder torque has a higher value.

Nominally 3 specimens were removed from each weld panel and metallographically prepared to view the transverse section. The specimens were taken from the beginning section of the weld and designated M01, the middle of the weld and designated M02, and the end of the weld and designated M03. The specimens were mounted in a phenolic, ground, polished, and etched using Keller's to reveal the macrostructure.

Macrographs were made of the etched and polished specimens using a Nikon digital camera with a macro lens. Optical microscopy with a Leica was used to obtain bright field and dark field montages.   Higher magnification images were made using an environmental, field emission (FE) FEI Quanta 600 scanning electron

microscope (SEM) operated at 8 and 15 keV and configured with an energy dispersive spectrometer (EDS) operated at 15 keV. SEM images were obtained using the backscatter detector (BSI).

A total of 6 specimens were tested at room temperature for each of the 6 panels per material thickness in addition to the BOP. The tensile tests were conducted in displacement control at a rate of 0.127 mmpm at room temperature (RT).   Stress measurements were calculated using the load cell data and specimen cross sectional area. Strain measurements were obtained directly from the use of extensometers for the butt welds and from the cross head displacement for the BOP weld.

To evaluate the oxygen content of the SR-FSW nugget region, 3 specimens were sent out to Westmoreland Laboratories for LECO analysis in addition to the parent material. At the conclusion of the summer, this analysis has not been completed.

Evaluation of the surface material into the weld nugget was evaluated by the use of 0.15 mm thick Cu applied using a plasma spray process to the surface of 6.4mm thick 2219 panels. The Cu was plated onto either the AS crown or root surfaces as shown in Figure 3 just prior to the transition zone.   X-ray radiographs were made at the NASA-MSFC of the resulting plan and transverse views to document Cu entrainment into the weld nugget.

Table II. SR-FSW Schedule

Panel ID	Thickness (cm)	Pinch force (kN)	Weld pitch (rev/mm)	Spindle torque (N-m)	Pin torque (N-m)
P13	0.95	0.9	0.64	113	147
P14	0.95	0.9	0.64	107	154
P15	0.95	0.9	0.64	108	154
P16	0.95	0.9	0.67	118	143
P17	0.95	0.9	0.67	125	140
P18	0.95	0.9	0.67	124	137
P01	1.27	2.2	0.73	143	265
P02	1.27	2.2	0.73	143	262
P03	1.27	2.2	0.73	145	260
P04	1.27	2.2	0.84	162	215
P05	1.27	2.2	0.84	163	213
P06	1.27	2.2	0.84	164	215
P07	1.59	2.0	0.79	170	292
P08	1.59	2.0	0.79	161	295
P09	1.59	2.0	0.79	154	301
P10	1.59	2.2	0.87	179	250
P11	1.59	2.2	0.87	162	262
P12	1.59	2.2	0.87	168	259
BOP 1	1.59	2.0	0.79	161	297
BOP 2	1.59	2.2	0.82	162	279
BOP 3	1.59	2.2	0.87	170	244
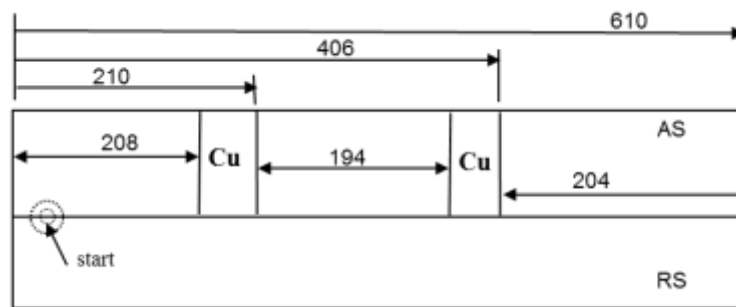
Figure 3. Configuration of weld panels with Cu plating over a 38mm wide zone. Units are in mm.

III. Results and Discussion

III-1   Mechanical Properties

Although 3 thickness panels were welded and evaluated, only the results from the 1.59 cm thick SR-FSWs will be presented in this report. The remainder of the data is published elsewhere[31]. Figures 4 and 5 present the mechanical property data for the 1.59 cm panel thickness for the butt weld and bead on plate configurations, respectively. The strength values are normalized to the acceptance values[32]. A reference line is drawn at 100% of the design allowable for the UTS and at 10% strain for the elongation to failure plots.

Only one of the butt welded panels displayed reduced UTS and elongation to failure at the higher weld pitch. A similar reduction in strength was observed for BOP 3, which was run at the same SR-FSW process parameters as 625-P10.   Overall the differences in the properties between the butt weld and the BOP SR-FSWs could be attributed to the difference in weld length. The butt weld was 61 cm long vs the 18 cm long BOP. Both the butt weld and the BOP weld showed reduced UTS at the higher weld pitch. Thus the faying surfaces of the weld seam are not solely responsible for reduced properties.
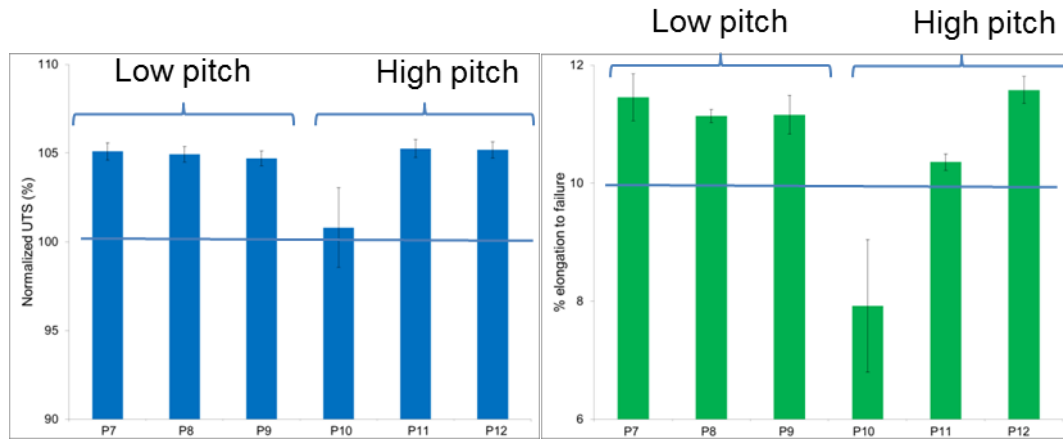
Figure 4. Summary of the normalized UTS (a) and % elongation to failure (b) of the 1.59 cm thick SR-FSW panels tested at RT.
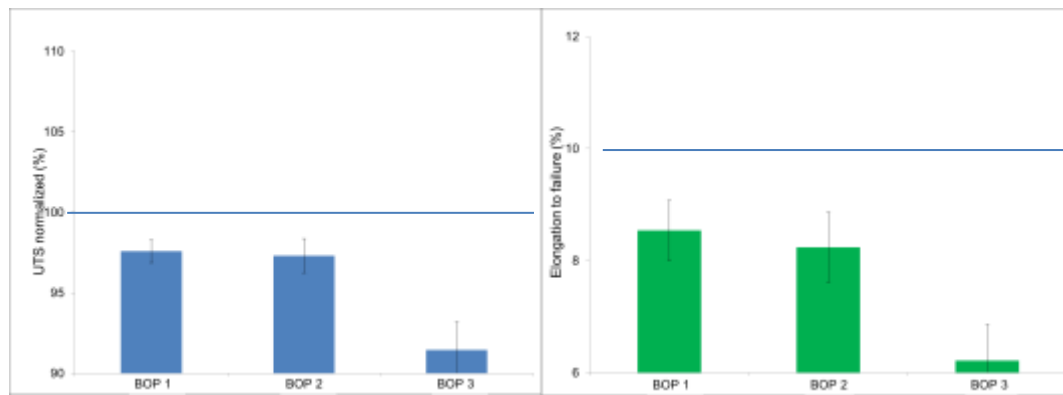
Figure 5. Summary of the normalized UTS (a) and % elongation to failure (b) of the 1.59 cm thick SR-FSW BOP panels tested at RT.

III-2   *Metallographic studies*

Representative specimens for metallurgical analysis were selected on the basis of nominal and lowest properties. Figure 6 and 7 present a group of images taken of specimen 625-P10, which had the lowest mechanical properties and was welded at the higher weld pitch weld in the 1.59 cm thick, butt welded panels.

An overall photograph of the transverse section of the etched weld is shown in Figure 6a. Image montages were made of the specimen in the unetched condition to show the location of line features. Montages were made of the specimen using bright field (Figure 6b) and dark field (Figure 6c). Various line features were found and are highlighted on Figure 6b and 6c. This area was marked with carbon tape and a corresponding BSI montage was made in the SEM and is shown in Figure 6d. These line features were common to all the SR-FSWs made in this study.
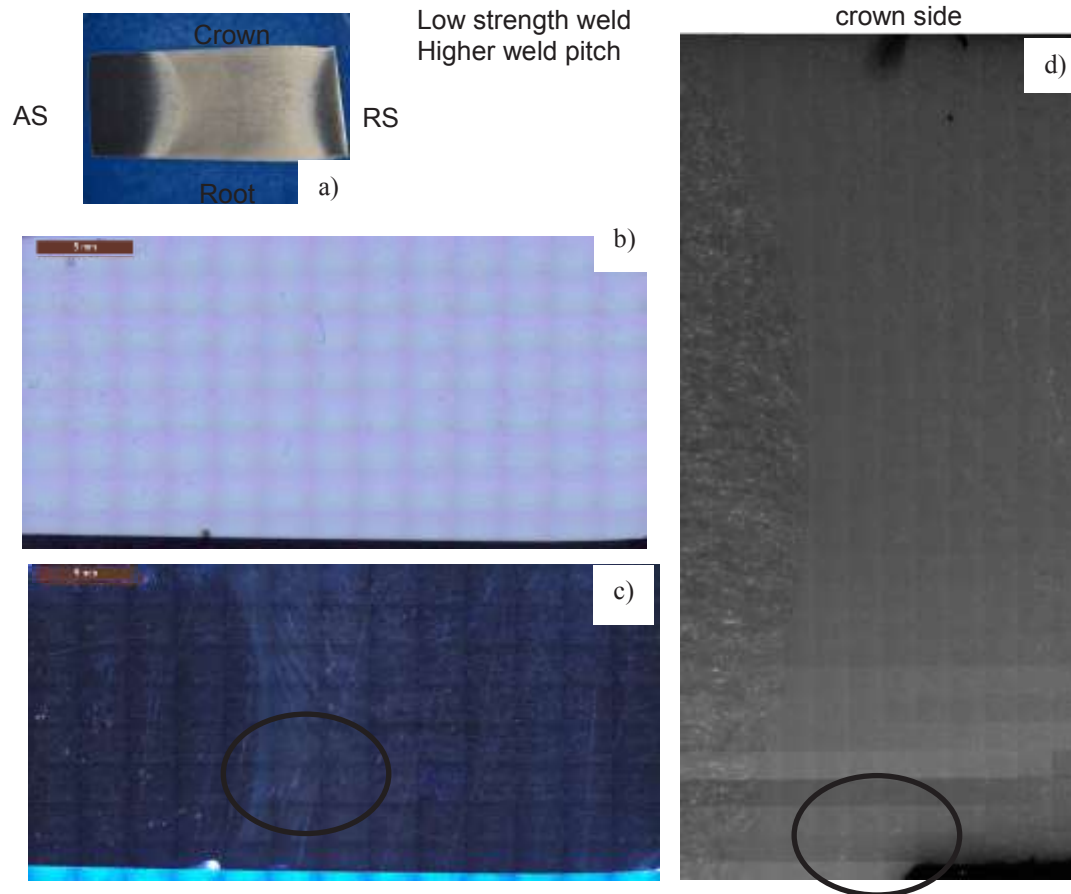
Figure 6. Optical images of the unetched metallographic of specimen 650-P10. This specimen was welded at the higher weld pitch and displayed the lowest UTS and ductility. An overall photograph of the transverse section of the weld is shown (a). Montages were made of the specimen using bright field (b) and dark field (c). Identified regions (shown in circle on (c) were imaged in the SEM and a montage is shown of this region (d).

Figure 7 shows higher magnification SEM BSI of the region of the unetched metallographic specimen circled in Figure 6d. The white regions observed are Cu rich (30 to 35 wt%). The Cu rich regions also showed slight amounts of Mn (1-2 wt%) and Fe (4 to 6 wt%). EDS analysis showed no appreciable indication of oxides present (0.5 to 0.6 wt%) in any of the regions.
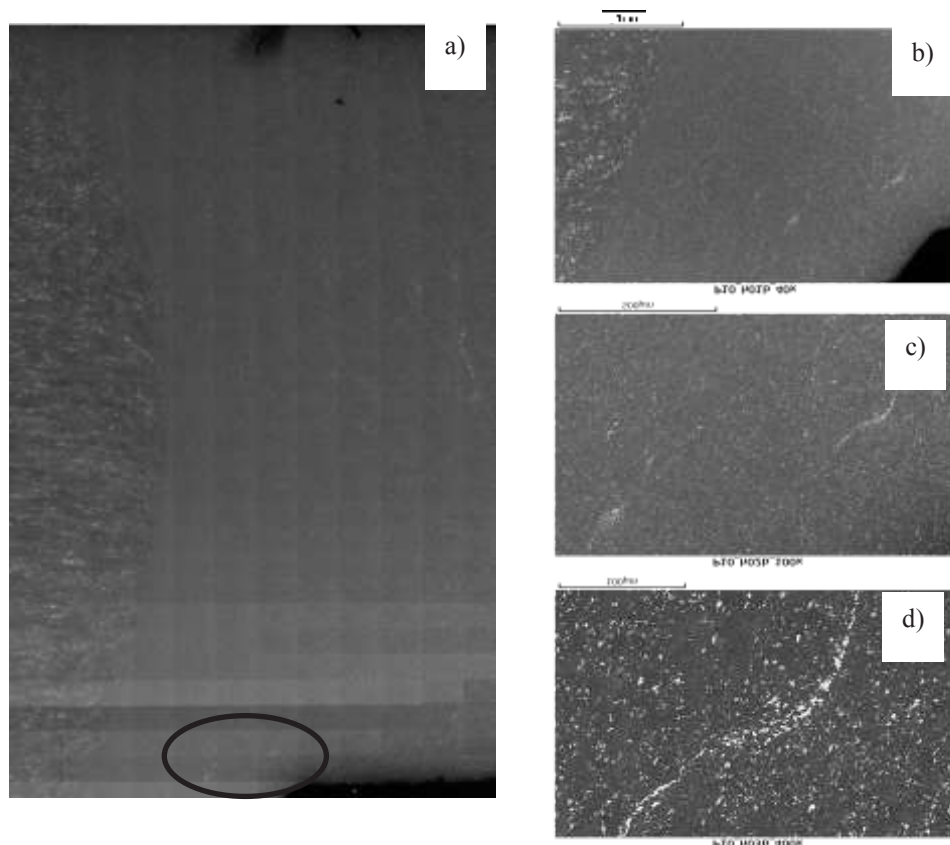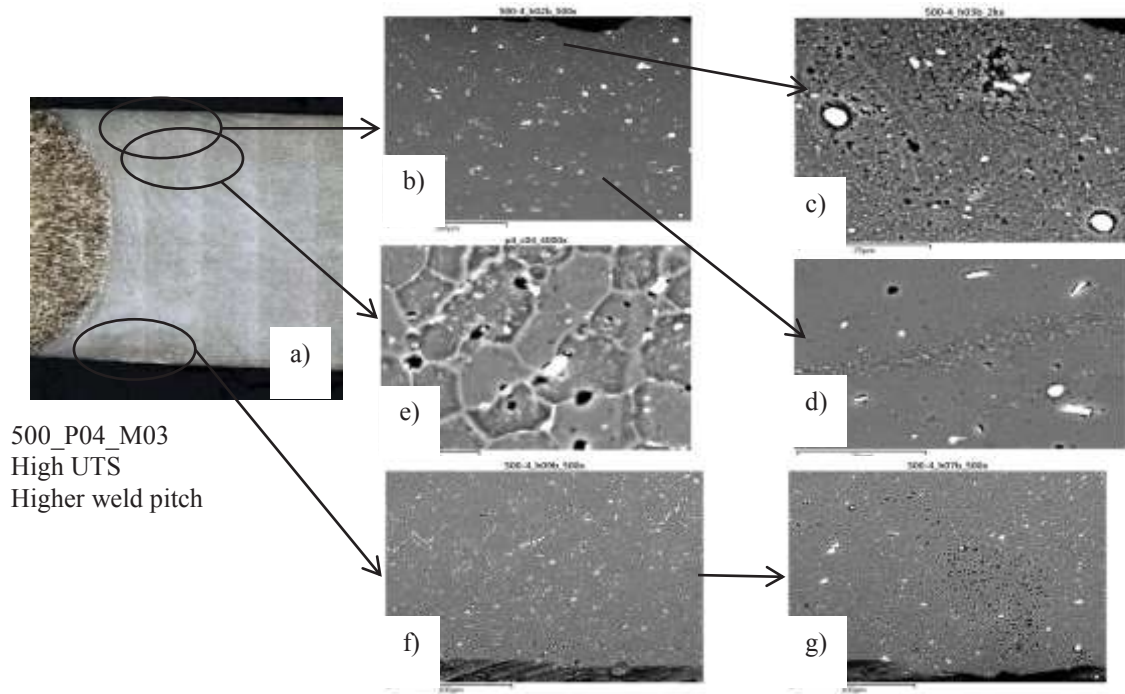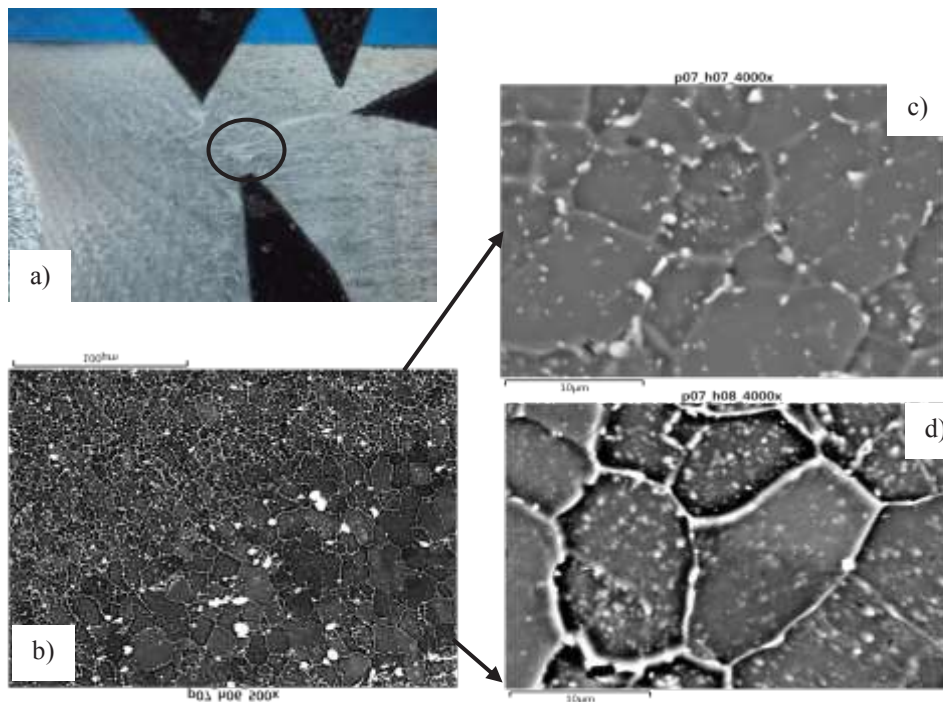
Figure 7. SEM of the unetched metallographic BS image of specimen 650-P10 (a). This specimen was welded at the higher weld pitch and displayed the lowest UTS and ductility. The white regions are Cu rich with negligible indication of oxides present. (b-d) show magnifications of the region circled in (a).

SEM-BSI for the etched metallographic specimen 500-P04 are shown in Figure 8. This specimen was welded at the higher weld pitch, but displayed nominal UTS and ductility. A range of porosity is observed at the crown (Figure 8b and 8c) and root (Figure 8f and 8g) surfaces. Pores are noted to contain Cu rich particles as shown in Figure 8e. From EDS, the Cu rich regions have 27 wt% Cu with similar levels of Mn and Fe as the Cu rich regions in Figures 6 and 7. However, this region has more oxygen (5-6 wt%) than measured in Figures 6 and 7. The base material in this region has an oxygen content of 2-3 wt% with no detectable Mn or Fe.

SEM-BSI for the etched metallographic specimen 625-P07 are shown in Figure 9. This specimen was welded at the lower weld pitch and displayed nominal UTS and ductility. An overview of the specimen in Figure 9a shows light and dark banded regions. A close up of the banded structure circled in Figure 9a is presented in Figure 9b. From this magnification, it appears that the bands correspond to "fine" and "coarse" grains. Close up of the fine grained region in Figure 9c, compared to the close up of the coarse grained region in Figure 9d, show comparable grain sizes. However in Figure 9c there appear to be more sub-boundaries present within a grain. The similar surface appearance of each grain in this etched specimen, suggests an overall crystallographic texture in this region. While there are Cu particles along the grain boundaries in Figure 9c, they do not appear to be continuous. In contrast, the coarse grain region in Figure 9d shows more variation on the etched grain surfaces suggesting a more random orientation of the grains. Very few sub-boundaries can be observed. In addition, the grain boundaries appear to have more continuous Cu present. Such variations within a FSW nugget have been correlated with various textures resulting from the thermo-mechanical deformation occurring during the FSW process[33, 34].

Figure 8. SEM-BSI of the etched metallographic BS image of specimen 500-P04 (a). This specimen was welded at the higher weld pitch and displayed nominal UTS and ductility. A range of porosity is observed at the root and crown surfaces (b, c, f, g). Pores are noted to contain Cu rich particles (e).

Figure 9. SEM-BSI of the etched metallographic BS image of specimen 625-P07. This specimen was welded at the lower weld pitch and displayed nominal UTS and ductility. Variations in weld texture (a) and grain boundaries (c and d) are observed within the weld nugget. A close up of the banded structure shown in (a) is presented in (b). Close up of fine grained region is shown (c) along with the coarse grained region (d).

148

Gratecap, et al.[35] has recently published a study on the mechanisms of band formation which are shown in Figure 10a. In this theorized mechanism, the tool oscillations force the sheared bands of metal together in the wake of the FSW. This thermo-mechanical history would be expected to be captured in the metallographic structure, especially in lower pitch welds which would correspond to lower temperatures. Higher pitch welds would be expected to anneal out these variations across the sheared metal band. Figure 10b shows an optical microscopy image of an etched cross section of typical flash formed during a FSW of 2219. A range of microstructural variations can be observed from the tool interface shearing surface to the outer free edge. This variation in microstructure would be expected from variations in temperature, strain, and strain rate in material transported during each tool rotation. Thus it is proposed that this microstructural variation across the layers of sheared material is responsible for the light and dark regions observed in the transverse metallographic images of the weld nugget. More detailed electron back scatter diffraction (EBSD) would be required to verify this hypothesis.

(a)   (b)
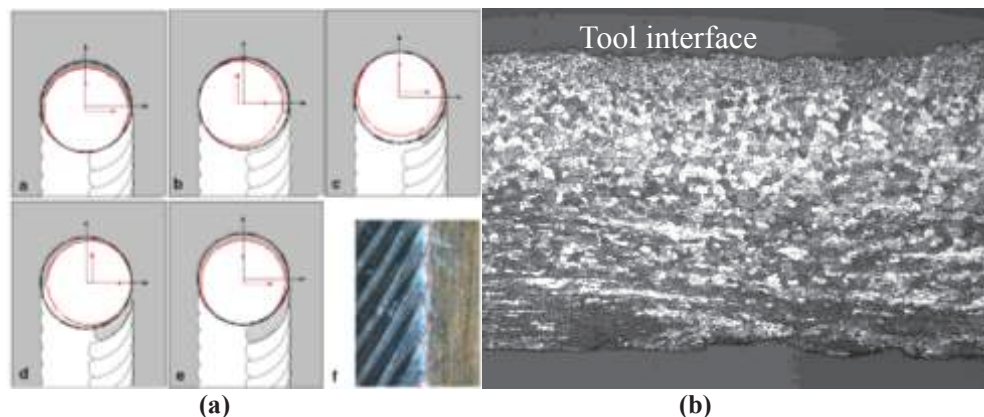
Figure 10. Gratecap's[35] mechanism of band formation during a FSW (a). Optical microscopy image of an etched cross section of typical flash formed during a FSW of 2219 (b). A range of microstructural variations can be observed from the tool interface shearing surface to the outer free edge.

Figure 11 shows additional images from specimen 625-P07 in which Cu particles are aligned within the weld nugget, presumable along shear bands from the SR-FSW process. Most noteworthy on these Cu particles are the features within them which resemble the forehead of a Klingon. The light regions have a high concentration of Cu (42-45 wt%) with 1-2 wt% of oxygen. A similar amount of Mn and Fe are noted as in the areas in Figure 7 and 8, but there now appears Sb (2-3 wt%). The lighter region surrounding the bright Cu particle has approximately 34 wt% Cu with minor 0.5 wt% oxygen and none of the trace elements (Mn, Fe, Sb). The Cu rich regions are approximately 7 μm in diameter.
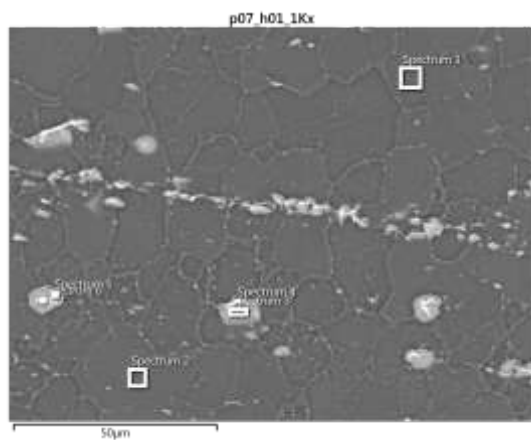
Figure 11. Cu rich bands in weld nugget of specimen 625-P07. This specimen was butt welded at the lower weld pitch in 1.59 cm thick panels.

For comparison, Figure 12 shows the Cu rich regions in the parent material used in 2015 welds vs 2016 welds. The morphology and elemental content is similar to that shown in Figure 11 for the refined Cu rich region in the FSW nugget. Figure 12b shows larger light regions which correspond to the θ phase. This area is surrounded by a slightly lower concentration of Cu which corresponds to the eutectic composition.
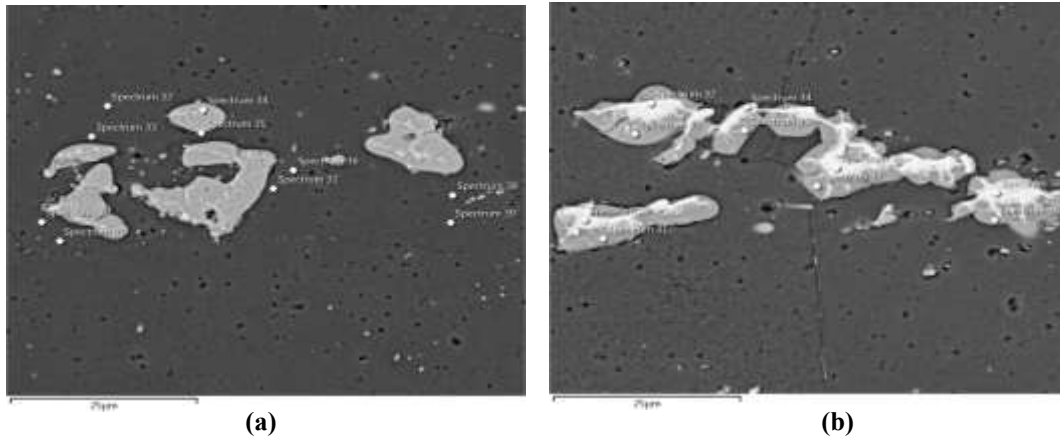

(a)   (b)

Figure 12. SEM BSI of Cu rich regions in the parent material from SR-FSWs made in 2015 with an average size of 10 μm (a) and in in 2016 with an average size of 20 x 7 μm.

Table III summarizes the elemental composition, recommended heat treatment temperatures and a summary of the expected welding temperatures for AA 2219. The range of Cu content for AA2219 of 5.8 to 6.8 wt% exceeds the solid solution composition of 5.65 wt%. Thus AA2219 is a two phase alloy comprised of α + θ phases. The recommended heat treatment is to solid solutionize at 535º C, which is just below the eutectic temperature of 548º C.

Table III. AA2219 elemental composition, eutectic temperature, heat treatment temperature, and expected welding temperature.

θ composition: Al_2Cu (54 wt% Cu)
Eutectic composition: 33 wt% Cu
Eutectic temperature: 548º C

Heat treatment:
    535º C (SS)
    175º C/18 h (age)

Welding temperature:
    0.90 Tmp = 567º C
    0.85 Tmp = 520º C
    0.80 Tmp = 473º C

The expected temperatures during a FSW process are in the range of 0.90 to 0.80 homologous temperatures. These temperatures are noted to be close to the eutectic temperature which could be easily exceeded in a weld with a higher pitch or higher RPM.

In a survey of heat treatment on aluminum alloys, noted defects are reported for 2xxx series alloys during either the solutionizing or quenching steps of heat treatments[36]. The quenching defects are primarily related to

cracking and distortion. However during the solutionizing step, either oxidation or incipient melting is reported. The oxidation occurs at elevated temperatures and if sufficient moisture is present, the moisture can decompose releasing hydrogen and related porosity.

Incipient melting is reported to occur when coarse particles of Al_2Cu are present. High up-quenching rates in 2xxx series alloys provide inadequate time for the Al_2Cu particles to dissolve[37]. Thus they melt if of sufficient size and the temperature exceeds that of the eutectic. Incipient melting has been reported in FSW of 2219 when Cu content was at the higher 6.31wt% end of the compositional range rather than the lower 5.83wt% end[38].

Figure 13 shows an optical metallographic image of an etched specimen which had Cu plated on the AS root surface. Minimal entrainment of the Cu into the weld nugget is observed. The Cu appears to distribute over the surface under the shoulder and highlights flow lines.

Figure 13. Optical microscopy image of an etched sample of a transverse SR-FSW made in 0.63 cm thick plates. Cu was plated on the AS root surface and is shown to have minimal entrainment into the weld nugget region.

Another source of oxygen entering the FSW is related to the temperature and the enhanced oxidation rates above 500º C. As the oxidation rate is noted to increase with increasing temperature, it is conceivable that the faying surface would be prone to increased oxidation during the FSW if exposed to entrained air. At the estimated FSW temperature of aluminum alloys (530 to 580 ºC), the oxidation behavior rate changes from parabolic to linear. The literature reports that the temperature of the FSW panel has been most strongly correlated with the tool rotation[27, 28].

It is generally assumed that minimal entrained air enters the faying surface during a butt weld. However as the weld panels increase in thickness, it has been observed that gaps form along the weld seam in advance of the tool form. As this gap increases, it can provide a passage way for air to enter causing enhanced oxidation at the elevated temperatures. This would be further exasperated if the work piece material was to locally liquate at the welding temperature. Exposure to air at these temperatures would oxidize these molten regions which would tend to be located at the grain boundaries.

Additionally at higher weld pitches, the heat profile may extend outside the shoulder envelope as shown in Figure 14a. This would expose high temperature surface material to air promoting oxidation. Under lower weld pitch, the heat profile maybe kept within the shoulder envelope as shown in Figure 14b. This would reduce the potential for surface oxidation during the SR-FSW.
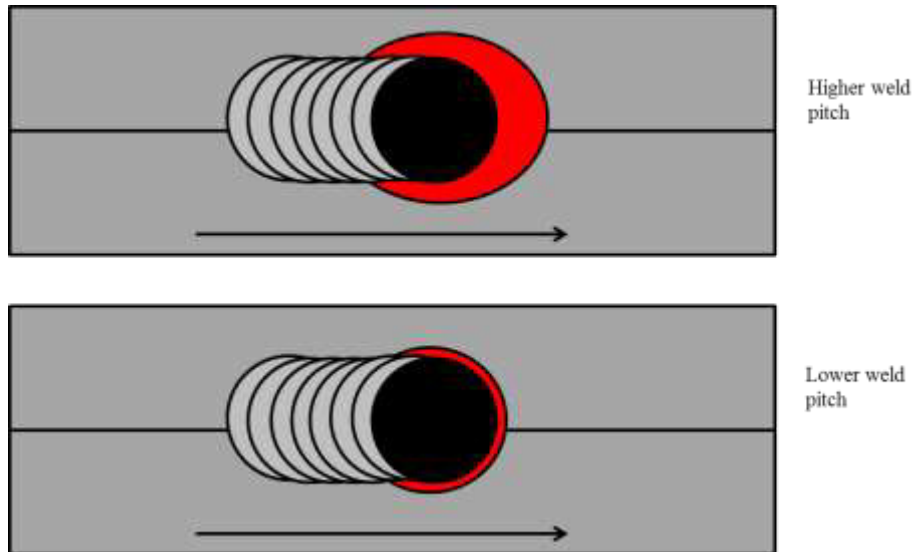
Figure 14. At higher weld pitch, the heat profile extends past the tool shoulder (a) while at lower weld pitch, it is possible to keep the heat profile within the tool shoulder envelop.

The chemical composition will also affect the resulting 2nd phases present in the panels. Cu content can vary in AA2219. With higher Cu concentrations, there would be more excess θ phase which could explain variation among different lots of AA2219 or even along the length of a weld panel. Refinement of the θ phase may also vary as a function of the initial panel thickness. As the initial panel thickness increases, it may not be possible to get sufficient work into the plate to refine the excess θ particles.

V. Summary

Studies in the literature on the remnant line defect in C-FSWs have concluded that non-optimized parameters are responsible for the reduction observed in mechanical properties. However the seemingly random occurrence of reduced strength in FSWs suggests there is another underlying cause. This study considered the effect of line features observed in FSW nuggets with the weld quality.

Oxidation is not always associated with the line features, which can be either variations in the texture or strings of Cu rich particles. Since thicker oxides require higher temperatures, in excess of 500ºC to form, these would be promoted on the interior surfaces during a FSW if exposed to entrained air especially in regions of localized liquation.

Understanding the underlying cause and effect of the presence of internal oxide within the FSW nugget would improve the robustness of the process. Possible causes include:

1) Variations in amount of alloying elements in the workpiece.
2) Size of initial Al_2Cu particles, possibly as a function of the initial panel thickness.
3) Higher temperatures during SR-FSWs may promote localized liquation in the presence of coarsened Al_2Cu particles.

This study did not find a correlation between line features in metallographs of SR-FSW specimens and reduced weld strength. However, it can be concluded that if the parent material contains coarse θ particles, the up-quenching rate during the FSW process could cause localized (incipient) melting to occur.

As shown in the images presented, θ particles decorate the grain boundaries within the weld nugget. If incipient melting were to occur, the molten material would be most susceptible to oxidation at weld temperatures. The resulting solidification would leave a weakened area at the grain boundary that is difficult to find during routine metallography. Subsequent tensile testing would result in cracks forming along these weakened grain boundaries.

152

Thus it is not believed that the cracks observed in the metallographs of tensile specimens occurred during the welding process nor are they believed to result from native oxides on the surfaces of the weld panels. These cracks, observed post-test, are likely indications of weakened grain boundary regions. These are more prone to occur during the crown and root surfaces and can serve as fracture initiation sites.

Acknowledgments

References

[1]Li, B.. Shen, Y., and Hu, W., "The study on defects in aluminum 2219-T6 thick butt friction stir welds with the application of multiple non-destructive testing methods," *Materials and Design*, Vol. 32, , 2011, pp. 2073–2084.

[2]Chen, H-B., Yan, K., Lin, T., Chen, S-B., Jiang, C-Y., and Zhao.Y., "The investigation of typical welding defects for 5456 aluminum alloy friction stir welds," *MSEA* Vol. 433, , 2006, pp. 64–69.

[3]Klages, H. K., "The "Lazy S" feature in friction stir welding of AA2099 Aluminum-Lithium alloy," Navy Postgraduate School, Monterey, CA, MS Thesis, December 2007.

[4]Leonard, A.J., and Lockyer, S.A., "Flaws in friction stir welds," *4th Intl. Symp. FSWing*, Park City, Utah, May 14-16, 2003.

[5]Liu, H.J., Chen, Y.C., and Feng, J.C., "Effect of zigzag line on the mechanical properties of friction stir welded joints of an Al–Cu alloy," *Scripta Mat*., Vol 55, 2006. pp. 231-234.

[6]SDS 6103 SR-FSW Reference Book, Section 2.1: FY02 SDS 3774 Phase II Friction Stir Welding: Task 1: Characterize Weld Pin Tooling for SR-FSW Process. 0.320-inch-thick 2219-T87/2195-T8M4SR-FSW 0.5-20 Left-Handed Thread Pin Extreme Weld Parameter Map and Verification Welds, Lockheed Martin.

[7]SDS 6103 SR-FSW Reference Book, Section 2.2 SDS 3774 FY02 Phase II Friction Stir Welding Task 1 Characterize Weld Pin Tooling for SR-FSW Process 0.320-inch-thick 2219-T87/2195-T8M4 SR-FSW Extreme Weld Parameter Maps and Process Envelopes, Lockheed Martin.

[8]SDS 6103 SR-FSW Reference Book, Section 3.1, SDS 3774 FY02 Phase II Friction Stir Welding Task 1 Characterize Weld Pin Tooling for the SR-FSW Process Draw Filed Weld Joint Quick Look, Lockheed Martin.

[9]SDS 6103 SR-FSW Reference Book, Section 3.2, SDS 6103 FY03 Phase II Friction Stir Welding Task 1 0.320t Weld Schedule Development Pre Weld Cleaning Method. Lockheed Martin.

[10]Private conversation with Murray Mahoney, formerly of Rocketdyne, January 2016.

[11]Krishnan, K.N., "On the formation of onion rings in friction stir welds," *MSEA*, Vol. 327, 2002, pp. 246–251.

[12]Nunes, Jr., A. C., "Metal Flow in Friction Stir Welding," Conf. Proc., MS&T, 2006.

[13]Sato, Y.S., Yamashita, F., Sugiura, Y., Park, S.H.C, and Kokawa, H., "FIB-assisted TEM study of an oxide array in the root of a friction stir welded aluminum alloy," *Scripta Mater*., Vol. 50, 2004, pp. 365–369.

[14]Cao, G., and Kou, S., "Friction stir welding of 2219 aluminum: behavior of θ (Al2Cu) particles," *Welding J. Supp*., 2005, pp. 1s-8s.

[15]Sutton, M.A., Yang, B., Reynolds, A.P., and Taylor, R., "Microstructural studies of friction stir welds in 2024-T3 aluminum," *MSEA*, Vol. A323, 2002, pp. 160–166.

[16]Sherman, P.S., "Investigation of agglomerated theta particle formation in 2219 aluminum," Final Report NASA SFFP, NASA-MSFC, 2006.

[17]Liu, H.J., Fujii, H., Maeda, M., and Nogi, K., "Tensile fracture location characterization of friction stir welded joints of different aluminum alloys," *J. Mater. Sci. Technol*., Vol. 20, 2004, pp. 103–105.

[18]Kim, Y.G., Fujii, H., Tsumura, T., Komazaki, T., and Nakata, K., "Three defect types in friction stir welding of aluminum die casting alloy," *MSEA*, Vol. 415, 2006, pp. 250–254.

[19]Doherty, P.E., and Davis, R.S., "Direct Observation of the Oxidation of Aluminum Single-Crystal Surfaces," *J. Appl. Phys.*, Vol. 34, 1963, pp. 619-628.

[20]Thomas, K., and Roberts, M.W., "Direct Observation in the Electron Microscope of Oxide Layers on Aluminum," *J. Appl. Phys.*, Vol. 32, 1960, pp. 70-75.

[21]Steinheil, A., "Struktur und wachstum duenner obserflaechenschiechten auf metallen bei oxydation an luft," *Ann. Phys.*, Vol. 19, No. 5, 1934, pp. 465-483.

[22]Trunox, M.A., Schoenitz, M., Zhu, X., and Dreizin, E.L., "Effect of polymorphic phase transformations in Al_2O_3 film on oxidation kinetics of aluminum powders," *Combustion & Flame*, Vol. 140, 2005, pp. 310-318.

[23]Sanchez-Lopez, J.C., Gonzalez-Elipe, A.R., and Fernandez, A., "Passivation of nanocrystalline Al prepared by the gas phase condensation method: an XPS study," *J. Mater. Res.*, Vol. 13, No. 3, p. 703-710, 1998.

[24]Hart, R.K., "The oxidation of aluminum in dry and humid oxygen atmospheres," Proceed. Royal Society of London, Series A. Mathematics & Physical Sciences, Vol. 236, No. 1204, 1956, pp. 68-88.

[25]Smeltzer, W.W., "Oxidation of Aluminum in the Temperature Range of 400º to 600º C," *J. Electrochemical Soc.*, 1956, pp. 209-214.

[26]Jeurgens, L.P.H., Sloof, W.G., Tichelaar, F.D., and Mittemeijerc, E. J., "Growth kinetics and mechanisms of aluminum-oxide films formed by thermal oxidation of aluminum," *J. Appl. Phys.*, Vol. 92, 2002, pp. 1649.

[27]Record, J.H., Covington, J.L., Nelson, T.W., Sorensen, C.D., and Webb, B.W., "A look at statistical identification of critical process parameters in friction stir welding," *Welding J.*, Vol. 86, No. 4, 2007, pp. 97s - 103s.

[28]Schneider, J.A., Stromberg, R., Schilling, P., Cao, B., Zhou, W., Morfa, J., and Myers, O., "Processing effects on the friction stir weld stir zone," *Welding J.*, 2013, pp. 11s-19s.

[29]Larsson, H., Karlsson, L., Stoltz, S., and Bergqvist, E-L., "Joining of dissimilar Al-alloys by Friction Stir Welding," *2nd Intl. Symp. FSW*, TWI, Gothenburg, Sweden, 2000.

[30]http:\\www.matweb.com, accessed 8/10/16.

[31]Schneider, J.A., Chen, P-S., and Nunes, Jr., A.C., "Formation of oxides in the interior of friction stir welds," Session 9B, *11th Intl. Symp. FSW*, TWI, Cambridge GB, May 17-19, 2016.

[32]Fisher, M., Boeing Company Memo, #EYBF-MAF-14-029, October 16, 2014.

[33]Field, D.P., Nelson, T.W., Hovanski, Y., and Jata, K.V., "Heterogeneity of Crystallographic Texture in Friction Stir Welds of Aluminum," *MMTA*, Vol. 32, 2001, pp. 2869-2877.

[34]Schneider, J.A., and Nunes, Jr., A.C.,"Characterization of plastic flow and resulting micro textures in a friction stir weld," *MMTB*, Vol. 35, 2004, pp. 777-783.

[35]Gratecap, F., Girard, M., Marya, S., and Racineux, G., "Exploring material flow in friction stir welding: Tool eccentricity and formation of banded structures, *Intl J. Matl Forming,* Vol. 5, No. 2, 2012, pp. 99-107.

[36]MacKenzie, D.S., "Heat treating aluminum alloys for aerospace applications," *Heat Treating Progress*, 2005, pp. 36-43.

[37]Reiso, O., Overlie, H-G., and Ryun, N., "Dissolution and melting of secondary Al2Cu phase particles in an AlCu alloy," *MMTA*, Vol. 21, 1990, pp. 1689-1695.

[38]J. Kang, Z-C. Feng, G.S. Frankel, I.W. Huang, G-Q. Wang, and A-P. Wu., "Friction Stir Welding of Al Alloy 2219-T8: Part I-Evolution of Precipitates and Formation of Abnormal Al_2Cu Agglomerates," *MMTA*, Vol. 47, No. 9, 2016, pp. 4553-4565.

Integrating Lightning Interferometers and Mappers to Understand On-Orbit Lightning Observations

Richard G. Sonnenfeld*

New Mexico Tech, Socorro, New Mexico, 87801, USA

William J. Koshak[†] and Richard J. Blakeslee [†]

Earth Science Office, Mail Stop ZP11 Huntsville, AL 35805, USA

The Geostationary Lightning Mapper (GLM) will provide continuous coverage of lightning activity over much of the Western Hemisphere, including over the continental US. Lightning Mapping Arrays (LMAs) will be among the devices used for ground validation. We demonstrate why a new instrument, the lightning interferometer (INTF), is likely to better correspond to what is seen on orbit. Initial progress has been made on better integrating INTFs with LMAs to enable analysis that cannot be done with either instrument alone.

Nomenclature

deltaE	Electric-field change
FOV	Field of View
GLM	Geostationary Lightning Mapper
INTF	Broadband Digital Lightning Interferometer
LIS	Lightning Imaging Sensor
Langmuir	Langmuir Laboatory for Atmospheric Physics
LEFA	Langmuir Electric-field Array
LMA	Lightning Mapping Array
SNR	Signal to Noise Ratio

I. Introduction

The Geostationary Lightning Mapper, to be launched with GOES-R in late 2016 will revolutionize lightning observations in the US by providing continuous coverage of all lightning observable from space over the continental US. As with any new sensor, it is necessary to *validate* that it performs according to certain performance criteria. Beyond validation, one wants to glean all that one can from GLM's output. After we consider validation briefly, we will discuss how a new instrument, the Broadband Digital Lightning Interferometer (INTF) can extend what we learn with GLM. It is also worth noting that LIS on the International Space Station (LIS-ISS), a flight-qualified spare of the now discontinued LIS on the Tropical Rainfall Measuring Mission (LIS-TRMM) will be orbitted at the same time as GLM.

II. Validation

The validation requirements for GLM are simply put.

Detection Efficiency At least 70% of all lightning flashes over the observed area (averaged over a 24 hour period) should be detected

---

*Professor and Research Scientist, Physics Dept and Langmuir Laboratory
[†]Senior Scientists, NASA/MSFC

False Alarm Rate No more than 5% of flashes reported by GLM (over 24 hours) can be something else (e.g. transients due to solar glint, brightness edges, or triggers from radiation)

Location Accuracy Flashes are to be located to within 1/2 pixel of the on-board CCD. This accuracy corresponds to 4 km at nadir (directly below the instrument) and 7 km at zenith (at the edges of the FOV).

Time Accuracy The sample rate of GLM is 500 Hz. It is required that time stamps on flashes be accurate to within one sample period.

GLM detects light with $\lambda = 777.4 \pm 1$ nm wavelength. This is a tuned to a P-S emission line of atomic Oxygen (see page 319 of Kuhn)[1] which is collisionally excited by both heat and free electrons in a partially ionized lightning channel.[?] Tuning to this narrow emission line of lightning helps reduce background, but there is still overall only a 6:1 SNR for the instrument. Detection Efficiency of GLM is reduced during the day simply because there is more scattered light. GLM uses a real-time event processor (RTEP) which continually subtracts out "background" illumination and looks for sudden changes in pixel brightness relative to background.
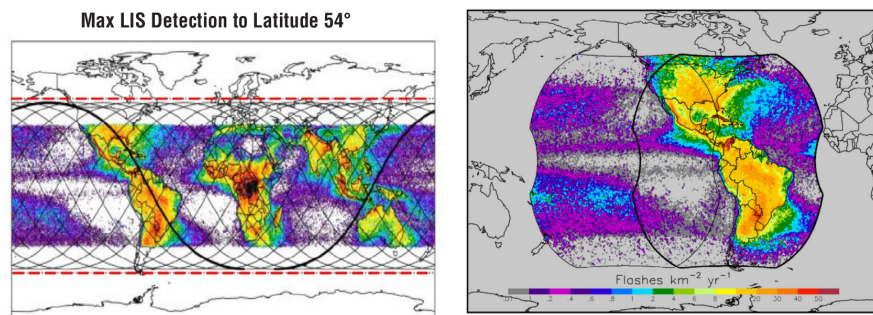
Figure 1. The orbital inclination of ISS coupled with the 2° FOV of LIS will give coverage up to 54 ° latitude. GLM will reach 52 ° latitude, but will be staring around the clock.

The coverage of both LIS and GLM is shown in figure 1.[2,3] Note that LIS was in low-earth orbit (400 km) and so only dwelt about 90 seconds on any given FOV. This provided less continuous coverage and also made background subtraction more challenging as the "background" was changing simply because the satellite was rapidly moving. Contrast edges like coastlines challenged the RTEP on LIS (though it worked). Since GLM is geostationary, one would expect background subtraction to work better. Thus, it seems likely that GLM will pass its validation test as studies with LIS show a detection rate of better than 80%. citepChristian.

An obvious question for validation is what the reference for perfection will be. There are two answers, the US National Lightning Detection Network, and Lightning Mapping Arrays. The NLDN is national in scope, whereas LMAs, cover between two and five percent of the US land area[a]. The sensitivity of the US NLDN has been determined by multiple studies citepCummins. The Lightning Mapping Array is assumed to detect 100% of flashes that are within its sensitivity region. The sensitivity region is itself not well defined, and varies from LMA to LMA, but is generally accepted to be at least 100 km from array center for practical accuracies.[4,5] It is scientifically interesting to understand better what flashes GLM missed that LMA saw. It gets even more interesting if one wants to understand what GLM does *beyond* flash counting. In particular, what processes contribute to perceived brightness at 777.4 nm? Let us look at all the parameters the GLM can provide and see what instruments are most likely to correspond to them.

III.   Toward understanding on-Orbit Radiance

III.A.   Parameters Provided by GLM

After validation, GLM will reliably provide the following parameters, within its hemispheric field of view.

(a) Flash time, date, and centroid Determined from the "groups" function of processed GLM data

---

[a]I assumed an effective range of 100-200 km from center, weighted based on known array performance and divided by the 48-state land area

(b) Flash extent Another fundamental GLM output.

(c) Received optical energy Determined as a sum of pixel brightness and area for each flash

(d) Brightness vs. time Integrated area vs. time can be measured with < 2 ms resolution

Many lightning climatology studies just use parameter (a), and focus on on flash-rate. However each GLM parameter b–d, "flash extent", "Received energy" or "Brightness vs. time" implies a question about what precise physical processes in the lightning flash contributes to them, and they are interrelated. Flash extent is a combination of projected lightning channel length *and brightness* blurred through cloud layers of varying thickness. Received optical energy is also a combination of area and brightness, and brightness vs. time also includes the area of the bright region. Furthermore, the 777.4 nm band sensed by LIS and GLM corresponds to deexcitation of a particular excited state of (neutral) atomic Oxygen, which corresponds to 1.6 eV or 18,500 Kelvin. Clearly the air must be substantially heated to excite such a line to appear. Thus to fully understand GLM data, one wants a detailed map of the channel *and an understanding of where/when it is most luminous*. I believe that the INTF can be just such an instrument.

III.B. LMA, INTF and Field-Change

The Lightning Mapping Array has revolutionized our understanding of lightning, and has also become a useful and convenient operational tool.[7] However, an LMA is not necessarily the ideal tool for understanding and confirming what space-based optical sensors detect, because LMAs measure RF power (which is roughly proportional to time rate of change of channel current (dI/dt)), while optical power or radiance (R) at 777 nm, (measured by GLM and LIS) requires high temperatures to collisionally excite this transition, and is thus more nearly a function of current (I) than of dI/dt. To put it another way, one can have a large dI/dt (e.g. leader steps) without a large I and one can have a large (I) (e.g. long continuing currents) without a large dI/dt.

Another sensor that measures current (and thus, indirectly, luminosity) better than it measures dI/dt is the venerable electric field change sensor. Electric field E is of course proportional to charge (Q) and charge motion through time (dQ/dt) is current. Krehbiel et al[6] were able to use field-change data at multiple stations to reduce CG flashes to monopole charges and IC flashes to dipole charges, but using field change alone did not allow a more complex map of the channel. Sonnenfeld and Lu were able to use vector field-change to put charge on a channel in multiple locations, which they constrained with the aid of a lightning mapping array.[7] More recently, Bitzer, Christian and Marshall used time of arrival techniques on fast-field change measurements to locate quite a number of additional sources on the channel.[8,9] Most importantly for our topic, *Bitzer showed that fast-field changes corresponded well to LIS strokes, while LMA sources did not.*

Starting in 2012, an "old sensor", the lightning interferometer, pioneered by Hayenga,[10] Rhodes, Shao, and Krehbiel,[11,12] became "new" again, as increasingly capable digital signal processing techniques solved the well-known "phase-wrap" problem and were applied at Osaka,[13] and then in New Mexico.[14,15] Both the LMA and the INTF are RF-based detectors. The LMA uses a 6 MHz band around 60 MHz while the INTF uses a "broadband" between 10 and 80 MHz. This broader band, combined with more sophisticated processing than LMA uses, allows the INTF to locate roughly 10X as many sources per second as the best LMAs. As a result, INTF's can detect much smaller dI/dt impulses than LMAs, and in particular more rapidly moving channels (such as dart leaders and "K-changes") which are ALSO high current events (compared to stepped leaders).

In summer 2015, Sonnenfeld acquired numerous flashes over Langmuir Laboratory in New Mexico with LMA, INTF and LEFA (a deltaE network) simultaneously. Figure 2 well demonstrates the properties of those three instruments for an intra-cloud flash that was centered directly above all of them. The top curve (red, LMA), shows a classic bilevel IC flash that originates at 7 km altitude with a negative leader propagating upward into the upper positive charge center of the storm. Between 7.85 and 7.95 seconds, propagation at 8 km continues with a few points at 6 km in the presumed negative charge region. Late in the flash, between 8.15 and 8.25 second, there appears to be more activity in the lower negative region at 5 km (or perhaps it is more visible because it has reaches a lower positive screening charge). The LMA result matches the Field-change record (green) only in a broad sense. For example, there is an increase in Electric field between 7.95 and 8.0 seconds which reasonably corresponds to the descent of a negative leader also seen in the LMA during that time.[16] What is nearly absent in the LMA data is a quite dramatic feature of the field-change
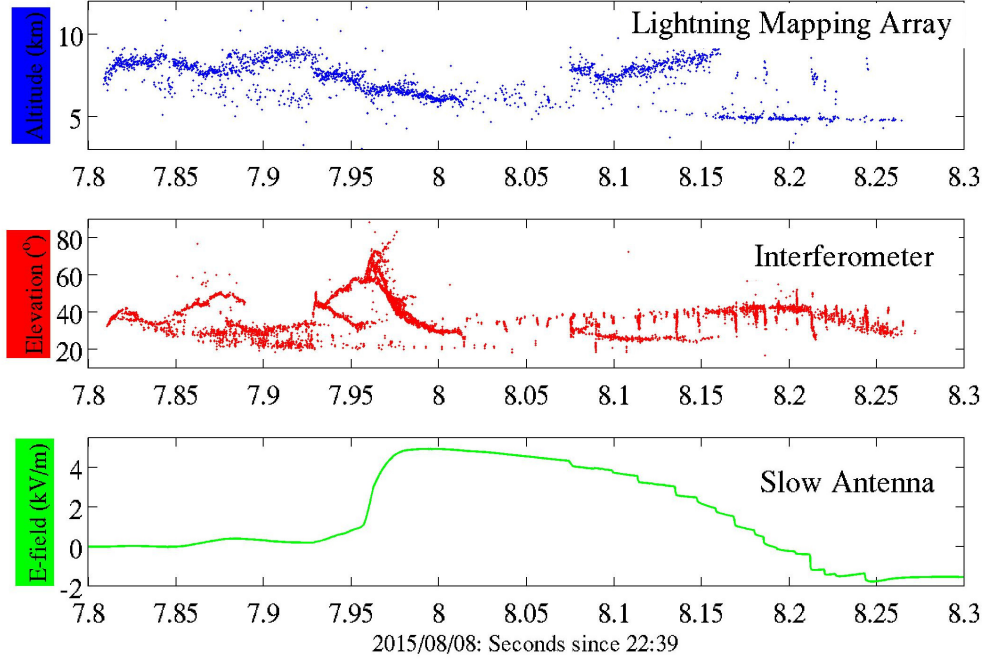
Figure 2. LMA time height, INTF time elevation and deltaE for an IC flash that passed nearly directly over all instruments.

record, a series of at least 13 sharp downward steps in E-field between 8.07 and 8.25 s. The interferometer (red), on the other hand, clearly shows rapid declines in elevation corresponding to each of the downward steps in electric field. These indicate rapid reionizations of previously formed channels (which are called K-changes when they stay in the clouds, and dart-leaders when they come to ground.) The takeaway message from this discussion is as follows. LMAs wonderfully locate channels as they are being formed, but do not show rapid events (which can also be high current events) particularly well. Field-change meters do show high-current events quite well, and used in a network can provide location information, but interferometers provide very detailed location information and are fast and sensitive enough to clearly locate both stepped and dart breakdowns.

IV.   Mapping INTF to LMA

Despite its apparent advantages, the INTF only measures direction cosines $cos(\alpha), cos(\beta)$ or equivalently, Azimuth and Elevation. For a full 3-D map of lightning emission sources, one needs range. The LMA provides X, Y and Z, but we have established that it misses some rapid events. Thus we need to develop techniques to get the range information from an LMA to an INTF. An initial approach was to map the LMA data down to direction cosine space using the following mapping:

$$R = \sqrt{X^2 + Y^2 + Z^2} \tag{1}$$

$$cos(\beta) = \frac{X}{R} \tag{2}$$

$$cos(\alpha) = \frac{Y}{R} \tag{3}$$

The mapping from Azimuth[b] and Elevation[c] to $cos(\alpha), cos(\beta)$ is

$$cos(\beta) = cos(EL)\ sin(AZ) \tag{4}$$

$$cos(\alpha) = cos(EL)\ cos(AZ) \tag{5}$$

---

[b]AZ is defined to be positive CCW 0° along the X-axis, which is defined as 'East'.
[c]Elevation is defined at 0° in the X, Y plane and 90°at zenith.
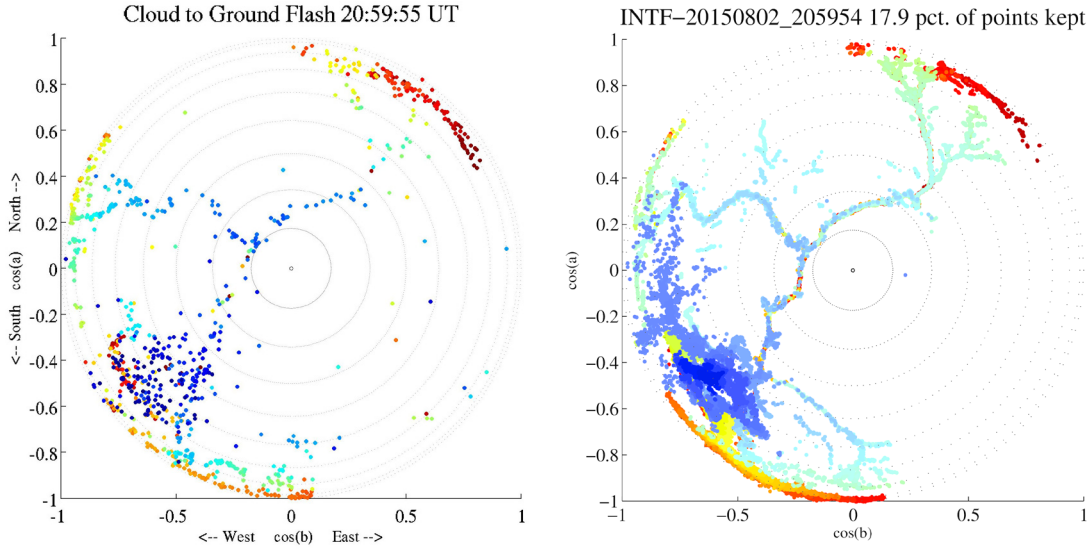
Figure 3. Comparison of same CG flash in cosacosb space observed by LMA (left) and INTF (right).
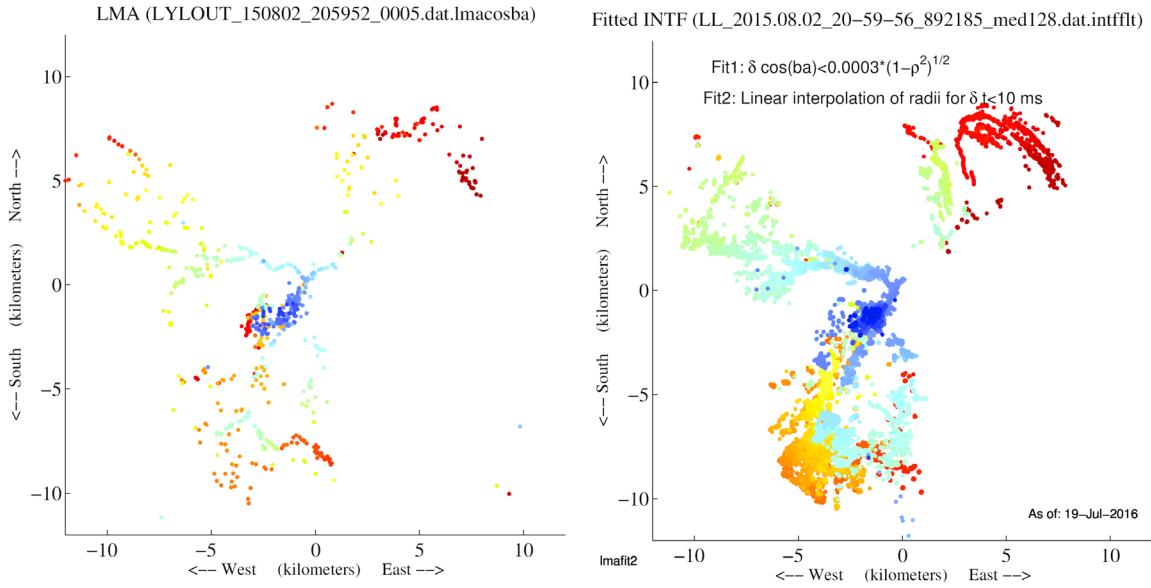
Figure 4. Comparison of same CG flash in planview observed by LMA (left) and INTF (right).

Figure 3 (left) shows a CG flash as measured by the interfometer, while the right panel shows the same flash measured by an LMA. Clearly there is a lot more detail in the INTF data. In fact, there are several branches of the flash visible in INTF that show only a single point in the LMA. The encouraging thing to see is that the mapping does not induce any additional distortions on the LMA data. $cos(\beta)$ can be interpreted as a geographical East-West coordinate and $cos(\alpha)$ is North-South. The next phase is more difficult.

One needs to upsample the LMA data to try to fill in the gaps, while taking into account what is physically reasonable. A two-step process has brought the best results so far. First, a circle in cosine-space is defined around every INTF point and a corresponding LMA point is sought. Where one is found, the range R of the LMA point is assigned to the INTF point. This INTF point is now located in space as follows.

$$X_{INTF} = R\,cos(EL)\,cos(AZ) \tag{6}$$
$$Y_{INTF} = R\,cos(EL)\,sin(AZ) \tag{7}$$
$$Z_{INTF} = R\,sin(EL) \tag{8}$$

The technique of finding corresponding points in LMA and INTF is robust in assigning ranges to INTF points but cannot produce any more locations than the LMA already obtained. To locate the rest of the INTF points, the previously located INTF points are used to locate their neighbors *in time*. A tight time window (10 ms) is selected, and a linear fit in ranges between already located INTF points is used to assign ranges to their neighbors. 10 ms was the minimum necessary window size to get all INTF points to fit, but it increased the risk of mislocation. Results are presented in figure 4. The left is a "planview" of the raw LMA where all points are located in X and Y (real space, not cosine space). The corresponding fitting INTF data is also shown. The parameter ρ reported in the figure refers to a radius in cosine-space. The value $\rho = 0.0003$ should be compared to the maximum value $\rho = 1$ to see how tightly the LMA and INTF points were required to match. It is encouraging to see that the right panel shows many more located sources, but the right panel of figure 4 is clearly fuzzier than that of 3. The fitted range errors are the source of this problem. Some of the data, such as the red arcs in the Northeast, probably are close to correct (looking back at the LMA data). On the other hand, the green arcs on the Northwest are probably purely artifacts of degenerate range fittings.

The next level of sophistication would use more than nearest neighbor points and would also discriminate against noise. An additional method worth exploration is to use pulse-graph algorithms developed by Hager[17] and Lapierre [Lapierre2014]. These algorithms attempt to connect isolated sources into 3D channels. If we do this in advance of mapping X,Y,Z to direction cosine, we are hopeful that it will remove some of the ambiguity in locations.

The ultimate goal remains to combine detailed locations and currents vs. time and predict the integrated brightness of the flash as seen from space. This would allow rapid feedback between lightning flash models based on INTF data and GLM/LIS flash brightness results and we will end up with a much deeper understanding of the wonderful output from our space-based servants.

V.   Conclusion

Data presented here comparing INTF, LMA and LEFA suggests that INTFs detect certain rapid events (e.g. dart leaders, K-changes) that correspond to large and rapid changes in electric-field are largely invisible to LMA. This is consistent with other published results. For that reason, we can expect INTFs to provide a better map of the optical sources sensed from space than LMAs. It is straightforward to map INTF and LMA data into $cos(\alpha)/cos(\beta)$ space, and work is progressing on automated mapping of INTF data onto LMA to provide the missing range information which will make INTF a tool for understanding lightning of unparalled precision.

Acknowledgments

References

[1]H. G. Kuhn, F., *Atomic Spectra*, Academic Press, New York and London, 1969 2nd Ed.

[2]Blakeslee, R. J. and Koshak, W. J., "LIS on ISS: Expanded Global Coverage and Enhanced Applications," Tech. rep., NASA Goddard, "The Earth Observer", May-June 2016.

[3]Steven J. Goodman, Richard J. Blakeslee, W. J. K. D. M. J. B. D. B. L. C. C. S. M. B. E. M. J. G. S., "The GOES-R Geostationary Lightning Mapper (GLM)," *Atmos. Res.*, Vol. 125-126, 2013, pp. 34–49.

[4]Thomas, R. J., Krehbiel, P. R., Rison, W., Hunyady, S. J., Winn, W. P., Hamlin, T., and Harlin, J., "Accuracy of the Lightning Mapping Array," *J. Geophys. Res.*, Vol. 109, 2004, pp. D14207.

[5]Koshak, W. J., Blakeslee, R. J., Goodman, S. J., Christian, H. J., Bateman, M. G., Boccippio, D. J., Solakiewicz, R. J., Hall, J. M., Bailey, J. C., Krider, E. P., Mach, D. M., Stewart, M. F., Buechler, D. E., Petersen, W. A., Cecil, D. J., and McCaul, E. W., "North Alabama Lightning Mapping Array LMA: VHF Source Retrieval Algorithm and Error Analyses," *J. Atmos. Oceanic Tech.*, Vol. 21, No. 4, 2004, pp. 543–558.

[6]Krehbiel, P. R., Brook, M., and McCrory, R. A., "An analysis of the charge structure of lightning discharges to ground," *J. Geophys. Res.*, Vol. 84, No. C5, 1979, pp. 2432–2456.

[7]Lu, G., Winn, W. P., and Sonnenfeld, R. G., "Charge transfer during intracloud lightning from a time-dependent multidipole model," *Journal of Geophysical Research: Atmospheres*, Vol. 116, No. D3, 2011, pp. n/a–n/a.

[8]Karunarathne, S., Marshall, T. C., Stolzenburg, M., Karunarathna, N., and Orville, R. E., "Modeling stepped leaders using a time-dependent multidipole model and high-speed video data," *Journal of Geophysical Research: Atmospheres*, Vol. 120, No. 6, 2015, pp. 2419–2436, 2014JD022679.

[9]Bitzer, P. M., Christian, H. J., Stewart, M., Burchfield, J., Podgorny, S., Corredor, D., Hall, J., Kuznetsov, E., and Franklin, V., "Characterization and applications of VLF/LF source locations fromlightning using the Huntsville Alabama Marx Meter Array," *Journal of Geophysical Research: Atmospheres*, Vol. 118, No. 8, 2013, pp. 3120–3138.

[10]Hayenga, C. O. and Warwick, J. W., "Two-dimensional interferometric positions of VHF lightning sources," *J. Geophys. Res.*, Vol. 81, 1981, pp. 7451–7462.

[11]Rhodes, C. T. and Krehbiel, P. R., "Interferometric observations of a single stroke cloud-to-ground flash," *Geophys. Res. Lett.*, Vol. 16, No. 10, 1989, pp. 1169–1172.

[12]Shao, X. M. and Krehbiel, P. R., "The spatial and temporal development of intracloud lightning," *J. Geophys. Res.*, Vol. 101, No. D21, 1996, pp. 26641–26668.

[13]Ushio, T., Z. K. Y. O. and Matsuura, K., "Broadband interferometric measurement of rocket triggered lightning in Japan," *J. Geophys. Res.*, Vol. 24, 1997, pp. 2769–2772.

[14]Akita, M., Stock, M., Kawasaki, Z., Krehbiel, P., Rison, W., and Stanley, M., "Data processing procedure using distribution of slopes of phase differences for broadband VHF interferometer," *Journal of Geophysical Research: Atmospheres*, Vol. 119, No. 10, 2014, pp. 6085–6104, 2013JD020378.

[15]Stock, M. G., Akita, M., Krehbiel, P. R., Rison, W., Edens, H. E., Kawasaki, Z., and Stanley, M. A., "Continuous broadband digital interferometry of lightning using a generalized cross-correlation algorithm," *Journal of Geophysical Research: Atmospheres*, Vol. 119, No. 6, 2014, pp. 3134–3165.

[16]Sonnenfeld, R. G., Battles, J., Lu, G., and Winn, W. P., "Comparing E-field changes aloft to lightning mapping data, D20209, doi: 10.1029/2006JD007242," *J. Geophys. Res.*, Vol. 111, 2006.

[17]Hager, W. W., Aslan, B. C., Sonnenfeld, R. G., Crum, T. D., Battles, J. D., Holborn, M. T., and Ron, R., "Three-dimensional charge structure of a mountain thunderstorm," *Journal of Geophysical Research: Atmospheres*, Vol. 115, No. D12, 2010, pp. n/a–n/a.

Vacuum Test Measurements of Novel Green-Propellant Thruster for Small Spacecraft

Stephen A. Whitmore[1]
Stephen L. Merkley[2]

Utah State University, Logan, Utah, 84322

The Propulsion Research Laboratory (PRL) at Utah State University recently developed a promising "green" alternative to space propulsion systems currently based on environmentally unsustainable hydrazine-based propellants. The power-efficient USU- system can be started and restarted with a high degree of reliability and various ground-test units with thrust levels varying from 4.5 N to 900 N have been developed. Based on NASA and USAF assessment tools, the technology readiness level (TRL) of the current prototype thruster system lies between 3 and 4 with a primary deficiency being systems functionality and performance assessments in a vacuum environment. USU does not possess sufficient vacuum tunnel facilities to allow such testing. To upgrade the TRL a series of vacuum tests were performed in the MSFC ER-23 Propulsion Research Laboratory. This paper presents preliminary results from those tests. These tests demonstrated that the system was reliably re-startable under hard vacuum conditions, and the near-vacuum specific impulse exceeded 280 seconds. During the testing campaign it was discovered that the motor case and nozzle become considerably hotter than was experience during earlier ambient ground tests, and this result necessitated minor changes to the thrust chamber configuration to ensure greater survivability. These changes are documented in the report.

I. Nomenclature

A^* = nozzle throat area, cm^2

A_{exit} = nozzle exit area, cm^2

c^* = thruster characteristic velocity, *m/sec*

c^*_{max} = theoretical maximum value of characteristic velocity, *m/sec*

D = fuel port diameter, *cm*

E_{out} = HVPS output voltage, *V*

F_{max} = maximum thrust, *N*

F = mean thrust, *N*

I_{out} = output current, *mA*

---

[1] Professor, Mechanical and Aerospace Engineering Department, Propulsion Research Laboratory, Utah State University, 4130 Old Main Hill, UMC 4130, Logan UT 84322.
[2] Graduate Research Associate and MSFC Summer Intern, Mechanical and Aerospace Engineering Department, Propulsion Research Laboratory, Utah State University.

I_{sp}	=	specific impulse, *s*
g_0	=	mean acceleration of gravity at sea level, *9.8067 m/sec²*
O/F	=	oxidizer-to-fuel ratio
M_{fuel}	=	consumed fuel mass, *g*
M_{ox}	=	consumed oxidizer mass, *g*
M_{total}	=	*total* consumed propellant mass, *g*
$\dot{m}_{ox}$	=	oxidizer massflow rate, *g/s*
$\dot{m}_{total}$	=	total propellant mass flow rate through nozzle, *g/s*
P_c	=	thruster chamber pressure, *kpa*
P_{reg}	=	GOX regulator set point, *kpa*
P_{vac}	=	vacuum chamber altitude pressure, *kpa*
p_e	=	exit plane pressure, *kpa*
p_∞	=	freestream or ambient pressure, *kpa*
R_g	=	gas-specific constant (per unit molecular weight) of exhaust products, *J/kg-K*
T_0	=	combustion flame temperature, *°K*
t	=	time, *s*
t_{burn}	=	burn time, *s*
τ_{rise}	=	motor ignition rise time, *s*
ε	=	expansion ratio
γ	=	ratio of specific heats
η^*	=	thruster combustion efficiency

II. Introduction

The Propulsion Research Laboratory (PRL) at Utah State University recently developed a promising "green" alternative to current space propulsion systems that are based on environmentally unsustainable hydrazine mono-propellants. This alternative system concept derives from the unique electrical breakdown properties of 3-D printed acrylonitrile butadiene styrene (ABS), discovered serendipitously while investigating the thermodynamic performance of ABS as a hybrid rocket fuel. This concept has been developed into a power-efficient system that can be started and restarted with a high degree of reliability. Various ground-test units with thrust levels varying from 4.5 N to 900 N have been developed and Various ground-test units with thrust levels varying from 4.5 N to 900 N have been developed and tested.

The layered structure of the printed ABS provides very small radius surface features. When electrodes are added to the structure and voltage is applied across the electrodes, these features concentrate charge at many discrete points on the material surface and allow a strong electrical arc to occur at moderate voltage levels. The electric field generated by the arc produces joule level heating and results in pyrolysis along the conduction path. When a combustible gas is introduced a pyrolysis occurs which rapidly leads to a self-sustaining combustion along the entire fuel port surface.

Based on NASA and USAF assessment tools, the technology readiness level (TRL) of the current prototype thruster lies between 3 and 4. This TRL level is not competitive for most existing propulsion system flight opportunities that require a minimum entry-level of 5.0. The primary deficiency to the system's maturity is the lack of comprehensive re-start and performance assessments in a vacuum environment. USU does not possess sufficient vacuum tunnel facilities to allow such testing. The described research and development campaign leveraged vacuum test facilities available at NASA MSFC to perform vacuum assessments on a Cubesat-scale prototype of the thruster concept. Demonstrating reliable vacuum performance is essential in maturation of the system concepts to TRL 5.0.

The experimental campaign teams the Mechanical and Aerospace Engineering (MAE) Department at Utah State University (USU) and the Space Propulsion Branch (ER23) at Marshall Space Flight Center (MSFC) according to the agreements laid out by Cooperative Agreement NNM16AA01A, Approved March 11, 2016. Specific tasks accomplished include pulsed-operation tests under vacuum conditions to characterize any corona effects during arc-ignition at low pressures. In addition to assuring minimal corona effects and proper system operation under vacuum conditions, the transient ignition tests characterized the achievable minimum impulse bit during pulsed operation.

A. Why This Technology is Important to NASA and the USAF

Although the market for commercially designed and manufactured small spacecraft has grown enormously during the last decade, technology development has mostly centered on spacecraft bus design and miniaturization of sensor components. The propulsion industry in general has not kept pace with the growth trend. With the current state of the art for space propulsion, hydrazine is by far the most commonly used-propellant. Unfortunately, hydrazine is highly toxic, potentially explosive, and environmentally unsustainable. Although procedures are in place to allow hydrazine to be managed on tightly controlled military or government-operated test reservations, with a growing regulatory burden, complex infrastructure requirements associated with hydrazine transport, storage, servicing, and significant clean up procedures associated with accidental releases, using hydrazine as a propellant is becoming increasingly cost prohibitive. As a result Hydrazine is inherently not "rideshare friendly."

Both NASA and the USAF recognize that the development of an effective replacement for hydrazine is a critical[i], and have initiated multiple programs to develop "green" propellant alternatives. Concurrently the European Space Agency affiliate ECological Advanced Propulsion Systems (ECAPS) has also initiated a program to develop less toxic alternatives to hydrazine. These alternative propellant are based on the ionic liquids (IL) Hydroxylamine Nitrate (*HAN*)[ii,iii,iv] and Ammonium Dinitramide (*ADN*)[v,vi,vii,viii] The developed IL propellant formulations go by the product names AF-M315E and LMP-103S respectively. ECAPS recently tested a thruster based on LMP-103S in its Prisma flight demonstration program[ix]. NASA recently awarded a contract to Ball Aerospace, Boulder CO for the Green Propellant Infusion Mission (GPIM) to space-test a thruster system based on the USAF-developed "green" Ionic-Liquid (*IL*) propellant AF-315E.[x]

Currently, several operational and developmental issues preclude the use of IL-based propellants for CubeSat-scale spacecraft where power and mass budgets are extremely limited. The lack of a cold-start capability is a primary drawback of the current generation of green

propellant thrusters. IL-based propellants are notoriously hard to ignite and a reliable "cold-start" capability does not currently exist. *IL*-catalyst beds must be pre-heated to greater than *350 C* before firing. This preheating requires substantial power,[xi,xii] creating a very significant disadvantage for small spacecraft where power budgets are extremely limited. Additionally, catalyst beds are expensive to build and add significant dry mass to the spacecraft. Heating the catalyst bed under vacuum conditions has proved very problematic.

Also, multiple case reports have demonstrated that working with ionic liquids can be quite dangerous, even for experienced organizations. [3, xiii,xiv,xv] Thus it is reasonable to conclude that the use of IL-propellants is beyond the level of practical experience of most CubeSat vendors and end-users. Because CubeSat fabricators are not structurally organized to deal with such potentially hazardous propellants, for the foreseeable future, the use of ionic liquids for CubeSat propulsion is technologically and economically infeasible. With currently proven technology only low-efficiency cold-gas systems are available for CubeSat propulsion, consequently the types of orbits achievable by CubeSats on rideshare missions remain very limited. In addition to replacing hydrazine for many applications, the thruster system that was demonstrated during this activity also offers as a practical alternative to Ionic-liquid propellants for some critical near-term applications.

B. Alignment with the NASA Space technology Roadmap

NASA has recognized that the development of alternatives to hydrazine-based systems is important. The proposed research activity aligns with several key elements of NASA strategic plan[xvi] including multiple elements of the In-Space Propulsion Road Map (TA02),[xvii] and Advanced Materials, Structures, Mechanical Systems, and Manufacturing (TA12) Road Map.[xviii] Specific key elements of the proposed program that are directly described within the TA02 and TA12 roadmaps include

- Innovative use of advanced manufacturing for complex propulsion elements
  - Innovative designs enabled by advanced manufacturing
- Advanced In-Space Chemical Propulsion
  - Innovations in green propulsion
  - Novel, low mass, low-part count subsystems
- Nano/Micro propulsion for small spacecraft/satellites
  - Innovative integration of small/micro propulsion systems
  - Novel propellants/concepts (liquids/solids/electric/hybrid)
- Low-Cost Nano-Launch Capabilities
  - Low-cost, small reaction control systems (RCS).
  - Low-cost, end-of-lifetime de orbit systems.

---

[3] "DOE Response to the May 14, 1997 Explosion at Hanford's Plutonium Reclamation Facility," August 4, 1997, Memorandum Secretary Federico Peña to Program Secretarial Officers and Field Element Managers.

III. Technical Background

The system concept to be tested derives from the unique electrical breakdown properties of 3-D printed acrylonitrile butadiene styrene (ABS), discovered serendipitously while investigating the thermodynamic performance of ABS as a hybrid rocket fuel.[xix] Additive manufacturing is an essential feature of this concept. The layering of the printed ABS creates very small radius surface features. When electrodes are embedded into the system and a as voltage is applied across the electrodes, these features concentrate charge at many discrete points on the material surface and allow a strong electrical arc to occur at moderate voltage levels. The electric field generated by the arc produces joule level heating and results in pyrolysis along the conduction path. When this pyrolysis occurs concurrently with oxidizer flow into the combustor, there exists a mixture of combustible gaseous and a source of activation energy (provided by the arc). This sequence of events rapidly leads to self-sustaining combustion along the entire fuel port surface. Identical ABS fuel segments made from extruded/machined ABS do not exhibit these moderate voltage arcing properties.

This concept has been developed into a power-efficient system that can be started and restarted with a high degree of reliability. This prototype system, when fully developed, could become as a "drop in" replacement for hydrazine thrusters for a variety of space propulsion applications. Figure 1a shows an example of the additively manufactured grain with embedded electrodes. Identical ABS fuel segments made from extruded/machined ABS do not exhibit these moderate voltage arcing properties. Multiple prototype devices based on this concept with thrust values ranging from 4.5 to 900 N have been developed and tested[xx,xxixxii,xxiii,xxiv,xxv,xxvi,xxvii] All units are capable of

a) Printed Fuel Grain with Electrodes b) Static test Firing
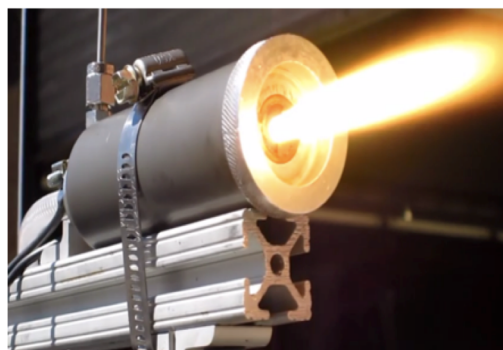
Figure 1. Flight-Weight Green Propellant Thruster.

multiple restarts and can be operated in either continuous or pulse modes. Ground tests have demonstrated that the system is operable in either continuous thrust or pulse-burn modes. Figure 1b shows the prototype flight weight unit with an additively-manufactured ABS fuel grain during static hot-firing with gaseous oxygen (GOX) as the oxidizer. Prior to this test series the achievable mean minimum impulse bit, response latency for pulsed burns, and impulse-bit standard deviation have not been well-characterized being characterized.

The GOX/ABS thruster has achieved specific impulse (I_{sp}) values near 220 seconds under ambient operating conditions. Detailed models of the system have been developed and verified with ground test data. Based on these models the measured I_{sp} value extrapolates to greater than 300 seconds for vacuum conditions. This value exceeds the hydrazine performance level by more than 20%. This performance enhancement is achieved by a comparably simple configuration layout with an inherently safe and environmentally-sustainable system design. In fact, the current system offers the safety and environmental friendliness of a cold-gas system, but at a significantly higher performance level.

IV. Experimental Apparatus Description

The experimental apparatus and rocket-system components used for the test are considered Special Test Equipment (STE). Test Cell C of Room 104 (Chemical Synthesis and Testing) Laboratory of Building 4205 at MSFC. The test hardware, oxidizer feed system, pressure panel, and the associated rocket systems were considered to be Special Test Equipment (STE). Prior to testing a full safety assessment (SA) was performed, and identified hazards were identified and mitigated. The SA was performed to demonstrate the ability to safely perform the proposed Novel Green-Propellant Thruster testing and to ensure compliance with NASA, OSHA, and national consensus standards. This assessment also serves as a summary of identified hazards to be used by decision makers when examining the risk level for the tests. The experiment was signed off as "low" risk by the appropriate approving MSFC authorities.

C. Test Article

The hardware is composed of the test-article and support systems, pressurization system, oxidizer feed system, altitude system, and the rocket performance- measurement system. The following paragraphs present descriptions of each system. Figure 2 (a) presents a 3-D exploded-view image and 2-D schematic drawing (b) of the motor assembly. Figure 3 presents the piping and instrumentation diagram (P&ID) of the end-to-end test system. Figure 4 presents the Electrical schematic (ES) of the Test Stand. Figure 5 shows the thruster systems mounted in the vacuum chamber.

The 25-N hybrid rocket thruster dubbed *"MicroJoe"* by the test team, features the patented non-pyrotechnic, low wattage, arc-ignition system developed at Utah State University. The rocket propellants were gaseous oxygen (GOX) (as the oxidizer) and additively-printed ABS (as the fuel). The fuel grains were fabricated from commercially-available Stratasys ABSplus-340® feed-stock[4] using a Stratasys Dimension 1200-ES FDM 3-D printer.[5] In order to evaluate the effects of material density under high altitude conditions, the test grains were printed at the highest print-density selection *(1.170 g/cm³),* and at the next lower print-density selection *(0.842 g/cm³).* The lower print density was investigated because previous experience has shown the potential for a significantly higher regression rate and greater fuel massflow rate. All ABS fuel grains were entirely inert with no additional burn-enhancement additives.

---

[4] Anon., "ABSplus Spec Sheet," http://usglobalimages.stratasys.com/ Main/Secure/Material%20Specs%20MS/Fortus-Material-Specs/Fortus-MS- ABSplus-01-13-web.pdf [retrieved 25 Jul. 2016].
[5] Anon., "Dimension 1200ES, Large, Durable Parts, http://www.stratasys.com/3d-printers/design-series/dimension-1200es, [Retrieved 25 Jul. 2016].
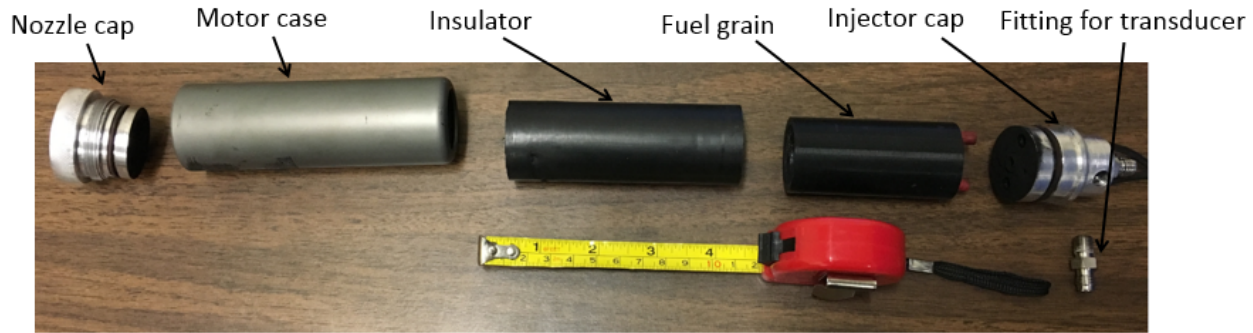
a) Exploded View 3-D Image of Motor Assembly.
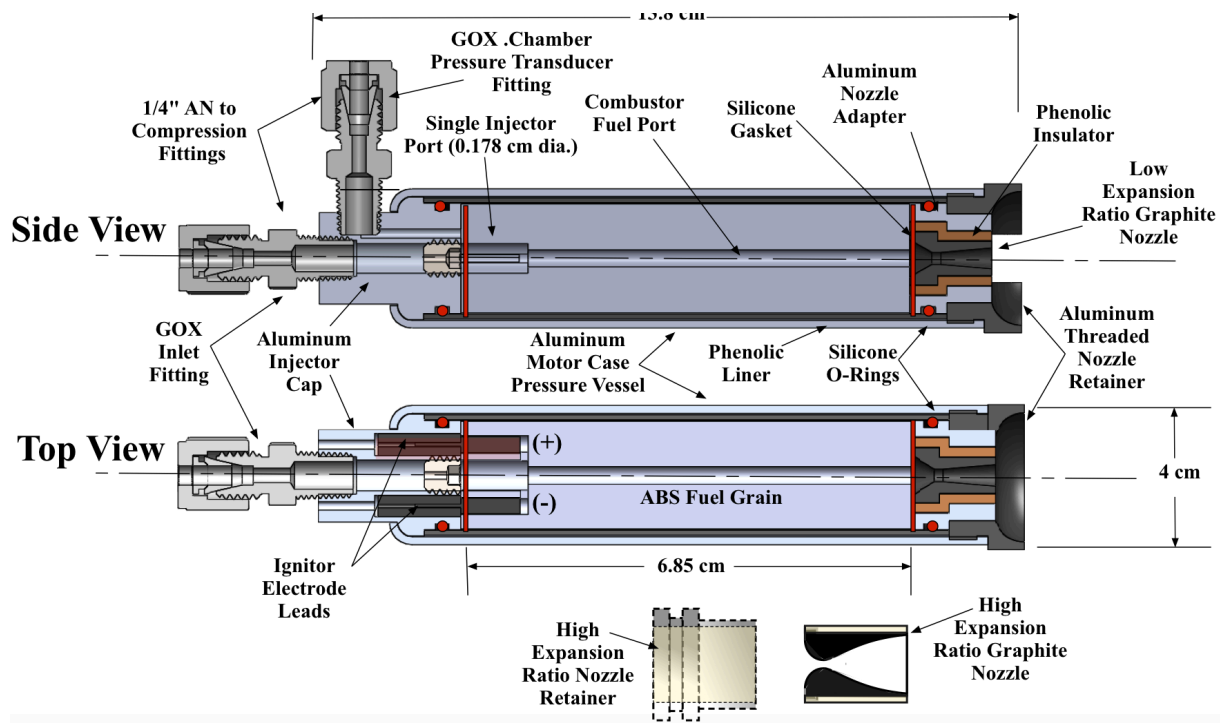
a) Two-Dimensional Schematic

Figure 2. Thrust Chamber 2- and 3-D Images.

Table I lists the key motor component parameters. The test article features 1) a thrust chamber, 2) phenolic line, 3) motor cap with integral oxidizer injector, 4) fuel grain with embedded electrodes, 5) graphite nozzle, and 6) nozzle retainer. The rocket nozzle, nozzle retainer, and injector cap were manufactured by Utah State University, and have been previously tested and well-characterized under ambient pressure operating conditions. The rocket thrust chamber is constructed from 6061-T6 high-temperature aluminum, and was procured commercially from Cesaroni Inc. as COTS equipment. The phenolic liner was purchased from an on-line retail distributer. Both low (2.064:1) and optimal (9.5:1) expansion ratio nozzles were evaluated. Figure 7 shows the nozzle geometries tested in this development campaign.

Table 1: Motor Geometry Parameter Specifications.

Parameter	Injector		Single Port, 0.127 cm (0.05 in.) Diameter	
Fuel Grain	Diameter: 3.168 cm (1.246 in.)	Length: 6.850 cm	Initial Weight: High Density: 50.0 g Low Density: 36.0 g	Initial Port Diameter: 0.625 cm (0.246 in.)
Motor Case	Diameter: 3.8 cm (0.150 in.)	Length: 13.8 cm (5.43 in.)	Wall Thickness: 1.5 mm (0.659 mm)	
Low Expansion Ratio Nozzle	Initial Throat Diameter: 0.401 cm (0.158 in.)	Exit Diameter: 0.577 cm (0.277 in.)	Initial Expansion Ratio: 2.064:1	Nozzle Exit Angle: 5.0 deg.
Intermediate Expansion Ratio Nozzle	Initial Throat Diameter: 0.401 cm (0.158 in.)	Exit Diameter: 1.215 cm (0.478 in.)	Initial Expansion Ratio: 9.5:1	Nozzle Exit Angle: 20.0 deg.

D. Pressurization System

The pressurization system is responsible for regulating the oxidizer feed to the thruster injector pressure at the desired level. The three-stage system consists of a low pressure (125 psig) air-feed that provides the dome-regulation a high-pressure (max 1400 psig) nitrogen gas (GN2) system, that in turn provides the dome control input for the GOX feed system regulator. The three-stage system is necessary to allow the regulated pressure to be controlled remotely with the test cell blast-door closed.

- The facility 125 PSIG High Purity Air Supply line was used for actuating the remote valves and is contained on a completely different set of lines from the GN2 propellant pressurization system.
- Regulators IP-201 and HOR-203 supply the low-pressure air dome control for the second stage dome-loaded regulator DLR-104.
- Regulator DLR-104 supplies the intermediate pressure (max 1400 psig) GN2-dome control input to GOX dome-loaded regulator DLR-7.
- A GN2 purge line is teed into the GOX feed line and flow is initiated via HOV-103.
- Dual-redundant check valves CV-100 and CV-101 downstream of GN2 manual valve HOV-103 preclude the high-pressure GOX (max 2400 psig) flow from entering the GN2 intermediate-stage pressurization system.
- Check-valve CV-300 prevents GN2 from entering the high-purity air system.

E. Motor Ignition System

Figure 6 shows the signal flow diagram from the motor ignition system power-processing unit (PPU). The ignition system PPU is based on the UltraVolt® D-series line of high-voltage power

supplies (HVPS).[6] This unit provides the inductive ignition spark that pyrolyzes sufficient ABS material to seed combustion. The D-series HVPS units take a 15-volt DC input and provide a current-limited (7.5 mA) high voltage output -- up to 1000 V or 6 watts total output. Previous experience with this ignition system has demonstrated that ignition can be reliably achieved using as little as 3 watts.[xxviii] The high voltage output is initiated by a commanded TTL-level input signal. Depending on the impedance on the arc path between the ignitor electrodes, the dissipated voltage typically varies between 10 and 400 volts. The HVPS provides output voltage signals that are proportional output current (I_{out}) and voltage (E_{out}) for tracking the unit operation.

F. Oxidizer Delivery System

The oxidizer delivery system is responsible for containing and delivering gaseous oxygen at the desired pressure level to the thruster injector cap. The GOX rate of flow is measured by a custom built and calibrated Venturi flow meter VEN-12 and associated pressure transducers PT-401 and DPT-402. The GOX storage tank is isolated from the thruster with SOV-13, and manual valves HOV-6, and HOV-2. The chamber pressure transducer PT-403 is installed via 1/8" stainless line into the motor cap and measures the motor head-end combustion pressure. When the hand-operated isolation valves (HOV-2, HOV-6) are opened, two additional remotely operated valves ROV-10 and SOV-13 isolate the GOX feed from the motor combustion chamber. The upstream pneumatic valve ROV-10 remotely allows the system to be remotely pressurized prior to initiating the run-sequence via SOV-13.

The remotely operated solenoid valve SOV-13, initiates the oxidizer flow into the thrust chamber and serves as the "run valve" for the system. The Venturi pressure measurement via PT-401 is used to judge that the system is fully pressurized and ready for opening of the GOX run valve. The third-stage dome-loaded regulator DLR-7 sets the desired inlet pressure to the thruster injector. The output from DLR-7 is controlled by the dome-inputs from DLR-104 and the output difference between IP-201 and HOR-203. The firing-systems control software sets the commanded current input to IP-201.

All GOX wetted materials have been precision cleaned and have been judged to be compatible with High Pressure GOX at the prescribed flow levels. In the unlikely event of a thrust chamber overpressure or a catastrophic regulator failure, a 500-psig-relief valve, RV-9 has been installed in the GOX feed line just upstream of the Venturi. Calculations have demonstrated that the choking mass flow at 500 psig through the relief valve is sufficient to maintain the system pressure below the rating of all system components.

G. Vacuum Altitude System

The altitude system consists of an altitude chamber, roughly 4.5 ft^3 in volume, evacuated by a rotary vacuum pump, with the pump discharging outside of the building into a stainless steel drum. The chamber can be purged with air via HOV-ROV-11 from the facility 125 PSIG High Purity Air Supply or GN2 via either ROV-11 or HOV-103. ROV-11 purges the system downstream of ROV-

---

[6] Anon., "High Power 8C-30C Series, Single Output High Voltage DC/DC Modules," UltraVolt, Inc., *http://www.ultravolt.com/uv_docs/HP8C-30CDS.pdf*, [Retrieved 9 July 2016].

10. HOV-103 purges any residual GOX that may lie between the GOX inlet and ROV-10. The
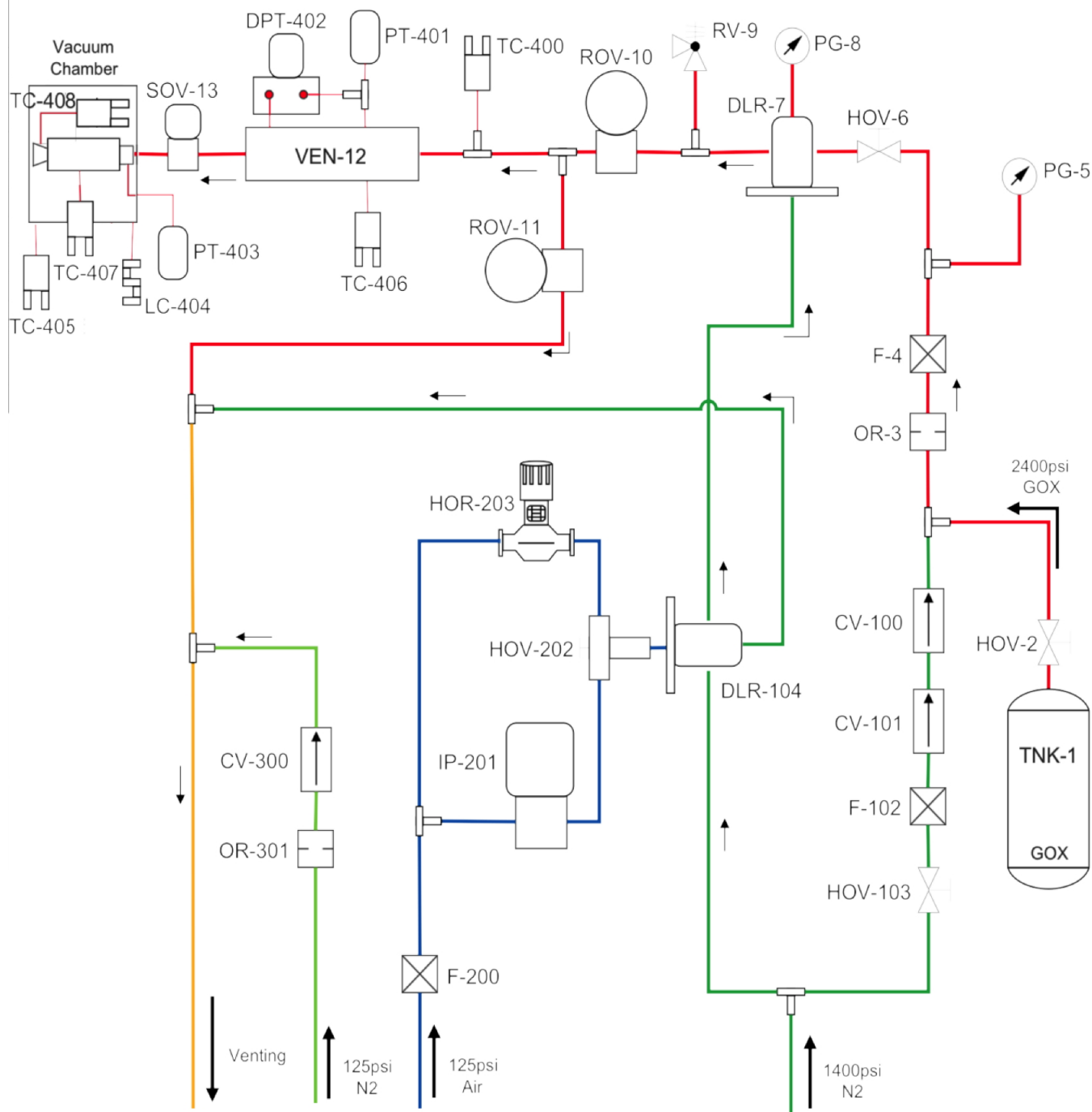vacuum pump has been serviced to safely pump GOX and is filled with perfluoropolyether oil.

Figure 3. Piping and Instrumentation Diagram of Test System.

Because of the low anticipated mass flow of the thruster system, less than 9 g/s, no active temperature control system is necessary. A 3" diameter by 4" long graphite rod is attached to rear wall view port of the vacuum chamber and thruster plume impinges on this rod. The rod distributes the thruster generated heat to the steel chamber door wall, which acts as a heat sink. The graphite buffering material keeps the impinging exhaust plume from spalling, warping, or otherwise damaging to vacuum chamber door. A thermocouple was attached to the external wall of the vacuum chamber door to ensure that the material does not reach a temperature sufficient to warp the door seal. A door temperature exceeding *800 deg. C* triggers a motor firing abort.
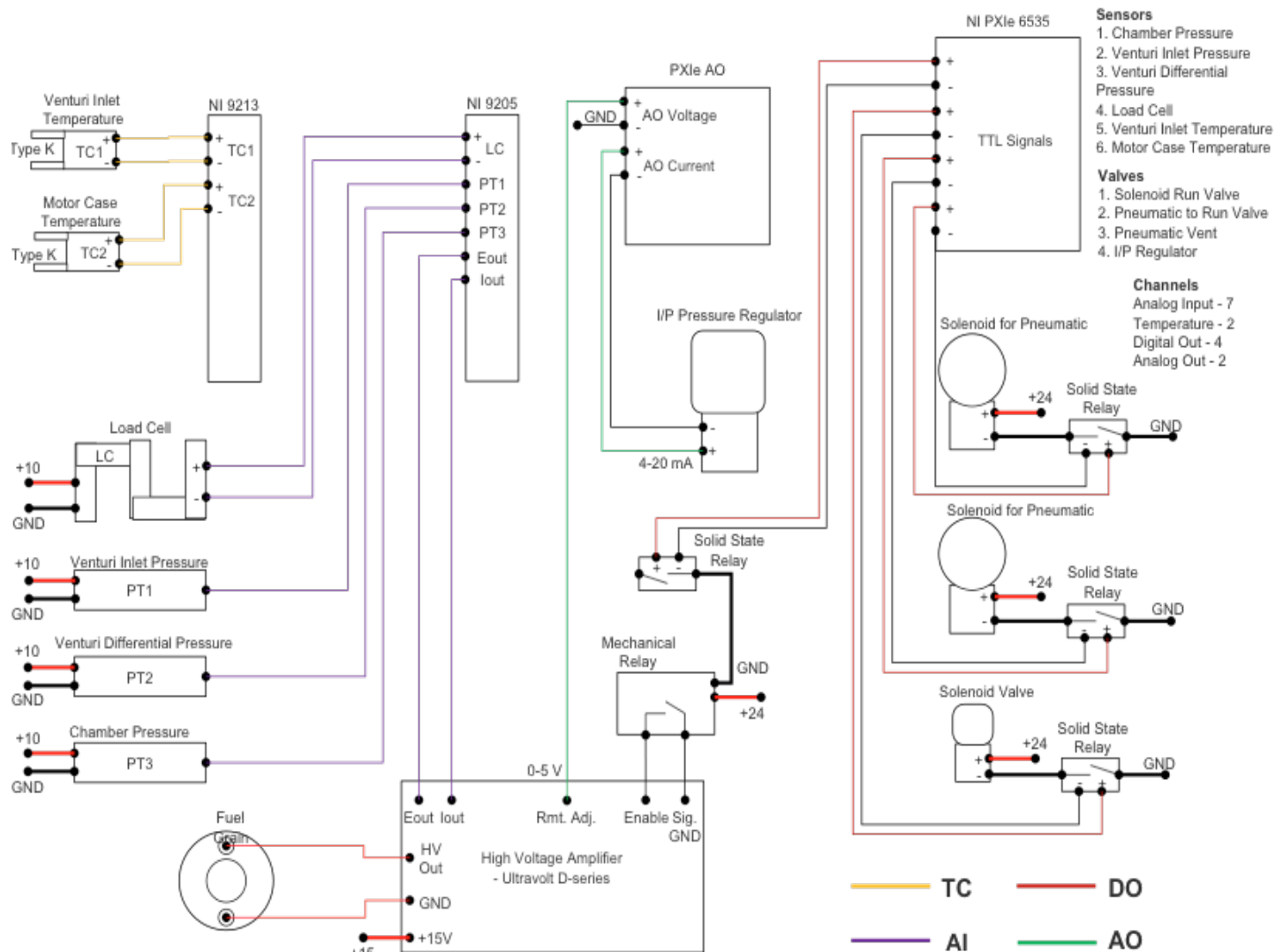
Figure 4: Electrical Schematic of Test Stand.

H. Thruster Performance Measurement System

The thruster performance measurement system is wholly contained within the altitude chamber. A single Omega LCCA 25 lbf load cell LC-404 was used to measure longitudinal force

generated by the motor. Thermocouples are attached to the Venturi (TC-406), motor thrust chamber (TC-407), and nozzle exit plane (TC-408) sense critical motor temperatures. TC-406 is used to calculate the flow density in the compressible GOX mass flow calculations. A motor case temperature exceeding *250 deg. C* and a nozzle exit plane temperature exceeding *500 deg. C* triggers a motor firing abort. A thermocouple (TC-405) was also attached to aft wall of the vacuum chamber. A chamber wall temperature exceeding *800 deg. C* triggers a motor firing abort. Locations of these sensors are shown on the P&ID of Figure 3. The thrust stand load measurements were calibrated using the installed configuration with the pressure lines loaded as full pressure levels.
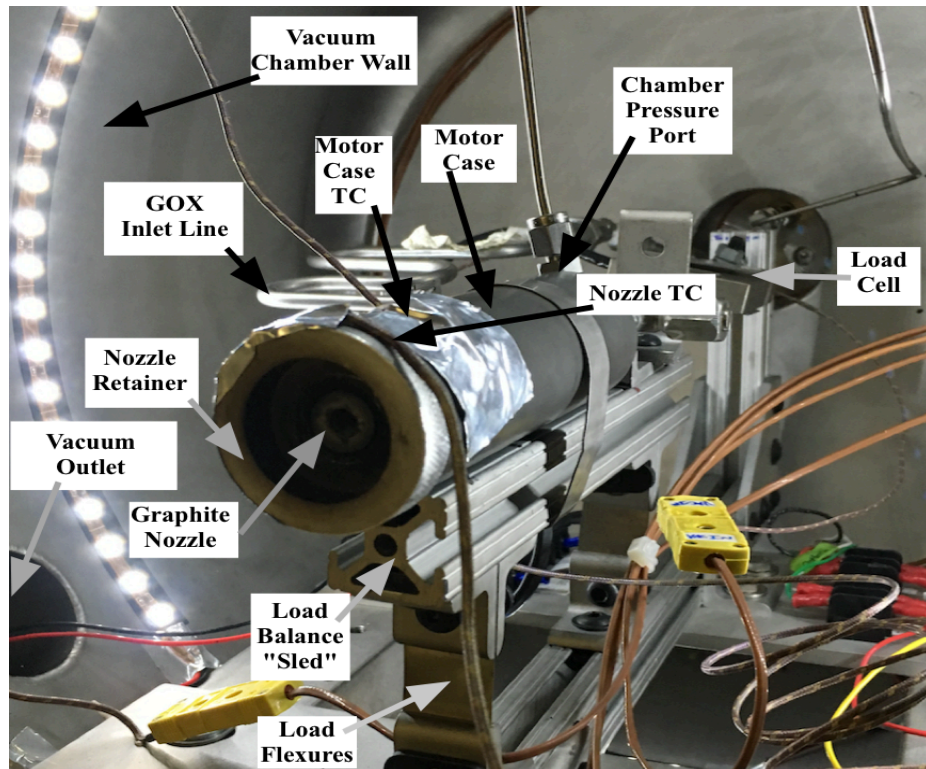
Figure 5: Thruster Mounted in Vacuum Chamber with Labeled Features.
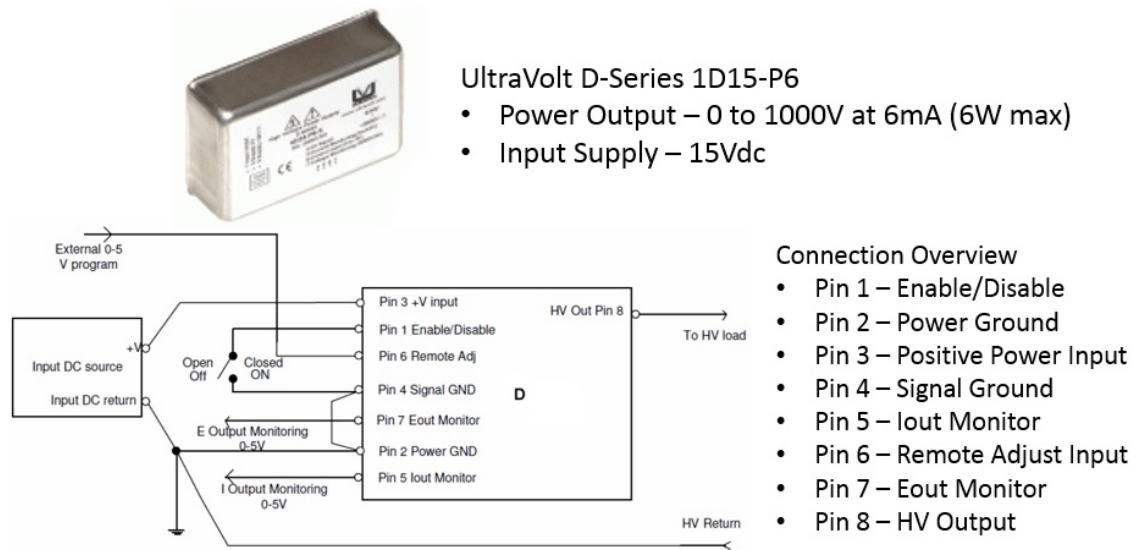
Figure 6. Schematic of UltraVolt HVPS Interface.
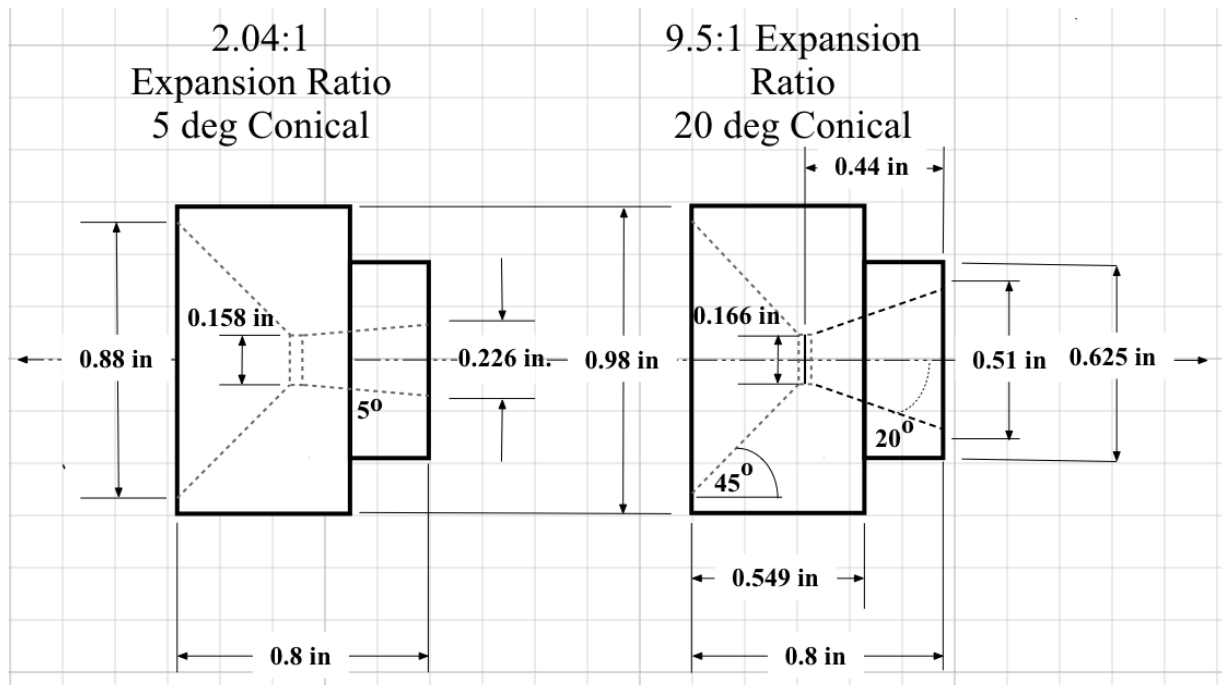
Figure 7. Nozzles Evaluated During Vacuum Testing Campaign.

V. Preliminary Test Results

A major objective of the testing campaign was to demonstrate the ability of the thruster systems to operate reliably under high altitude test conditions. Previous studies at ambient test conditions demonstrate that low-density grains burn at a higher massflow rate for a given oxygen massflux, and offered the potential for a small fuel grain length and more compact form factor. Thus, the initial series of tests attempted multiple consecutive burns of the system using both the low and high-density fuel grains. The Ignition Evaluation Tests also served as an end-to-end "wring out" of the entire system. Following, the ignition-evaluation tests, multiple, identical one-second pulses were performed in order to evaluate the system performance including parameters ignition response time, burn-to-burn thrust and impulse consistency, specific impulse (Isp), characteristic velocity (c*), combustion efficiency (h*). The initial burn-reliability tests were performed using only the low-expansion ratio nozzle, the performance. The motor characterization tests were performed using both the low- and high-expansion ration nozzles.

I. Calculating the Fuel Massflow Rate, Oxidizer-to-Fuel ratio, and Combustion Efficiency

As described previously, the oxidizer massflow was measured using an in-line calibrated Venturi massflow meter. The nozzle exit massflow was calculated from the measured chamber pressure Pc, nozzle throat area A^*, and exhaust gas properties using the 1-dimensional De Laval choking mass flow equation,[xxix]

$$\dot{m}_{total} = A^* \cdot P_c \cdot \sqrt{\frac{\gamma}{R_g \cdot T_0}\left(\frac{2}{\gamma+1}\right)^{\frac{\gamma+1}{\gamma-1}}} \quad . \tag{1}$$

The combustion flame temperature T_0, gas-specific constant R_g, and ratio of specific heats γ, were calculated from lookup tables developed using the NASA industry-standard program "Chemical Equilibrium with Applications," (CEA).[xxx] Chamber pressure, oxidizer-to-fuel ratio O/F, and combustion efficiency η^* were the independent inputs to the lookup tables. For the CEA calculations enthalpy of formation and chemical formula for ABS assumed the values previously published by Whitmore, Peterson, and Eilers.[xxxi] Changes in A^* due to nozzle erosion were accounted for by measuring the throat diameters before and after each 4-pulse burn sequence, and linearly interpolating based on the actual motor burn time.

For each 4-burn test the mean O/F was calculated as the ratio of the integrated oxidizer massflow divided by the measured fuel mass consumed over the burn duration

$$O/F = \frac{\int_0^{t_{burn}} \dot{m}_{ox}\,dt}{M_{fuel}} \quad . \tag{2}$$

Using the CEA-derived properties, the fuel massflow rate was calculated as the difference between the measured oxidizer massflow and the calculated total nozzle exit mass flow

$$\dot{m}_{fuel} = \dot{m}_{total} - \dot{m}_{ox} \quad . \tag{3}$$

The fuel massflow rate was integrated over the burn duration to calculate the total consumed fuel mass,

$$M_{fuel} = \int_0^{t_{burn}} \left(\dot{m}_{total} - \dot{m}_{ox} \right) dt = \int_0^{t_{burn}} \dot{m}_{fuel} \, dt \; .$$ (4)

Equation (5) calculates the mean specific impulse by dividing the total consumed mass into the total impulse delivered by the thruster.

$$I_{sp} = \frac{\int_0^{t_{burn}} F \cdot dt}{g_0 \cdot M_{total}} = \frac{\int_0^{t_{burn}} F \cdot dt}{g_0 \cdot \left(\int_0^{t_{burn}} \dot{m}_{ox} \cdot dt + M_{fuel} \right)} \; .$$ (5)

Equation (6) calculates the characteristic velocity of the motor.

$$c^* = \frac{P_c \cdot A^*}{\dot{m}_{total} \cdot (O/F)} \approx \frac{P_c \cdot A^*}{\dot{m}_{ox} \cdot \left(\dfrac{O/F+1}{O/F} \right)} \; ,$$ (6)

Equation (7) calculates the combustion efficiency by dividing the measured combustion efficiency by the theoretical maximum for the selected propellants.

$$\eta^* = \frac{c^*}{c^*_{max}} \; ,$$ (7)

Adjusting the input combustion efficiency upwards has the effect of increasing the calculated fuel mass consumption, and downwards decreases the calculated fuel mass consumption. The fuel massflow calculation starts with an assumed combustion efficiency of $\eta^* = 0.90$. The calculations of Equations (1)-(6) were iterated, adjusting η^* input to the CEA tables until the calculated fuel mass equals the measured mass within a prescribed level of accuracy (½ of a percent). The characteristic velocity of the converged solution is calculated by

$$c^*_{actual} = \frac{P_c \cdot A^*}{\dot{m}_{total} \cdot (O/F)} \approx \frac{P_c \cdot A^*}{\dot{m}_{ox} \cdot \left(\dfrac{O/F+1}{O/F} \right)} \; .$$ (7)

J. Vacuum Ignition Evaluation Tests

For the Ignition Evaluation Tests tthe control software was programmed to perform a series of 1-2-1 second pulses spaced at regular 2-second intervals. The recovery time between pulses allowed vacuum pump systems to "catch-up" and return the internal chamber to vacuum conditions. For the first the ignition in the series the "spark" was programmed to pre-lead the opening of the run valve by 1-second and continue for ½ second after the run valve is open. For the two subsequent pulses the pre-lead was reduced to be ½ second.

The GOX regulator output pressure was manually set to a value such that the pressure ratio across the injector is at or slightly greater than the choking pressure ratio for gaseous oxygen. This set point value was calculated to be approximately 350 psig (2515 kpa absolute pressure) for the GOX massflow of 8 g/s required to achieve a 25 N vacuum thrust level. The thrust and massflow calculations were performed using the GOX/ABS thruster model developed by Whitmore and Merkley.[xxxii]

Figure 8 plots the results of the initial test series performed using a high-density fuel grain. Plotted are the thrust (a), Chamber pressure (b), Oxidizer Massflow (c), Vacuum Chamber Pressure (d), Ignition Current (e), and Ignition Voltage (f). Several features are notable in the presented time history plots.

First, the thrust levels only vary slightly between burns with the design *25 N* and *8 g/s being* oxidizer massflow being effectively achieved. This result verified the pre-test calculations. The chamber pressure range from 185-200 psia results in an injector pressure ratio ranging from 1.82-1.97, or right at the injector choke point. Choking the injector helps to decouple the combustion chamber from the oxidizer feed system and produces highly stable motor combustion.
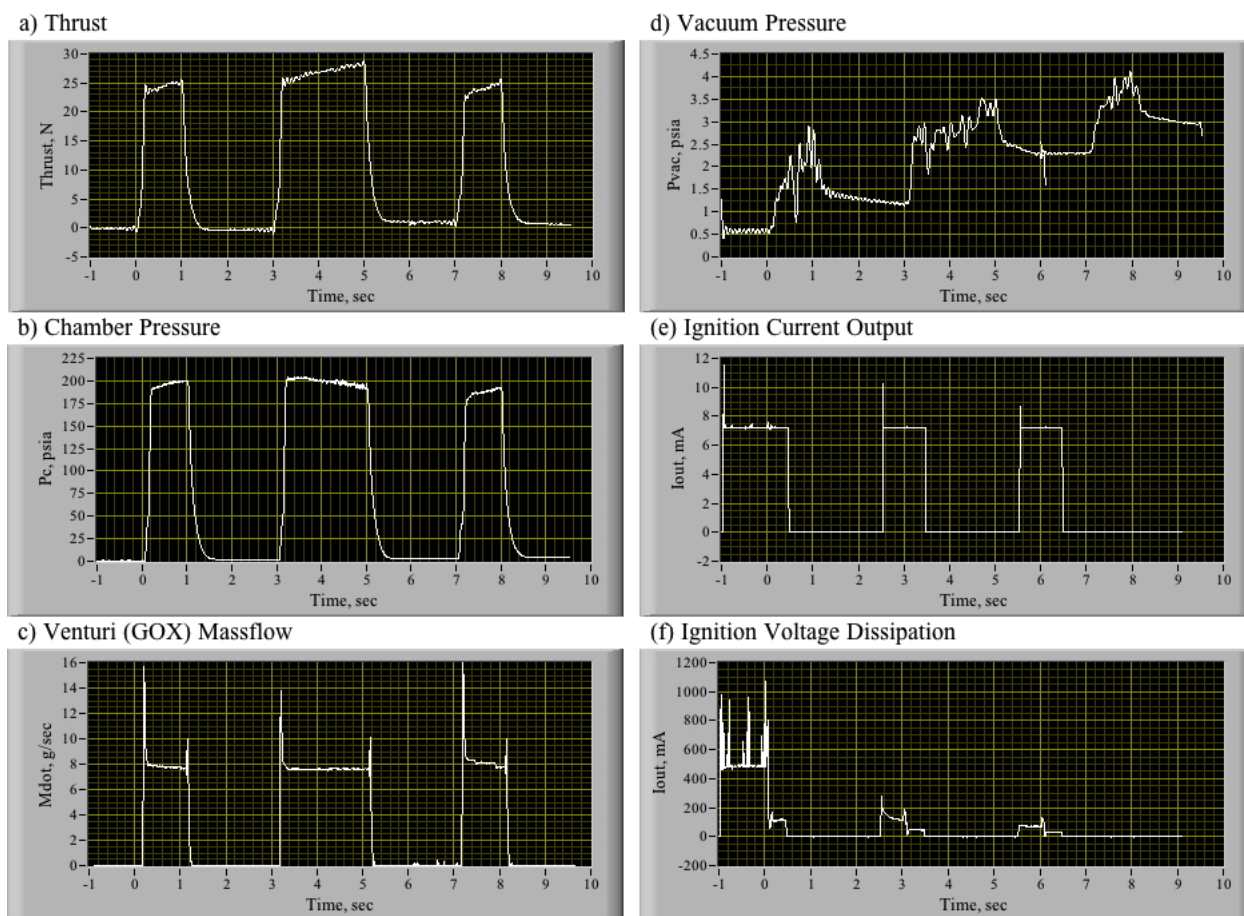
Figure 8. Initial Vacuum Ignition Tests of 25-N Arc-Ignition Thruster with High Density Fuel Grains.

Second, with the short recovery times between the consecutive burns, the vacuum pump cannot keep up with the generated flow, and the internal vacuum chamber pressure rises from slightly over ½ *psia* (*0.97 atms vacuum*) to above *3.5 psia* (0.76 atms vacuum). Clearly, the recovery time must be extended significantly. Extrapolating the decay slope n the first burn shows that as long as 10 seconds between 1-second burns is required to return to the original vacuum pressure level.

Finally, as can be observed from Figures 8(e) and 8(f). For all pulses current limits at *7.2 mA* with the induced voltage varying from slightly below *100 V* to slightly above *400 V*. The precise values of the induced voltage depend on the current path though the fuel material. After the first burn, the dissipated the voltage level drops considerably for subsequent burns indicating that the circuit path has been "set" into the fuel grain. Also once the motor starts, the dissipated voltage drops significantly indicating a significant drop in flow path resistance. It is likely that the drop in resistance is caused by the circuit loop jumping from the inside of the fuel material to the plasma stream generated by the nearly 3000 deg. C combustion- products.

K. Density Effects on Vacuum Ignition Effectiveness

The pulse-burn series of the previous section was repeated as 4-consecutive 1-second burns with a 10-second recovery time between burns. The 10-second recovery time was allowed to ensure that the vacuum chamber returned to near its minimum pressure level between each burn. For this test series the burn sequence was first performed using a high-density fuel grain, and then repeated using a low-density grain. For both tests the grain had been previously "set" at ambient conditions by energizing the arcing system for up to 5 seconds without oxidizer flow.

Figure 9 shows the test results for the high-density fuel grain. The high-density grain fired successfully each time, and the motor exhibits properties that are very similar to the results of Figure 8. Because of the longer recovery time the vacuum chamber pressure drops below *1 psia* (0.*931 atms* vacuum pressure) following each burn, with the resulting thrust levels being slightly higher than those plotted by Figure 8. The slight increase in thrust level is due to a small amount of nozzle erosion during the burn sequence. The resulting chamber pressure and GOX massflow are essentially the same value for each burn. Because the grain was "pre-set" before this test the required spark energy is considerably less, with the voltage level dropping further from approximately 80 V to 40 V during the burn series.
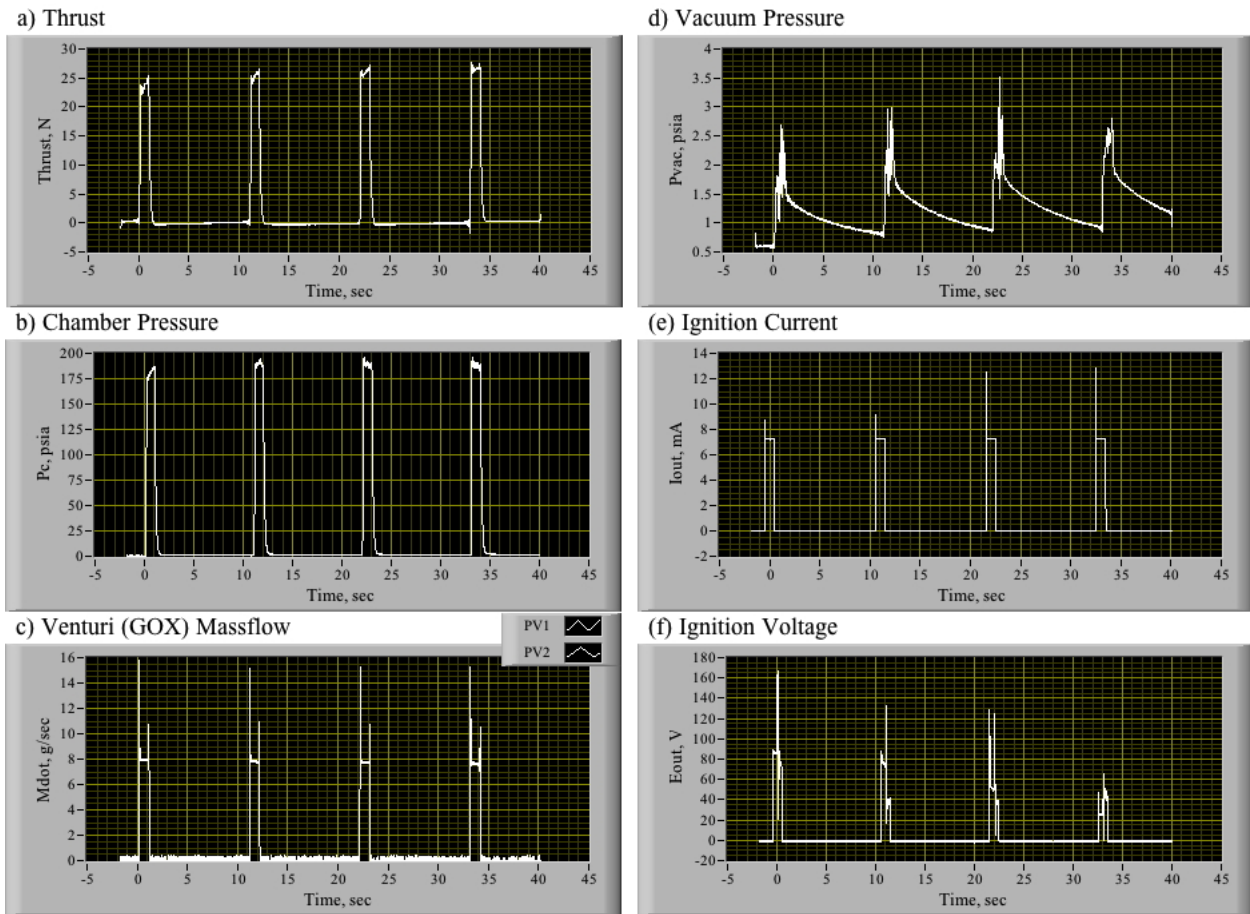
Figure 9. Ignition Evaluation Pulse Tests, High-Density Fuel Grain.

Figure 10 shows the 4-pulse test results for the low-density fuel grain. As indicated by the thrust and chamber pressure time history traces, for this example the grain ignites for the first two burns and then does not ignite for the last two burns. Multiple additional attempts were performed with no success. Examination of the voltage trace shows that the dissipated power jumps significantly after the second burn, indicating that the circuit path has buried internal to the fuel grain and any pyrolysed material cannot interact with the incoming oxidizer flow. This effect is likely a result of the higher porosity of the low-density material where voids in the subsurface can provide current flow paths that are lower impedance than the available surface flow paths.

For the two cases where the motor ignited, the resulting thrust levels were significantly higher than those produced by the high-density grains; greater than 30 N for the low density grains contrasted with 25 N for the high density grains. Thus, there still exists some potential advantages to using the low print-density if the ignition obstacles can be overcome. For the current configuration, it appears that the higher density material provides a more reliable solution.

179
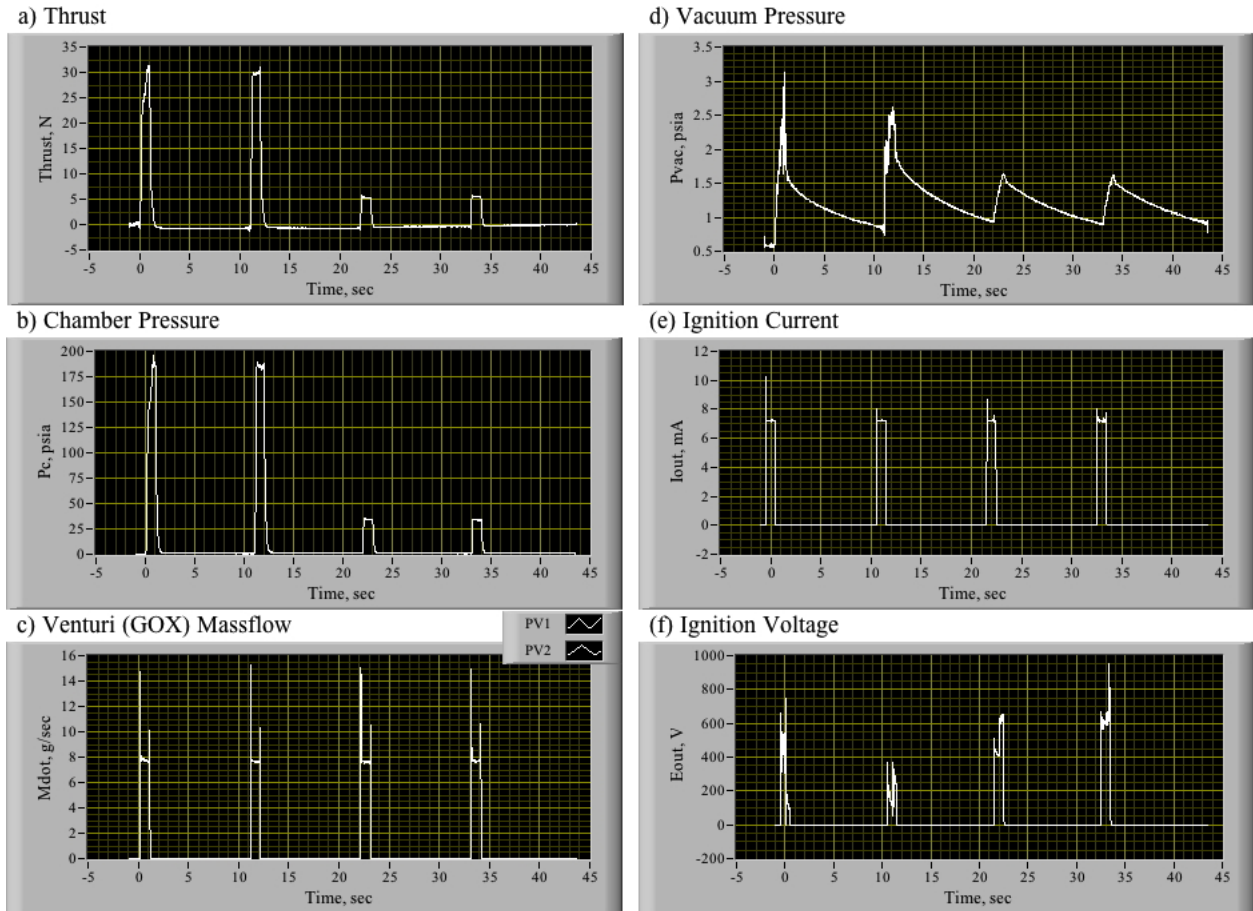
Figure 10. Ignition Evaluation Pulse Tests, Low-Density Fuel Grain.

L. Thrust, Total Impulse, and I$_{sp}$ Characterization

The thruster characterization tests evaluated the vacuum performance of the motor systems with only the high-density fuel grains. Also presented are performance data from the test thruster at ambient pressure conditions. These data were collected at the Propulsion Research Laboratory in Logan Utah.[7] prior to the arrival of the test team at the Marshall Space Flight Center. In this test series a total of 8 1-second burns were collected for each of the two nozzle expansion ratios. Fuel grains were selected at random from the pool of available high-density grains. The 4-pulse tests of Figure 9 were repeated twice for each expansion ratio nozzle, with the pre and post test masses weighed after each test to measure the total consumed fuel mass. Pre and post-burn nozzle throat areas were also measured to account for the effects of nozzle erosion. Table 2 summarizes the results from all of the motor characterization tests. Results from each of the test configurations will be described in the following sections.

---

[7] These tests were performed in the Utah State Propulsion Test Laboratory Test Cell at an elevation of approximately 1400 meters (4600 ft.) altitude. Nominal atmospheric pressure at this altitude is approximately 85.6 kpa (12.415 psia).

Table 2: Summary of Thruster performance Characterization Tests.

Motor Configuration	Pc	F	F_{max},	I_{sp}	Ignition Energy	τ_{rise},	O/F Ratio	Combustion Efficiency, η^*
2.064:1 initial ε, Ambient Conditions	178.66 ±9.32 psia	20.49 ±1.16 N	22.04 ±0.49 N	212.84 ±7.41 s	1.67 ±0.23 J	214.0 ±46.0 ms	N/A	N/A
2.064:1 initial ε, Vacuum Conditions	180.01 ± 5.75 psia	24.65 ± 1.06 N	26.58 ±0.89 N	235.27 ±7.57 s	1.38 ±1.01 J	132.5 ±30.9 ms	2.37 ±0.35	95.5% ±1.70%
9.5:1 initial ε, Vacuum Conditions	183.92 ± 9.63 psia	30.84 ± 1.36 N	32.98 ±0.92 N	280.01 ±7.23 s	1.63 ± 0.43 J	122.5 ±44.3 ms	1.94 ±0.46	94.1% ±0.96%

1. Baseline Thruster Performance Evaluation at Ambient Pressure Conditions

Figure 11 presents a typical 4-pulse burn test at ambient pressure collected from an identical thruster using 2.064:1 expansion ratio nozzle. Whitmore and Mathias[xxxiii] give a complete description of the test stand and the instrumentation system used to collect these measurements. Plotted are the thrust, chamber pressure, ignitor current, and ignitor voltage. Oxidizer massflow measurements were not available for these tests. The Thrust and chamber pressure time history traces are contrasted with the vacuum test results of Figures 8 and 9. Although the chamber pressure levels are nearly identical to the results from the vacuum tests, the resulting thrust levels are approximately 10% lower – peaking at slightly above 22 N.

The voltage dissipation profiles are quite similar for both the vacuum and ambient tests with the initial of each test showing the higher power dissipation, and the required power dropping for subsequent burns once the grain material has "set." As occurs with the previous vacuum, once the motor starts the dissipated voltage drops significantly indicating a significant drop in flow path resistance through the combustion-generated plasma stream.

Figure 12 plots the results of 8 consecutive burns of the thruster under ambient pressure conditions. The time histories of each of the 8 individual pulse-burns have been overlaid with the same starting point. This plot style allows the qualitative variations in the burn properties to be visually evaluated. Plotted time histories include measured thrust (a), chamber pressure (b), thrust calculated from chamber pressure (c), calculated nozzle exit pressure (c), ignition voltage dissipation (e), total ignition energy (f), and nozzle exit massflow (g), consumed propellant mass (h), total impulse (i), and specific impulse (j).

Since no oxidizer massflow measurement was available for this test, the total nozzle exit massflow was calculated from chamber pressure using the previously described message. The O/F ratio input to the CEA lookup tables was adjusted until the root mean square (RMS) difference between the measured thrust and the calculated thrust reached a minimum value. Some nozzle erosion occurred during this series of burns. The starting throat diameter of was *0.401 cm (0.158 in.)* and the ending diameter was *0.418 cm (0.165 in.).* This change in throat diameter caused the initial expansion ratio to drop from the initial value of *2.064:1 to 1.893:1.* Nozzle erosion accounts for most of the variability in the test burns.
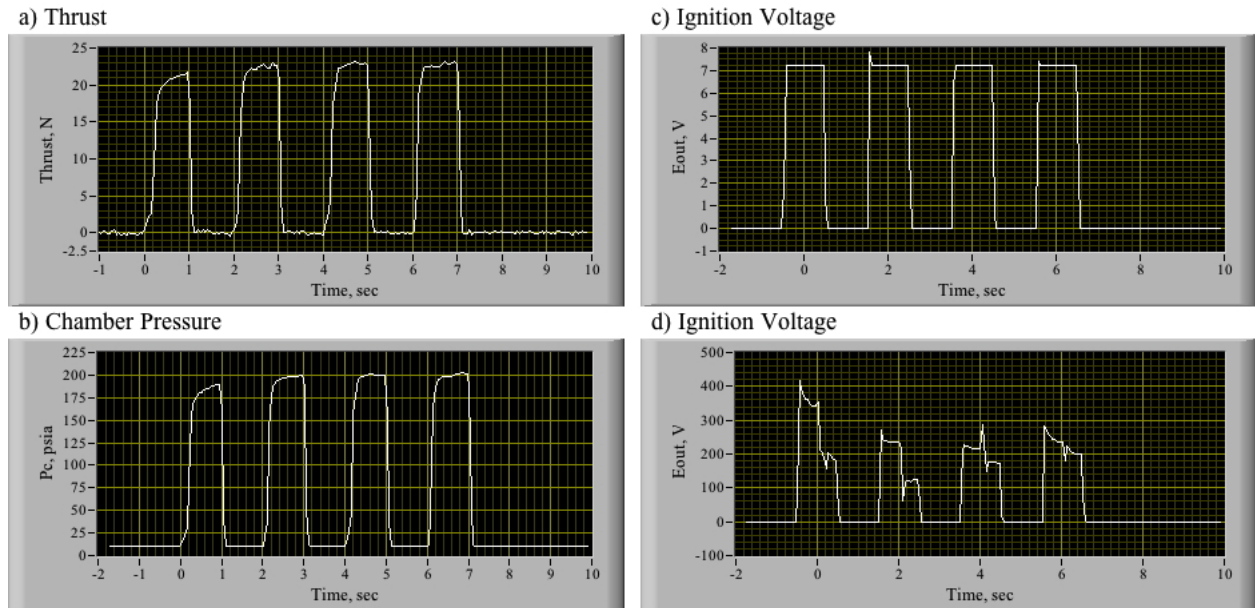
a) Thrust

b) Chamber Pressure

c) Ignition Voltage

d) Ignition Voltage

Figure 11. Ambient Pressure Ignition Tests of 25-N Arc-Ignition Thruster with High Density Fuel Grains.

For each thruster pulse effective mean thrust level is calculated by dividing the total accumulated impulse by the burn time. For the 8–thruster pulses the ensemble mean thrust level was *20.49 N* with a sample standard deviation of *1.67 N*. Using the *student-t* with 7 degrees-of-freedom[xxxiv] at the 95% confidence level, the estimated error range for the ensemble mean thrust is $\pm$1.16 N. The ensemble mean of the maximum thrust generated by a 1-second pulse is 22.04 N with a standard deviation of 0.70 N. At the 95% confidence level the estimated error range for the maximum thrust is $\pm$0.49 N.

The ensemble mean chamber pressure is 178.66 psi with a standard deviation of 13.43 psia. At the 95% confidence level the estimated error range for the ensemble mean is $\pm$9.32 psia. The ensemble mean I_{sp} is 212.84 seconds with a standard deviation of 9.61 sec. At the 95% confidence level the estimated error range for the ensemble mean I_{sp} is $\pm$7.41 psia.

The motor ignition energy is calculated as the integral of the product of the HVPS output current and dissipated voltage. For all 8 cases the ignition energy is less than 2 J. The ensemble mean of the ignition energy is *1.62 J* with a sample standard deviation of *0.33 watts.* At the 95% confidence level the estimated error range for the ensemble mean ignition energy is $\pm$0.23 J.
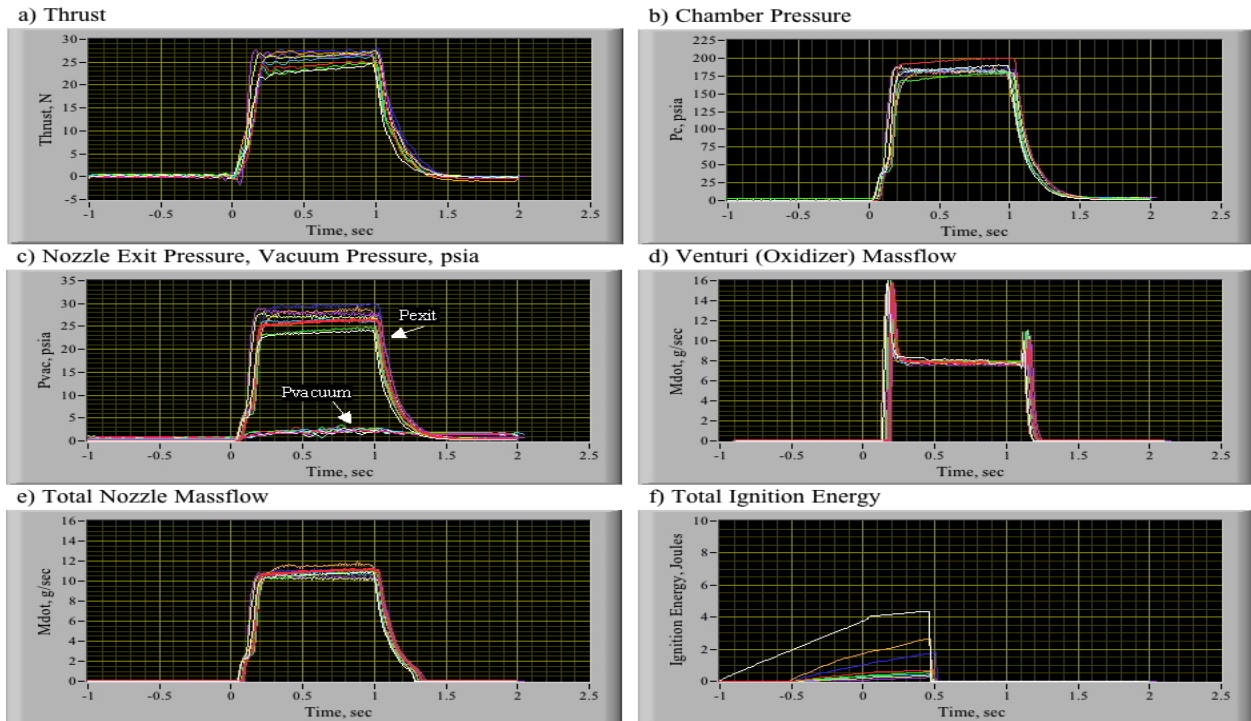
As can be observed from the plotted data of Figure 12, there exists some small startup latency for the motor where a finite amount of time is required for the motor to ignite and build up to full chamber pressure. For this analysis the motor startup or "rise time" τ_{rise} is the elapsed time from the opening of the run valve until the motor reaches 85% of the maximum chamber pressure. For the ambient pressure tests the ensemble mean rise time is *214 milliseconds* with a standard deviation of 66 ms. At the 95% confidence level the estimated error range for the ignition rise time is $\pm$46 ms.
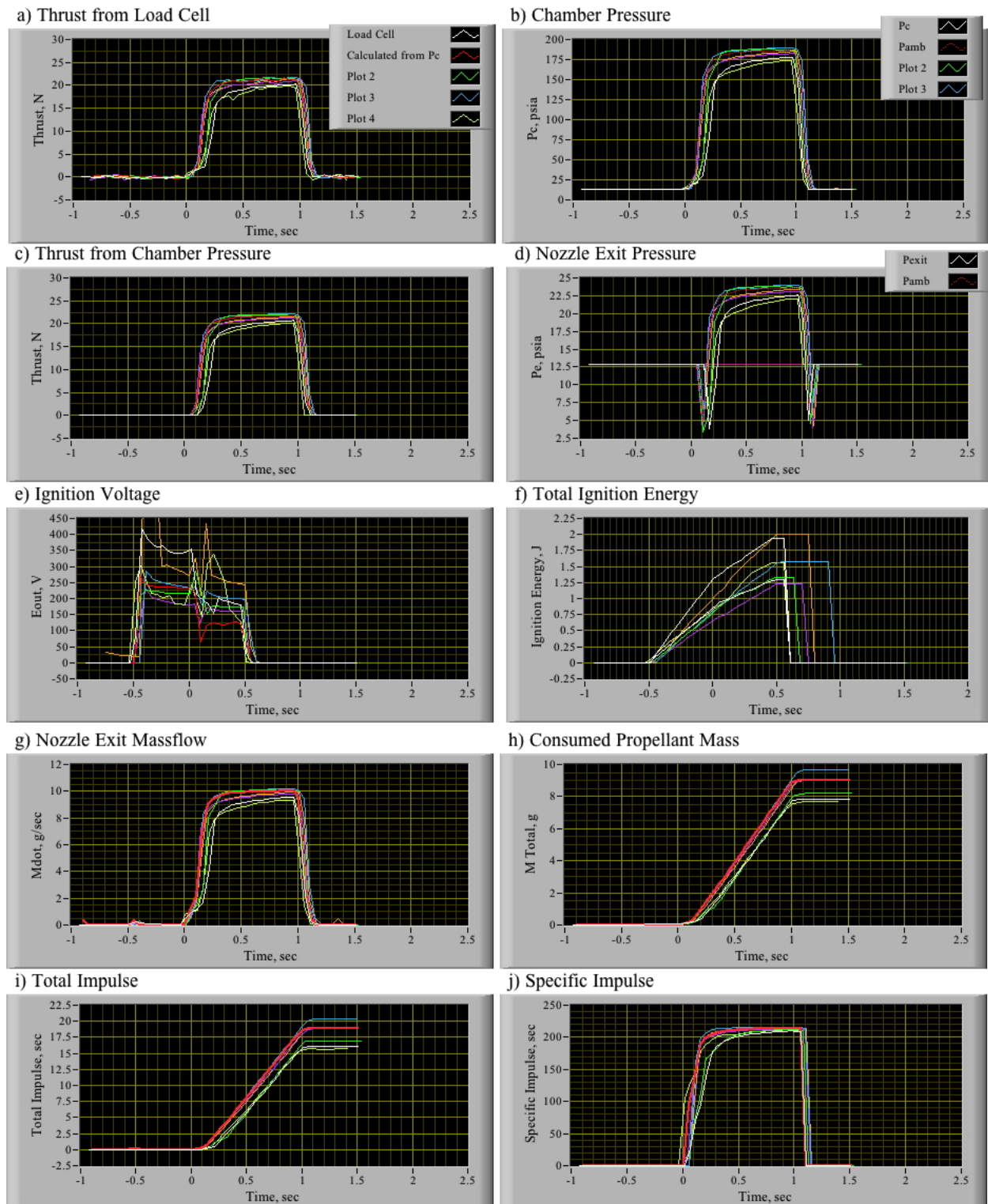
Figure 12. Baseline Motor Performance, Low Expansion Ratio Nozzle at Ambient Conditions.

2. Low Expansion Ratio Nozzle Characterization Tests

Figure 13 summarizes the results of the low-expansion ratio nozzle tests. The time histories of each of the 8 individual pulse-burns have been overlaid with the same starting point. This plot style allows qualitative variations in burn properties to be visually evaluated. Plotted direct measurements include measured thrust *(a)*, chamber pressure *(b)*, vacuum pressure *(c)*, and oxidizer massflow *(d)*. Derived data plotted include nozzle exit pressure *(c)*, total nozzle massflow *(e)*, ignition energy *(f)*, consumed propellant masses *(g)*, total impulse *(h)*, specific impulse *(i)*, instantaneous O/F *(j)*, characteristic velocity *(k)*, and combustion efficiency *(l)*.

Because the injector is choked, the oxidizer massflow is set by the injector area, gas temperature and upstream pressure. Because the regulator pressure was carefully set to 350 psig each test, there is very little run-to-run variability in the oxidizer massflow rate. During the test series the graphite nozzle eroded substantially, starting at a diameter of *0.401 cm (0.158 in.)* and ending with a diameter of *0.435 cm (0.171 in.)*. This change in throat diameter caused the initial expansion ratio to drop considerably from the initial *2.064:1 to 1.575:1*. As a result the mean nozzle exit pressure rose from approximately 23.5 psia (162 kpa) to 29.5 psia (203 kpa), and the mean chamber pressure dropped from *195.1 psia (1345 kpa)* to *181.2 psia (1249 kpa)*. Because the oxidizer massflow is essentially constant, and the regression rate of the fuel is mostly independent of the chamber pressure (Ref. xxxii), the total nozzle massflow does not change significantly during the burn series. The primary effect on the delivered thrust and total impulse is the changing nozzle expansion ratio.

The ensemble mean thrust level is *24.65 N* with a standard deviation of *1.52 N*. At the 95% confidence level with the 7 degrees-of-freedom the estimated error range for the ensemble mean thrust is *±1.06 N*. The ensemble mean of the maximum thrust generated by a 1-second pulse is 26.58 N with a standard deviation of 1.28 N. At the 95% confidence level the estimated error range for the maximum thrust is ±0.89 N.
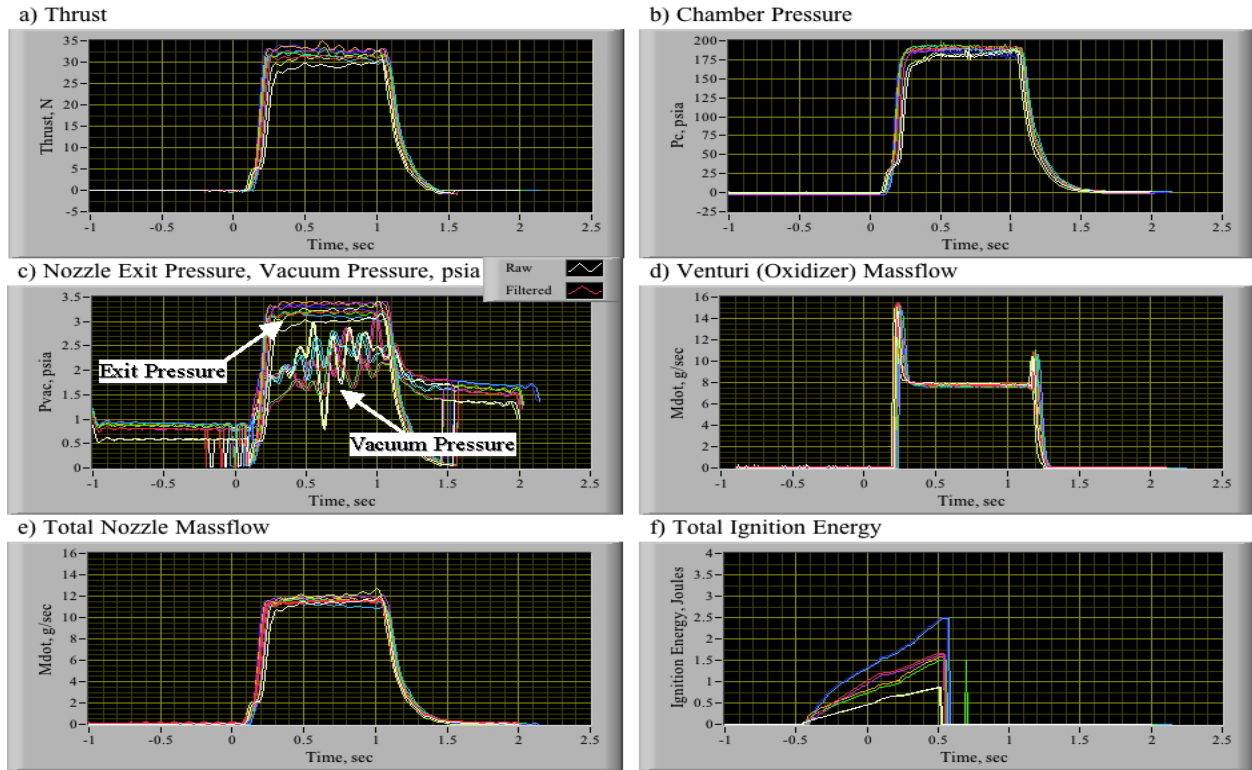
The ensemble mean chamber pressure is 180.02 psia with a standard deviation of 8.30 psia. At the 95% confidence level the estimated error range for the ensemble mean chamber pressure is ±5.75 psia. The ensemble mean I_{sp} is *235.26 sec* with a sample standard deviation of *10.92 N*. At the 95% confidence level the estimated error range for the ensemble mean I_{sp} is ±7.57 sec.

The motor combustion efficiency is excellent, mostly owing to its small size where radiation heating has a strong effect upon the fuel regression rate (Ref. xxxii). The ensemble mean η^* is *95.6% sec* with a sample standard deviation of *2.5%*. At the 95% confidence level the estimated error range for the ensemble mean is η^* is *±1.7%*. The ensemble mean O/F ratio is 2.37 with a standard deviation of 0.52. At the 95% confidence level the estimated error range for the ensemble mean of *O/F* is *±0.35%*. This O/F ratio is slightly leaner than the stoichiometric point for GOX ABS that lies at approximately 2.0. (Ref. xix) For all cases the motors were observed to become increasingly more fuel rich as the port opens up due to regression.

The ignition energy is calculated as the integral of the product of the HVPS output current and dissipated voltage. The initial burn requires *4.42 J* of input energy, and that value continuously drops for each subsequent burn. The final burn requires only *0.30 J* of energy to initiate combustion. The ensemble mean of the ignition energy is *1.38 watts* with a sample standard

184

deviation of *1.46 watts.* At the 95% confidence level the estimated error in the mean ignition energy is ±1.01 *watts.*

As with the previous analysis τ_{rise} is calculated as the elapsed time from the opening of the run valve until the motor reaches 85% of the maximum chamber pressure. For the vacuum tests of the low-expansion ratio nozzle the ensemble mean rise time is *133 milliseconds* with a standard deviation of 45 ms. At the 95% confidence level the estimated error range for the ignition rise time is ±31 ms. This rise time is approximately ½ of the value measured during the ambient pressure tests. The low external vacuum pressure that causes the nozzle throat to choke sooner under vacuum conditions, thus allowing the chamber pressure to build up faster, likely causes this result.

Finally, figure 13(c) compares the nozzle exit pressure against the vacuum chamber pressure, and the exit pressure lies considerably above the vacuum pressure of the test chamber. Thus, it is clear that the low expansion ratio nozzle is significantly under expanded. Thus, it is expected that the higher expansion ratio nozzle should exhibit considerably better performance with respect to both thrust and specific impulse. The data presented in the next section will verify that expectation.

a) Thrust b) Chamber Pressure c) Nozzle Exit Pressure, Vacuum Pressure, psia d) Venturi (Oxidizer) Massflow e) Total Nozzle Massflow f) Total Ignition Energy

185
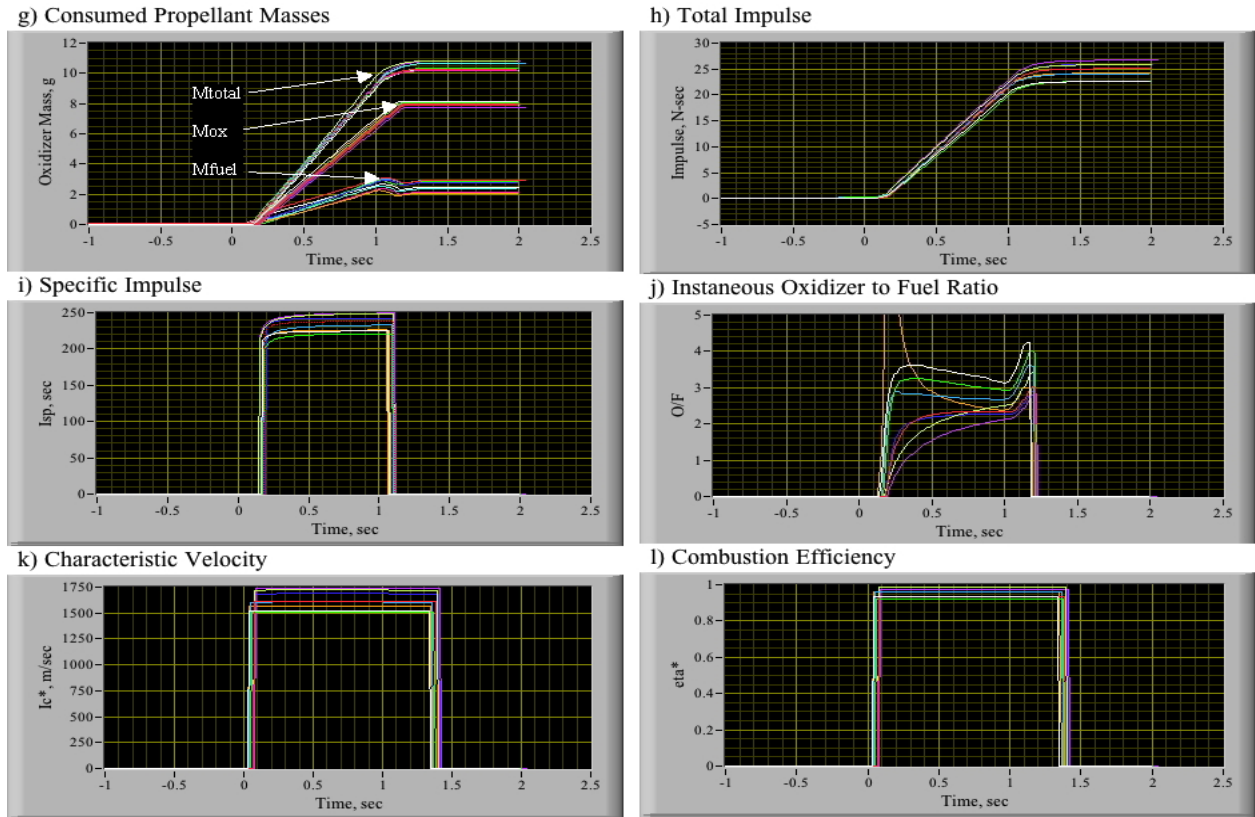
Figure 13. Motor Characterization Test Series Results, Low Expansion Ratio Nozzle.

3. High Expansion Ratio Nozzle Characterization Tests

An identical set of tests as those described in the previous section were performed with the high expansion ratio nozzle. Figure 14 present the overlay time history plots. As expected the achieved thrust, total impulse, and specific impulse are all significantly greater than both the ambient and low expansion ratio results.

The ensemble mean thrust level is *30.85 N* with a standard deviation of *1.96 N*. At the 95% confidence level with the 7 degrees-of-freedom the estimated error range for the ensemble mean thrust is ± 1.36 *N*. The ensemble mean of the maximum thrust generated by the 1-second pulse is 32.92 N with a standard deviation of 1.32 N. At the 95% confidence level the estimated error range for the maximum thrust is ± 0.92 N.

The ensemble mean chamber pressure is 183.02 psia with a standard deviation of 9.6 psia. At the 95% confidence level the estimated error range for the ensemble mean chamber pressure is $\pm 6.68.75$ psia. The ensemble mean I_{sp} is *280.01 sec* with a sample standard deviation of *8.44 N*. At the 95% confidence level the estimated error range for the ensemble mean I_{sp} is ± 6.24 sec. The ensemble mean O/F ratio is 1.95 with a standard deviation of 0.67. At the 95% confidence level the estimated error range for the ensemble mean of *O/F* is ± 0.4.

As with the previous tests the motor combustion efficiency is quite good, with ensemble mean η^* of *94.1% sec* with a sample standard deviation of *1.4%*. At the 95% confidence level the

estimated error range for the ensemble mean is η^* is $\pm0.96\%$. The ensemble mean of the ignition energy is *1.63 J* with a sample standard deviation of *0.62 J.* At the 95% confidence level the estimated error in the mean ignition energy is ±0.43 *J.*

For the high expansion-ratio vacuum tests the ensemble mean rise time is *123 milliseconds* with a standard deviation of 45 ms. At the 95% confidence level the estimated error range for the ignition rise time is ±44 ms. Again this rise time is approximately ½ of the value measured during the ambient pressure tests. Finally, figure 14(c) plots the nozzle exit and the vacuum chamber pressure overlays, and demonstrates that the high expansion-ratio nozzle is near optimum for the operating chamber pressure.

Figure 15 plots the 1-D De Laval (Ref. xxix) model for the thrust and I_{sp} levels as a function of altitude assuming 2.064:1, 9.5:1, and 25:1 expansion ratios. Also overlaid on these plots are the ensemble mean laboratory values and uncertainties for thrust and I_{sp}. The data points agree with the models within the values of the error bars; thus, verifying the model accuracy. When the 25:1 modeled 25:1 expansion ratio nozzle curve is examined, it shows that the I_{sp} of the thruster unit should exceed 300 seconds under "hard-vacuum" conditions.

a) Thrust b) Chamber Pressure c) Nozzle Exit Pressure, Vacuum Pressure, psia d) Venturi (Oxidizer) Massflow e) Total Nozzle Massflow f) Total Ignition Energy
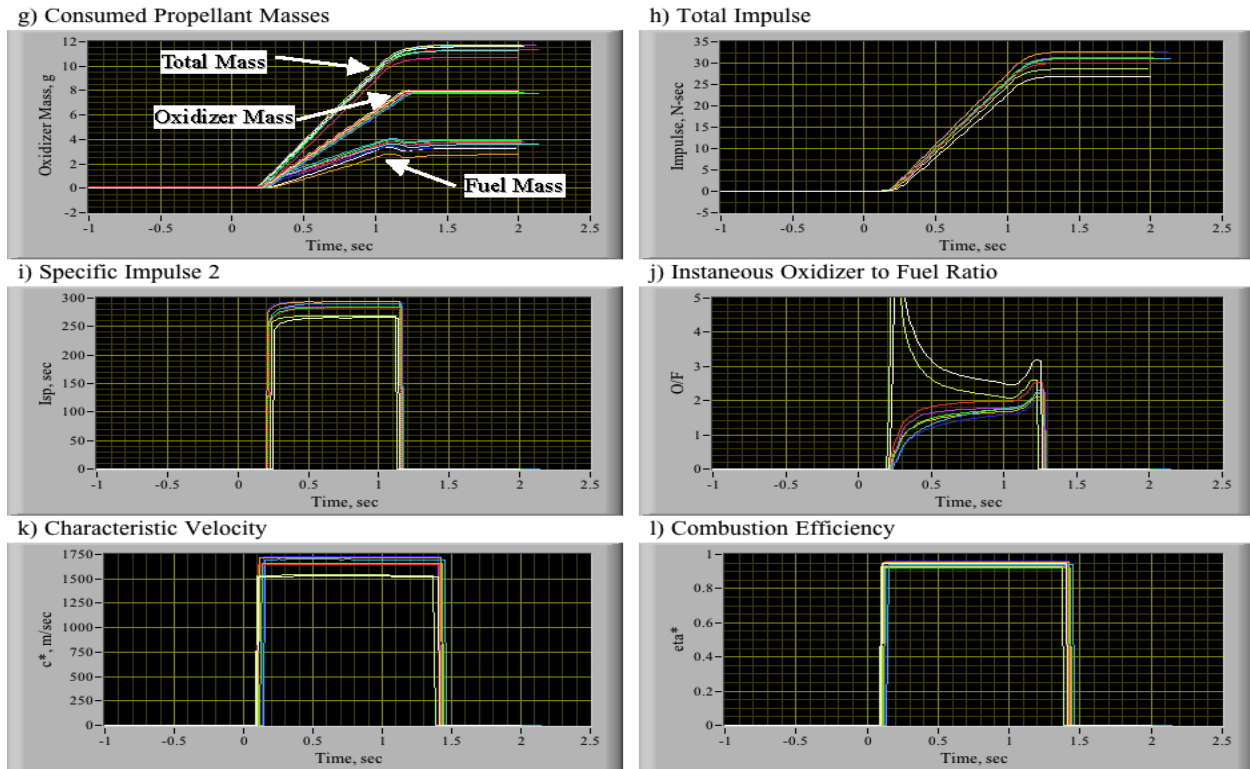
Figure 14. Motor Characterization Test Series Results, Optimized Expansion Ratio Nozzle.
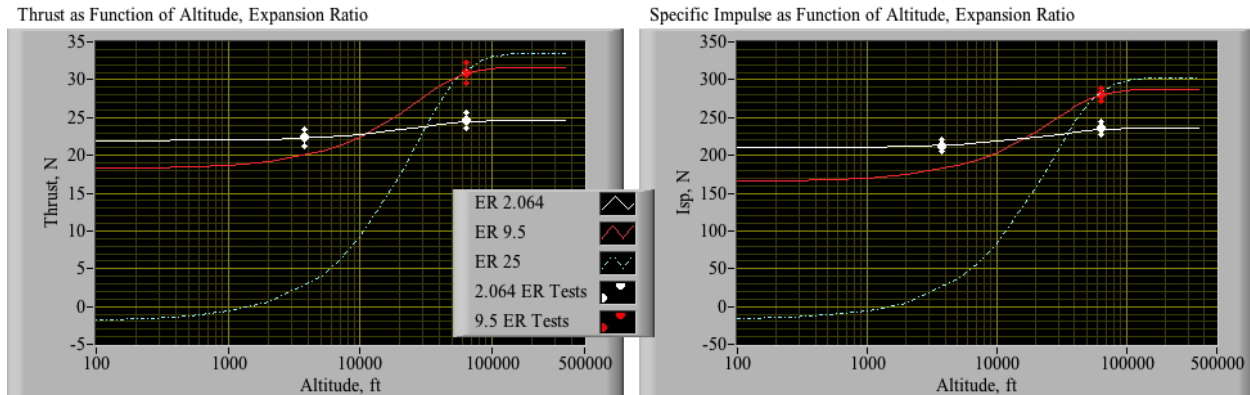
Figure 15. Comparison of Calculated, Measured Thrust and Specific Impulse, and Extrapolation to Hard Vacuum conditions for 25:1 Expansion Ratio Nozzle.

Figure 16 shows photographic images taken of the exhaust plume for the low and high expansion ratio nozzles during the vacuum tests. Image (a) shows the "spayed" exhaust plume that is characteristic of an under expanded nozzle. The exit pressure is substantially higher than the background pressure in the vacuum chamber, and the plume expands immediately after aft of the nozzle exit plane. Image (b) shows a more uniform exhaust plume with only a slight expansion of

the plume aft of the nozzle exit plane. Thus the 9.5:1 nozzle is close to the optimally expanded configuration for the achievable vacuum pressures with the MSFC facility used for this test campaign.
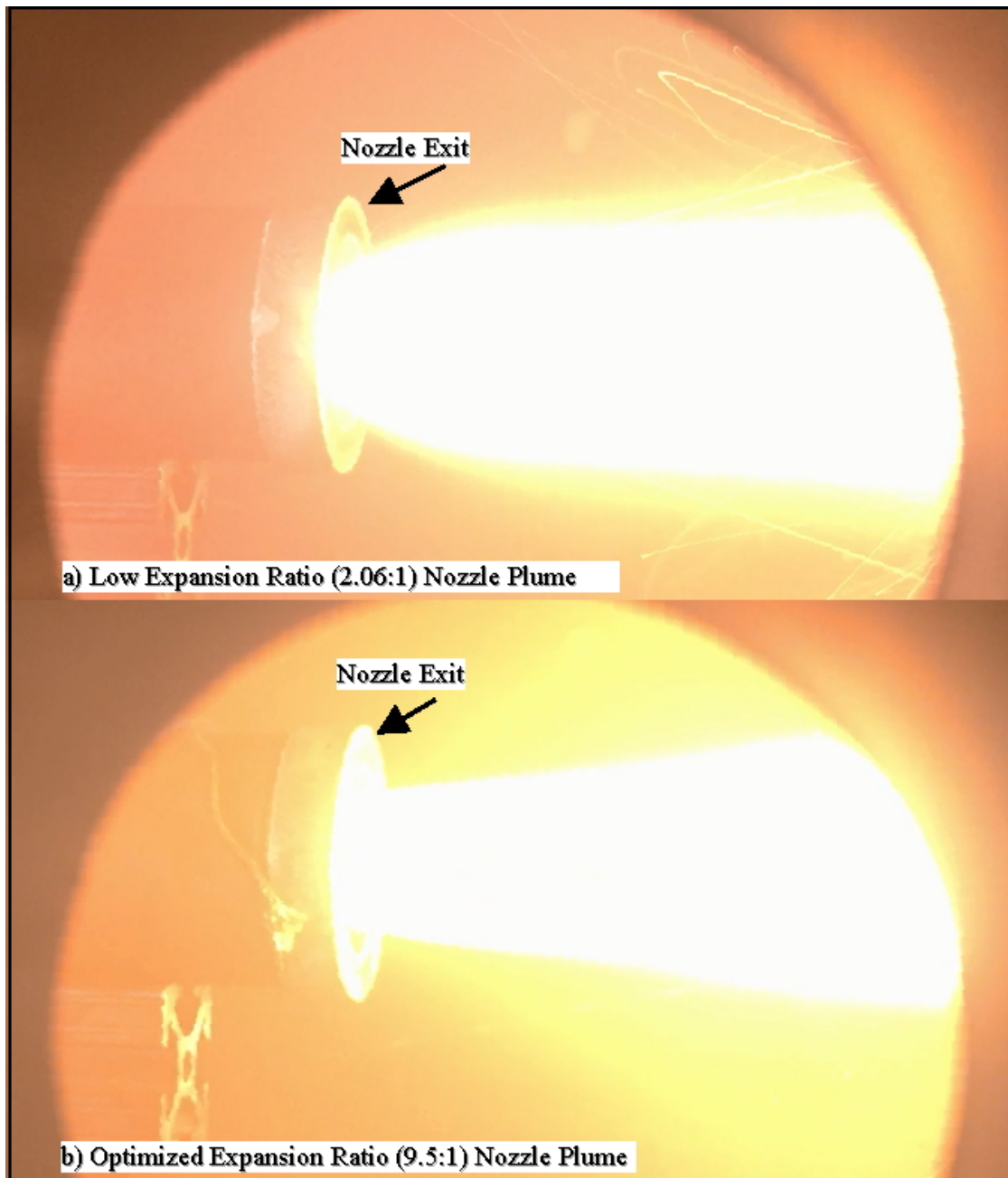
Figure 16. Comparison of Thruster Exhaust Plumes, Low and Optimized Expansion Ratio Nozzles.

M. Identified Design Issues and Potential Solutions.

Previous experience during the ambient pressure baseline tests has shown that the test-article thruster remains relatively cool during burns. Even after long-duration burns exceeding 8-seconds (Ref. xxxiii) during developmental testing at USU, motor case temperatures never exceeded 45 $^{\circ}$C, with the nozzle retainer exhaust temperature generally remaining below 45 $^{\circ}$C. However, it was immediately clear during this vacuum testing campaign was the aft end of the motor became significantly hotter than was experienced during the earlier ambient pressure test campaign. Figure 17 compares the measured motor case, nozzle retainer, and vacuum chamber exhaust gas temperatures for a typical 4-pulse burn. With each motor pulse the exhaust port temperatures become increasingly due to the residual entrapped gas and hot chamber walls, and this increase allows a gradual growth in both the nozzle and motor case temperatures. The peak nozzle temperature reaches 400 $^{\circ}$C, with the motor case temperature growing to 150 $^{\circ}$C.
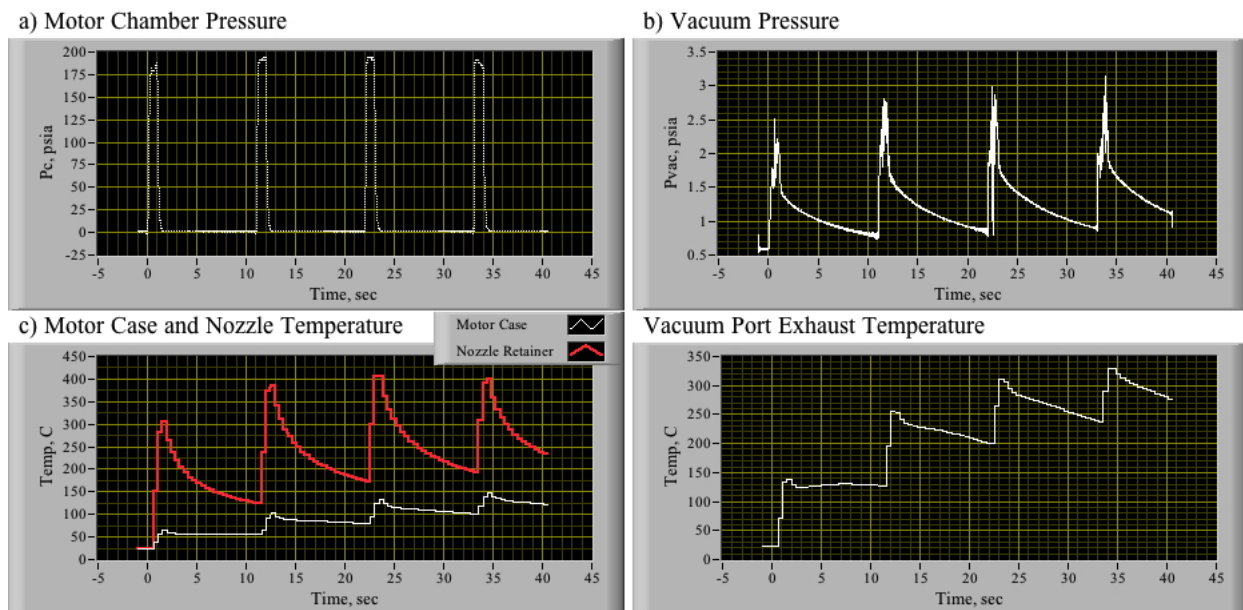
Figure 17. Example Temperatures Experienced During 4-burn Vacuum Motor Test.

The lack of a convective heat transfer mechanism during due to the vacuum may account for some of this additional heating; but a more likely cause was the high internal gas temperatures due to the entrapped plume exhaust. For the ambient pressure tests the exhaust plume was free to expand into the surrounding environment of the test cell and caused essentially no change in the surrounding air temperature. Thus, the nozzle radiated to a cold background at the outside air temperature. However, for these vacuum tests the hot exhaust plume was contained within the vacuum chamber and was forced to evacuate through only the small 2 inch exhaust port pictured in figure 5. This configuration allowed the internal gases to become significantly hotter, and the motor aft end radiated to a much higher background temperature.

190

Although ABS is an amorphous material and has no true melting point, the material become soft and pliable at temperatures above 200 °C.[8] Normally, during ABS hybrid rocket combustion pyrolysis occurs only along a thin flame zone adjacent to the fuel port surface; when coupled with the low thermal conductivity of ABS, the test-article typically thruster remains cool along the length of the grain. Virtually all of the heat of combustion is imparted to the exhaust plume leaving the motor. The structural integrity of the fuel grain remains intact.

However, the higher temperatures experienced during these vacuum tests compromised the fuel material structural integrity at the aft-end of the motor and had the deleterious effect of warping the aft-end of the fuel grain causing erosive burning. A stop-gap fix was provided by provided by shortening the fuel grain by ½ cm and inserting a silica-phenolic (Garolite®) insulating ring. Figure 18(a) presents a typical fuel-warping result showing both the burned and unburned fuel grains. The observed aft end warping limits the total safe burn time to only 8-seconds, and resulted in significant unburned fuel. Figure 18(b) compares the modified configuration to the original fuel-length fuel grain. The insulated fuel grain was burned for two consecutive 4-second tests with only minor damage. Figure 18(b) also shows these post burn images. The aft end warping was significantly reduced and there was little erosive burning.
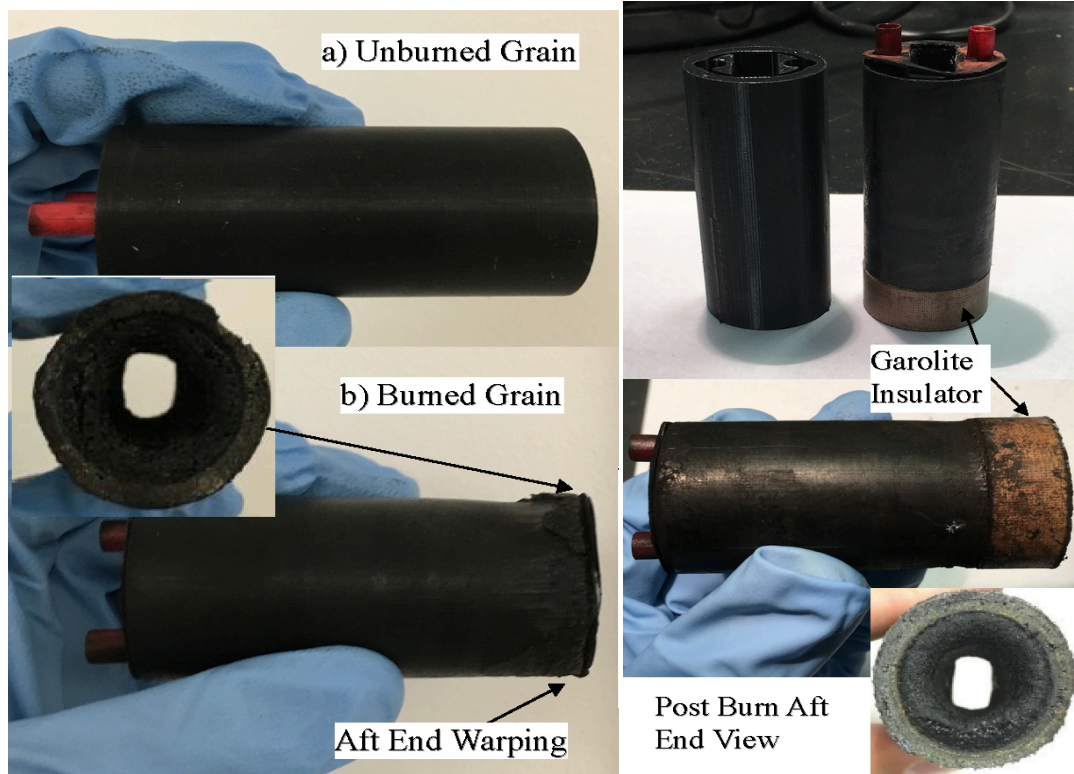
a) Normal Length, Uninsulated Fuel Grain   b) Shortened, Insulated Fuel Grain

Figure 18. Fuel Grain Warping Due to High Nozzle Retainer Temperatures, and Solution Using Garolite® Insulator.

---

[8] Anon., ABS, "A temperature of 230 °C has been established as the industry standard for 3-D printing," http://reprap.org/wiki/ABS, [Retrieved 21 August 2016].

VI. Future Work

The arc-ignition thruster system described in this paper has been accepted and funded for a sub-orbital flight test by the NASA Student Flight Opportunities (SFO) program. This flight demonstration project will design; build, and flight-test a novel arc-ignition green-propellant Cubesat thruster system. The proposed experiment will assess the restart-capability and vacuum performance of a prototype of the space thruster prototype currently under development at Utah State University (USU). Thus the experience gained with the MSFC vacuum facilities will rove to be extremely valuable. The tests will also perform plume contamination measurements to characterize potential deleterious effects on spacecraft optical sensors, external electronics, and solar panels.

The proposed hard-vacuum flight tests will allow the system to be operated with a high expansion ratio nozzle, and allow an accurate measurement of the achievable in-space specific impulse (I_{sp}). Specific tasks to be accomplished include pulsed-operation tests under vacuum conditions to characterize any corona effects during arc-ignition at low pressures. In addition to assuring minimal corona effects and proper system operation under vacuum conditions, the transient ignition tests will characterize the achievable minimum impulse bit during pulsed operation. Continuous operation tests will characterize the system impulse consistency, I_{sp} performance, and total system burn lifetime.

The experiment will be developed for suborbital flight test under the guidance of the NASA Sounding Rocket Program Office (SRPO) at Wallops Flight Facility (WFF). The improved Orion[xxxv] sounding rocket with a standard Ignition Recovery Module Assembly (IRMA) recovery system is proposed as the launch vehicle. Although real time telemetry is proposed to relayed sensitive data from the flight vehicle to WFF for archival, post flight recovery of the experiment module will allow redundant onboard data archival and post flight inspection of system components.

Figure 19 shows the Proposed Flight Test Concept of Operations. The assumed total payload - based on a rough order of magnitude (ROM) estimate -- is 140 lbf. With this trajectory 1) a 140 lbf (63.5 kg) payload achieves an apogee altitude of 100 km with an 84 deg.
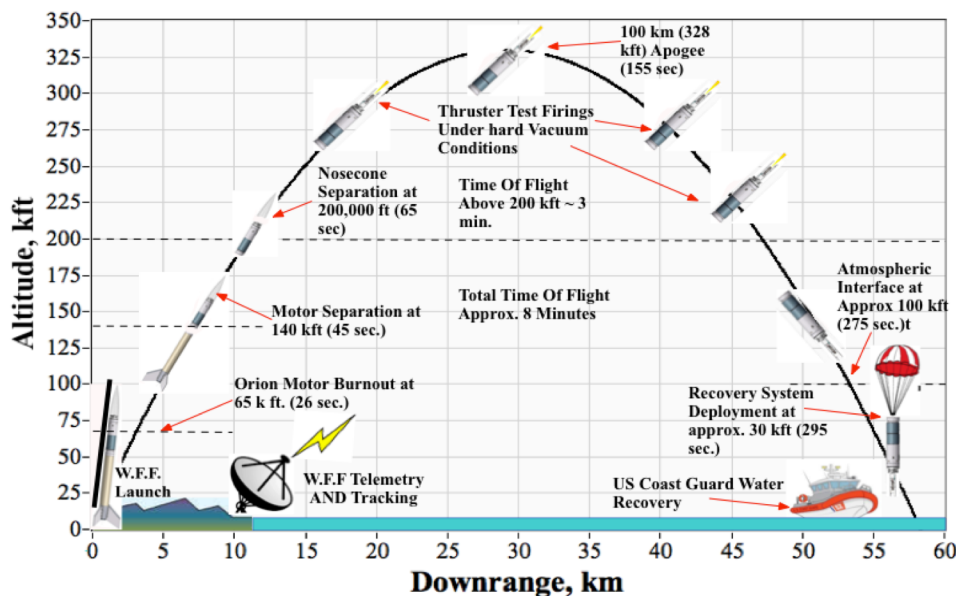
Figure 19. Proposed Flight Test Concept of Operations (CONOPS).

Launch angle, 2) the payload remains above 61 km (200,000 ft) for more than 3 minutes during the exo-atmospheric portion of the flight, 3) the rocket experiences more than 5 minutes of zero-g flight, 4) the peak acceleration occurs soon after launch and is less than 20 g's. Multiple thruster pulses with 15-20 seconds of total burn time will be pre-programmed to occur during the hard-vacuum portion of the flight -- above 200,00 ft. altitude. The water-landing occurs approximately 60 km downrange. As mentioned earlier, although a safe systems recovery is not required -- flight data will be telemetered to ground during flight -- ground recovery allows post flight measurements of the consumed propellant masses, and salvage of some of the more valuable flight components.

VII. Conclusion

This paper described the results of a vacuum testing campaign of a novel-arc ignition hybrid thruster for small spacecraft. The testing program teamed the Mechanical and Aerospace Engineering (MAE) Department at Utah State University (USU) and the Space Propulsion Branch (ER23) at Marshall Space Flight Center (MSFC). Preliminary results from the testing campaign are presented.

A major objective of the testing campaign was to demonstrate the ability of the thruster systems to operate reliably under high altitude test conditions. Thus, the initial series of tests attempted multiple consecutive burns of the system using fuel grains printed at both high and low material densities. Previous studies at ambient test conditions demonstrate that low-density grains burn at a higher massflow rate for a given oxygen massflux, and offered the potential for a small fuel grain length and more compact form factor. Although both printed grain densities ignited reliably under ambient pressure test conditions, only the high-density grains ignited reliably under vacuum conditions. Ignition of the low density grains was at best intermittent, with some grains failing all together after an initial burn sequence.

Following, the ignition-evaluation tests, multiple, identical one-second pulses were performed in order to evaluate the system performance. The motor characterization tests were performed using both the low- and high-expansion ration nozzles. The baseline motor tested with a 2.064:1 expansion ratio nozzle, when tested at ambient pressure conditions achieved a thrust level slightly greater than 20 N with a specific impulse of 212 seconds. When the same thruster was tested in the vacuum chamber, a thrust level of approximately 25 N with a specific impulse of 235 seconds was achieved. When the nozzle was expanded to a near-optimal 9.5:1 expansion ratio, the respective thrust and specific impulse improved to nearly 31 N and 280 seconds. Verified models calculate that the same thruster with a 25:1 expansion ratio nozzle would achieve a thrust level slightly greater than 32 N and a specific impulse of 300 seconds under hard vacuum conditions. For the current configuration, it appears that the higher density material provides a more reliable solution.

During the testing campaign it was discovered that aft-end of the motor and the retainer nozzle became considerably hotter than was experience during earlier ambient ground tests. The excessive nozzle temperatures resulted in aft-end fuel warping that limited the safe burn time of the fuel grain. The result was substantial unburned fuel residuals. The result necessitated minor changes to the thrust chamber configuration to ensure greater survivability. A stop-gap fix was provided by

provided by shortening the fuel grain by ½ cm and inserting a silica-phenolic (Garolite®) insulating ring. These changes are documented in the report. The insulated fuel grain was burned for two consecutive 4-second tests with out damage. The aft end warping was significantly reduced and there was little erosive burning.

Finally, the arc-ignition thruster system described in this paper has been accepted and funded for a sub-orbital flight test by the NASA Student Flight Opportunities (SFO) program. During the proposed flight test the test payload will achieve an apogee altitude of 100 km and will remain above 61 km (200,000 ft) for more than 3 minutes during the exo-atmospheric portion of the flight. The payload experiences more than 5 minutes of zero-g flight.. Multiple thruster pulses with 15-20 seconds of total burn time will be pre-programmed to occur during the hard-vacuum portion of the flight -- above 200,00 ft. altitude. The vacuum-test experience gained by the test team from this project will proved to be highly valuable as a risk buy-down for the flight test. Design changes resulting from this experiment will greatly improve the chances of the flight test experiment.

VIII.   Acknowledgments

IX. Appendix

Fuel Grain No.	Date	Density (kg/m³)	Pre-Mass (g)	Post-Mass (g)	Burn Description	Total Burn Time (s)	Nozzle Throat Diameter (in)	Nozzle Exit Diameter (in)	Aft-End Fuel Grain Picture
1	8/10/2016	1169.4	51.86	36.36	1-sec single burn, then 1-sec burn, 2-sec wait, 2-sec burn, 2-sec wait, 1-sec burn	5	0.162	0.216	
2	8/12/2016	1169.4	51.06	35.95	Four 1-sec pulses where only the last one lit. Did another series of four 1-sec pulses where all lit. 10-sec wait between burns.	5	0.1695	0.208	
3	8/15/2016	841.76	37.33	29.9	Four 1-sec pulses where only the first two pulses lit. 10-sec wait in between pulses.	2	Not measured	Not measured	
3	8/15/2016	841.76	29.9	22.91	Two 1-sec pulses with 15-sec wait in between.	2	0.17	0.21	
4	8/15/2016	841.76	37.3	36.23	¼-sec pulse with back bulkhead bolt removed, so it was burned in ambient conditions.	0.25	Not measured	Not measured	
5	8/17/2016	1169.4	48.36	36.61	Four 1-sec pulses with 10-sec waits in between. All burns lit successfully. Gained about an extra 1-lbf of thrust from high expansion ratio nozzle.	4	0.185	0.49	
5	8/17/2016	1169.4	36.61	24.3	Four 1-sec pulses with 10-sec waits in between.	4	0.185	0.49	
6	8/17/2016	1169.4	54.07	45.41	Three 1-sec pulses with 10-sec waits in between. System abort due to thermocouple in plume.	3	0.194	0.49	

6	8/18/ 2016	1169.4	37.43	28.1	Four 1-sec pulses with 10-sec waits in between. This was the first of the shortened fuel grain series.	4	0.198	0.482	
6	8/18/ 2016	1169.4	28.1	24.57	Four 1-sec pulses with 10-sec waits in between.	4	0.189	0.482	
7	8/19/ 2016	1169.4	42.3	33.5	Two series of 4-second duration burns. Time between burns approximately 5-15 seconds. Initial burn had a transient.	7.5	0.216	0.474	
7	8/19/ 2016	1169.4	33.5	24.43	Two series of 4-second duration burns with 10-second wait in between. Initial burn had a transient.	7.5	0.228	0.474	

196

X. References

[i] Goldstein, Edward, "The Greening of Satellite Propulsion," *Aerospace America*, February, 2012, pp. 26-28.

[ii] Rheingold, A. L., Cronin, J. T., Brill, T. B., and Ross, F. K., "Structure of Hydroxylammonium Nitrate (HAN) and the Deuterium Homolog," *Acta Crystallographica*, Vol. 43, No. 1, 1987, pp. 402-404.

[iii] Pembridge, and J. R., Stedman, G., "Kinetics, Mechanism, and Stoicheiometry of the Oxidation of Hydroxylamine by Nitric Acid," J. *of Chemical Society, Dalton Transactions*, Issue 11, 1979, pp. 1657-1663.

[iv] Hawkins, T. W., Brand, A. J., McKay, M. B., and Tinnirello, M., "Reduced Toxicity, High performance Monopropellant at the U.S. Air Force research Laboratory," AFRL-RZ-ED-TP-2010-219, *4th International Association for the Advancement of Space Safety Conference, Huntsville, AL, 19-21 May 2010.*

[v] Venkatachalam, S., Santhosh, G., Ninan, K. N, "An Overview on the Synthetic Routes and Properties of Ammonium Dinitramide (ADN) and other Dinitramide Salts". J. *Propellants, Explosives, Pyrotechnics*, Vol. 29, No. 3, March, 2004, pp.178–187.

[vi] Nagamachi, M. Y., Oliveira, J. I., Kawamoto, A. M., and Dutra, R., C., "ADN – The new oxidizer around the corner for an environmentally friendly smokeless propellant," J. of Aerospace Technology Management, Vol. 1, No. 2., December 2009, pp. 153-160.

[vii] Goldstein, Edward, "The Greening of Satellite Propulsion," *Aerospace America*, February 2012, pp. 26-28.

[viii] Anflo, K., and Crowe, B., "In-Space Demonstration of an ADN-based Propulsionstem," AIAA-2011-5832, *47th AIAA/ASME/SAE/ASEE Joint Propulsion Conference & Exhibit*, , San Diego, CA, USA, 31 July - 03 August 2011.

[ix] Anon., "NASA Goes Green: NASA Selects Green Propellant Technology Demonstration Mission," http://www.nasa.gov/home/hqnews/2012/aug/HQ_12-281_Green_Propellants.html, [Retrieved 12 December 2012].

[x] Anon., "NASA Goes Green: NASA Selects Green Propellant Technology Demonstration Mission," *http://www.nasa.gov/home/hqnews/2012/aug/HQ_12-281_Green_Propellants.html*, [Retrieved 12 December 2012].

[xi] Pokrupa, N., Anglo, K., and Svensson, O., "Spacecraft System Level Design with Regards to Incorporation of a New Green Propulsion System," AIAA-2011- 6129, *46th AIAA/ASME/SAE/ASEE Joint Propulsion Conference and Exhibit*, San Diego, CA, USA, July 31-Aug 3, 2011.

[xii] Persson, M., Anflo, K., and Dinardi, A., "A Family of Thrusters For ADN-Based Monopropellant LMP-103S," AIAA-2012-3815, *48th AIAA/ASME/SAE/ASEE Joint Propulsion Conference & Exhibit,* 30, Atlanta GA, USA, July - 01 August 2012,.

[xiii] Anon., Westinghouse Savannah River Co. Occurrence Report, SR–WSRC–FCAN–1996–0030, Elmgreen, R., February 10, 1997.

[xiv] Westinghouse Hanford Co. Memorandum from R.J. Bliss to L.F. Ermold, et.al., "Lessons Learned from Purex Chemical Makeup Reaction Event," January 30, 1990.

[xv] E.I. duPont de Nemours & Co., SRP, Separations Incident, SI–78–10–117, D.F. Chostner, October 4, 1978.

[xvi] Anon., "*Office of the Chief technologist, Space Technology Roadmaps: The Future Brought to You by NASA*," http://www.nasa.gov/offices/oct/home/roadmaps/index.html, [Retrieved 29 November, 2012].

[xvii] Anon., "NASA Space Technology Roadmaps, TA02, In-Space Propulsion," http://www.nasa.gov/sites/default/files/501329main_TA02-ID_rev3-NRC-wTASR.pdf, [Retrieved 10 may 2015].

[xviii] Anon., "NASA Space Technology Roadmaps, TA12: Materials, Structures, Mechanical Systems, and Manufacturing."" http://www.nasa.gov/sites/default/files/atoms/files/2015_nasa_technology_roadmaps_ta_12_materials_structures_final.pdf, [Retrieved 15 July 2015].

[xix] Whitmore, Stephen A., Peterson, Zachary W., and Eilers, Shannon D., "Comparing Hydroxyl Terminated Polybutadiene and Acrylonitrile Butadiene Styrene as Hybrid Rocket Fuels," *J. Propulsion and Power*, Vol. 29, No. 3, May–June 2013.

[xx] Whitmore, Stephen A., Inkley, Nathan R., and Merkley Daniel P., "Development of a Power Efficient, Restart-Capable Arc Ignitor for Hybrid Rockets, AIAA-2014-3949, 50th AIAA/ASME/SAE/ASEE Joint Propulsion Conference and Exhibit, Cleveland OH, USA, 28-30 July 2014.

[xxi] Stephen A. Whitmore, Nathan R. Inkley, Daniel P. Merkley, and Michael I. Judson. "Development of a Power-Efficient, Restart-Capable Arc Ignitor for Hybrid Rockets", *J. Propulsion and Power*, Vol. 31, No. 6 (2015), pp. 1739-1749.

[xxii] Stephen A. Whitmore. "Additively Manufactured Acrylonitrile-Butadiene-Styrene–Nitrous-Oxide Hybrid Rocket Motor with Electrostatic Igniter", *J. Propulsion and Power*, Vol. 31, No. 4 (2015), pp. 1217-1220. DOI: 10.2514/1.B35681

[xxiii] Whitmore, Stephen A., Walker, Sean D., and Merkley Daniel P., "High Regression Rate Hybrid Rocket Fuel Grains with Helical Port Structures," AIAA-2014-3751, *50th AIAA/ASME/SAE/ASEE Joint Propulsion Conference and Exhibit*, Cleveland OH, USA, 28-30 July 2014.

[xxiv] Stephen A. Whitmore, Sean D. Walker, Daniel P. Merkley, and Mansour Sobbi. "High Regression Rate Hybrid Rocket Fuel Grains with Helical Port Structures", *J. Propulsion and Power*, Vol. 31, No. 6 (2015), pp. 1727-1738.

[xxv] Whitmore, Stephen A., "Additively Manufactured Acrylonitrile-Butadiene-Styrene–Nitrous-Oxide Hybrid Rocket Motor with Electrostatic Igniter," *J. of Propulsion and Power*, Vol. 31, No. 4, July-August 2015, pp. 1217-1220.

[xxvi] Whitmore, Stephen A., "Additive Manufacturing as an Enabling Technology for "Green" Hybrid Spacecraft Propulsion," RAST-1039, *Conference* on *Recent Advances in Space Technology* 2015, Istanbul Turkey, June 16-19 2015.

[xxvii] Whitmore, Stephen A., Merkley, Stephen L., Zachary S., Walker, Sean D., "Development of a Power Efficient, Restartable, "Green" Propellant Thruster for Small Spacecraft and Satellites," SSC15-P-34, *29th AIAA/USU Conference on Small Satellites*, Logan UT, 8-13 August, 2015.

[xxviii] Whitmore, S. A., Merkley, S. L., Walker, S. D., Tonc, L., Spurrier, Z. S., and Mathias, S., "Survey of Selected Additively Manufactured Propellants for Arc-Ignition of Hybrid Rockets," AIAA 2015-2616, *51st AIAA/ASME/SAE/ASEE Joint Propulsion Conference and Exhibit*, Orlando FL, 27-29 July, 2015.

[xxix] Sutton, G. P., and Biblarz, O., *Rocket Propulsion Elements, 7th ed*., Wiley, New York, 2001, Chaps 4-5.

[xxx] Gordon, S., and McBride, B. J., "Computer Program for Calculation of Complex Chemical Equilibrium Compositions and Applications," *NASA RP-1311*, 1994.

[xxxi] Whitmore, S. A., Peterson, Z. W., and Eilers, S. D., "Comparing Hydroxyl Terminated Polybutadiene and Acrylonitrile Butadiene Styrene as Hybrid Rocket Fuels*," J. Propulsion and Power*, Vol. 29, No. 3, May-June 2013. Pp. 582-592.

[xxxii] Whitmore, S. A., and Merkley, S. L., "Effects of Radiation Heating on Additively Printed Hybrid Fuel Grain O/F Shift", AIAA 2016-4867, *52nd AIAA/SAE/ASEE Joint Propulsion Conference, Propulsion and Energy Forum*, Salt Lake City, UT, USA, July 25-18, 2016.

[xxxiii] Whitmore, S. A., and Mathias, S., "Development and Testing of Three Alternative Designs for Additively Manufactured Hybrid Thrusters", AIAA 2016-4867, *52nd AIAA/SAE/ASEE Joint Propulsion Conference, Propulsion and Energy Forum*, Salt Lake City, UT, USA, July 25-18, 2016.

[xxxiv] Beckwith, T. G., Marangoni, R. D., and Lienhard V, J. H., *Mechanical Measurements, 6th Ed*., Addison-Wesley Publishing Company New York, 2006, pp. 43-73.

[xxxv] Anon., "NASA Sounding Rockets User Handbook," 810-HB-SRP, NASA Goddard Space Flight Center, Wallops Flight Facility, Wallops Island, VA 23337, July 2015, pp. 139-140.

Additive Manufacturing of Avionics: an Introduction to Aerosol Jet® Printing

Chih-Hao Wu[1] and Furman V. Thompson[2]

NASA Marshall Space Flight Center, Huntsville, AL, 35812

Additive Manufacturing of Avionics (AMA) is a process that involves a growing variety of material deposition technologies to directly print 3D electrical, electronic, and electromechanical (EEE) parts for aerospace applications. Aerosol Jet® Printing (AJP) is considered to be a Direct Write (DW) Additive Manufacturing (AM) technology capable of producing fine, scalable, controlled depositions of ink-based electronic materials. From this non-contact process various three dimensional (3D) geometric structures and patterns of materials can be printed to develop novel to advanced Avionics components, systems, and architectures. In this report, the general AJP process is outlined and introduced along with viable applications for its use in Aerospace applications.

I. Introduction

Additive Manufacturing of Avionics has been a prime focus area for National Aeronautics and Space Administration (NASA) and Marshall Space Flight Center (MSFC) EEE Parts Packaging Team, due to the unique in-house advanced avionics manufacturing research and development capabilities it supports. As NASA's portfolio as an agency expands to include transportation and space systems development for deep space exploration with the Space Launch System (SLS) and Orion, the increased dependence on Avionics is certain. Therefore NASA must continue to invest in ways to reduce the overall operational cost for Avionics technology development and use while responding to the growing demands of space-electronics functionality and flexibility. Marshall Space Flight Center has historical significance as being an advanced manufacturing center which positions it well to be an incubator for adopting relative technologies like Aerosol Jet® Printing and many other AM technologies. With recent ISS experiments involving successful 3D printing in microgravity, the desire to pursue metals and electronics AM processes in space began to foster a clearer picture of human's long term presence and self-sustainability in space. Thus, leading to new opportunities to study AM technologies relative to printing electronics in a microgravity environment. From these in-space opportunities the likely development of completely new manufacturing processes will have potential payoffs to AM processes on earth. MSFC has adopted a variety of Additive Manufacturing technologies to assess and consider in the planning and development of ground based and in-space Additive Electronics/Avionics Capabilities.

II. The Aerosol Jet® Printing Process

The key technology under focus in this report is AJP Technology. The Aerosol Jet® Printing process produces precise deposits of ink-based materials that have been atomized into an aerosol mist and delivered to a substrate by means of aerodynamic focusing. AJP is a non-contact high standoff printing process capable of printing spot sizes down to 5 microns and layer thicknesses of 25 nanometers and up. As a result of these capabilities, AJP is very attractive to innovators in the field of EEE Parts Packaging for Aerospace because it enables the feasibility to produce highly dense, flexible, and lightweight three dimensional (3D) packaging solutions for Avionics. AJP deposits many kind of materials onto a wide variety of substrates minimizing the complexity and infrastructure required in traditional semiconductor industry packaging processes such as masking, thin-film processing, and photolithography. Consequently, AJP and other AM electronics technologies have laid the foundation for the next generation of electronics manufacturing.

---

[1] Summer Faculty Fellow, EEE Parts Packaging (ES 43), NASA MSFC, Harding University.
[2] Focus Area Champion, EEE Parts Packaging (ES 43), Huntsville, AL, 35812, NASA MSFC.
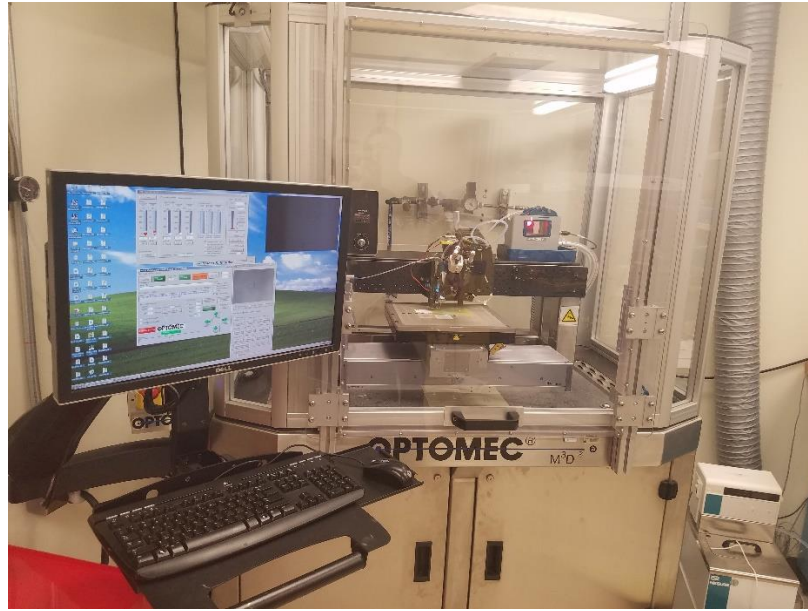
Figure 1. Optomec Aerosol Jet® printer 300 (AJ 300) Series Located at MSFC

The Pneumatic Atomization Process with Virtual Impactor Module

The AJ 300 utilizes a pneumatic atomizer with virtual impactor. The general concept for the pneumatic atomizer involved utilizing a high-velocity gas stream to break up the silver nanoparticle ink into a femto-liter size droplets. On the average, these droplets size are between 1 to 5 micron. The compressed air stream is expanded through the atomizer nozzle. As a result of that, a high velocity of jet stream of droplet which contains silver nanoparticle is formed. The above ink is drawn from the ink reservoir into the atomizer nozzle. The high velocity gas stream that composed of suspended droplets, leaves the nozzle and impinges on the sidewall of the atomizer reservoir. The process usually creates both large and small size droplets. For the large droplets, they impact the sidewalls of the reservoir and drain back into the reservoir, similar to a recycling process. The smaller droplets will continue to stay suspended in the gas ready to be transported to the next stage. The gas flow rate needed to form the high velocity aerosol is too high for the deposition head. One more device needs to come along to reduce the pressure generated, which is the virtual impactor. The virtual impactors main purpose is to concentrate the aerosol mist by removing excess atomization gas from the above system. After this virtual impactor stage, the output gas is then push forward to the print head, such as shown in Figure 2 [9].
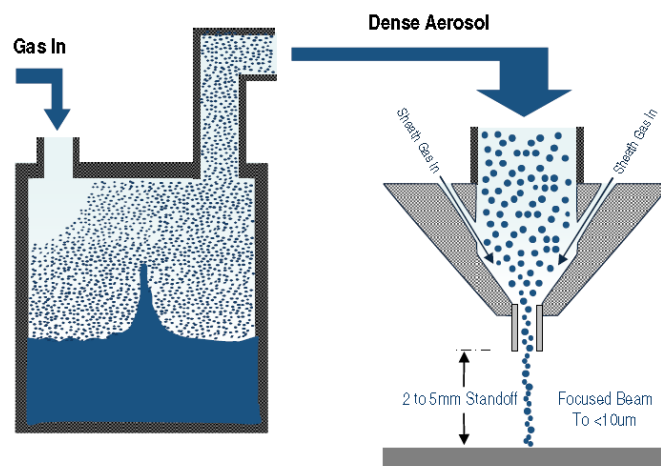

Figure 2. Schematic of the general Aerosol Jet® process [9]

200

The Description of Print Module

The print module includes alignment camera, tube heater, laser module, laser alignment camera, processing viewing camera and print head.
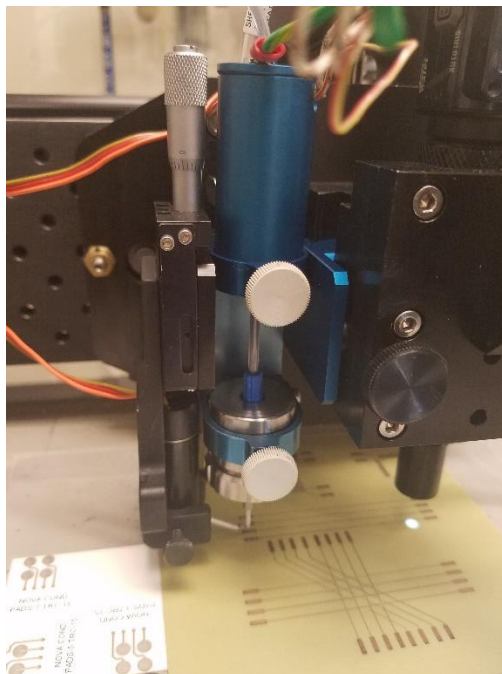

Figure 3. The photograph of Aerosol Jet® deposition head, ceramic nozzle and shutter

A. Print Head

The print head in our AJ 300CE as illustrated in the above Figure 3 is able to print trace widths onto any surface with feature sizes as small as 10 µm. In previous paragraph, the described pressure-reduced aerosol stream after the virtual impactor from the atomizer provides the aerosol droplets that are used in our final printing process using our print module. The aerosol stream generated is then pushed into the print head where the aerosol droplets are surrounded by a sheath gas stream. The purpose of the sheath gas stream is to focus and accelerate the droplets so that they are impacted onto the substrate. Based on the concept of Computation Fluid Dynamics (CFD) studies and research, this type of focusing effect in the study of fluid dynamics is usually referred to as aerodynamic focusing. As the print head is scanned across the substrate, printed features such as functional circuit is therefore created. A process shutter as appeared in Figure 3 is to stop and reinitiate the flow of the focused aerosol jet stream. In the Additive Electronics Laboratory of Marshall Space Flight Center, electrical components of conductors, resistors, insulators, ultra-capacitor and polymers have all been successfully printed and tested for its functionality as illustrated in following Figure 4.

Figure 4. A few functional parts Aerosol Jet® printed by MSFC Additive Electronics Lab

B. Vision Systems

The vision system in the following Figure 5 is composed of an alignment camera and a print processing viewing camera. The purpose for the alignment camera is to position the substrate alignment before toolpath execution. The deposition process viewing camera is utilized for the purpose of watching the deposition process.
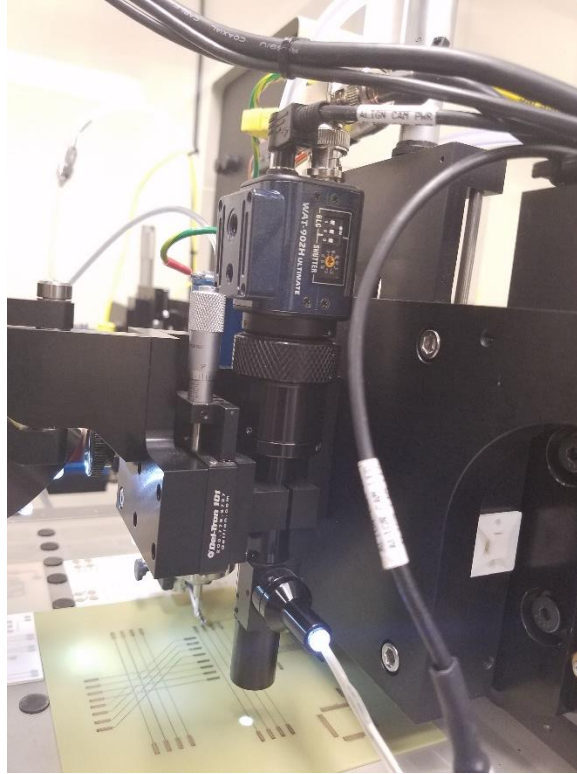

Figure 5. The vision system of AJ 300 Aerosol Jet® Printing system

III. The Comparison between Aerosol Jet® Printing and Inkjet Printing

The features of the Aerosol Jet® Printing and Inkjet Printing can be summarized in the following Table 1. [11]

	Features	Existing Inkjet Printing	Patented Aerosol Jet® Printing
1.	Single-Pass Layer Thickness	0.1 to 10 microns	25 nanometer to 10 microns
2.	Minimum Resolution	30 microns	10 microns or less
3.	Material Viscosity	5 - 15 c.P.	1-1000 c.P.
4.	Solids Loading Capability	20 % of its weight	70 % of its weight
5.	Print Head Stand Off Distance	1 millimeter	3-5 millimeter
6.	Multi-Material Printing	Multiple print heads	Dual print heads with aerosol mixing
7.	Three Dimension Direct Write	Fixed – planar only with adjustable z	3 axis (x, y and z direction)

Table 1 The comparison features between Aerosol Jet® printing and inkjet printing [11]

The above seven distinct features can be further elaborated to show the Aerosol Jet® printing technology provides unique advantages over existing inkjet printing technology. For instance, in the minimum resolution comparison, using patented Aerosol Jet® printing process can demonstrate a finer feature size. In a single-pass layer thickness

comparison, Aerosol Jet® printing process has improved process control. In the preparation of material viscosity comparison, Aerosol Jet® printing allows the engineers to have wider material choices and control over deposition thickness. In the solid loading comparison, Aerosol Jet® printing benefits the users with higher metal and ceramic contents. In the process of multiple material printing, the aerosol jet printing allows functional gradient materials. In the comparison of print head standoff distance, Aerosol Jet® printing is not sensitive to surface irregularities. This feature enables conformal deposition and allows access into corners. Finally, for the direct three dimensional direct writing capability, the Aerosol Jet® printing users benefit from a true three dimensional printing. [11]

IV.   Aerospace Applications for Aerosol Jet® Printing

One of the key challenges for Electrical and Electronics engineers involved with the packaging and organization of Avionics is feasibly reducing the overall weight of the system while maintaining reliability and functionality. AJP process are being utilized to do just that in a variety of Aerospace applications. NASA, DOD, and various other Commercial organizations are using AJP to manufacture the next generation of lightweight printable energy storage, sensors, antennas, and solar cells. NASA is investigating ways to continue to add to their In-Space Manufacturing portfolio by including technologies like 3D printing and AJP to provide a self-sustainable means of avionics parts production for long term duration missions.

V.   Conclusion

The novel Aerosol Jet® deposition system is presented in this report with detailed functional analysis, this includes its features, benefits, and some selected application areas. The advancing of the state of the art in additive manufacturing of electronics has been elaborated. This direct write technology with AutoCAD, VMtool and Graphical User Interface (GUI) features of Optomec's unique Aerosol Jet® concept is currently being used with a wild range of Military and Aerospace avionics application. With this successful technological invention, electrical engineers and material scientists can now benefit from the unique features of Aerosol Jet® patented technology to create three dimensional electronics component designs of reduced cost and time.

Acknowledgments

References

[1]Sunol, F., Gonzalez-Cinca, R., Liquid Jet Breakup and Subsequent Droplet Dynamics Under Normal Gravity and in Microgravity Conditions. *Physics of Fluids 2, 077102.* (2015).

[2]Horteis, M., and Glunz, S. W., Fine Line Printed Silicon Solar Cells Exceeding 20% Efficiency: *Progress in Photovoltaics: Research and Applications* 2008: 16:555-560 Published online in Wiley InterScience (www.interscience.wiley.com)DOI: 10.1002/pip.850

[3]Hedges, M., Kardos, M., King, B., and Renn, M. J., Aerosol-Jet Printing for 3-D Interconnects, Flexible Substrate and Embedded Passives. *Proceedings of the International Wafer Level Packaging Conference*, San Jose, CA, November, 2006.

[4]Cho, J. H., Lee, J., Xia, Y., Kim, B., He, Y., Renn, M. J., Lodge, T. P., and Frisbie, C. D., "Printable Ion Gel Gate Dieletics for Low Voltage Polymer Thin Film Transistor on Plastic", *Nature Materials 7(11): 900-6* (2008)

[5]Xia, Y., Cho, J. H., Paulsen, B., Renn, M. J., Lodge, T. P., and Frisbie, C. D., "Correlation of ON-State Conductance with Referenced Oxidation Potential in Ion Gel Polymer Transistor". *Appl. Phys. Lett. 94, 0133004* (2009).

[6]Vaillancourt, J, Zhang, H., Vasinajindakaw, P., Xia, H., Lu, X., Han, X., Janzen, D. C., Shih, W., Jones, C. S., Stroder, M., Chen, M. Y., Subbaraman H., Chen, R. T., Berger, U., and Renn, M. J., "All Ink-jet-printed Carbon Nanotube Thin-film Transistor on a Polyimide Substrate with an Ultrahigh Operating Frequency of over 5 GHz". *Appl. Phys. Lett. 93, 243301* (2008)

[7]Paulsen, J. A., and Renn, M. J., "Printing of Miniature Polymer Thick Film Resistors for Embedded Applications", *IPC 3rd International conference on Embedded Technology*, Chelmsford, MA, May 4, 2006.

[8]Gibson, I., *Additive Manufacturing Technologies*, 2nd edition, Springer, New York, 2015.

[9]Christenson, K. K., Paulson, J. A., Renn, M. J., McDonald, K., Bourassa, J., Optomec; St. Paul, Minnesota/USA., "Direct Printing of Circuit Boards Using Aerosol Jet", *2011 Society for Imaging Science and Technology*.

[10]Aerosol Jet and Optomec are trademark of Optomec, Inc.

[11]Hedge, M., *"Aerosol Jet Process – Technology and Advantages"*, unpublished Optomec, Inc. document. 2011.

Improved Mechanics Model of Plug Welding

Q. K. Zuo [1]
University of Alabama in Huntsville, Huntsville, AL, 35899

A. C. Nunes, Jr.[2], J. Littell[2]
NASA Marshall Space Flight Center, MSFC, AL, 35812

P. S. Chen[3]
Jacobs ESSSA Group/Qualis Corporation, 689 Discovery Dr NW #400, Huntsville, AL, 35806

The preliminary model developed previously by the authors for friction plug welding process has been improved upon. The main improvement is the accounting for, in an elementary manner, the effects of local melting on the shear stress and pressure on the interface. The local melting is modeled by specifying a critical temperature at which local melting of the copper-rich secondary particles occurs. A simple kinetics model is introduced for the evolution of the liquid phase in the semi-solid metal. The model predictions of the torque, energy, and pull force on the plug are compared to the experiment data of a plug weld. Comparison of the pull force predicted by the current model with the measured data show a significant improvement over the original model.

Nomenclature

ω	=	plug rotation rate
R	=	radius of hole in workpiece
δ	=	thickness of workpiece layer stuck on plug
$\emptyset$	=	taper angle of plug
V_P	=	plug pull velocity
w	=	travel (penetration) distance
q	=	heat flux due to plastic heating
T	=	temperature
K	=	thermal conductivity
$L(t)$	=	radius of heat diffusion
τ	=	shear strength
P	=	pressure

I. Introduction

Plug welding is a process used to close holes left in welds by the Self-Reacting Friction Stir Welding (SR-FSW) process. In the SR-FSW process a shoulder is attached to the pin bottom, and the pin is pulled up through a hole in the workpiece against a second shoulder. The two shoulders, which rotate with the pin, exert a "squeeze force" on the workpiece that prevents escape of metal from the weld in SR-FSW just as the "plunge force" does with the standard FSW tool. [1] The SR-FSW pin can be removed from the workpiece only by stopping the weld and either detaching the pin bottom shoulder or detaching the pin from the upper shoulder so that the pin may be extracted from the weld. This leaves a hole in the weld. The hole is customarily filled in by a plug weld. A sketch of the plug weld process is shown in Fig. 1. [1]

A theoretical model that is based on a sound understanding of the physics and mechanics of the process can help the welding engineer to better select the process parameters of a plug weld (e.g., the hole diameter and thickness of

---

the workpiece, the geometry and material of the plug), which can in turn reduce the development time and cost required for a new application of plug welding. Due to the high rotational speed of the plug (about 6000 RPM in a typical plug weld studied in this research) and the short time of the plugging process (on the order of a few seconds), the plug welding is a transient process, which, combined with a highly coupled nature of thermal heating and plastic deformation during the deformation, makes the process very challenge to model theoretically. We have recently developed a preliminary model for friction plug welding process. The model was shown, by comparing with the test data, to be able to qualitatively capture the main features in the early stage of the plugging process. [1] However, the model was not able to predict the softening behavior of the plug (a drop in the full force on the plug), which has often been observed in welds that show high quality. The objective of this effort is to improve upon the preliminary model so that it can predict this important feature. The objective has been achieved by incorporating in the model the physics of local melting of the metal next to the plug/workpiece interface. As shown later in the report, the current, improved model gives a much improved comparison with the experimental data.
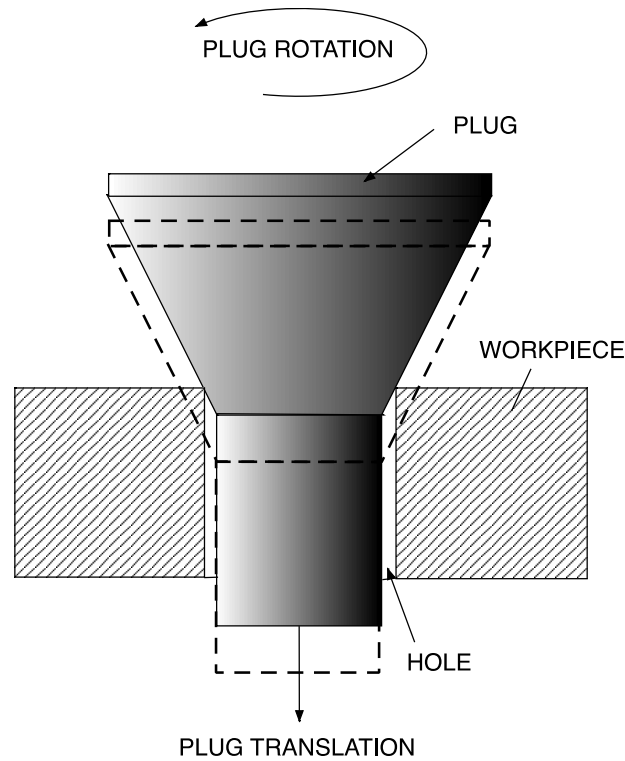

Figure 1. Sketch of plug weld process (a much-simplified plug is shown). Plug is rotated and pulled into hole in workpiece. Workpiece contact metal is extruded out along the contact surface.[1]

II.   Mathematical Model

A. Interface Temperature and shear

The temperature and shear stress at the interface between the plug and the workpiece metal are determined by the consideration of energy conservation and the formulation of a temperature-dependent strength model for the metal. The details of the derivation and formulation are given in a previous report. [1] For the sake of completeness and ease of reference, a brief summary of the key features of the model is given next.

Consider the interaction between the plug and the workpiece. Let the plug surface be represented by the plug bonded to the workpiece metal, as shown in Fig. 2. The plug moves into the paper with velocity approximately ωR, where ω is the spinning rate of the plug and R is the radius of the hole in workpiece; the plug sticks at the plug/workpiece surface and a thin layer of workpiece metal of thickness δ, which may vary along the plug surface, rotates with the plug. The workpiece metal beyond the shear surface remains stationary; hence the shear surface

represents a singular surface across which the tangential (into the paper) velocity of workpiece metal experiences a jump. In this study, for simplicity, δ is treated as constant along the plug surface.
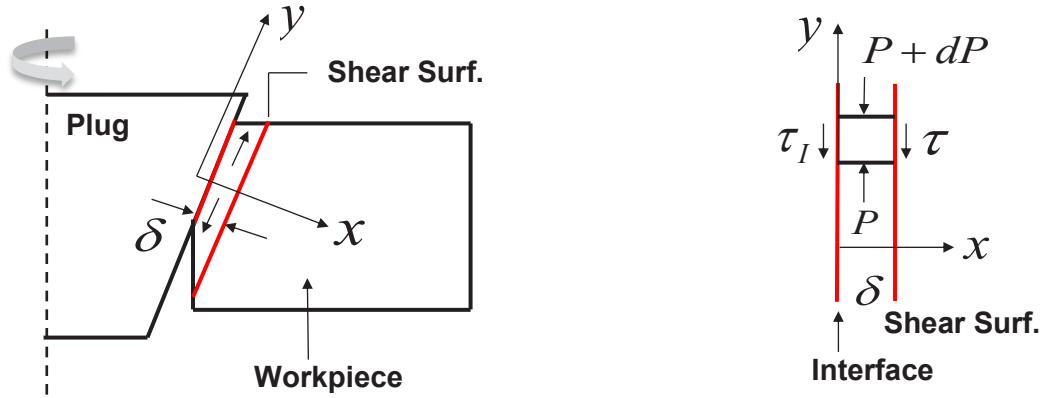

Figure 2. Simplified interface model of the plug and workpiece interaction. [1]
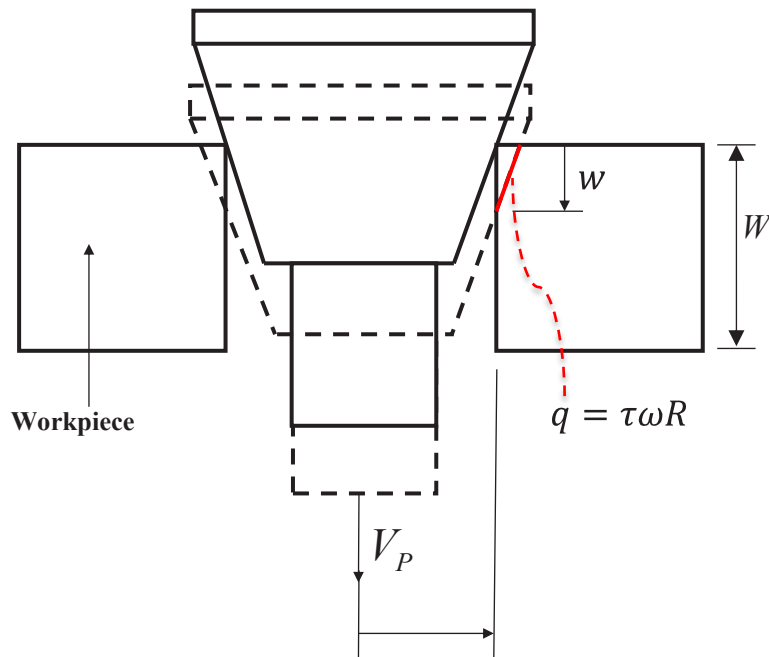

Figure 3. Plug and workpiece interaction showing contact surface and heat flux. [1]

The temperature at the interface is given by requiring the rate at which the heat is being generated is the same as that of absorption of the heat by the material. Let the ambient temperature T_∞ of the workpiece. If the shear stress of the weld metal at the interface temperature is τ, then the interface represents a heat source (flux) of magnitude $q = \tau\omega R$. For a constant pull velocity V_P, the depth of penetration (along the thickness of the workpiece) is $w = V_P t$, as shown in Fig. 3. The temperature at the interface is related to the shear at the interface by

$$\pi \bar{K}\left(T-T_{\infty}\right)=\frac{\omega R\left(V_P t\right)}{\cos\left(\phi/2\right)}\tau \tag{A1}$$

In Eq. (A1) since τ is a function of the temperature of the material, we need to have a model for the material strength to solve for the temperature and hence the shear.

B. Strength Model

For the meal (aluminum alloy 2219) under the conditions prevalent in the plug welding process (i.e., high temperature and high strain rate), the plastic deformation process occurs as the result of breakthroughs of dislocations past pinning point barriers. Bases on the consideration of the deformation process, a model for the strength of the plug material and the workpiece material (2219 aluminum) as a function of the temperature and strain rate is developed

$$\tau\left(T,\dot{\gamma}\right)=\frac{E}{v}+\frac{k_B T}{v}\ln\left(\frac{\dot{\gamma}}{\dfrac{b}{L}\dfrac{\Delta a}{L^2}nf}\right) \tag{B1}$$

where γ is the strain rate, E is the activation energy, v is the activation volume ($v=b\Delta x\Delta s/4$), b is the Burgers vector, k_B is the Boltzmann constant, L is the size of the representative volume over which statistical averaging of deformation is carried out to construct the continuum representation of the deformation ($L\approx 1{,}000A=0.1\mu m$), Δa is the area swept out by the dislocation line (loop) that have successfully broken through the pinning point barriers. n is the number of jump sites in the representative volume (L^3) so that n/L^3 is the number density of jump sites in the material. f is the natural oscillation frequency (the Debye frequency, $f\approx 8x10^{12}\ 1/s$). Eq. (B1) can be rewritten as

$$\tau\left(T,\dot{\gamma}\right)=\left(\frac{E}{v}-\frac{k_B T}{v}\ln\dot{\gamma}_0\right)+\frac{k_B T}{v}\ln\dot{\gamma} \tag{B2}$$

where

$$\dot{\gamma}_0\equiv\frac{b}{L}\frac{\Delta a}{L^2}nf \tag{B3}$$

It is seen from Eq. (B1) (or Eq. (B2)) that the strength of a metal is much more sensitive to the change in the temperature (it drops linearly with the temperature) than to that in the strain rate (it depends on the strain rate via logarithm hence much weaker).

For the aluminum alloy and the conditions encountered in plug welding, the following values are reasonable approximations of the parameters in Eq. (B1):

$$L\approx 1{,}000A,\ b\approx 3A,\ \Delta a\approx\frac{\pi}{4}\left(\Delta s\right)^2\sim 10{,}000\pi b^2,\ n\approx 0.1 \tag{B4}$$

giving

$$\dot{\gamma}_0\approx 6.8x10^8/s,\ v=\frac{b}{2}\frac{\Delta x\Delta s}{2}\approx 1.35\,nm^3 \tag{B5}$$

$$\frac{k_B}{v}=\frac{1.38x10^{-23}J/^{\circ}K}{1.35x10^{-27}m^3}=10.2x10^3\,\frac{Pa}{^{\circ}K}=1.48\,\frac{psi}{^{\circ}K} \tag{B6}$$

It is seen from Eq. (B2) that

$$\frac{\partial \tau}{\partial T} = -\frac{k_B}{v} \ln\left(\frac{\dot{\gamma}_0}{\dot{\gamma}}\right) = -1.48 \ln\left(\frac{\dot{\gamma}_0}{\dot{\gamma}}\right) \frac{psi}{{}^o K} \tag{B7}$$

and

$$\frac{\partial \tau}{\partial \dot{\gamma}} = \frac{k_B T}{v} \frac{1}{\dot{\gamma}} \tag{B8}$$

It follows that the strength (yield stress) decreases linearly with an increase in the temperature. Furthermore, the slope of decrease with temperature decreases with the strain rate (that is the slope is more pronounced for low strain rate processes than for high rate processes. For typical strain rates encountered in the plug welding, $\dot{\gamma} \approx 10^4 / s$ and the slope of the strength-temperature curve is

$$\frac{\partial \tau}{\partial T} = -\frac{k_B}{v} \ln\left(\frac{6.8x10^8}{1.0x10^4}\right) = -\frac{k_B}{v}(11.13) = -16.5 \, psi / {}^o K \tag{B10}$$

which compares reasonably well with the available data[2] on the strength of the workpiece material (2219 aluminum). Based on the data[2], to keep the model simple and yet physical, a piecewise linear, model $\tau = \tau \, T$ has been constructed which gives an excellent fit with the data (a comparison with the data are given in Ref. 1).

C. Pressure Distribution

Consider the plastic deformation of workpiece metal between interface and the shear surface. It is seen from the micrograph of plug/workpiece contact surface, as shown in Fig. 4, that the metal between the plug-workpiece interface and the shear surface (inside the workpiece) flows along the interface. We refer to this flow as "channel" flow. The cause of this flow is the pressure gradient in the direction of the interface. [1]
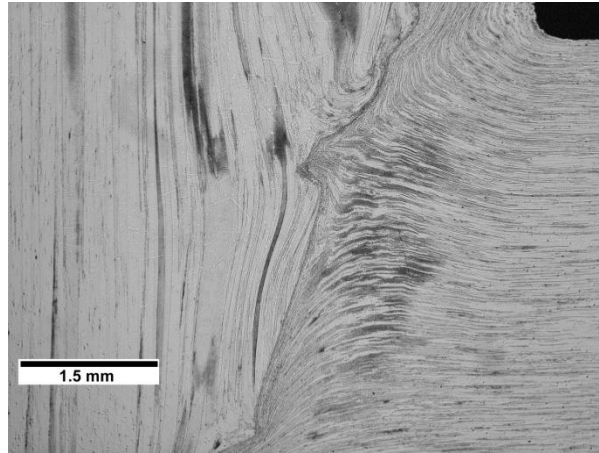

Figure 4. Micrograph (Courtesy of J.C. McClure) showing plug/workpiece contact surface. Flat elongated grains of the rolled workpiece on the left mark a workpiece-side flow against the plug surface, straight in at the center, upswept above and down swept below, as the plug forces the workpiece metal out of its way. Very close to the plug interface the workpiece grain structure vanishes and is replaced by a refined structure; this is thought to be due to passage through a shear surface (adiabatic shear band) separating metal rotating with the plug from the stationary metal of the workpiece. [1]

Consider the distribution of pressure along the direction of the channel. The contact length is $w' = w/cos \, \emptyset/2$, where $w = V_P t$ is the depth of penetration defined previously. Let the y axis be along the interface with the origin at the center of the contact length. Let the shear stress on the interface between the plug and the workpiece metal be τ_I

208

and the contact pressure (normal to the interface) be P_x. The magnitude of the interfacial shear τ_I is the *smaller* of the friction (stress) on the contact surface and the (shear) yield stress of the metal:

$$\tau_I = \min\left(\mu P_x, \tau\right) = \begin{cases} \mu P_x, & P_x \le P_{min} \\ \tau, & P_x > P_{min} \end{cases} \tag{C1}$$

where $P_{min} = \tau/\mu$ is the *minimum contact pressure* required on the interface below which it is easier for the plug to slip (slide) over the workpiece metal than to plastically deform. When the contact pressure is large enough ($P_x > P_{min}$), the frictional resistance to slip is greater than the yield stress of the metal and it becomes easier for the metal to shear (plastic deformation) than to slip; that is, the workpiece stick to the plug.

Let the pressure in the direction parallel to the interface be P_y. Then the equilibrium condition for the metal inside the channel is

$$\frac{\partial P_y}{\partial y} \pm \frac{\tau_I + \tau}{\delta} = 0 \tag{C2}$$

where the plus and minus signs apply to, respectively, the upper flow ($y > 0$) and the lower flow ($y < 0$). For clarity, only the upper flow ($y > 0$) will be considered in detail so only "+" needs to be considered (the pressure distribution in the lower flow can be inferred by symmetry).

The metal inside the channel is plastic and the yield condition may be given by the maximum shear criterion (the Tresca theory):

$$P_x - P_y = 2\tau \tag{C3}$$

The pressure parallel to the interface reduces to zero at the top edge of the contact:

$$P_y\left(y = \bar{w}\right) = 0 \tag{C4}$$

where $\bar{w} = w'/2$ was introduced for convenient.

It follows from Eq. (C3) that (since τ is a constant)

$$dP_y = dP_x \tag{C5}$$

The substitution of Eq. (C5) into Eq. (C2) yields

$$\frac{\partial P_x}{\partial y} + \frac{\tau_I + \tau}{\delta} = 0 \tag{C6}$$

The boundary condition on P_x is given by substituting Eq. (C4) to Eq. (C3):

$$P_x\left(y = \bar{w}\right) = 2\tau \tag{C7}$$

Equations (C6), with the interfacial shear τ_I given by Eq. (C1), and the boundary condition (C7) solves for $P_x\left(y\right)$, which in turn determines τ_I.

First consider the case $P_x \geq P_{\min} = \tau / \mu$. This corresponds to a sticking interface and the interface shear stress is the shear strength of the metal: $\tau_I = \tau$. The equilibrium equation of the metal inside the channel reduces to

$$\frac{\partial P_x}{\partial y} + 2\frac{\tau}{\delta} = 0 \tag{C8}$$

The solution of Eq. (C8) with the boundary condition (C4) gives the pressure distribution as

$$P_x(y) = \begin{cases} P_m\left(1 - \dfrac{y}{\overline{w}}\right) + 2\tau, & 0 \leq y \leq \overline{w} \\[2mm] P_m\left(1 + \dfrac{y}{\overline{w}}\right) + 2\tau, & -\overline{w} \leq y \leq 0 \end{cases} \tag{C9a}$$

where $P_m = (w'/\delta)\tau$ is the maximum pressure at the center of the contact surface. The corresponding distribution of the pressure in the direction parallel to the interface is

$$P_y(y) = \begin{cases} P_m\left(1 - \dfrac{y}{\overline{w}}\right), & 0 \leq y \leq \overline{w} \\[2mm] P_m\left(1 + \dfrac{y}{\overline{w}}\right), & -\overline{w} \leq y \leq 0 \end{cases} \tag{C9b}$$

It is seen that for a sticking interface the pressures starts as smallest at the free edges of the plate and increases linearly towards the center of the plate, while the shear stress on the interface is the shear strength of the material.

Next consider the case $P_x < P_{\min} = \tau / \mu$. In this case the contact pressure on the interface is insufficient for the metal to stick onto the plug but instead it slips. The shear on the interface is the friction given by $\tau_I = \mu P_x$. Eq. (C2) now becomes

$$\frac{\partial P_x}{\partial y} + \frac{\mu P_x}{\delta} + \frac{\tau}{\delta} = 0 \tag{C10}$$

The solution of the differential equation (C10), subjected to the boundary condition given in Eq. (C7), is

$$\frac{P_x(y)}{\tau} = \left(2 + \frac{1}{\mu}\right)\left[\exp\left(\mu\frac{\overline{w} - y}{\delta}\right) - 1\right] + 2 \tag{C11}$$

The shear stress on the interface is then the friction given by

$$\frac{\tau_I(y)}{\tau} = (2\mu + 1)\left[\exp\left(\mu\frac{\overline{w} - y}{\delta}\right) - 1\right] + 2\mu \tag{C12}$$

It is seen that slip can occur (and hence the applicability of solutions given in Eq. (C11) and Eq. (C12)) only for low values of the friction coefficient: $\mu < 0.5$. For higher friction coefficient ($\mu > 0.5$), the friction on the whole interface, including the free surface ($y = \overline{w}$), is above the shear strength τ; consequently, the whole interface will stick and no slip can occur.
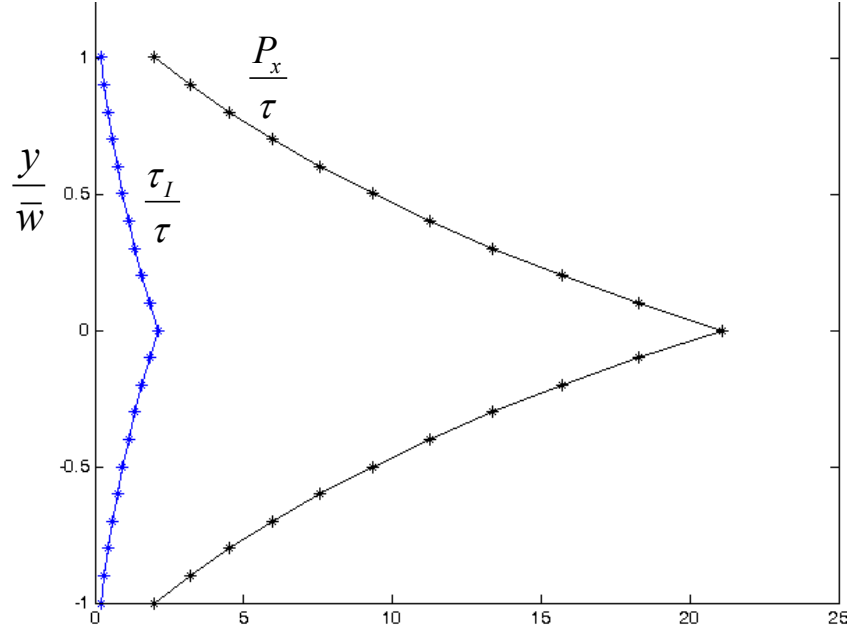
Figure 5. Distributions of the pressure and shear stress on the plug/workpiece interface where slip condition prevails ($\mu P_x \leq \tau$), as given in Eqs. (C11) and (C12).

As an example, consider a friction coefficient of $\mu = 0.1$. The distributions of the pressure and interface shear stress on the interface given by Eqs. (C11) and (C12) are shown in Fig. 5. The contact pressure starts with $P_x = 2\tau$ at the top and bottom of the interface (since $P_y = 0$ there) and increases exponentially towards the middle of the interface. At the center of the interface, $y = 0$, the contact pressure and shear reach their maximum values given by

$$\frac{P_x(y=0)}{\tau} = \left(2 + \frac{1}{\mu}\right)\left[\exp\left(\mu\frac{\overline{w}}{\delta}\right) - 1\right] + 2 \tag{C13}$$

$$\frac{\tau_I(y=0)}{\tau} = (2\mu+1)\left[\exp\left(\mu\frac{\overline{w}}{\delta}\right) - 1\right] + 2\mu \tag{C14}$$

It is seen from Eq. (C14) that for a slipping interface the shear at the center of the interface increases with the friction coefficient and with the depth of penetration (recall $\overline{w} = w'/2 = V_P t / (2\cos(\phi/2))$). For a given value of friction coefficient μ, there is a critical value of $\overline{w}$ below which the slip solution given by Eq. (C11) and Eq. (C12) applies and above which a part of the interface sticks and the pressure on the stick portion is given by Eq. (C9a). The critical depth of penetration is given next.

The critical depth

Consider the case in which the friction coefficient is low: $\mu < 0.5$. For a sufficiently large depth of penetration, the middle portion of the interface will stick and shear while the portions next to the free edges will slip. The

distance along the interface (from the free edges) at which the interface behavior changes from slip to stick can be found by setting τ_I in Eq. (C14) to τ:

$$\frac{d_c}{\delta} = \frac{1}{\mu}\ln\frac{2}{2\mu+1} \tag{C15}$$

The critical depth of penetration at which the interface behavior changes from purely slip to part slip and part stick is then given by

$$w_c = \frac{2\cos(\phi/2)}{\mu}\left(\ln\frac{2}{2\mu+1}\right)\delta \tag{C16}$$

For given values of μ and the channel thickness δ, the w_c critical depth of penetration given by defines the minimum depth of penetration below which the whole interface will only slip.

For penetration depth above this critical value (i.e., $w = V_p t > w_c$), there will be a portion of the interface that slips and over the rest the workpiece stick to the plug and shear. For the slip region, given by $(\bar{w}-d_c) \le y \le \bar{w}$), the pressure and shear are given by Eqs. (C11) and (C12); for the stick region, given by $0 \le y \le (\bar{w}-d_c)$, the pressure (normal to the channel) is given by Eq. (C9a) and the shear is simply the shear strength $\tau_I = \tau$.

D. Partial Melting

Partial (or local) melting due to the melting of copper-rich particles ($CuAl_2$) is considered in the current model. Partial melting starts in the metal when the temperature at the plug/workpiece interface reaches a critical value:

$$T = T_{LM} = aT_M \tag{D1}$$

where a is a constant. In the current model, we set $a = 0.95$. Upon local melting, the shear strength of the metal is reduced according to

$$\tau = \tau_y(1-f) \tag{D2}$$

where τ_y is the temperature-dependent yield strength of the solid metal given in Eq. (B1) and f is the volume fraction of the liquid phase. To keep the model simple, the evolution of the liquid phase is modeled by a constant rate process:

$$f = f_0 + b(t - t_{LM}) \tag{D3}$$

where f_0 is the volume fraction of the copper-rich particles and b is the growth rate and are the model parameter and t_{LM} is the time at which local melting occurs ($f_0 = 0.05$ and $b = 0.14$ are used in the model). As local melting progresses in the metals immediately next to the interface, the heat also conducts away into the workpiece and cools the interface, and as a result there is a limit to the volume fraction of the liquid phase. In the current model, the upper limit of the volume fraction of the liquid is set at $f_{max} = 0.25$.

$$\dot{\delta} = c \tag{D4}$$

The thickness of the channel stops grow as the heat is conducted away from the interface. This is modeled by setting an upper limit on δ : $\delta_{\max} \approx 50 \mu m$.

With the shear strength and the pressure on the interface solved, the torque, power, and energy applied to the plug can be calculated in a straightforward manner.

III. Comparison with Experimental Data

As an experimental validation the analytic model presented above was applied to some experimental plug welding data.[4] The experiment was run under the following conditions: $V_P = 27\,IPM$, $\omega = 6,300\,RPM$, $R = 0.6875\,in$, $W = 0.625\,in$. The plug used in the experiment is shown in Fig. 6. In the original model, a single constant taper angle ($\emptyset = 13^o$) was use for the plug. In the current model, a better (more realistic) model of the plug geometry was used-- the profile of the plug was modeled as two conical surfaces, each with its own taper angle ($\emptyset_L = 13^o$ and $\emptyset_U = 35.4^o$, respectively, for the lower and upper portion of the plug). In addition to the parameters specified by the experiment conditions and the strength model, the following thermal properties for aluminum 2219 were used in the calculations: $\rho = 2,830\,kg/m^3$, $c = 860\,J/\,kg \cdot K$, $K = 170\,W/\,m \cdot K$, and $T_m = 543\ ^oC$.

The results of interface temperature T and the material strength τ, using the parameters given above, are shown in Fig. 7. It is seen that the interface, starting at the ambient temperature and very high shear strength ($\tau \approx \tau_c = 26\,ksi$), is heated up rapidly by the intense heating flux ($q = \tau \omega R$) initially. As the interface gets hotter, the shear strength reduces, leading to smaller heating flux, and hence slower increasing in the interface temperature, as expected from physics. Figure 7 clearly show the transit nature of the plug-weld process, which is accounted for in the current model.

The model predictions of the torque, energy input, and pull (plunge) force as functions of the penetration time are compared with the experimental data,[4] as shown in Figs. 8-10a. Note time here is measured from when the penetration first occurs (i.e., plug starts to engage the work-piece metal). It is seen that the model gives reasonable predictions of the torque, energy input, and the pull force. The effects of incorporating local melting into the model can be seen in Fig. 10, where Fig. 10a is the results using the current, improved model and Fig. 10b shows the results from the original preliminary model. It is clear that the results of the current model are significantly better than the original one.

IV. Conclusion

The following are some observations and conclusions resulted from this study:

1. In plug welding processes the transient nature of heat transfer needs to be accounted for, whereas Friction Welding Process can be treated, to good accuracy, as steady-state.

2. By taking into consideration of local melting, the results of the current model match the experiment data more closely. In particular, the phenomenon of a drop in the plug pull force with penetration depth in the later stage of plug is now reproduced by the model.

It should be pointed out that we have only compared the model calculations with limited data. A more rigorous and thorough comparison with the data of experiments of various geometries and welding parameters needs to be done before the model can be considered a successful physical model for plug welding. We plan to conduct the comparisons in the future.

Acknowledgments

References

[1]Zuo, Q.K. and Nunes, A.C., Jr., "Mechanics Model of Plug Welding", *NASA Technical Report* M15-4833; Document ID: 20150019530, 2015, pp. 1-8.
[2]Crank, J., *The Mathematics of Diffusion*, Oxford University Press, 1975, Chap. 1.
[3]Davis, J.R., et al., *Metals Handbook* (10th Edition), Vol 2 (Properties and Selections: Nonferrous Alloys and Special-Purpose Materials, ASM International, 1990, pp. 79-81.
[4]Cleghorn, D., Hepburn, F., Girgis, A., Chen, P. and Littell, J., "SLS 0.625" Friction Pull Plug Weld Development", *NASA Technical Report* (to be published).
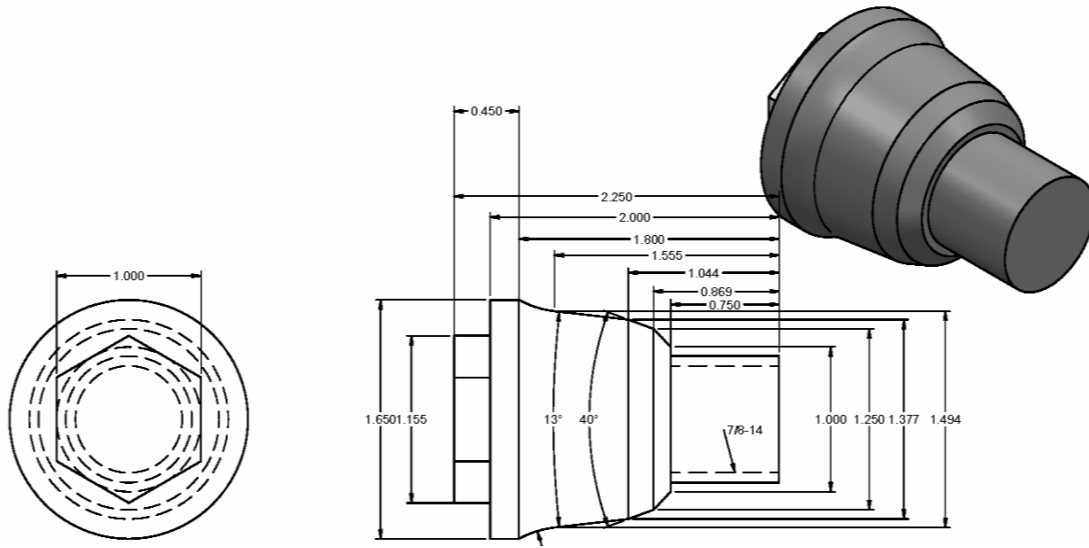
Figure 6. The details of the plug used in the experiment (the dimension is in inches).
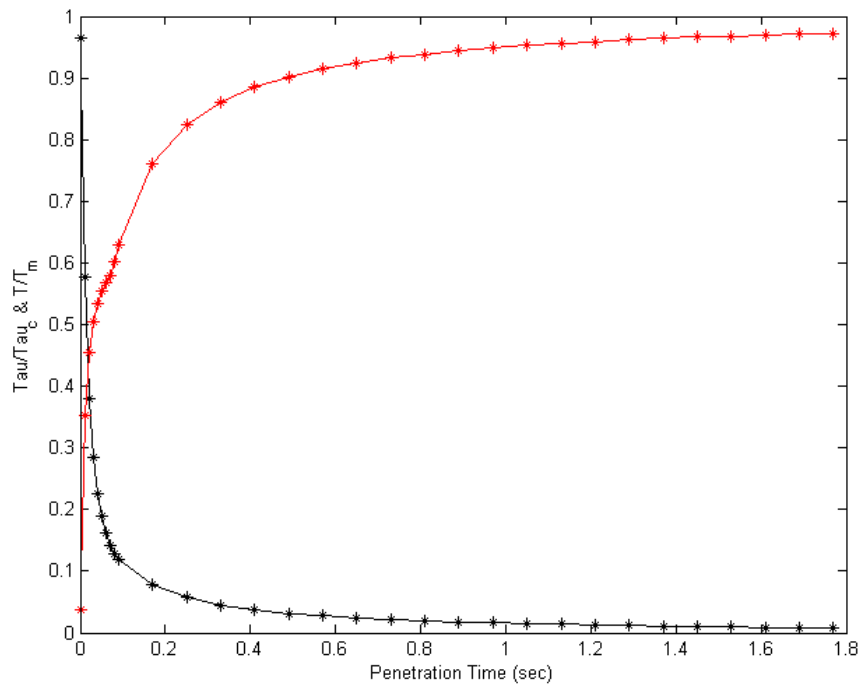

Figure 7. The normalized interface temperature (red) and material strength (black) as functions of penetration time. The temperature and strength are normalized by, respectively, the melting point ($T_m = 543\ ^oC$) and the strength of cold metal (τ_c).
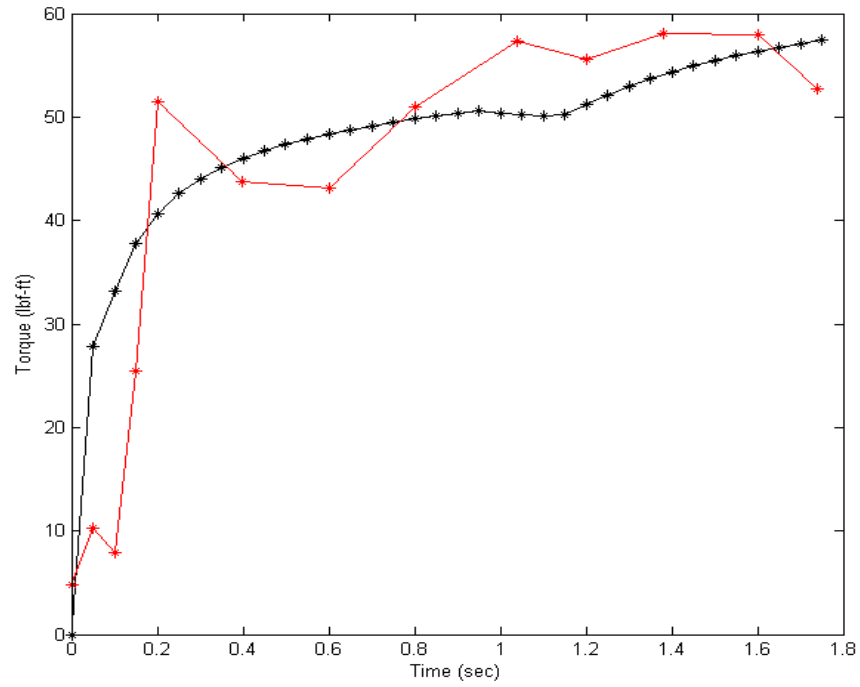
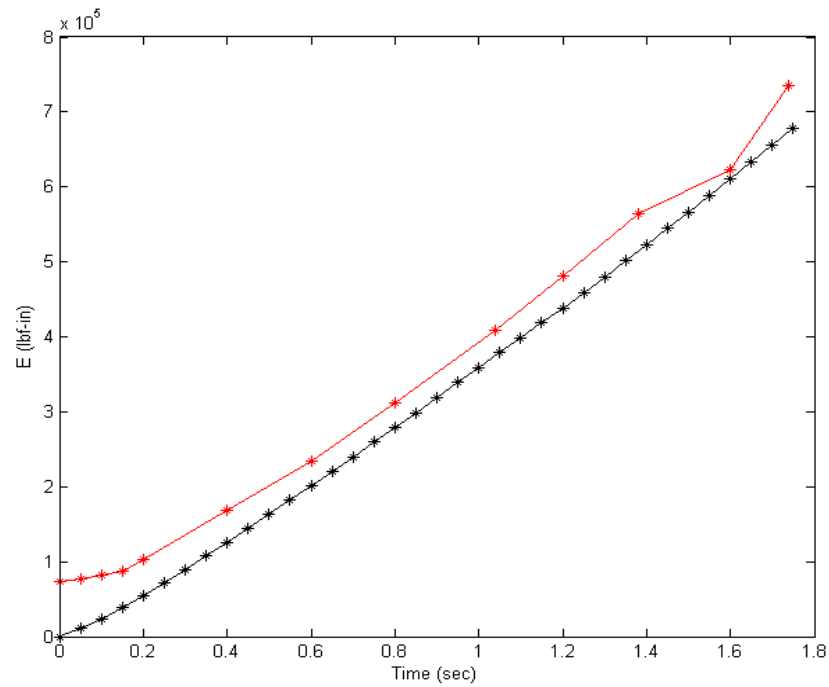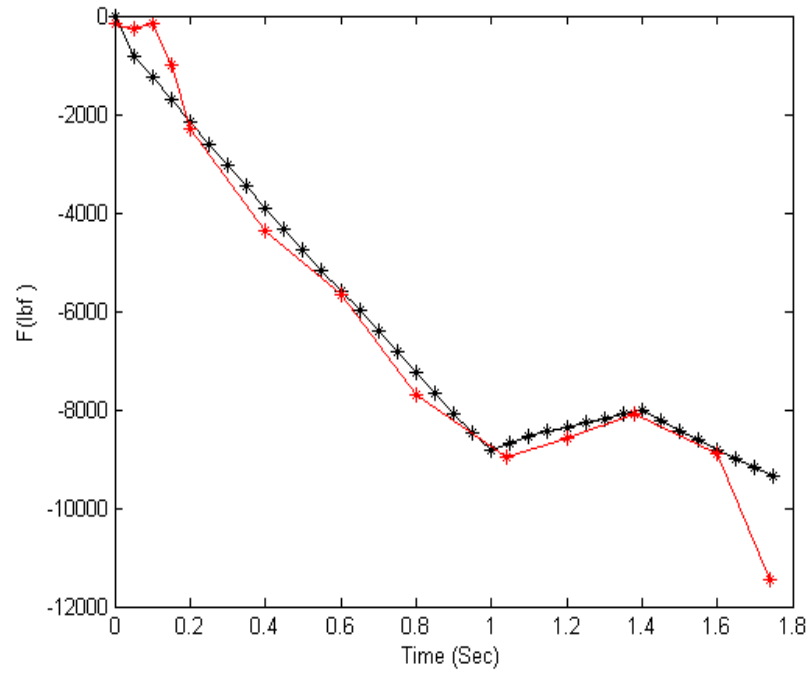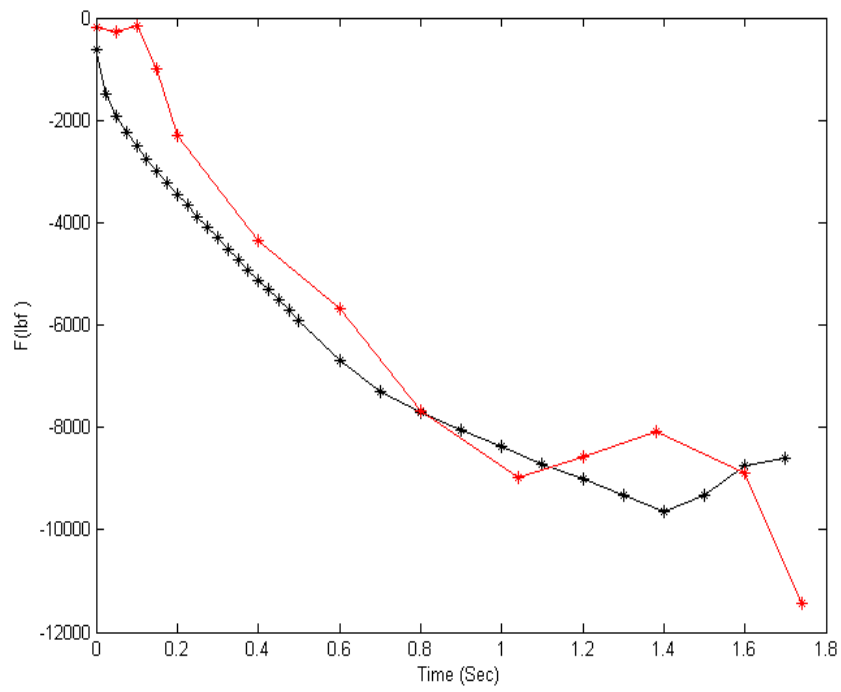**Figure 8. Comparison of the predicted torque with the data.**

Figure 9. Comparison of the predicted energy with the data. The data is shown as red.

(a)

(b)

Figure 10. Comparisons of the history of pull (plunge) force by the current model (a) and by the original model (b). The test data is shown as red.

APPENDIX A— NASA MARSHALL SPACE FLIGHT CENTER FACULTY FELLOWSHIP PROGRAM ANNOUNCEMENT

MARSHALL FACULTY FELLOWSHIP PROGRAM

JUNE 6, 2016 – AUGUST 12, 2016

Application Deadline February 15, 2016

- The Marshall Space Flight Center is offering Faculty Fellowships for qualified STEM faculty at U.S. colleges and universities to conduct research with NASA colleagues during a ten-week residential program in Huntsville, Alabama.
- Faculty Fellows will receive stipends of $15,000 (Assistant Professor, Research Faculty), $17,000 (Associate Professor), or $19,000 (Professor).
- A relocation allowance of $1,500 will be provided to those fellows who live more than fifty miles from MSFC and a $500 travel supplement for one round-trip.
- Applicants must be U.S. citizens who hold full-time teaching or research appointments at accredited U.S. universities or colleges.
- During the ten-week program, fellows are required to conduct their research on-site at the Marshall Space Flight Center.

Women and under-represented minorities, and persons with disabilities are encouraged to apply.

APPENDIX B—NASA MARSHALL SPACE FLIGHT CENTER FACULTY FELLOWSHIP PROGRAM DESCRIPTION

NASA Marshall Faculty Fellowship Program

<u>Program Description</u>

- The Marshall Faculty Fellowship program is a residential research experience. Fellows are required to conduct their research, during the ten-week program, on-site at the Marshall Space Flight Center.
- Participants cannot receive remuneration from other entities or other programs or other university or government sources during the Faculty Fellowship 10-week period.
- An oral presentation by the Fellow to the Marshall group with which s/he has been affiliated is required, near the end of the fellowship period.
- A written final report is required at the end of the Fellowship.
- A written evaluation of the program by the Fellow is expected at the end of the Fellowship.

<u>Eligibility</u>

- US citizen
- Full time teaching or research appointment at accredited US university or college.
- Fellowship is awarded for one summer period, but Fellow may apply again for a second year.
- Women, under-represented minorities, and persons, with disabilities are encouraged to apply.

<u>Selection</u>

The applications selected to be Faculty Fellows will be chosen by the Marshall group which has been assigned the area of investigation (concentration) chosen by the applicant.

<u>Marshall Collaborator</u>

A Marshall Collaborator will be identified to serve as the co-investigator and day-to-day contact. At the end of the ten-week period, the Faculty Fellow and the Marshall Collaborator will prepare a white paper summarizing the summer effort, including results and recommending follow-up work.

<u>Compensation</u>

Stipends for Faculty Fellows are set as follows for the 10-week period:
    Assistant Professors and Research Faculty $15,000
    Associate Professors $17,000
    Professors $19,000

A relocation allowance of $1,500 will be provided to fellows who live more than fifty miles from the Marshall Center.

A travel supplement of $500 will be provided to those fellows receiving the relocation allowance.

REPORT DOCUMENTATION PAGE

The public reporting burden for this collection of information is estimated to average 1 hour per response, including the time for reviewing instructions, searching existing data sources, gathering and maintaining the data needed, and completing and reviewing the collection of information. Send comments regarding this burden estimate or any other aspect of this collection of information, including suggestions for reducing this burden, to Department of Defense, Washington Headquarters Services, Directorate for Information Operation and Reports (0704-0188), 1215 Jefferson Davis Highway, Suite 1204, Arlington, VA 22202-4302. Respondents should be aware that notwithstanding any other provision of law, no person shall be subject to any penalty for failing to comply with a collection of information if it does not display a currently valid OMB control number.
PLEASE DO NOT RETURN YOUR FORM TO THE ABOVE ADDRESS.

1. REPORT DATE *(DD-MM-YYYY)*	2. REPORT TYPE	3. DATES COVERED *(From - To)*
01–03–2017	Technical Memorandum	

4. TITLE AND SUBTITLE	5a. CONTRACT NUMBER
Marshall Space Flight Center Faculty Fellowship Program	5b. GRANT NUMBER
	5c. PROGRAM ELEMENT NUMBER
6. AUTHOR(S)	5d. PROJECT NUMBER
N.F. Six, Program Director and G. Karr, Compiler*	5e. TASK NUMBER
	5f. WORK UNIT NUMBER

7. PERFORMING ORGANIZATION NAME(S) AND ADDRESS(ES)	8. PERFORMING ORGANIZATION REPORT NUMBER
George C. Marshall Space Flight Center Huntsville, AL 35812	M–1425

9. SPONSORING/MONITORING AGENCY NAME(S) AND ADDRESS(ES)	10. SPONSORING/MONITOR'S ACRONYM(S)
National Aeronautics and Space Administration Washington, DC 20546–0001	NASA
	11. SPONSORING/MONITORING REPORT NUMBER
	NASA/TM—2017–218234

12. DISTRIBUTION/AVAILABILITY STATEMENT
Unclassified-Unlimited
Subject Category 31
Availability: NASA STI Information Desk (757–864–9658)

13. SUPPLEMENTARY NOTES
Prepared by the Academic Affairs Office, Office of Human Capital
*The University of Alabama in Huntsville

14. ABSTRACT

The research projects conducted by the 2016 Faculty Fellows at NASA Marshall Space Flight Center included propulsion studies on propellant issues, and materials investigations involving plasma effects and friction stir welding. Spacecraft Systems research was conducted on wireless systems and 3D printing of avionics. Vehicle Systems studies were performed on controllers and spacecraft instruments. The Science and Technology group investigated additive construction applied to Mars and Lunar regolith, medical uses of 3D printing, and unique instrumentation, while the Test Laboratory measured pressure vessel leakage and crack growth rates.

15. SUBJECT TERMS
wireless sensors, propulsion, green propellant, materials, 3D printing, friction stir welds, instruments, solar neutrinos, gamma-ray polarimeter, lightning

16. SECURITY CLASSIFICATION OF:			17. LIMITATION OF ABSTRACT	18. NUMBER OF PAGES	19a. NAME OF RESPONSIBLE PERSON
a. REPORT	b. ABSTRACT	c. THIS PAGE			STI Help Desk at email: help@sti.nasa.gov
U	U	U	UU	232	19b. TELEPHONE NUMBER *(Include area code)* STI Help Desk at: 757–864–9658

National Aeronautics and
Space Administration
IS02
George C. Marshall Space Flight Center
Huntsville, Alabama 35812